Study of Ga, GaN, Li and LiF Laser Ablation Plumes using Spectroscopic and Fast Imaging Techniques

A Thesis submitted for the Degree of

Doctor of Philosophy

By

A.P. McKiernan B.Sc.

School of Physical Sciences

Dublin City University

Research Supervisor

Dr. J.-P. Mosnier

December 2003

Declaration

I hearby certify that this material, which I now submit for assesment on the programme of study leading to the award of Doctor of Philosophy, is entirely my own work and has not been taken from the work of others save and to the extent that such work has been cited and acknowledged within the text of my work.

Signed: Alan Mc Kiernan

ID No.: 92437460

Date: 30/01/04

To the memory of Margaret Jane
(11^{th} March 2003)

Contents

Abstract

The thesis describes the design and implementation of (1) a spatially resolved ultraviolet emission spectroscopy system and (2) an ultrafast imaging experimental setup to study the dynamics and composition of laser ablation plumes suitable for Pulsed Laser Deposition (PLD) of materials. These techniques allow the simultaneous recording of the plume absolute emission intensities up to 4 cm above the target surface, in the spectral range from 240 nm to 900 nm with a series of frames of the expanding plume, thus furnishing spatial, temporal an spectral information on the plume's evolution.

Emission spectra of Ga and GaN ablation plumes, in typical PLD conditions, were obtained with this system and are presented as a function of N_2 ambient gas pressure from 1×10^{-7} to 5 mbar and ablation laser wavelengths of 266, 355, 532 and 1064 nm . Atomic level populations and excitation temperatures are estimated from these spectra. A series of temporally resolved images of the luminous plume expanding into N_2 pressures of 1×10^{-5}, 1×10^{-2}, 1×10^{-1}, 1 and 5 mbar were recorded and plume velocities are estimated from these data.

Emission spectra are also presented for Li and LiF plumes expanding into vacuum and the corresponding atomic level populations and excitation temperatures were estimated. Ultrafast images were recorded as a function of laser wavelength (266, 532 and 1064nm) and spotsize (115×80, 340×250, 90×525, 1000×000 and 2000×2000 μm) yielding plume velocities. An anomalous emission line ratio feature of these spectra was observed and discussed.

Acknowledgements

I would like to express my gratitude to my supervisor Dr. Jean-Paul Mosnier for his patience and enthusiasm over the years. His constant availability and eagerness for discussion was greatly appreciated.

To the other members of the group, Prof. Eugene Kennedy, Dr. John Costello and Dr. Paul van Kampen, thanks for the advice and encouragement over the past four years. Thanks to Dr. Mark Stapleton, soon to be Dr. Pat Yeates and Dr. John Hirsch for all the craic and sessions and to Eoin, Jonathan, Kevin, Ricky, Adrian, Jaione and Nely for the coffee breaks.

To the technicians; Des Lavelle for all the last minute metalwork jobs, Pat Wogan for the electronics components, Victor Fagg for the lending of equipment and to Alan Hughes and Ray Murphy for the extra diskspace and privileges.

I would also like to thank the numerous other people from whom I have borrowed various pieces of equipment down through the years. To the rest of the DCU physics community thanks for all their assistance at various times.

Thanks, also, to my family for their support, encouragement, lifts and the boxty - very much appreciated. Finally to Valérie, for her patience, support and creole cuisine; "merci in bon peu".

Acknowledgements

I would like to express my gratitude to my supervisor Dr. Jean-Paul Mosnier for his patience and enthusiasm over the years. His constant availability and eagerness for discussion was greatly appreciated.

To the other members of the group, Prof. Eugene Kennedy, Dr. John Costello and Dr. Paul van Kampen, thanks for the advice and encouragement over the past four years. Thanks to Dr. Mark Stapleton, soon to be Dr. Pat Yeates and Dr. John Hirsch for all the craic and sessions and to Eoin, Jonathan, Kevin, Ricky, Adrian, Jaione and Nely for the coffee breaks.

To the technicians; Des Lavelle for all the last minute metalwork jobs, Pat Wogan for the electronics components, Victor Fagg for the lending of equipment and to Alan Hughes and Ray Murphy for the extra diskspace and privileges.

I would also like to thank the numerous other people from whom I have borrowed various pieces of equipment down through the years. To the rest of the DCU physics community thanks for all their assistance at various times.

Thanks, also, to my family for their support, encouragement, lifts and the boxty - very much appreciated. Finally to Valérie, for her patience, support and creole cuisine; "merci in bon peu".

Chapter 1

Introduction

1.1 Motivation

Todays computers and telecommunications devices will reach the physical limit of chip miniaturisation in the not too distant future. Optical devices, such as optical computers, will replace microelectronics as the technology of choice for Information and Communication Technology (ICT). However, silicon (Si), the most important and widely used semiconductor in microelectronics, is not an efficient photonic material due its indirect bandgap and, so, is not widely used in optoelectronic applications.

Semiconductor light-emitting devices and lasers, emitting red or infra-red light, have been used in products from optical communications systems to compact disc players. But these and other applications have been limited by the lack of materials that can emit blue light efficiently. For example, one needs to combine at least three colours, usually red, green and blue, to produce any visible colour suitable for full-colour displays. A white light-emitting device made from such a combination would be more durable and use less power than conventional bulbs or fluorescent lamps [1].

There are many other applications that could benefit from blue light-emitting devices. The shorter wavelength means that the light can be focused more sharply, which would increase the storage capacity of magneto-optical and optical

disks. DVDs currently rely on red semiconductor lasers and have a data capacity of about 4.7 Gbytes, compared with 0.65 Gbytes for compact discs. By moving to blue wavelengths, the capacity could be increased to 15 Gbytes.

Efficient blue-emitting devices were first demonstrated in 1995 [2] after about 30 years of research by groups around the world. They have been made using materials from the III and V groups of the periodic table which give semiconductors with a wide bandgap. The bandgap of a semiconductor is a measure of the amout of energy required to move an electron from the valence band, in which electrons are not free to conduct, to the conduction band, where they are. If, in falling from the conduction to the valence band, an electron emits a photon of light, the higher the bandgap of the material, the higher that photon's energy will be [3]. This explains why compounds of the Gallium Nitride(GaN) system, with bandgaps from $1.9-6.2eV$ [4] emit from $\sim 700nm$ down to $\sim 230nm$ (see figure 1.1).

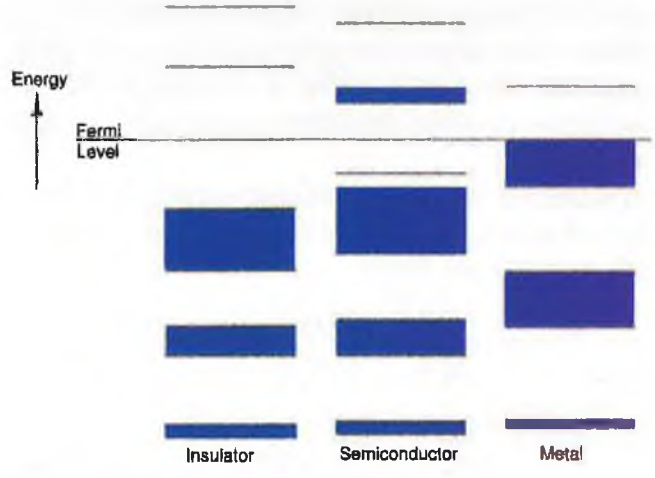

Figure 1.1: Schematic of energy bands in various material classes.

Another photonics material of great interest is lithium niobate ($LiNbO_3$). This is a well known material with excellent nonlinear optical properties. These make it ideally suited for applications in harmonic generation, optical parametric

oscillation and electro-optic modulation such as fast optical switches and electro-optically-controlled multiplexers and demultiplexers.

Pulsed Laser Deposition (PLD) is a well established technique for the preparation of thin films for a wide range of materials. More than 120 different materials had been grown using this technique by 1991 [5], most notably high temperature superconductors [6, 7], diamond-like carbon (DLC) [8, 9, 10] and ferroelectrics [6, 11]. The basic idea of the deposition process is quite simple (Figure 1.2). A pulsed laser vaporises the surface of a target creating a plasma which expands in vacuum or a reactive atmosphere, before condensing on a suitable substrate. The properties of the film produced in such a way then depend on the substrate temperature, laser fluence, target to substrate distance, the nature and pressure of the reactive gas in the deposition chamber and, of course, the target material.

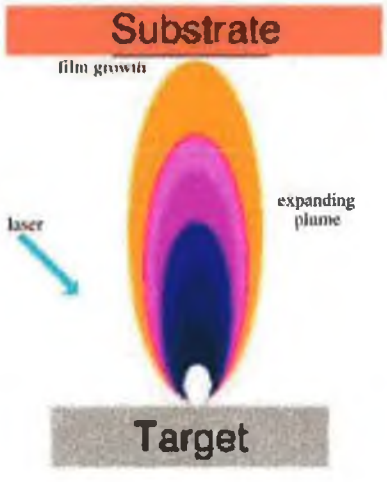

Figure 1.2: Schematic of Pulsed Laser Deposition.

PLD allows deposition of multicomponent materials by employing a single target and can also be utilised by loading multiple targets on a rotating holder into a chamber, which can be used to expose different targets to the laser beam, thereby enabling the in-situ growth of heterostructures.

1.2 Objectives

Recently, PLD has attracted much attention for the synthesis of thin films of III-nitride materials, in particular GaN [12, 13, 14]. Studies on PLD of GaN have examined the quality of the deposited film (Optical, Crystallographic and Electrical properties) and the growth parameters such as ambient gas, pressure, laser fluence, repetition rate, target properties (Ga or GaN), substrate temperature and target-substrate distance [12, 13, 14, 15, 16, 17].

However, regarding diagnostics of the ablation plumes of GaN, no detailed studies have been carried out. Since the plume travels from target to substrate and contains much of the material to be deposited, then knowledge of its constituents and dynamics should bring a better understanding of the whole PLD process. Thus it is important to study the influence of typical PLD growth parameters, such as the laser wavelength, background pressure or target material, on the properties of the plume.

As part of this work we have used emission spectroscopy to investigate differences in the dynamics of plumes created in some of these conditions (e.g. laser wavelength and fluence, target composition, pressure of background gas). We have realised a special spectroscopic apparatus with imaging capability for this study. This provided spatial information on the state of ionisation and excitation of the plume between target and substrate (typically 0 to 40 mm). Fast ICCD imaging was also used to provide temporal information to complement the spectroscopy.

Although PLD has proven to be successful in the synthesis of many materials, low Li content $LiNbO_3$ remains a barrier to fabricating device quality lithium niobate films [18]. Films of lithium flouride (LiF), another lithium-based compound, are under investigation due its suitability as an active tunable waveguide in the green-red visible region. To further understand lithium ablation, we have studied ablation plumes of lithium metal and lithium flouride using emission spectroscopy.

1.3 Organisation of thesis

This Thesis comprises 6 chapters.

Chapter 2 presents some fundamentals of laser ablation. Theoretical considerations in the experimental configurations are described. A summary of the current developments in laser ablation of Ga, GaN, Li and LiF materials is presented.

Chapter 3 presents details on the emission spectroscopy, ultrafast imaging and ion probe experimental setups and the corresponding measurement techniques. Chapter 4 presents the results and analysis of the work with Ga and GaN, chapter 5 presents the results and analysis of my work with Li and LiF and chapter 6 presents the conclusions of the work and future prospects.

Chapter 2

Laser Ablation of Condensed Target Materials

2.1 Fundamentals of Laser ablation

2.1.1 Laser-target interaction

Laser light-material interaction

When laser radiation is absorbed in the surface region of a solid target the electromagnetic radiation is initially converted into electronic excitation. When the EM field of the radiation reaches the metallic target surface it penetrates only to a very short depth called the skin depth. This is given by [19]:

$$\delta = \left(\frac{2}{\pi \frac{c}{\lambda} \mu_0 \sigma'} \right)^{1/2} \tag{2.1}$$

where σ' is the electrical conductivity of the material (Ω^{-1} m^{-1}), μ_0 the permeability of free space (Hm^{-1}), λ is the laser radiation wavelength (m) and c is the velocity of light (ms^{-1}).

From table 2.1, which lists δ values for Nd:YAG laser radiation incident on gallium metal, we can see that the skin depth is of the order of a few nanometres.

$\lambda_{laser}(nm)$	$\delta(nm)$
1064	≈ 15.7
532	≈ 11.0
355	≈ 9.1
266	≈ 7.8

Table 2.1: Skin depth in Gallium metal.

The electric field amplitude E of the incoming laser radiation is given by [20]:

$$E = \left(\frac{2\Phi}{cn\epsilon_0}\right)^{1/2} \tag{2.2}$$

where Φ is the irradiance (Wm^{-2}, ϵ_0 the permittivity of free space (Fm^{-1} and n is the refractive index. So a material with a refractive index of 2 absorbing radiation of $5 \times 10^8\ Wm^{-2}$ power density will be subjected to a field strength of $\sim 4 \times 10^5\ Vm^{-1}$. When such fields interact with conduction electrons, heating, evaporation and ionisation occur before the end of the laser pulse.

In metals thermal conduction carries the heat, initially concentrated in the skin depth, deeper into the metal lattice to a depth of l_T, known as the thermal diffusion length, given by [21]

$$l_T = 2\sqrt{\kappa\tau} \tag{2.3}$$

where κ is the thermal diffusivity (cm^2s_{-1} and τ is the laser pulse duration (s). This results in the emission of thermal particles as the vaporisation front moves with a velocity of l_T/τ to a depth of l_T.

In ablation of semiconductors at the power densities under consideration here, it is desirable that the photon energy is greater than the bandgap E_g of the semiconductor. Thus, when an electron is excited from the valence to the conduction band an electron-hole pair is formed, which, on recombination, gives up its energy to the lattice, thus heating it. However, a small number of thermal electrons in the valence band are sufficient to absorb the laser in the material with consequent heating, evaporation and ionisation.

In the case of insulators, the laser photon energy is considerably less than the bandgap of the material and the material is transparent to the radiation. Nevertheless free electrons are produced, for example via multiphoton absorption. Once the initial electrons are produced the laser begins to be absorbed, proceeding as in the case of metals and semiconductors.

Interaction regimes

Depending on the time scale of the absorption and heating processes just described and also the irradiance, a number of different interaction regimes may be defined [22]. These are given in table 2.2 [23].

low	$I < 10^6$ Wcm^{-2}
medium	10^6 Wcm$^{-2} < I < 10^{12}$ Wcm^{-2}
high	$I > 10^{12}$ Wcm^{-2}

Table 2.2: Laser-material interaction regimes.

For gallium, which has a thermal diffusivity of 0.185 cm$^2 s^{-1}$, heat can penetrate only about 7×10^{-5} cm during a pulse duration of 6 ns (equation 2.3). However, if the pulse lasts 60 μsecs, then heat can penetrate to about 0.7 cm into the same metal. So, from equation 2.3 we can define a thermal time constant for a material of thickness x as $\frac{x^2}{4\kappa}$ [24].

The laser pulse duration should be close to the thermal time constant value for melting and welding applications. If the pulse duration is appreciably shorter than this or the irradiation is higher, then vaporisation occurs which can be applied to drilling. Both of these effects take place in the low irradiance regime.

In the medium irradiance regime laser absorption in the vapor becomes important. The amount of vaporised material is less than before but this material is heated and ionised by the laser to form a plasma. This is the regime of PLD applications.

In the high irradiance regime the laser light is significantly absorbed by the plasma and thus decoupled from the target surface. Consequently, most of the

laser pulse energy is used to heat the plasma to high temperatures, becoming highly ionised. For example, research into inertial confinement fusion falls into this regime.

Plasma formation and interaction with laser light

In nanosecond laser ablation of metals in vacuum, at irradiances higher than the irradiance threshold for evaporation, an ionised vapour (plasma) is formed above the target surface which can be heated and further ionised. In simplest terms plasma is matter in a state of ionisation, either partial or complete, i.e. it is a "gas" of electrons and ions. This "gas" is assumed to be quasi-neutral

$$n_e = \sum(n_Z \times Z) \tag{2.4}$$

where n_e is the electron number density and n_Z is the density of ions of charge number Z.

Unlike in neutral gases the Coulomb forces between charged particles in a plasma are both relatively strong and long-ranged. For this reason considerable numbers of particles in a plasma interact with one another and they tend to respond collectively to any disturbances. This dominance of collective effects is often quantified in terms of a sphere with a radius known as the Debye length, λ_D, beyond which the effects on a charge are screened. This radius is given by [25]:

$$\begin{aligned} \lambda_D &= \left(\frac{\epsilon_0 k_B T}{n_e e^2}\right)^{\frac{1}{2}} \\ &= 69.0\left(\frac{T}{n_e}\right)^{\frac{1}{2}} \end{aligned} \tag{2.5}$$

where the temperature, T, is in K, the electron number density, n_e, is in m^{-3} and λ_D is in units of m.

The dominant laser photon absorption process for a plasma obtained in our conditions is collisional absorption (also known as Inverse Bremsstrahlung). Other absorption mechanisms usually having much smaller cross sections, for example photoionisation [26] or resonant absorption (non-linear effect). Inverse

Bremsstrahlung (IB) is a process whereby electrons accelerated by the electric field of the focused laser light undergo momentum transfer collisions with ions via their Coulomb interaction. The absorption coefficient for IB is given by [27]

$$\kappa_\nu = \frac{7.8 \times 10^{-9} Z n_e^2 ln\Lambda\,(\nu)}{\nu^2\,(k_B T)^{\frac{3}{2}}} \left(\frac{1}{\left(1 - \frac{\nu_p^2}{\nu^2}\right)^{\frac{1}{2}}} \right) \tag{2.6}$$

where $k_b T$ is in eV, Z is the ionic charge, n_e is the electron number density, ν and ν_p are the wave and plasma frequencies, respectively, $\Lambda(\nu)$ is the minimum of $v_T/\omega_p p_{min}$ and $v_T/\omega p_{min}$, v_T is the thermal velocity of the electrons and p_{min} is the minimum impact parameter for electron-ion collisions ($p_{min} \cong$ maximum of $Ze^2/k_B T$ or $h/2\pi(m_e k_B T)^{1/2}$).

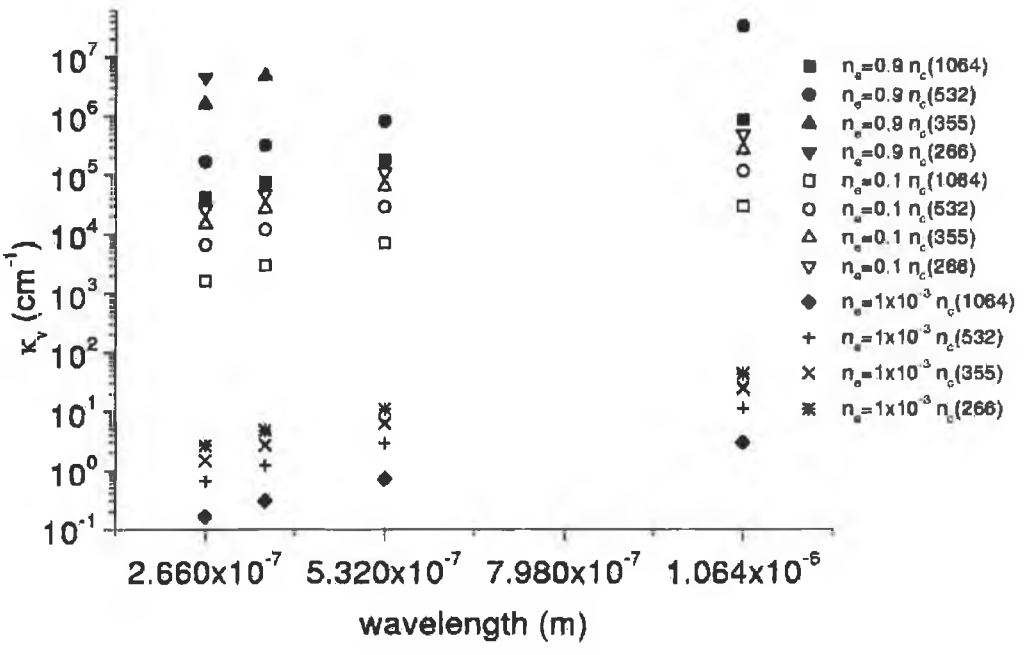

Figure 2.1: Dependence of κ_ν on wavelength for various electron densities at $T = 3$ eV.

At the beginning of the laser absorption process $\omega \gg \omega_p$ and the factor in large brackets in equation 2.6 may be taken as unity (where $\omega = 2\pi\nu$ and $\omega_p = 2\pi\nu_p$). Therefore the rate of absorption varies as n_e^2/ω^2 (figure 2.1). As

the energy is absorbed the electron temperature increases and produces further ionisation which increases n_e.

As the absorption increases and, thus, the ionisation, ω_p approaches and becomes comparable to ω_L (laser light frequency) at a surface with a density n_c, known as the critical density, at some distance into the plume. The critical density of a laser produced plasma may be determined using the equations [25]:

$$\begin{aligned} n_c(m^{-3}) &= \frac{\epsilon_0 m_e \omega_L^2}{e^2} \\ (m^{-3}) &= 3.14 \times 10^{-14} \omega_L^2 \\ (cm^{-3}) &= \frac{10^{21}}{\lambda_L^2} \end{aligned} \tag{2.7}$$

where ϵ_0 is the permittivity of free space, m_e is the electron mass, ω_L is the angular frequency of the laser radiation ($= \omega_p$, plasma frequency, at n_c), λ_L is the laser wavelength expressed in μm and e is the electronic charge. At this surface the plasma is opaque to the incoming laser radiation and it is reflected out again and in the region immediately before this surface the absorption coefficient becomes very large.

As a result of all this the laser radiation may no longer reach the target surface until the plasma has expanded sufficiently for n_e to drop below n_c. Equation 2.6 shows that the IB process is less efficient in the UV than in the visible or IR regions of the spectrum due to the ω^{-2} dependence. Table 2.3 lists n_c values for Nd:YAG laser radiation.

$\lambda_{laser}(nm)$	$n_c(cm^{-3})$
1064	$\approx 8.8 \times 10^{20}$
532	$\approx 3.5 \times 10^{21}$
355	$\approx 7.9 \times 10^{21}$
266	$\approx 1.4 \times 10^{22}$

Table 2.3: Critical density for Nd:YAG laser radiation.

2.1.2 Expansion of a laser ablation plume

During a typical PLD laser pulse a layer of ablated material is formed above the target. This layer then expands into its vacuum or atmospheric environment. These two regimes will be described in the following paragraphs.

Plume expansion in vacuum

Analytical solutions to the set of hydrodynamic equations describing the expansion of a laser ablation plume have been found [28, 29]. The plasma is assumed to behave as a high-temperature high-pressure gas initially expanding isothermally for the duration of the laser pulse, and subsequently expanding adiabatically after termination of the laser pulse. The isothermal expansion in vacuum during the time interval of the laser pulse is described by [28]

$$X(t)\left(\frac{1}{t}\frac{dX}{dt}+\frac{d^2X}{dt^2}\right)=Y(t)\left(\frac{1}{t}\frac{dY}{dt}+\frac{d^2Y}{dt^2}\right)=Z(t)\left(\frac{1}{t}\frac{dZ}{dt}+\frac{d^2Z}{dt^2}\right)=\frac{k_BT_0}{M} \tag{2.8}$$

where T_0 is isothermal temperature and $X(t)$, $Y(t)$ and $Z(t)$ are the dimensions of the expanding plume in the directions x, y and z, with x and y on the target surface and z along the normal to the target surface. These solutions can only be obtained for Gaussian pressure and density profiles.

The adiabatic expansion of an isothermal (uniform temperature profile) plume in vacuum after the laser pulse has terminated is given by [28]

$$X(t)\frac{d^2X}{dt^2}=Y(t)\frac{d^2Y}{dt^2}=Z(t)\frac{d^2Z}{dt^2}=\frac{k_BT_0}{M}\left(\frac{X_0Y_0Z_0}{X(t)Y(t)Z(t)}\right)^{\gamma-1} \tag{2.9}$$

where γ is the ratio of specific heat capacities at constant pressure and volume, T_0 is the temperature at the end of the laser pulse, M is the mass of one particle of the plume species and X_0, Y_0 and Z_0 are the plume dimensions at the end of the laser pulse.

During the adiabatic expansion phase the thermal energy gained by the plasma during the isothermal phase is transferred to the plume species as kinetic energy. Equation 2.9 predicts that the plume acceleration will be greater along the smaller

initial dimension. After a brief acceleration phase the motion of the plume becomes inertial.

Anisimov et al [29] have considered the case of an isentropic plume (uniform entropy profile) and also provide analytical solutions assuming elliptical pressure and density profiles. The inital heating phase by the laser was not considered by these authors.

Plume expansion in background gas

The interaction of laser ablation plumes with background gases, at typical pressures of the order of a few mbar or less, can result in the formation of molecular species due to gas-phase reactions between ablated material and ambient gas species. In reactive PLD these interactions are manipulated to produce novel species and materials. Background gas effects also play an important role in determining the spatial and velocity distributions of the species in the expanding plume.

As a laser ablation plume expands in a background gas it expends energy in the heating and moving of the gas (depending on gas pressure). This results in a deceleration of the plume-gas contact front. At higher pressures the plume dynamics differ from that of the free expansion regime observed in vacuum. Several models have been proposed to explain the expansion of PLD plumes into ambient gases [30, 31].

For a sufficiently high gas pressure, when the ablated mass is small compared to the mass of the background gas in motion, a shock front is formed and its position as a function of time is given by [31]

$$z(t) = \xi_0 \left(\frac{E_0}{\rho_0} \right)^{1/5} t^{2/5} \tag{2.10}$$

where E_0 is the laser energy deposited in the initial vapour, ρ_0 is the background gas density and ξ_0 is a constant (see figure 2.2).

At low pressures, when the ejected mass is much greater than the mass of the background gas set in motion, the drag force model can be applied. Here, the

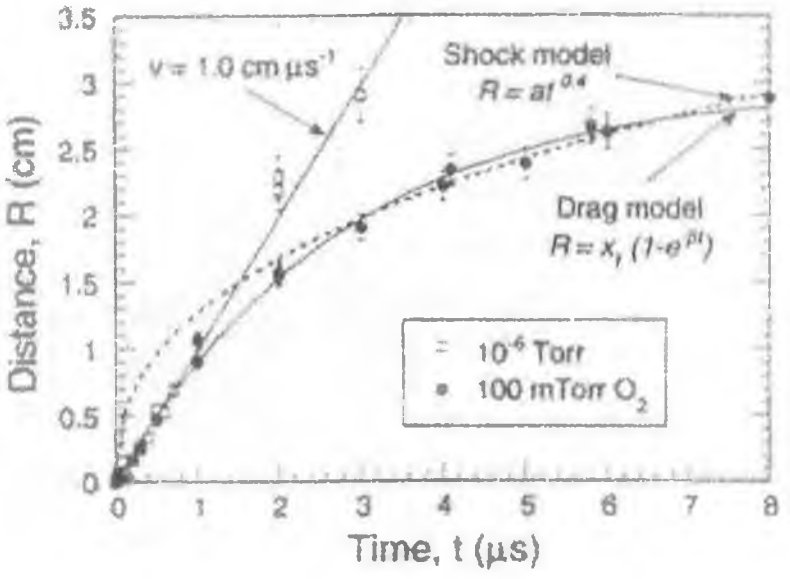

Figure 2.2: Plot of plume edge position vs time with Shock and Drag model fits after [30].

viscous force is proportional to the velocity of the ejected material. The equation of motion is $a = -\beta v$ and the plume propogation can be written as [30]

$$v = v_0 exp(-\beta t) = v_0 - \beta z \tag{2.11}$$

$$z(t) = z_f[1 - exp(-\beta t)] \tag{2.12}$$

where $z_f = v_0/\beta$ is the stopping distance and β is the slowing coefficient (see figure 2.2).

If the motion is high-speed another form of the drag model can be applied. Here the slowing force is proportional to the square of the velocity. The equation of motion is $a = -\beta' v^2$ and one obtains [32]

$$z(t) = \frac{1}{\beta'} ln\,(1 + \beta' v_0 t) \tag{2.13}$$

2.1.3 Plasma equilibrium

Ablation plumes seldom achieve thermodynamic equilibrium. Although the departure may be small, a system to which a pulse is added or subtracted is, at least momentarily, out of total thermodynamic equilibrium. Equilibria exist that are not complete thermodynamic equilibria.

Local thermodynamic equilibrium

Thermodynamic equilibrium may be restored via collisions. Since relaxation time increases with increasing size of a system, separate small parts of a system will reach a state of internal equilibrium long before they equilibrate with each other. Therefore, thermodynamic equilibrium is first restored locally and is called local thermodynamic equilibrium (LTE). At sufficiently high densities, collisional processes, especially those involving electrons, play a more important role than radiative processes in determining the excited state populations. LTE requires that the free electrons are distributed according to a Maxwellian velocity distribution given by [25]:

$$f(v) = n_e \left(\frac{m_e}{2\pi k_B T_e}\right)^{\frac{3}{2}} exp\left(\frac{-m_e v^2}{2k_B T_e}\right). \tag{2.14}$$

LTE also requires that the bound electrons occupy discrete levels according to a Boltzmann distribution given by [19]:

$$\frac{n_k}{n} = \frac{g_k}{U(T)} exp\left(\frac{-E_k}{k_B T_e}\right) \tag{2.15}$$

where k denotes the upper level, n is the population density and n_k the population in the k^{th} level, g is the statistical weight and E_k the energy of the k^{th} level. The partition function $U(T)$ is given by [19]:

$$U(T) = \sum g_i \left(\frac{-E_k}{kT}\right). \tag{2.16}$$

The free particle densities are required to follow the Saha equation given by [19]:

$$\frac{n_e n_Z}{n_{Z-1}} = 6 \times 10^{27} T_e^{\frac{3}{2}} exp\left(\frac{-\chi(Z-1)}{T_e}\right) \tag{2.17}$$

where $Z = 1$ for a singly ionised atom, $\chi(Z-1)$ is the ionisation energy of $Z-1$ times ionised atoms in eV and T_e is in eV.

For the LTE model to apply the plasma electron density must be sufficiently high for collisional de-excitation to be at least, say, ten times more probable than radiative decay for all transitions. One can show that this is equivalent to the requirement that [19]

$$N_e \geq 10^{12} T_e^{\frac{1}{2}} \chi^3(i,k) \tag{2.18}$$

where T_e is in K, $\chi(i,k)$ is the largest energy gap, in eV, between adjacent levels of the atoms and ions in the plasma and N_e is in units of cm^{-3}. In an optically thick plasma LTE is valid at lower densities due to radiation being closer to equilibrium.

When collisions occur, a Knudsen layer may be formed in the vicinity of the surface area of the irradiated material [33]. Within this layer, which extends up to a few mean free paths from the target surface, a highly non-equilibrium collision process develops and results in a transition from the half-range Maxwell-Boltzmann velocity distribution of equation 2.14 to a full-range Maxwell-Boltzmann distribution in a centre of mass coordinate system. In this case equation 2.14 contains a centre of mass velocity term and the flight distributions show a shift along the normal to target surface given by [33]:

$$F(v) = \frac{A}{v^3} exp\left(\frac{-m\left(v - v_K\right)^2}{2k_B T_K}\right) \tag{2.19}$$

where T_K stands for the Knudsen layer temperature and v_K is the centre of mass velocity.

Coronal equilibrium

In very low density plasmas, such as those found in the solar corona, equilibrium is maintained between collisional excitation and ionisation from the ground state and radiative de-excitation and recombination from the upper levels to all lower levels. As the rates of the collisional ionisation and radiative recombination processes are proportional to electron density, the populations of the various ion

species in the plasma are independent of electron density. The Saha equation no longer holds but is replaced by the coronal equation given by [19]:

$$\frac{N_{Z+1}}{N_Z} = \frac{S(Z,T_e)}{\alpha_r(Z+1,T_e)} \tag{2.20}$$

where $S(Z,T_e)$ is the collisional ionisation coefficient and $\alpha_r(Z+1,T_e)$ is the radiative recombination coefficient [34]. Interpreting data within coronal model limits will depend strongly on cross-sections used for $S(Z,T_e)$ and $\alpha_r(Z+1,T_e)$.

Collisional radiative equilibrium

In intermediate density plasmas neither LTE or CE models are valid. The coronal model, modified to take into account collisional transitions from the higher bound levels as well as radiative decay, and three-body recombination as well as radiative recombination, is known as the Collisional Radiative model. Using this model we have [35]

$$\frac{N_{Z+1}}{N_Z} = \frac{S(Z,T_e)}{\alpha_r(Z+1,T_e) + N_e\alpha_{3b}(Z+1,T_e)} \tag{2.21}$$

where α_{3b} is the coefficient for three-body recombination. This model is particularly appropriate in the $10^9 - 10^{11}$ Wcm^{-2} irradiance regime for medium to high atomic numbers. For low density plasmas $N_e\alpha_{3b} \ll 1$ and the CR model reduces to the CE model. For high densities the CR model approaches the LTE model.

2.2 Emission and absorption of radiation

A spectral line has a characteristic profile which is influenced by the conditions existing in the source. This profile can be used to ascertain local conditions in the source, for example temperature and density. Great care should be exercised when doing so, to remove unwanted contributions to the profile due to instrumental effects.

2.2.1 Einstein coefficients and the line profile

The absorption or emission of a spectral line is determined by the population of the lower or the upper level of the line, respectively, and by Einstein's transition probabilities and, in the case of absorption, by the intensity of the radiation field. Assuming thermal equilibrium, the relationships between the Einstein coefficients are provided by the application of the principle of detailed balancing and gives [19]:

$$\begin{aligned} A_{ki} &= \frac{g_i}{g_k} B_{ik} \frac{8\pi h\nu^3}{c^3} \\ B_{ki} &= \frac{g_i}{g_k} B_{ik} \end{aligned} \tag{2.22}$$

where A_{ki} is the Einstein A coefficient for spontaneous emission, B_{ki} the Einstein B coefficient for stimulated emission, g_i and g_k are the statistical weights of the lower and upper levels respectively. The Einstein coefficients are constants which depend only on the atomic properties and not on the actual situation of the atom, despite the inital assumption of thermal equilibrium. Thus 2.22 is valid even in the absence of thermal equilibrium.

The emission coefficient ϵ_ω is defined as the radiant energy emitted by a unit volume of the radiating gas per unit time, per unit solid angle, and per unit frequency, see figure 2.3. This can be resolved into a discrete and a continuous component [19]:

$$\varepsilon(\omega) = \varepsilon_L(\omega) + \varepsilon_C(\omega) \tag{2.23}$$

where $\varepsilon_L(\omega)$ contains the spontaneously emitted energy within the spectral line. This energy emitted within a line per second and per cm^{-2} is given by [19]:

$$\int_{line} \varepsilon_L(\omega) d\omega = \frac{h\omega}{4\pi} A_{ki} n_k \tag{2.24}$$

where n_k is the number of atoms per cubic centimetre in the upper quantum level k.

The linear absorption coefficient, $\kappa(\omega)$, is defined as the attenuation, $\Delta\phi$, of the intensity, ϕ, across an optical path (see figure 2.3), Δx, and is given by [19]

$$\kappa(\omega) = -\frac{\Delta\phi}{\phi \Delta x}. \tag{2.25}$$

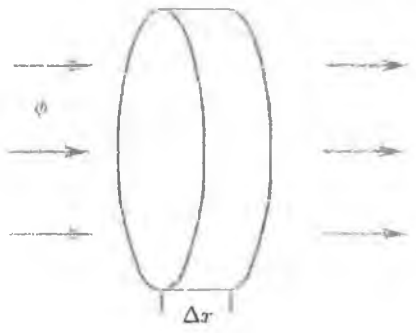

Figure 2.3: Schematic of absorption coefficient definition.

In Einstein's classical treatment of the interaction of a two-level atom with a radiation field that is a slowly varying function of frequency, the transition probabilities are effectively averaged over the frequency response of the atom, i.e. over the line profile. Since line absorption is a typical resonance phenomenon it depends strongly on frequency. This dependence can be described by a *normalised* line shape function, ϕ_ω. This profile is know as the Atomic Frequency Response given by [19]:

$$\int_{line} \phi_\omega d\omega = 1. \tag{2.26}$$

If the upper quantum level k is not populated then the absolute value of $\kappa_L(\omega)$ is given by [19]:

$$\int_{line} \kappa_L(\omega) d\omega = \frac{h\omega}{c} n_i B_{ik} \tag{2.27}$$

where ω is the line centre angular frequency. Then from equations 2.26 and 2.27 we obtain [19]:

$$\kappa_L(\omega) = \frac{h\omega}{c} n_i B_{ik} \phi_\omega. \tag{2.28}$$

If some of the atoms are in the upper level k then we need to include the contribution of stimulated emission. The effective absorption coeffecient becomes [19]:

$$\kappa'_L(\omega) = \frac{h\omega}{c} \phi_\omega \left(n_i B_{ik} - n_k B_{ki}\right)$$

$$= \kappa_L(\omega)\left(1 - \frac{n_k B_{ki}}{n_i B_{ik}}\right). \tag{2.29}$$

As with the emission coefficient, the absorption coefficient can be considered to have a continuous component and a discrete component [19]:

$$\kappa(\omega) = \kappa_L(\omega) + \kappa_C(\omega). \tag{2.30}$$

If there is stimulated emission then the κ terms should be replaced by κ' terms.

2.2.2 Radiative Transfer

The radiant energy which penetrates a unit area in unit time within a unit solid angle about the normal to the area is known as the total intensity, I, and is given by [19]:

$$I = lim\frac{\Delta E}{\Delta t \Delta A \Delta \Omega} \quad for \quad \Delta t, \Delta A, \Delta \Omega \to 0 \tag{2.31}$$

where the E is the radiant energy, t is the time, A is the area and Ω is the solid angle, see figure 2.4.

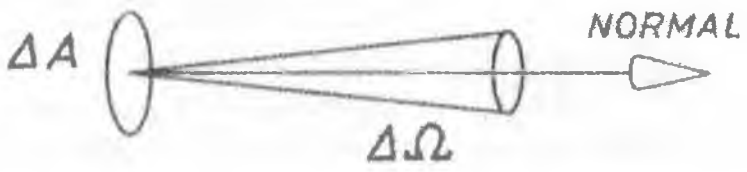

Figure 2.4: Schematic of intensity definition.

For a spectral distribution one refers to the intensity in units of wavelength or frequency and we have [19]:

$$\begin{aligned} I(\lambda) &= lim\frac{\Delta E}{\Delta t \Delta A \Delta \Omega \Delta \lambda} \quad for \quad \Delta t, \Delta A, \Delta \Omega, \Delta \lambda \to 0 \\ I(\omega) &= lim\frac{\Delta E}{\Delta t \Delta A \Delta \Omega \Delta \omega} \quad for \quad \Delta t, \Delta A, \Delta \Omega, \Delta \omega \to 0. \end{aligned} \tag{2.32}$$

At the surface of a plasma or radiating gas $I(\lambda)$ or $I(\omega)$ is a directly observable quantity. From figure 2.5, the light intensity reaching an observer positioned at

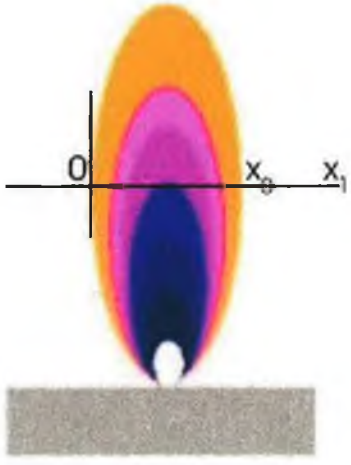

Figure 2.5: Schematic for discussion of radiation emission from plume.

x_1 has been accumulated from emission and absorption between $x = 0$ and x_0, the plume extent, but there is no emission or absorption outside this range. The relation between the emission and absorption coefficients and the intensity $I(\omega, x)$ is given by [19]

$$\frac{dI(\omega,x)}{dx} = \varepsilon(\omega,x) - \kappa'(\omega,x)I(\omega,x). \tag{2.33}$$

This equation can be solved introducing the optical depth [19]:

$$\tau'(\omega,x) = \int_x^{x_0} \kappa'(\omega,x)dx;\ d\tau' = -\kappa' dx \tag{2.34}$$

and the source function:

$$S(\omega,x) = \frac{\varepsilon(\omega,x)}{\kappa'(\omega,x)}. \tag{2.35}$$

In the case of an optically thin plasma ($\tau'(\omega,0) < 1$) we obtain:

$$I(\omega,x_0) = I(\omega,0) + \int_0^{x_0} \varepsilon(\omega,x)dx. \tag{2.36}$$

An absolute measurement of the total intensity of a spectral line emitted from optically thin layers primarily yields the density of atoms or ions in the upper state

k of the line integrated along the line of sight. This total intensity obeys [36]

$$\int_{line} I_{ki} d\lambda = \frac{2\pi hc^2 r_0}{\lambda_{ki}^3} f_{ki} \frac{g_i}{g_k} \int_0^{x_0} n_k dx \tag{2.37}$$

where r_0 is the classical electron radius, f_{ki} is the oscillator strength, g_i and g_k are the degeneracies of the lower and upper levels of the transition and the integral is over the line profile (see section 2.2.3).

From equations 2.15, 2.24, 2.36 and 2.37 one can derive an equation for the intensity of a spectral line emitted from LTE plasmas

$$\int_{line} I d\lambda = \frac{2\pi he^2 g_k f_{ki}}{\lambda^3 m} \frac{\int_0^{x_0} n dx}{U(T)} exp\left(\frac{-E_k}{k_B T_{exc}}\right) \tag{2.38}$$

where $U(T)$ is given by equation 2.16. Thus, if the plasma is in LTE, the population adhere to a Boltzmann distribution uniquely characterised by their excitation temperature, T_{exc}.

2.2.3 Line Broadening

One observes a spectral distribution $I(\lambda)$ of the emitted or absorbed radiation around a central wavelength $\lambda_0 = hc/(E_i - E_f)$ corresponding to a transition with energy difference $\Delta E = E_i - E_f$ between upper and lower levels. The interval $\delta\lambda = \mid \lambda_2 - \lambda_1 \mid$ between the two wavelengths λ_1 and λ_2 for which $I(\lambda_1) = I(\lambda_2) = I(\lambda_0/2)$ is the *Full Width at Half Maximum* of the line (FWHM), often called the *linewidth* or *half-width* of the line.

There are a number of physical mechanisms which give rise to this spectral distribution or broadening of a spectral line. These include lifetime broadening, broadening caused by the velocity distribution of the emitting species and Stark broadening from collisions with charged species.

Lifetime Broadening

The Heisenberg uncertainty principle shows that the uncertainty in the energy of a given state is inversely proportional to the uncertainty in the time during which

the corresponding energy level is occupied

$$\Delta E \Delta t \approx \frac{h}{2\pi} \tag{2.39}$$

where ΔE is the energy uncertainty, Δt is the lifetime of the level and h is Planck's constant. As a result of this energy uncertainty a distribution is required to describe the probability of seeing a transition involving light of a certain frequency. The FWHM of this distribution for a particular level, k, is determined by the radiative lifetime of that level

$$\Gamma_k = \frac{1}{\Delta t} = \frac{1}{\tau_k} \tag{2.40}$$

where τ_k is the radiative lifetime of level k. This gives a line profile which has a Lorentzian shape

$$I_{ki}(\omega) = I_0 \frac{\Gamma_{ki}/2\pi}{(\omega - \omega_{ki})^2 + \Gamma_{ki}^2/4} \tag{2.41}$$

with a FWHM of $\Delta\omega_{1/2} = \Gamma_{ki} = \Gamma_k + \Gamma_i$.

Doppler Broadening

The various atomic, ionic and molecular species in a PLD plume have velocity distributions. Light emitted from those in motion towards the observer is shifted to higher frequencies (blue-shift) and light emitted from those moving away is shifted to lower frequencies (red-shift) at the point of observation. The observed frequency is given by

$$\omega' = \omega_0 \left(1 - \frac{v \cdot \hat{n}}{c}\right) \tag{2.42}$$

where v is the velocity, $\hat{n}$ is a unit vector in the direction from the observer to the particle and c is the velocity of light (see figure 2.6).

If the velocities of the species are distributed according to a Maxwellian velocity distribution with temperature T, this gives a Gaussian line profile of FWHM [37]:

$$\Delta\omega_{D_{1/2}} = 2\frac{\omega_0}{c}\left(\frac{2k_B T}{M} ln2\right)^{\frac{1}{2}} \tag{2.43}$$

$$\Delta\omega_{D_{1/2}} = 7.16 \times 10^{-7}\omega_0\sqrt{\frac{T}{\mu}} \tag{2.44}$$

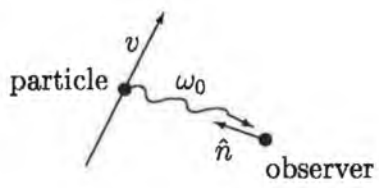

Figure 2.6: Schematic of Doppler effect geometry.

where M in (2.43) is the particle mass in kg, $\mu = M/m_u$ in (2.44) is the particle mass in atomic mass units, ω_0 is the centre frequency in Mhz and T is the plasma temperature in K.

Collisional Broadening

It is not always sufficient to consider species in PLD plumes as isolated from collisions with their neighbours. When a particle, A, with the energy levels E_i and E_k, aproaches another particle, B, the energy levels of A are shifted depending on the electron configurations of both particles and the distance, R, between the particles. These shifts, ΔE, may be different for each level and positive or negative. This interaction occurs when $R \leq R_c$, where $2R_c$ is known as the collision diameter.

If, during the collision time $\tau_c \simeq R_c/v$ (where v is the relative velocity), particle A undergoes a radiative transition between the levels E_i and E_k, the frequency of the emitted or absorbed radiation depends on the distance R at the time of the transition [38]

$$\omega_{ik} = \frac{2\pi \mid E_i(R) - E_k(R) \mid}{h}. \tag{2.45}$$

If the particles in a gas or plume can be described by a pressure and temperature the distance R will have a distribution with a mean value R_m. Thus, the emission or absorption lines will have a corresponding distribution and a peak value of $\omega_{ik}(R_m)$ which may be shifted by $\Delta\omega_{shift} = \omega_0 - \omega_{ik}$.

When some of the collision particles are ions and electrons, the broadening and shift is known as the Stark effect. The linewidth of a Stark-broadened atomic

line is approximately given by the sum of two (electron-impact and ion-impact) terms [5]

$$\Delta\lambda = 2W\left(\frac{n_e}{10^{16}}\right) + 3.5A\left(\frac{n_e}{10^{16}}\right)^{1/4}\left(1 - 1.2N_D^{-1/3}\right)W\left(\frac{n_e}{10^{16}}\right) \tag{2.46}$$

and can yield the electron density n_e if the two constants W (the electron-impact width parameter)) and A (the ion-broadening parameter) are among those tabulated from plasma spetroscopy measurements. The number of particles in the Debye sphere, N_D, at plasma temperature T_e is given by

$$N_D = 1.7 \times 10^9 \frac{T_e^{3/2}}{n_e^{1/2}} \tag{2.47}$$

with the Debye sphere radius (equation 2.5) now given by

$$\lambda_D = 740\left(\frac{T}{n_e}\right)^{\frac{1}{2}} \tag{2.48}$$

where T_e is in eV and n_e is in cm^{-3} in both 2.47 and 2.48.

2.3 Laser ablation of Ga and GaN

2.3.1 Deposition parameters

Various groups have utilised pulsed laser deposition to successfully grow thin films of crystalline GaN. Different experimental configurations and parameters such as laser wavelength and fluence, nature of target material, nature and pressure of ambient gas were used. In these studies the target was either (1) liquid or solid gallium, or (2) a polycrystalline pellet made from compressed GaN powder. The nitrogen source was N_2 or ammonia (NH_3) or atomic N from a plasma source.

Mah et al [12] have grown GaN thin films from a pressed target of GaN powder in 2.2×10^{-1} Torr N_2 with 248 nm KrF laser radiation ($\tau_{laser} = 23$ ns) at a target-substrate distance of 3 cm. Mah et al [13] have also grown GaN thin films from a pressed target of GaN powder in 2.2×10^{-1} Torr N_2 with 248 nm KrF laser radiation ($\tau_{laser} = 23$ ns) at a target-substrate distance of 3 cm

and a fluence of 4 Jcm^{-2} on target. O'Mahony et al [14] have grown GaN thin films from a pressed target of GaN powder in both 2×10^{-6} and 0.13 mbar N_2 with 248 nm KrF laser radiation ($\tau_{laser} = 23$ ns) with a spotsize of 4×1 mm, a fluence of 2.5 Jcm^{-2} and at a target-substrate distance of $3 - 5$ cm.

Xiao et al [39] have grown GaN thin films from a liquid Ga metal target 0.75 to 1.0 Torr NH_3 with 193 nm ArF laser radiation with a spotsize of 2.5×1 mm, a fluence of 10 Jcm^{-2} and at a target-substrate distance of 5 cm. Cole et al [15] have grown GaN thin films from a pressed target of GaN powder in 0.04 to 0.2 mbar N_2 and NH_3 with 248 nm KrF laser radiation ($\tau_{laser} = 23$ ns) with a fluence of 2.8 Jcm^{-2} and at a target-substrate distance of 4.5 cm. Middleton et al [16] have grown GaN thin films from a pressed target of GaN powder in 0.13 mbar N_2 with 248 nm KrF laser radiation ($\tau_{laser} = 23$ ns) a fluence of 2.8 Jcm^{-2} and at a target-substrate distance of 3.5 cm.

Cazzanelli et al [17] have grown GaN thin films from a pressed target of GaN powder in both 0.2 mbar NH_3 and 0.1 mbar N_2 with 248 nm KrF laser radiation ($\tau_{laser} = 23$ ns) with fluences of 3.6 Jcm^{-2} and 2.8 Jcm^{-2}, respectively, and at a target-substrate distance of 3.5 cm. Willmott at al [40] have grown GaN thin films from a liquid Ga target in 4×10^{-2}Pa N_2 and NH_3 with 248 nm KrF laser radiation ($\tau_{laser} = 17$ ns) with a spotsize of 0.15 ± 0.1 cm and a fluence of 5 ± 1 Jcm^{-2}. Niehus et al [41] have grown GaN thin films from a liquid Ga target with 1064 nm Nd:YAG laser radiation.

Takahashi et al [42] have grown GaN thin films from a pressed target of GaN powder in 1×10^{-2} Torr N_2 with 248 nm KrF laser radiation ($\tau_{laser} = 20$ ns) with a fluence of 3.0 Jcm^{-2} and at a target-substrate distance of 5 cm. Tong et al [43] have grown GaN thin films from a pressed target of GaN powder in 5 Pa N_2 with 248 nm KrF laser radiation at a target-substrate distance of $3 - 6$ cm. Sanguino et al [44] have grown GaN thin films from a liquid Ga target in both 0.2 mbar N_2 pressure and a RF discharge pressure of 1 mbar N_2 with 1064 nm Nd:YAG laser radiation ($\tau_{laser} = 5$ ns). Vinegoni et al [45] have grown GaN thin films from a pressed target of GaN powder in 2×10^{-3} to 0.15 mbar NH_3 with 248 nm KrF laser radiation, a fluence of $4 - 6$ Jcm^{-2} and at a target-substrate

distance of 3.5 cm.

Cole et al [46] have grown GaN thin films from a pressed target of GaN powder at a pressure of 3×10^{-10} Torr with 248 nm KrF laser radiation ($\tau_{laser} = 23$ ns) a fluence of $2 - 5.9$ Jcm^{-2} and at a target-substrate distance of 5 cm. Wang et al [47] have grown GaN thin films from a pressed target of GaN powder in 10^{-5} to 2 Torr N_2 with 266 nm frequency quadrupled Nd:YAG laser radiation at a fluence of 1.2 Jcm^{-2} and at a target-substrate distance of 3.5 cm.

Ohta et al [48] have grown GaN thin films from a pressed target of GaN powder in 5×10^{-2} Torr N_2 with 248 nm KrF laser radiation ($\tau_{laser} = 20$ ns) at a fluence of 3 Jcm^{-2} and at a target-substrate distance of 5 cm. Ohta et al [49] have also grown GaN thin films from a pressed target of GaN powder in 1×10^{-2} Torr N_2 with 248 nm KrF laser radiation ($\tau_{laser} = 20$ ns) at a fluence of 3 Jcm^{-2} and at a target-substrate distance of 5 cm.

Sudhir et al [50] have grown GaN thin films from a pressed target of GaN powder in 10^{-5} to 10^{-1} Torr N_2 with 248 nm KrF laser radiation ($\tau_{laser} = 38$ ns) at a fluence of $2 - 6$ Jcm^{-2}. Ito et al [51] have grown GaN thin films from a pressed target of GaN powder in 1×10^{-2} Torr N_2 with 248 nm KrF laser radiation ($\tau_{laser} = 20$ ns) at a fluence of 3 Jcm^{-2} and at a target-substrate distance of 5 cm. Basillais et al [52] have grown GaN thin films from a solid target of Ga in 0.01 mbar N_2 and a nitrogen R.F. discharge with 248 nm KrF laser radiation ($\tau_{laser} = 25$ ns) at a fluence of 6 Jcm^{-2}.

It can be concluded that despite the different experimental conditions all authors report successful growth, which suggests a need to unravel the elementary mechanisms at play. The above paragraphs are summarised in table 2.4.

Author	λ_L	P_{gas}	T	F	S	D_{T-S}
Mah [12]	248	2.2×10^{-1} Torr N_2	GaN			3
Mah [13]	248	2.2×10^{-1} Torr N_2	GaN	4		3
O'Mahony [14]	248	2×10^{-6}/0.13 mbar N_2	GaN	2.5	4×1	3-5
Xiao [39]	193	$0.75 - 1.0$ Torr NH_3	liq. Ga	10	1×2.4	5
Cole [15]	248	$0.04 - 0.2$ mbar N_2/NH_3	GaN	2.8		4.5
Middleton [16]	248	0.13 mbar N_2	GaN	2.8		3.5
Cazzanelli [17]	248	0.2 mbar NH_3/0.1 mbar N_2	GaN	3.6/2.8		3.5
Willmott [40]	248	4×10^{-3} Pa N_2, NH_3	Liq. Ga	5±1	1.5±1	
Niehus [41]	1064		liq. Ga			
Takahashi [42]	248	1×10^{-2} Torr N_2	GaN	3		5
Tong [43]	248	5 Pa N_2	GaN			3-6
Sanguino [44]	1064	0.2/1 mbar N_2	liq. Ga			
Vinegoni [45]	248	$2 \times 10^{-3} - 0.15$ mbar NH_3	GaN	4-6		3.5
Cole [46]	248	3×10^{-1} Torr	GaN	2-5.9		5
Wang [47]	266	$10^{-5} - 2$ Torr N_2	GaN	1-2		3.5
Ohta [48]	248	5×10^{-2} Torr N_2	GaN	3		5
Ohta [49]	248	1×10^{-2} Torr N_2	GaN	3		5
Sudhir [50]	248	$10^{-5} - 10^{-1}$ Torr N_2	GaN	2-6		
Ito [51]	248	1×10^{-2} Torr N_2	GaN	3		5
Basillais [52]	248	0.01 mbar N_2	Ga	6		

Table 2.4: Experimental parameters used by various groups (where λ_L is in nm, T is the target material, F is the fluence in Jcm^{-2}, S is the spotsize in mm and D_{T-S} is the target to substrate distance in cm).

2.3.2 Plume diagnostics

Diagnostic studies of ablation plumes of Ga or GaN are less numerous than those relating to material properties of GaN thin films.

A number of authors have studied plume dynamics using Ion Probes to measure the kinetic energies of ions in GaN PLD plumes. O'Mahony et al [14] reported a kinetic energy value of ~ 130 eV for Ga ions with a probe 3 cm from a target of pressed GaN powder with 248 KrF laser radiation at a fluence of 2.5 Jcm^{-2} in 10^{-6} mbar. Cole et al [15] reported a kinetic energy value of 70 eV for a target of pressed GaN powder with 248 nm KrF laser radiation at a fluence of 2.8 Jcm^{-2} at 4.5 cm above target surface. Cazzanelli et al [17] reported mean kinetic energy values of 69 and 14 eV for Ga and N ions in 0.1 mbar N_2 for a target of pressed GaN powder with 248 nm KrF laser radiation at a fluence of 2.8 Jcm^{-2}.

Time Of Flight Mass Spectrometry has been used to study plumes of Ga by Di Palma et al [53] in NH_3 at a fluence of 5 Jcm^{-2} using 532 nm frequency doubled Nd:YAG or 248 nm KrF laser radiation. This author reported $Ga(NH_3)_n$ clusters with $n = 1 - 9$.

Extreme Ultraviolet spectroscopy was used by Mah et al [54] to study ablation of Ga and GaN targets by 1064 nm laser radiation at 10 Jcm^{-2} in vacuum with the author reporting absorption spectra and absorption contour plots for various distances above the target surface and time delays after the laser pulse arrival. Singly ionised Ga density values of $3 \pm 1 \times 10^{16}$ cm^{-3} at 15 mm above target and 100 ns after laser and $2 \pm 1 \times 10^{14}$ cm^{-3} at 4 mm and 500 ns were reported along with a velocity of 5×10^5 cms^{-1} corresponding to a temperature of 4 eV.

Mizuno et al [55] used streak photography to estimate plume velocities and kinetic energies employing a Shifted Centre-of-Mass Maxwell Boltzmann velocity distribution to interpret the image results. A drift velocity of 9×10^5 cms^{-1} and a thermal velocity of 6×10^5 cms^{-1} were reported with corresponding drift and thermal kinetic energies of 29 eV and 13 eV.

To date, no detailed spectroscopic study of Ga and GaN laser ablation plumes has been performed.

2.4 Laser ablation of Li and Li compounds

$LiNbO_3$ has been grown by PLD by various authors and with varying degrees of success. Ritomov et al [56] reports growth of both $LiNbO_3$ and Li-deficient $LiNbO_8$ in 0.1-0.2 mbar O_2 using 248 nm KrF laser radiation at fluences of 2.5-3.5 Jcm^{-2} and target-substrate distances of 4-5 cm. Ghica et al [57] also reports growth of both $LiNbO_3$ and Li-deficient $LiNbO_8$ in 5-20 Pa O_2 using 248 nm KrF laser radiation at fluences of 4-8 Jcm^{-2} and a target-substrate distance of 3 cm.

Recently films of LiF have been successfully grown by PLD. Using 193 nm ArF laser radiation at 3-30 Jcm^{-2} Henley et al [58] has grown films in 1×10^{-6} Torr at a target-substrate distance of 5 cm. Perea et al [59] has grown LiF films with 2-10 Jcm^{-2} from a 193 nm ArF laser in both 10^{-5} mbar and 10^{-1} mbar He at a target-substrate distance of 3 cm.

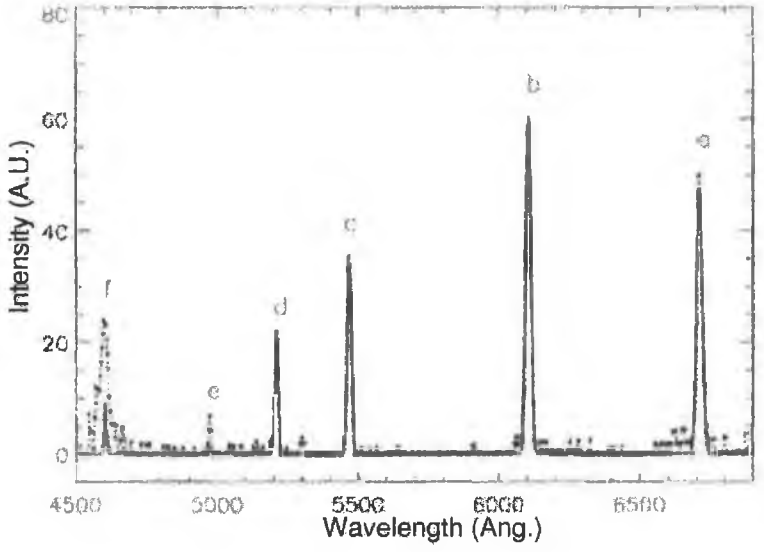

Figure 2.7: Spectrum of LiAg; broken - experimental; solid - synthetic (from [60] with permission of editor).

Spectrally resolved fast imaging was used by Sherrill et al [60] to study LiAg ablation with 1064 nm laser at 1 Jcm^{-2} (see figure 2.7). The author estimates an electron density of 5×10^{17} cm^{-3} and a temperature of 1 eV. Sherrill et

al [61] obtains an electron density of 1×10^{17} cm^{-3} in ablation of LiAg with 1064 nm laser at 1 Jcm^{-2}. In both cases a reversal of the lithium 670.8 nm ($1s^2.2s - 1s^2.2p$ transition) and 610.3 nm ($1s^2.2p - 1s^2.3d$ transition) emission line intensities from the expected ratio is reported.

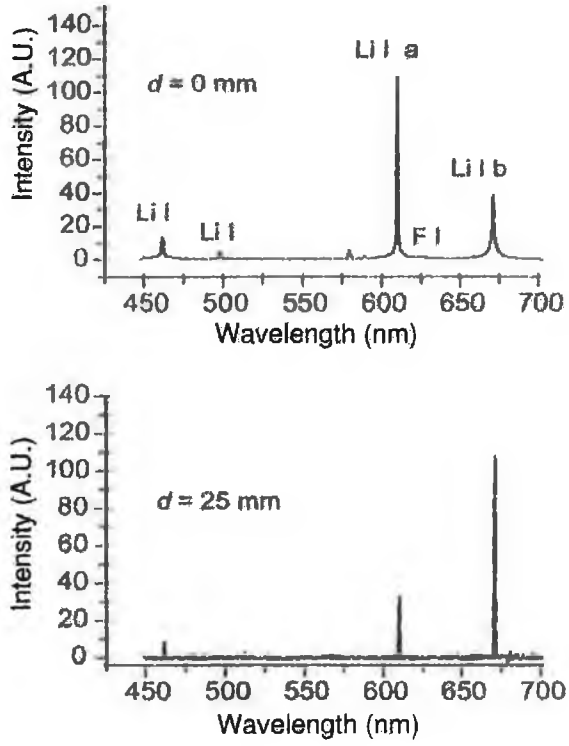

Figure 2.8: Spectra of LiF at 0 mm, and 25 mm, above target (from [58] with permission of editor).

Optical Emission Spectroscopy has been used by Henley et al [58] to study LiF plumes ablated with 193 nm ArF laser radiation at 6 Jcm^{-2}. Again the author reports a lithium line intensity reversal (see figure 2.8).

2.5 Conclusions and objectives of the present work

Despite the large interest in growing films of GaN by the Pulsed Laser Deposition technique, only a small number of authors have studied PLD-regime ablation plumes of Ga or GaN by spectroscopic techniques. Thus, this thesis presents a detailed spectroscopic and fast imaging study of Ga and GaN plumes over a range of N_2 pressures from 10^{-7} mbar to 5 mbar and laser wavelengths through 266 nm, 355 nm, 532 nm and 1064 nm.

Similarly, few spectroscopic studies of Li ablation plumes have been in the PLD regime and so this thesis presents spectroscopic and fast imaging study of Li and LiF ablation plumes expanding into vacuum using a number of laser wavelengths and spot dimensions typical of PLD conditions.

The spectroscopic setup will be described in detail in chapter 3. However, the principle consists of imaging the plume onto the entrance slit of an imaging spectrograph, equipped with a $2D$ detector, with the expansion axis of the plasma along the slit. Thus, an intensity point in the recorded spectrum corresponds to both a unique height above the target surface and a dispersed wavelength. Briefly, the imaging setup provides a series of images of the expanding plume at various times and, so, gives spatial and temporal information.

It has been suggested that the presence of excited species and ions near the substrate play an important role in thin film growth by PLD. From the spectra we extract atomic level populations and excitation temperatures inter alia and estimate species velocities from the fast-frame imaging and ion probe techniques.

Chapter 3

Experimental techniques and details

3.1 Experimental setup

3.1.1 Overview

Plan and elevation views of the stainless steel target chamber used for experiments are shown in figure 3.1. The chamber has two ports which were fitted with fused silica windows to transmit UV light, one for laser access to the target and the other for spectroscopic diagnostics of the ablation plume. There are also two BK7 glass ports for fast imaging purposes. The figure also shows the turbomolecular pump used to evacuate the chamber. The complete pumping system comprised two rotary pumps and one turbomolecular pump and the pumping operation is described in more detail in section 3.1.3. We introduced N_2 gas into the chamber and the pressure was controlled by means of a needle valve. The position of the ion probe, see section 3.4, is also shown and this could be rotated about the position of the laser spot on target.

We configured the target surface in a horizontal orientation to facilitate the use of molten gallium metal and the laser was incident on the target (Ga, GaN or Li) at a $45°$ angle to the surface normal. This horizontal target configuration

provided a vertical ablation plume which facilitated the imaging of the plume onto the spectrograph slit and this will be detailed in section 3.2. A stepper motor was used to rotate the target after each laser shot and this was mounted on a translation stage which could position the target either horizontally or vertically to avoid cratering of the target (in the solid target cases).

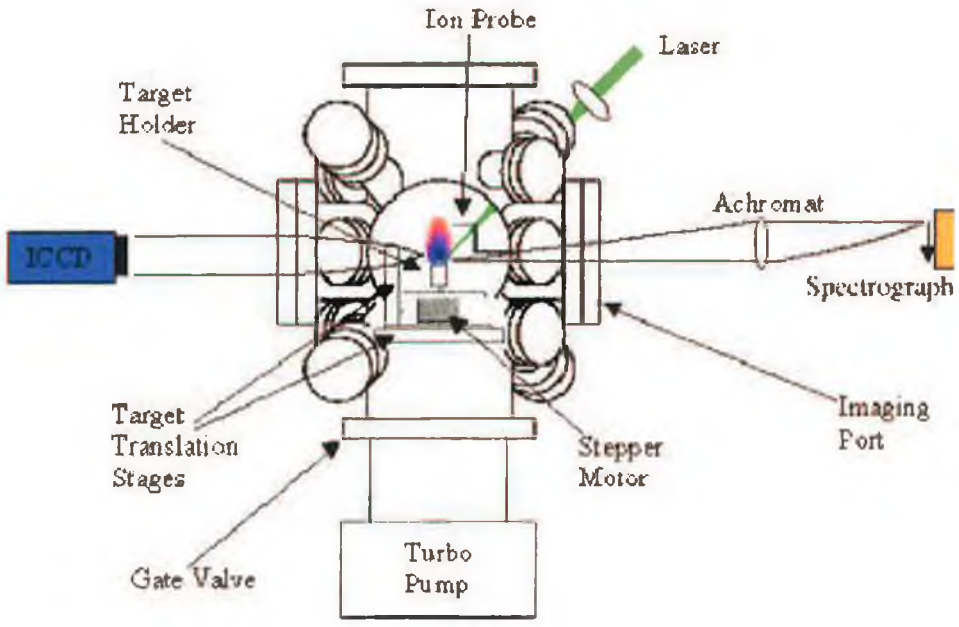

Figure 3.1: Schematic of laser and target chamber.

3.1.2 Laser and laser parameters

The laser used for the majority of the experiments was a Nd:YAG from Continuum. As well as the 1064 nm fundamental wavelength, there was also available the 2^{nd}, 3^{rd} and 4^{th} harmonics at wavelengths of 532, 355 and 266 nm. Table 3.1 displays the maximum output energy from each harmonic.

Some control of the energy output could be achieved by varying the flashlamp voltage or the delay between the flashlamp trigger pulse and that of the q-switch. This is plotted in figure 3.2 for three different flashlamp discharge voltages.

$\lambda_{laser}(nm)$	E (mJ)
1064	465
532	230
355	130
266	58

Table 3.1: Nd:YAG maximum pulse output.

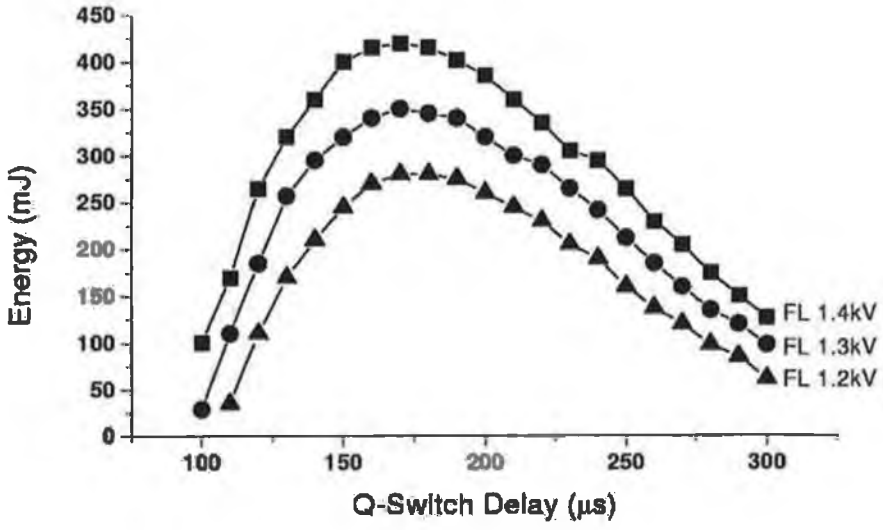

Figure 3.2: Q-switch delay v.s. pulse energy.

It can be seen that for this laser the maximum output occurs when the the q-switch delay is at ≈ 180 μs. The temporal profile of the output pulse was measured with a Tektronix TDS3032 oscilloscope (300MHz, 2.5 G samples/s) and is shown in figure 3.3 for this delay. As one increases the delay past 180 μs this temporal profile is degraded substantially. The FWHM was maintained at ≈ 10 ns.

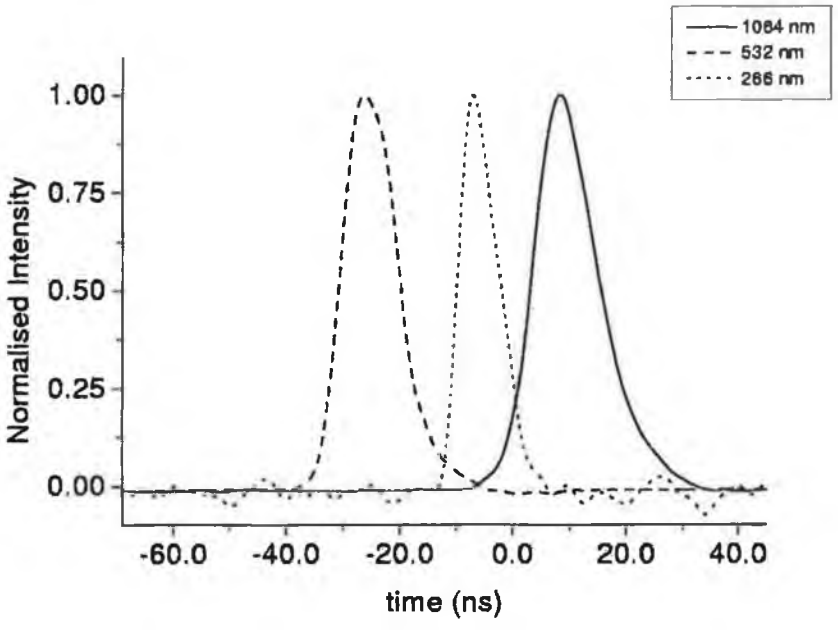

Figure 3.3: Laser pulse temporal profile.

Four plano-convex lenses were used to focus the laser onto the target surface. Each lens was specifically designed to have a focal length of 210 mm for the design wavelength, which were the four available laser wavelengths, respectively.

To control the laser fluence on target we estimated the spot size by firing through a target of aluminium foil while varying the position of the focusing lens by a translation stage. An optical microscope was used to photograph the single laser shot ablation craters on aluminium foil. The laser spot size was then approximated as the crater dimensions (assuming all of profile makes crater). A typical crater is shown in figure 3.4, with typical spotsizes used in this work listed

in table 3.2.

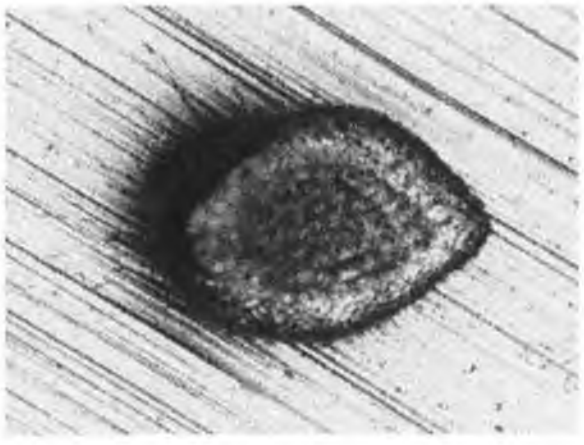

Figure 3.4: Typical ablation crater on aluminium foil.

Knowing the spot size it was then possible to control the energy on target by means of the flashlamp voltage. Additional control was provided by using a beamsplitter to dump energy out of the beam.

spot dimension
$115 \times 80 \pm 15$ μm
$340 \times 250 \pm 15$ μm
$590 \times 525 \pm 15$ μm
$1 \times 1 \pm 0.015$ mm
$2 \times 2 \pm 0.015$ mm

Table 3.2: Spot sizes used in experiments.

3.1.3 Procedures and operation

The system was pumped down in two steps: first an 8 m^3h^{-1} rotary pump was used to bring the chamber down to 10^{-2} mbar before being isolated by a valve; then a 500 ls^{-1} BOC Edwards EXT501 turbomolecular pump (previously isolated

from chamber by a gate valve), backed by an 18 m^3h^{-1} rotary pump, was used to reach a base pressure of 4×10^{-7} mbar.

An active pirani gauge was used to measure the pressure in the chamber down as far as 10^{-3} mbar after which an active inverted magnetron gauge was used to measure lower pressures. A second active pirani gauge was used to monitor the backing pump performance.

When N_2 gas was introduced into the chamber the turbo pump was isolated by the gate valve and the rotary roughing pump was used, in conjunction with the gas control needle valve, to maintain the pressure at the desired pressure in the range of 10^{-1} to 5 mbar.

3.2 Emission Spectroscopy

UV-visible emission spectroscopy can be employed to yield information about laser ablation plumes. Tables of atomic lines and molecular bands can be used to identify the emitting species in the plume. If the system is suitably configured these species can be studied as they travel from the target to the substrate.

Providing certain conditions are met, plume parameters such as T_{exc}, n_k and n_e can be obtained for the plume. We have used a medium-quartz spectrograph utilising photographic film as a detector to study ablation plumes of Ga, GaN and Li.

Equation 2.38, section 2.2.2, gives the intensity of a spectral line emitted from an LTE plasma. From this we may obtain the excitation temperature, T_{exc}. However, since the plasma is in LTE, the population adheres to a Boltzmann distribution and this temperature, T_{exc}, may be obtained from the slope of a Boltzmann plot [62]:

$$log\left(\frac{\left(\int_{line} Id\lambda\right)\lambda^3}{gf}\right) = log\left(\frac{2\pi he^2\left(\int_0^{x_0} ndx\right)}{mU(T)}\right) - \frac{E_k}{k_B T_{exc}}. \qquad (3.1)$$

Plotting these values for a number of spectral lines of different upper energy levels, T_{exc} can be extracted from the slope $m = -1/k_B T_{exc}$. The accuracy of this method is improved by increasing the number of lines used for the plot and

the energy spread along the x-axis (spread of E_k's). This method was used to calculate excitation temperatures for Ga, GaN, Li and LiF plumes in Chapters 3 and 4.

Using equation 2.37, absolute spectral line intensities, integrated over the line profile, can be used to calculate the population cross-section of the upper level of the transition. We have used this method to calculate upper level population cross-sections for Ga, GaN and Li plumes.

Equation 2.46 can be used to estimate n_e, the electron density, provided the instrument function is well known. This method was used to measure n_e in LiF. In the cases of Ga, GaN and Li the instrument function was estimated with a He-Ne laser but was found to be strongly dependent on wavelength. That is to say that the FWHM of the 633 nm line (He-Ne) was wider than the 610 nm line from a Li plume but narrower than the 670 nm line from a Li plume.

3.2.1 Medium Quartz Spectrograph

The experimental setup consists of imaging the plume, using a UV achromat, onto the entrance slit of a f/12 Hilger medium-quartz spectrograph with the expansion axis of the plume parallel to the entrance slit as shown in figure 3.5. Thus, an intensity point in the recorded spectrum corresponds to both a unique height above the target surface and a dispersed wavelength. No external shutter was used and, so, a point in the detector plane is integrated over the total duration of the plume emission.

The medium-quartz spectrograph has quartz refracting components, having a λ range of 2000 Å to 10000 Å. The instrument consists of a slit, collimating lens, dispersing element (prism), a two-component camera lens, and a photographic plate/film cartridge (see figure 3.6).

Quartz occurs in two forms which rotate the plane of polarisation of light in opposite senses. Thus a 60° prism can be constructed of two 30° prisms, one from each variety of quartz, the second prism introducing a compensating rotary effect. This is known as a Cornu prism.

The collimating lens renders light from the slit parallel and, hence, eliminates

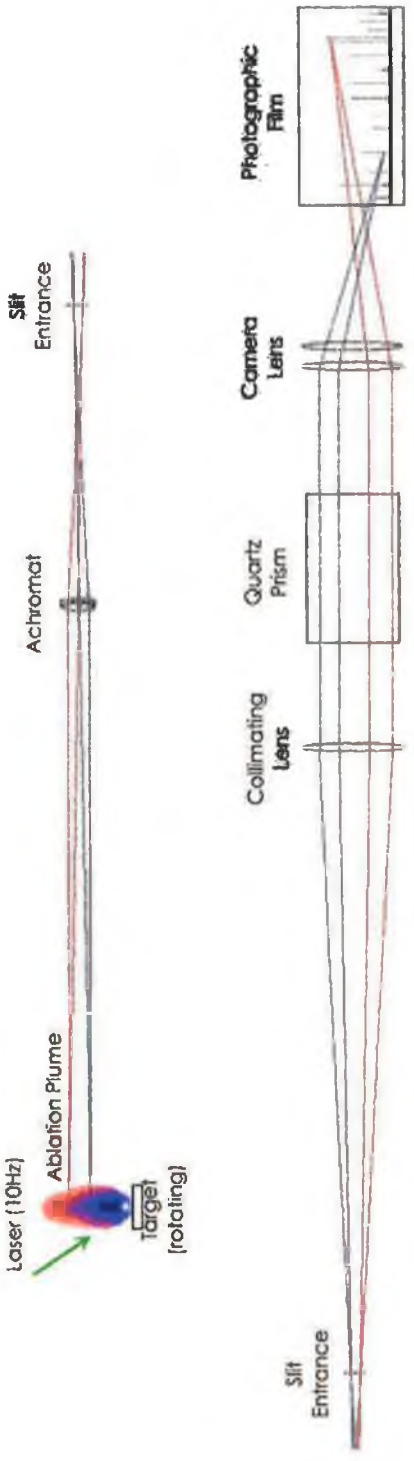

Figure 3.5: Ablation plume and spectrograph.

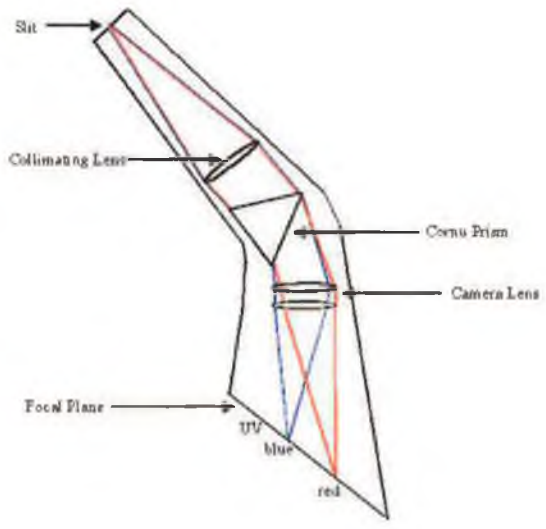

Figure 3.6: Hilger medium-quartz spectrograph.

astigmatism in the prism, while the camera lens brings to focus the beams of light of different wavelengths emerging from the prism at different angles. Images of the slit are produced in the focal plane and in this position the photographic film is fixed in the holding cartridge. Since the focal plane of a medium-quartz instrument is flat no adjustment of focus is necessary for any part of the spectrum.

Three of the parameters governing the performance of this instrument are particularly important: *reciprocal linear dispersion*, *spectral resolving power* and *curvature of spectral lines*. The refractive index of fused quartz vs wavelength varies in a non-linear fashion as can be seen in figure 3.7 (after [63]). The *reciprocal linear dispersion* for a medium quartz instrument varies from ≈ 5 Å/mm at 2000 Å, to almost 500 Å/mm at 10,000 Å. Thus, for studies in the UV region of the spectrum it is quite a useful instrument. The *spectral resolving power* can be expressed as

$$R = \frac{\lambda}{d\lambda}. \tag{3.2}$$

The theoretical resolving power was calculated and is plotted in figure 3.8. It also varies non-linearly with respect to wavelength and from this it can be seen that the instrument is most useful in the UV end of its range.

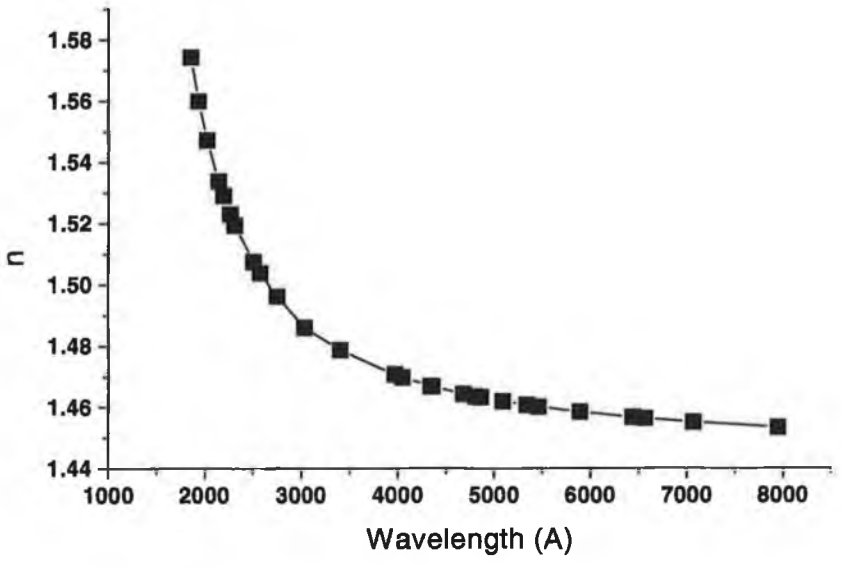

Figure 3.7: Refractive index of fused quartz.

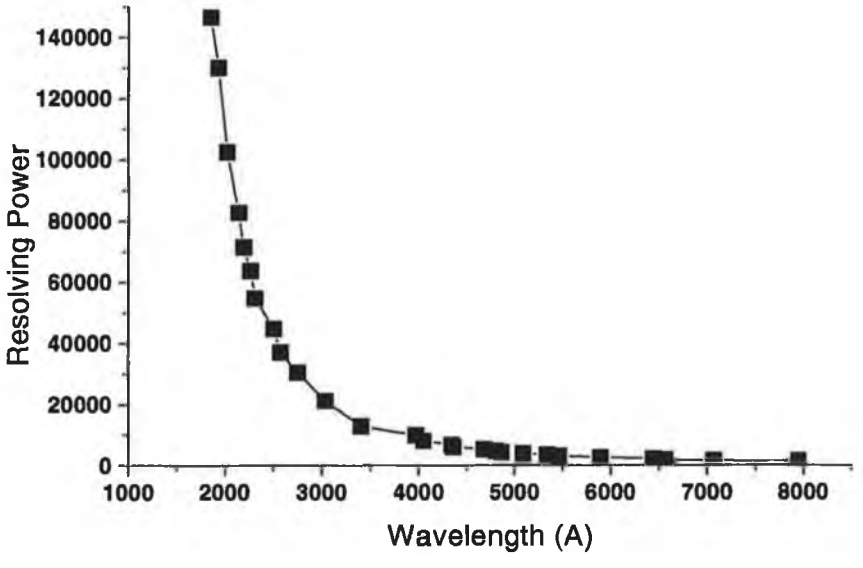

Figure 3.8: Theoretical resolving power of spectrograph.

Due to the fact that light originating at the two ends of the slit pass through the prism in a direction which is slightly inclined to the principal plane, this light will suffer slightly more deviation than the light from the midpoint of the slit, which lies on the plane. Hence the images (spectrum lines) will be curved with their ends displaced towards the blue end of the spectrum. This can be seen in figure 3.9, a typical image of Ga in 10^{-7} mbar N_2. This means that a wavelength

Figure 3.9: Section of typical experimental spectrum of Ga plume expanding into vacuum.

calibration along the spectrum at a certain distance from the midpoint along any line will differ from the wavelength calibration at the end of the line. The radius of curvature can be calculated for a 60° prism to be

$$\rho = \frac{f_2 n}{n^2 - 1}\left(1 - 0.25n^2\right)^{\frac{1}{2}}. \tag{3.3}$$

At 2500 Å, $\rho \approx 467$ mm and at 4046 Å, $\rho \approx 515$ mm, so the curvature varies across the spectrum.

The wavelength calibration of the spectrograph was performed using a mercury lamp with a quartz envelope (to transmit UV lines) and iron lines from a laser plasma. Figure 3.10 shows the mercury spectrum. Using a knife edge and the 250 nm line of galliumwe obtained the curve of figure 3.11. This is the edge function and corresponds to the integral of the line spread function [64]:

$$W_e(x) = \int_{-\infty}^{x} W_l du \tag{3.4}$$

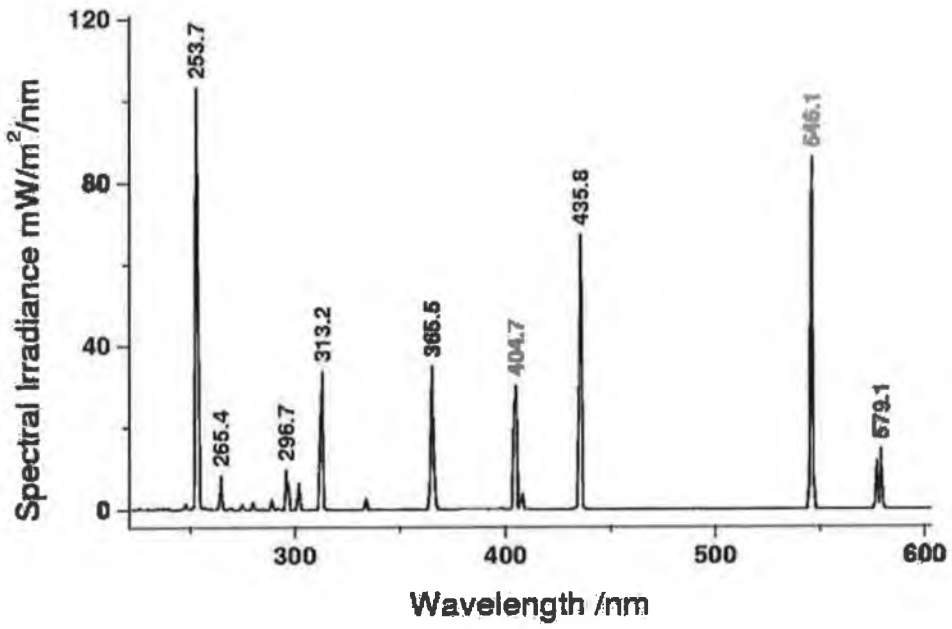

Figure 3.10: Spectrum of a Hg lamp.

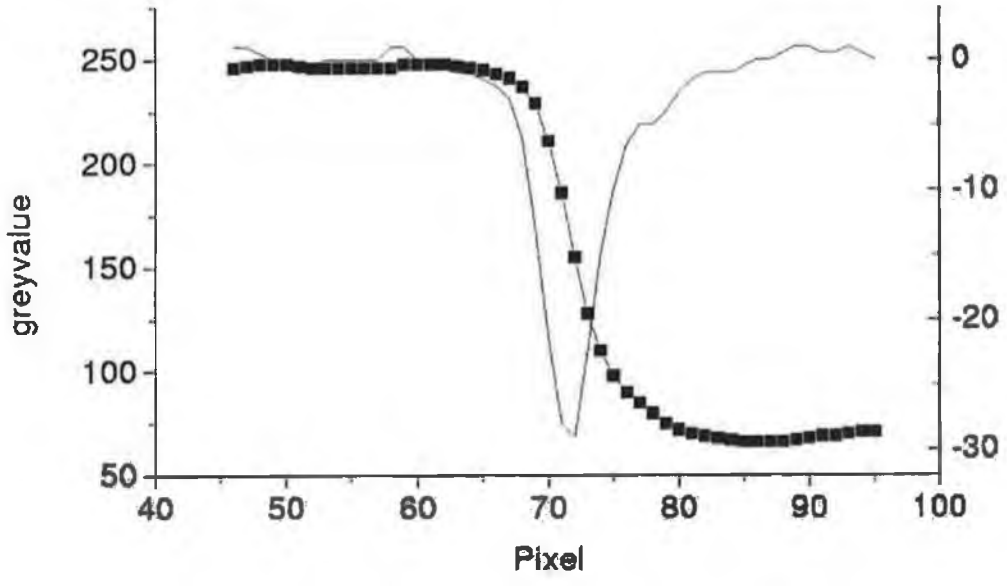

Figure 3.11: Scan across knife edge (data points) and line spread function (solid).

where W_e is the edge trace function and W_l is the line spread function. Differentiation of the edge function yields the line spread function and the width of this determines the spatial resolution. The value obtained is 80 μm. The solid angle subtended by the lens is given by $Q = \pi \frac{r^2}{R^2}$ where r is the radius of the clear aperture and R is the distance between plume and achromat and it's value is 1.593×10^{-3} Sr.

3.2.2 Photographic Film

Models of conventional photographic processes are usually based on the assumption that silver halide grains are simply photon receptors and recorders of specified absorption, size, shape and photon threshold. When the threshold number of photons has been absorbed, the grains become activated in such a way that after development they have a new absorption, size and shape. A grain in this new state is a single image unit and further absorption of photons in excess of the threshold makes no additional contribution to this image.

Following absorption of a sufficient number of light quanta, the silver halide grain has the property such that it may be preferentially reduced to silver with a suitable reducing agent (known as a developer). Although all grains will eventually be reduced to silver if developed for a sufficient time, the rate of reduction is very much greater for those grains which have absorbed the threshold number of quanta during exposure.

The exposure ε is defined as the light energy received by one cm^2 of the photographic layer during the exposure time t_e. If the light flux is denoted by $P(t)$ then [65]

$$\varepsilon = \int_0^{t_e} P(t)dt. \tag{3.5}$$

The most common quantative measure of photographic output is the optical density of the developed layer. Light of intensity I_0 is shone through the image (figure 3.12) and compared with the transmitted intensity I_T. This gives us

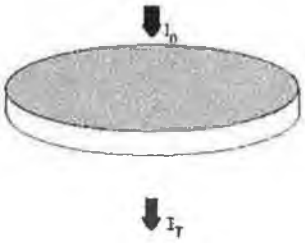

Figure 3.12: Incident and transmitted light.

$$D = log_{10}\frac{I_0}{I_T} \tag{3.6}$$

or

$$D = -log_{10}T = log_{10}O \tag{3.7}$$

where T and O are the transmittance and opacity respectively. In practice the density of a given image depends on the geometry of the measuring system and the wavelength over which the density is measured.

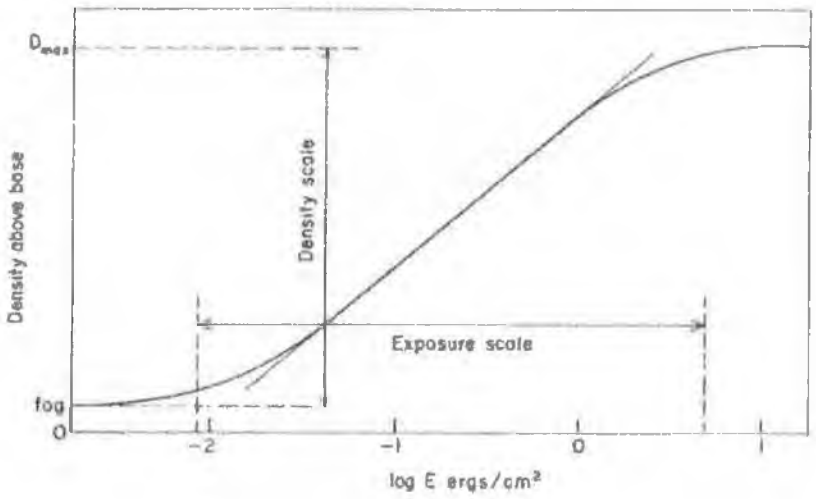

Figure 3.13: Typical characteristic curve (after [65]).

The characteristic curve relates the output density to the logarithm of the

input exposure as illustrated in the example of figure 3.13. The slope of the linear part of the curve is given by:

$$\gamma = \frac{dD}{d(log_{10}\varepsilon)}. \tag{3.8}$$

The fog, D_0, is defined as the density of unexposed parts of the developed film. Therefore absolute exposure values ($ergs/cm^2$) can be obtained for recorded spectra if γ and D_0 are known across the spectral range of the data. Figures 3.14 and 3.15 show the spectral sensitivity and characteristic curves for Kodak HSI film (High Speed Infrared), the film used in this work. This film type is well characterised and no batch variation was assumed. Work was done only in the linear region.

The development of film from experiments was performed under strict timing conditions, see table 3.3. The developer used was D-76. After being continuously agitated in the development tray for the correct amount of time, the film was then transferred to the stop bath (Kodak Indicator stop bath) for 30 s. It was then placed in the fixer bath (Kodak Fixer) and continuously agitated for 10 minutes.

Developer	18 °C	20 °C	21 °C	22 °C	24 °C
Kodak D-76	11	$9\frac{1}{2}$	$8\frac{1}{2}$	$7\frac{1}{2}$	$6\frac{1}{2}$

Table 3.3: Development time (minutes) for various temperatures.

The next step was to rinse the film under running water for 30 s. It was then placed in a tray of Kodak Hypo Clearing Agent for 2 minutes, to further wash the film, followed by 5 more minutes under running water. Lastly it was placed in a tray of Kodak Photo-Flo Solution to prevent water stains before being hung up to dry in a dust-free cupboard.

The Optical Densities across the films (spectral images) were measured by scanning with a 2000 dots-per-inch scanner. This scanner was calibrated using a set of known optical densities (calibrated neutral density filters: optical density known across the visible spectrum), figure 3.16, and the scanned images were

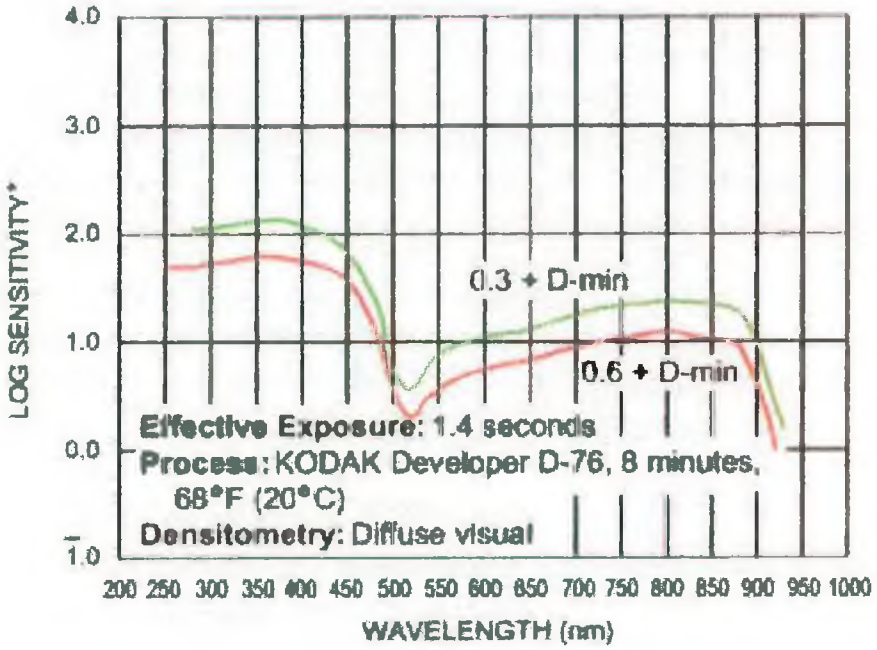

Figure 3.14: Spectral sensitivity curves for HSI film.

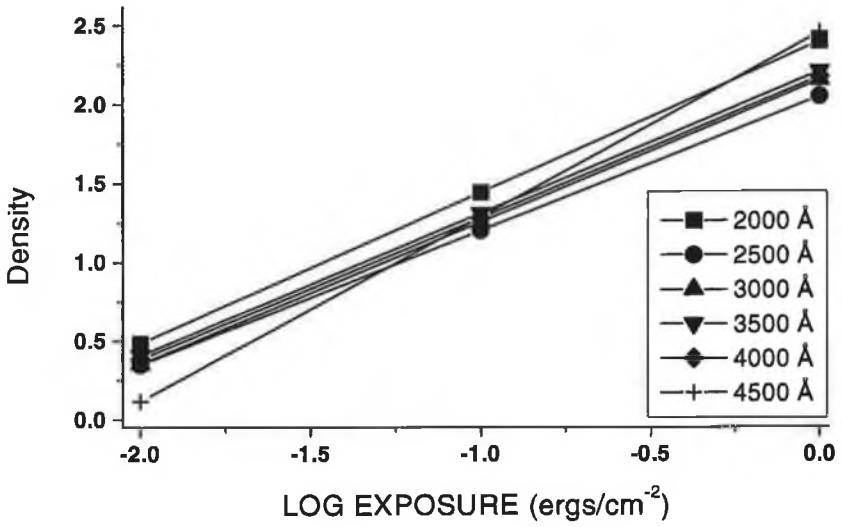

Figure 3.15: Characteristic curves of HSI at various λ (Å).

stored digitally (as 'raw' pixel images). Plotting the optical density of a pixel vs its x-position across the image yields a spectrum and these were extracted for various heights above the target surface (y-positions).

Using the wavelength calibration, these x-position values were converted to wavelength values. With these values the optical density values were then manipulated, using the wavelength-dependent characteristic curves γ values (figure 3.15) extracted from the spectral sensitivity curve of the film and measured D_0 values, together with the plume duration measured with the fast imaging technique of section 3.3, to give the intensity of the light, in $\mathrm{Wcm^{-2}}$, falling on the film at each pixel. The spectra were finally converted to plots of the spectral intensity in $\mathrm{Wcm^{-2}Sr^{-1}\AA^{-1}}$ vs λ in Å. Error bars of ± 15 % were estimated from the wavelength-dependent characteristic curves, plotted in figure 3.15, and the wavelength, γ and transmission fits.

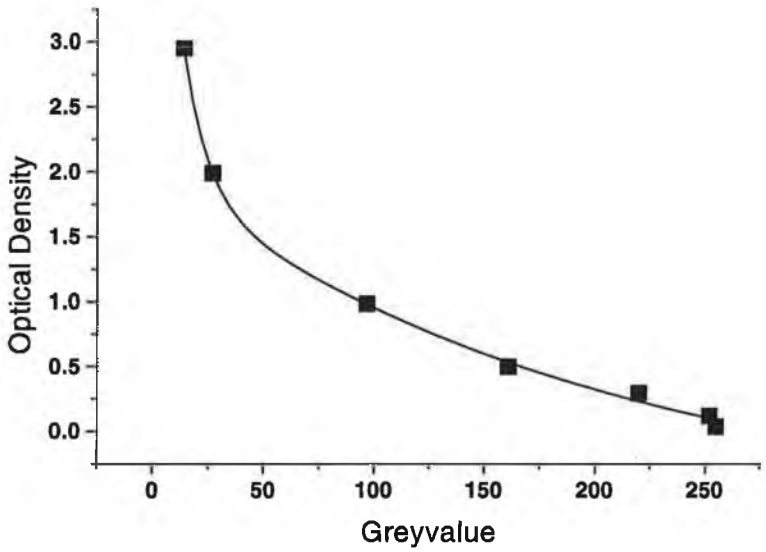

Figure 3.16: Calibration curve for scanner.

3.2.3 Time-resolved monochromator measurements

Temporal evolution measurements of emission lines in ablation plumes were measured using the setup shown in figure 3.17 at the Instituto de Optica, CSIC, Madrid.

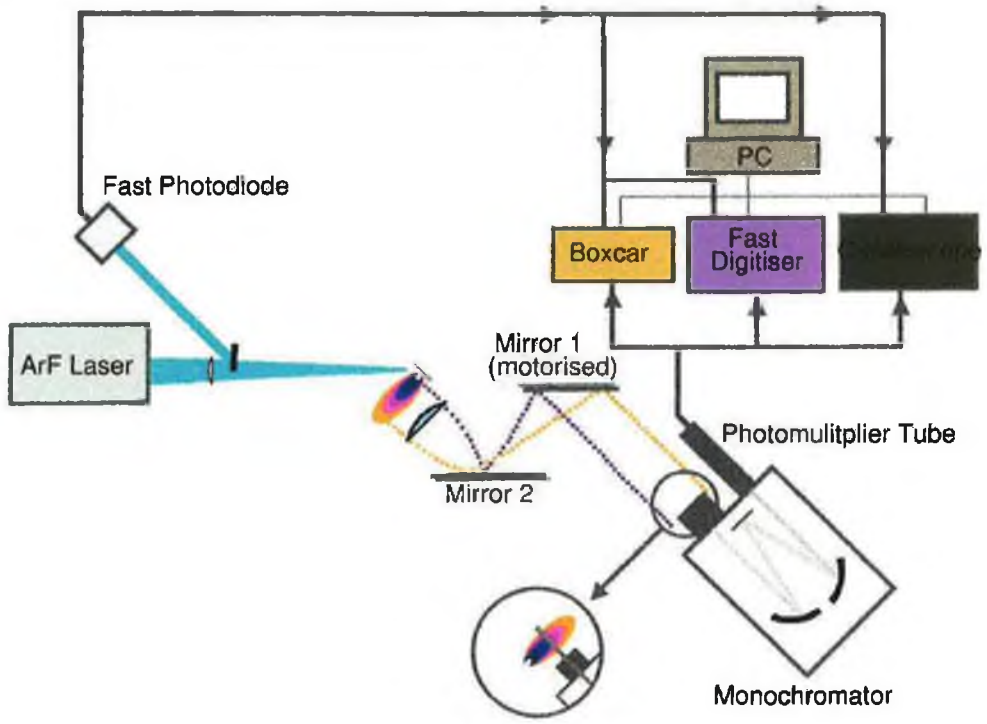

Figure 3.17: Monochromator measurements system setup.

An ArF excimer laser ($\lambda = 193nm$) was focussed on the target surface at an incident angle of $45°$. The target was mounted on a rotating holder placed in a vacuum chamber (not shown) which was evacuated to a residual pressure of 5×10^{-6}mbar.

The laser ablation plume is imaged onto the entrance slit of a 0.05Å resolution Czerny-Turner mount monochromator (3/4 m SPEX 1702) at a magnification of 1.78 using a lens and two steering mirrors. One of the mirrors was mounted on a motorised translation stage which allowed a controlled scan of the plume image across the vertical entrance slit of the monochromator. The optical image

of plume was scanned along the normal to the target. The light emitted was collected by a photomultiplier (15 ns rise time) [66] connected to a boxcar averager for spectral recording or to a fast digitiser for transient emission measurements. Triggering was achieved with a fast photodiode.

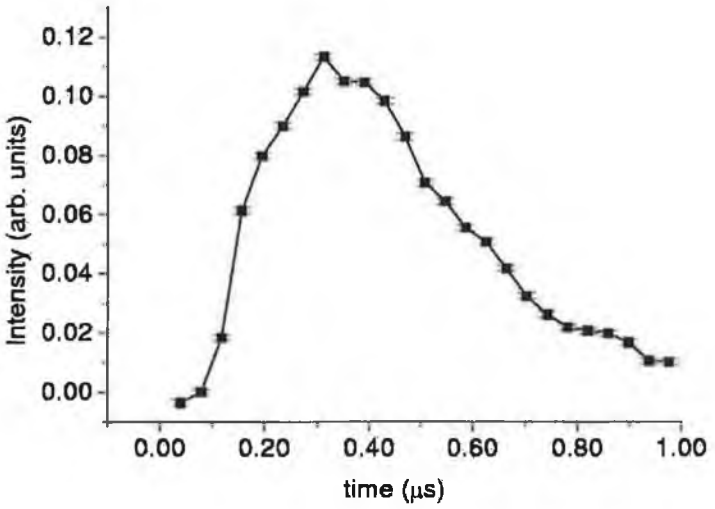

Figure 3.18: Typical monochromator experimental trace: emission as a function of time for 610 nm Li line.

Measurements were averaged over 5 laser shots in the case of spectra and were single shot traces in the case of monochromator traces. A typical experimental trace is shown in figure 3.18. The instrument function was measured to be 0.44 Å for this system for the 610.8 nm lithum line using a hollow-cathode lithium lamp.

3.3 Ultrafast Imaging

Using the frame photography technique, imaging of the evolution of laser ablation plumes was performed using an ICCD. The Andor DH5H7 ICCD camera has two main components which are a *CCD chip* coupled to a *gated image intensifier*. This camera has a spectral range of 180 to 850 nm.

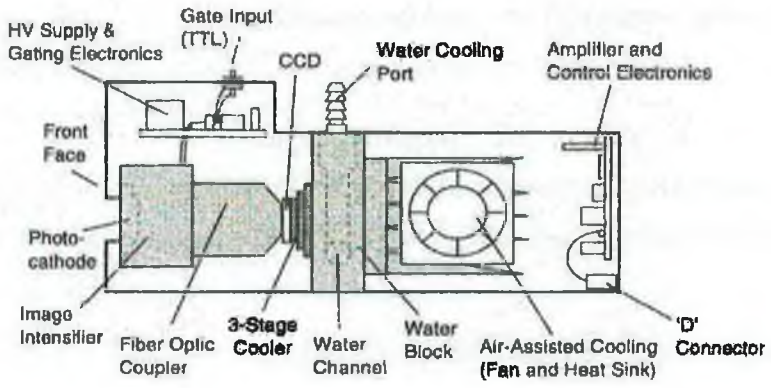

Figure 3.19: Schematic of the ICCD camera (adapted from [67]).

The silicon CCD chip consists of a 2-D matrix of 512×512 photo-sensors or pixels, each 24 μm square. When light falls on a pixel element photoelectrons are produced and are confined to their respective elements. Thus, if an image is projected onto the array, a corresponding charge pattern will be produced. This is then transferred (readout) off the chip and into computer memory. A typical experimental image is shown in figure 3.20.

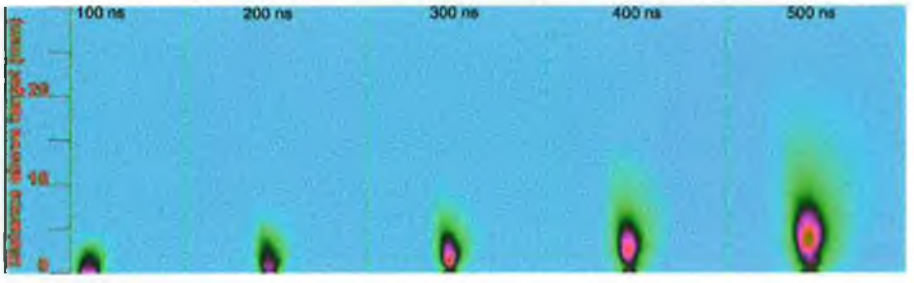

Figure 3.20: Typical images of Ga plume expanding into vacuum.

An image intensifier is a device that amplifies the intensity of an image. If it is placed before the CCD chip then it can enable imaging in low light level conditions, thus facilitating the observation of signals of intensities that might otherwise go undetected by the CCD chip alone. As well as amplifying, an image intensifier can be rapidly switched on and off, allowing it to be used as a very

fast shutter. The minimum optical gate time of the DH5H7 camera system is 2.9ns.

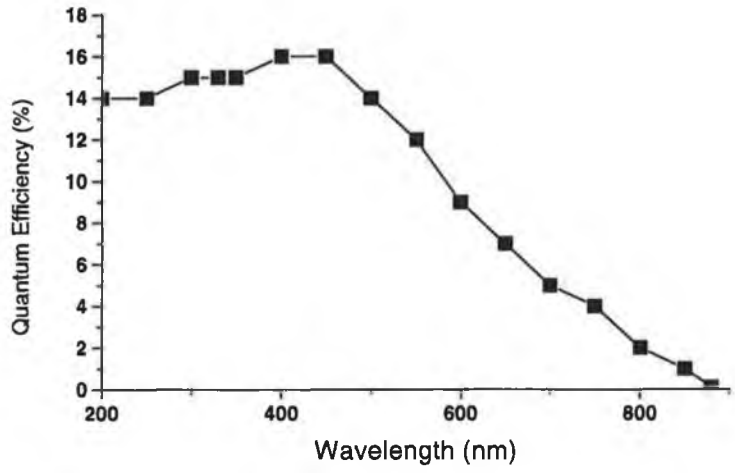

Figure 3.21: Spectral response of Intensifier (adapted from [67]).

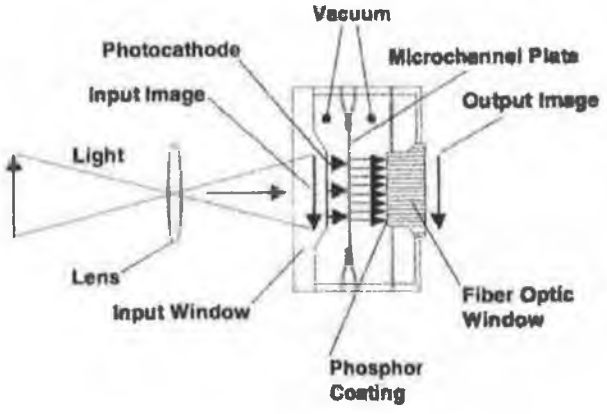

Figure 3.22: Schematic of the gated intensifier (adapted from [68]).

The intensifying unit itself has three main elements; photocathode, microchannel plate (MCP) and output phosphor screen. It is housed in an evacuated

tube with a front window which has a photocathode coated on its inside surface.

Photons from the image hitting the photocathode emit electrons from it, which are drawn across a short distance ($\sim$ 0.2mm) by an electric field towards the micro-channel plate (see fig 3.22).

The micro-channel plate is of a honeycomb glass construction $\sim$ 1mm in thickness and has a high potential across it (500 to 1000 V) so that the photo-electrons will cascade down a channel producing secondary electrons and exiting as a cloud of electrons giving gains up to 10^4. Altering the potential across the plate allows one to change the gain setting of the camera to an appropriate value.

The output electrons from the MCP are finally accelerated across another small gap ($\sim$ 0.5mm) by a potential of $\sim$ 6000 V to a phosphor coated fibre-optic window. This intensified image is then fibre-optic-coupled to the CCD chip where it is readout to the pc.

Using a knife edge the spatial resolution of the ICCD system was measured, in the same manner as in section 3.2.1, to be 384 μm (figure 3.23).

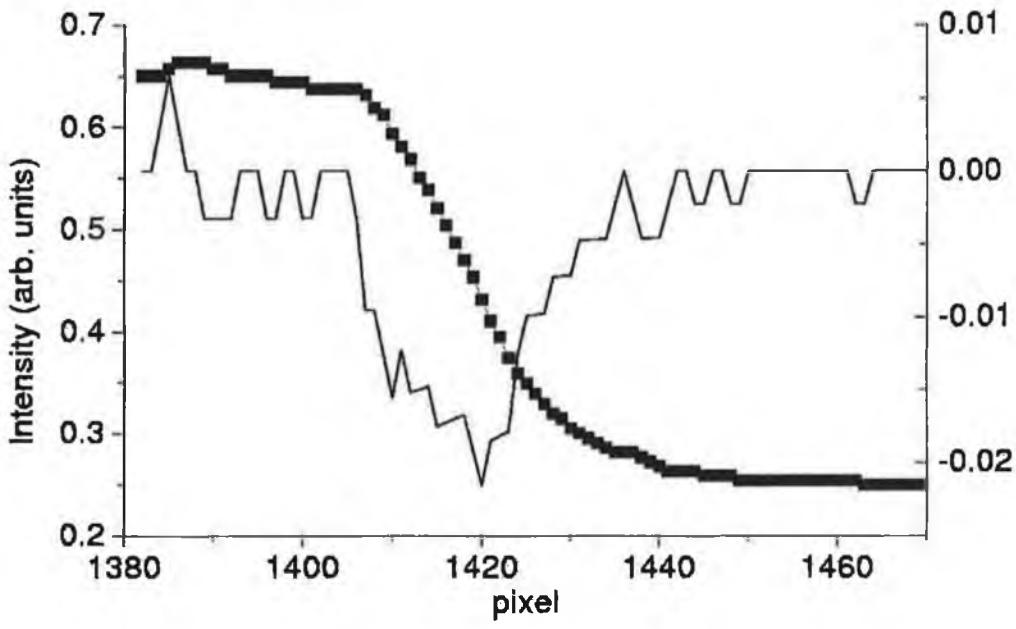

Figure 3.23: Scan across knife edge (data points) and line spread function (solid).

3.3.1 Spectrally resolved imaging

To facilitate spectrally resolved imaging of lithium ablation plumes two interference filters, transmitting light in a small band centred on the 670.8 nm ($1s^2.2s - 1s^2.2p$) and 610.3 nm ($1s^2.2p - 1s^2.3d$) neutral lithium transitions, respectively, were placed in front of the camera objective. This allowed the study of the expansion of the corresponding excited state species in the plume. The spectral transmission curves of the filters are shown in figures 3.24 and 3.25.

3.3.2 Measurement of velocity distributions

The ICCD images were calibrated spatially using a mm-scale ruler with 1 pixel corresponding to ≈ 0.1 mm, this is taken as the error bar. The spatial resolution was measured using a knife-edge and was found to be 0.4 mm (see figure 3.23). The position of the luminous edge of the plume was found by taking the second derivative of the spatial profile to find the point of inflection where the emission signal in the image goes to zero. When plotted versus time, the slope yields the velocity of the luminous edge of the plume. The luminous peak velocity can similarly be found by plotting the position of peak luminosity versus time. Velocities were estimated for Ga plumes expanding into N_2 and also Li plumes in vacuum ablated with various spot sizes.

Time-of-flight profiles of laser ablation plumes can be constructed from plume emission images by extracting and plotting the variation of intensity with time at fixed distances above the target. If collisions occur the dynamics of the ablation plume may be described by the formation of a Knudsen layer (see section 2.1.3) in the vicinity of the surface area of the irradiated material [33]. With a change of variables from velocity to time, equation 2.19 becomes

$$F(t) = \frac{A}{t^4} exp\left[\left(\frac{-m}{2k_B T_K}\right)\frac{(L - u_K t)^2}{t^2}\right] \tag{3.9}$$

where T_K stands for the Knudsen layer temperature and u_K is the Knudsen layer velocity. These parameters were also calculated for Ga plumes expanding into N_2 and also Li plumes in vacuum ablated with various spot sizes.

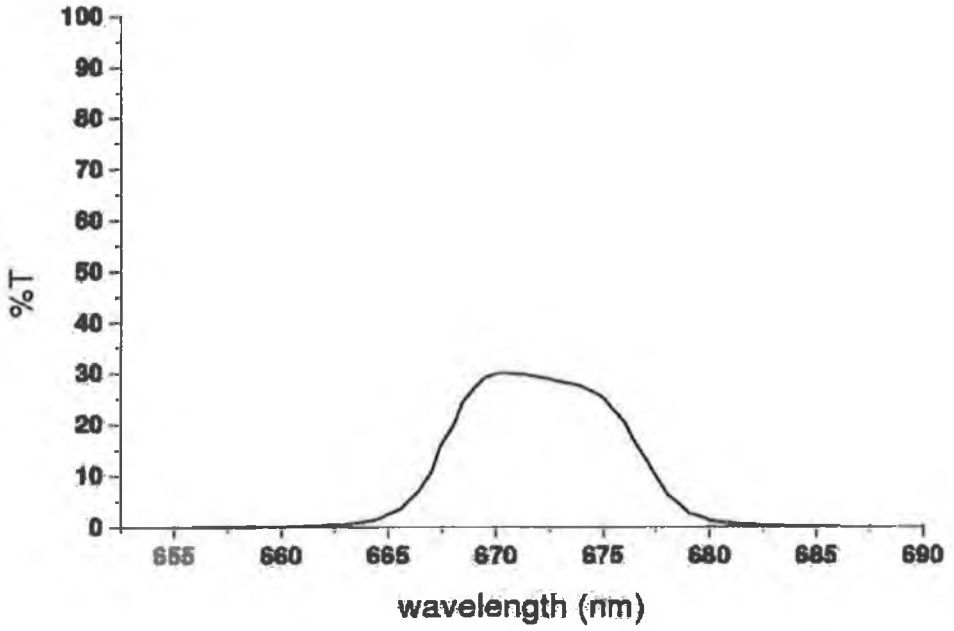

Figure 3.24: Transmission curve of I/F 671FS-10-25 ($\lambda_{centre} = 671.5$ nm).

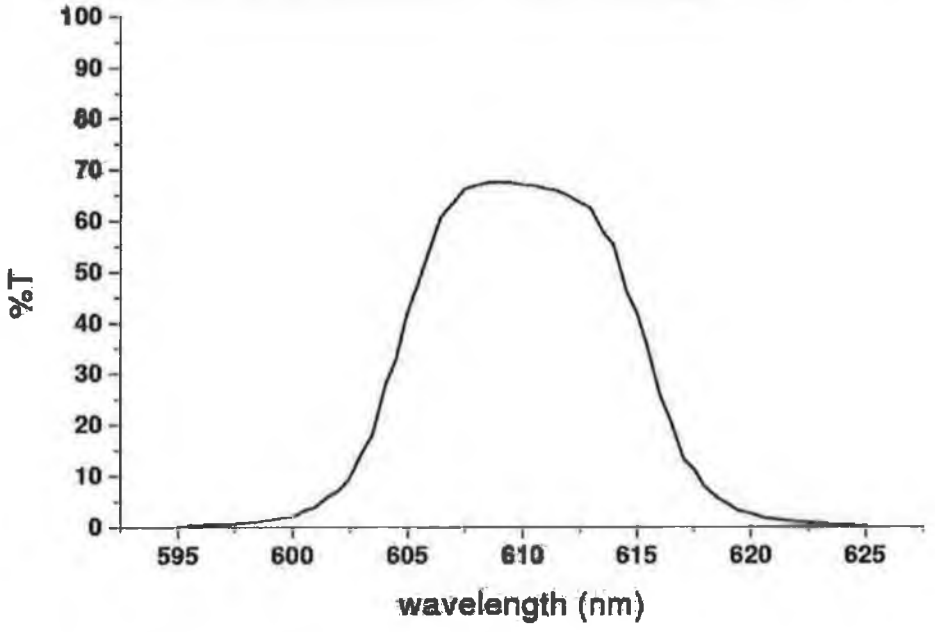

Figure 3.25: Transmission curve of I/F 59405#1 ($\lambda_{centre} = 608.8$ nm).

3.4 Ion Probe

A Langmuir ion probe was setup in the vacuum chamber in collaboration with Trinity College Dublin. It was used to estimate the time of flight (TOF), peak velocity and kinetic energy of ablation plumes from a liquid Ga target. It was also used to measure the charge collected by the probe, both as a function of fluence and as a function of angle to the target normal.

3.4.1 Probe description

The probe consists of metal electrode exposed beyond an insulating casing inserted into the plume, typically at a distance from the target equal to the target-substrate separation (d). Placing the probe at a negative bias ($0 - 30$V) will result in electrons being repelled and positive ions (which we assume to be Ga^+ ions) attracted towards the probe. A 0.47 μF capacitor is connected in series with a 25 Ω resistor and the biased probe and the charge collected in the probe can be determined by measuring the voltage drop across the load resistor with a fast oscilloscope.

3.4.2 Kinetic energy measurements

By looking at the current (or voltage) maximum in the time of flight spectra, the ion energy associated with the maximum flux of ions through the probe can be estimated

$$K.E._{peak} = \frac{1}{2} m_{Ga^+} \left(\frac{d}{t_{peak}} \right)^2 \tag{3.10}$$

where m_{Ga} is the mass of the gallium ion, d is the distance of the probe above the target and t_{peak} is the time of arrival of the peak.

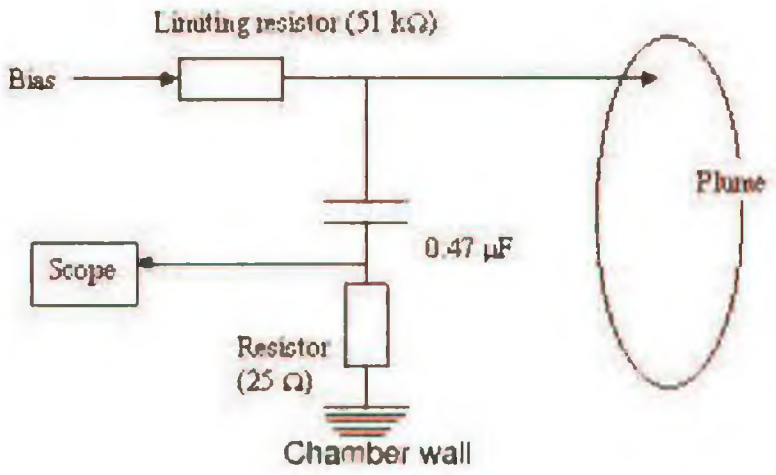

Figure 3.26: Schematic of the ion probe apparatus.

3.4.3 Charge measurements

Integration of the TOF current over the pulse duration yields the total charge on the probe per pulse.

$$Q_{pulse} = \frac{1}{R_{load}} \int_{t_0}^{t_{final}} V_{resistor} dt. \tag{3.11}$$

The integral is carried out over the duration of the TOF signal, from the time at which the laser strikes the target, t_0, to the end of the measured TOF signal, t_{final}.

Assuming the ions are singly charged ($Q_{Ga+} = 1.6 \times 10^{-19}$ C) at the distance of the probe above target (> few cm), the average flux per pulse is determined as

$$Flux = \frac{1}{A_{probe}} \frac{Q_{pulse}}{Q_{Ga+}}. \tag{3.12}$$

3.5 System synchronisation

A schematic of the experimental setup is shown in figure 3.27. The ICCD camera (see section 3.3, page 51) is sychronised and delayed with respect to the firing of the laser using two synchronised Stanford DG535 delay generator boxes. Using LabView virtual instruments these are controlled by a PC via the GPIB interface. The laser flashlamps are triggered at 10Hz continuously from 'delay generator 1'. The PC sets off a sequence of events that fire the laser and gate the camera (i.e. switch on the intensifier). The PC sends a 'fire' signal via the multi-I/O box to close the 'switch' box. This lets the 'enable' pulse from 'delay generator 1' trigger 'delay generator 2' which then triggers the laser, intensifier gate and the stepper motor at specified delays with respect to the flashlamp trigger pulse (figure 3.28).

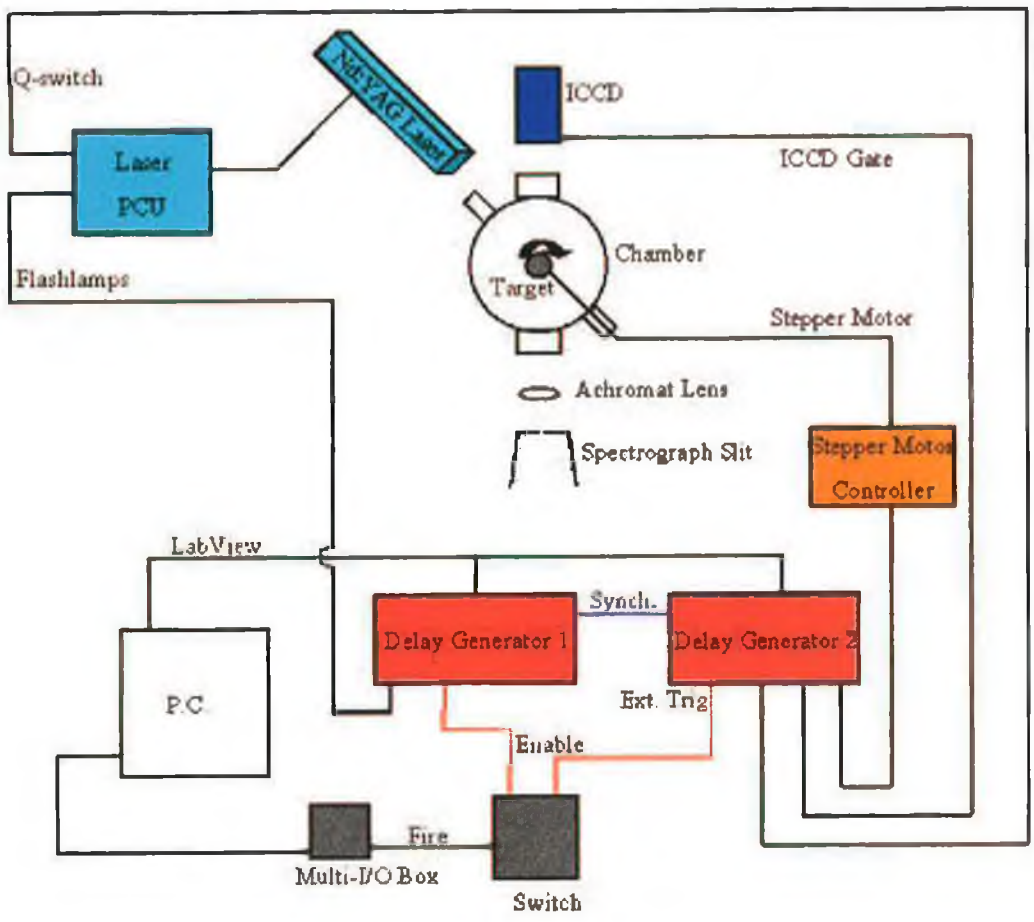

Figure 3.27: Experimental setup for ultrafast imaging of laser ablation.

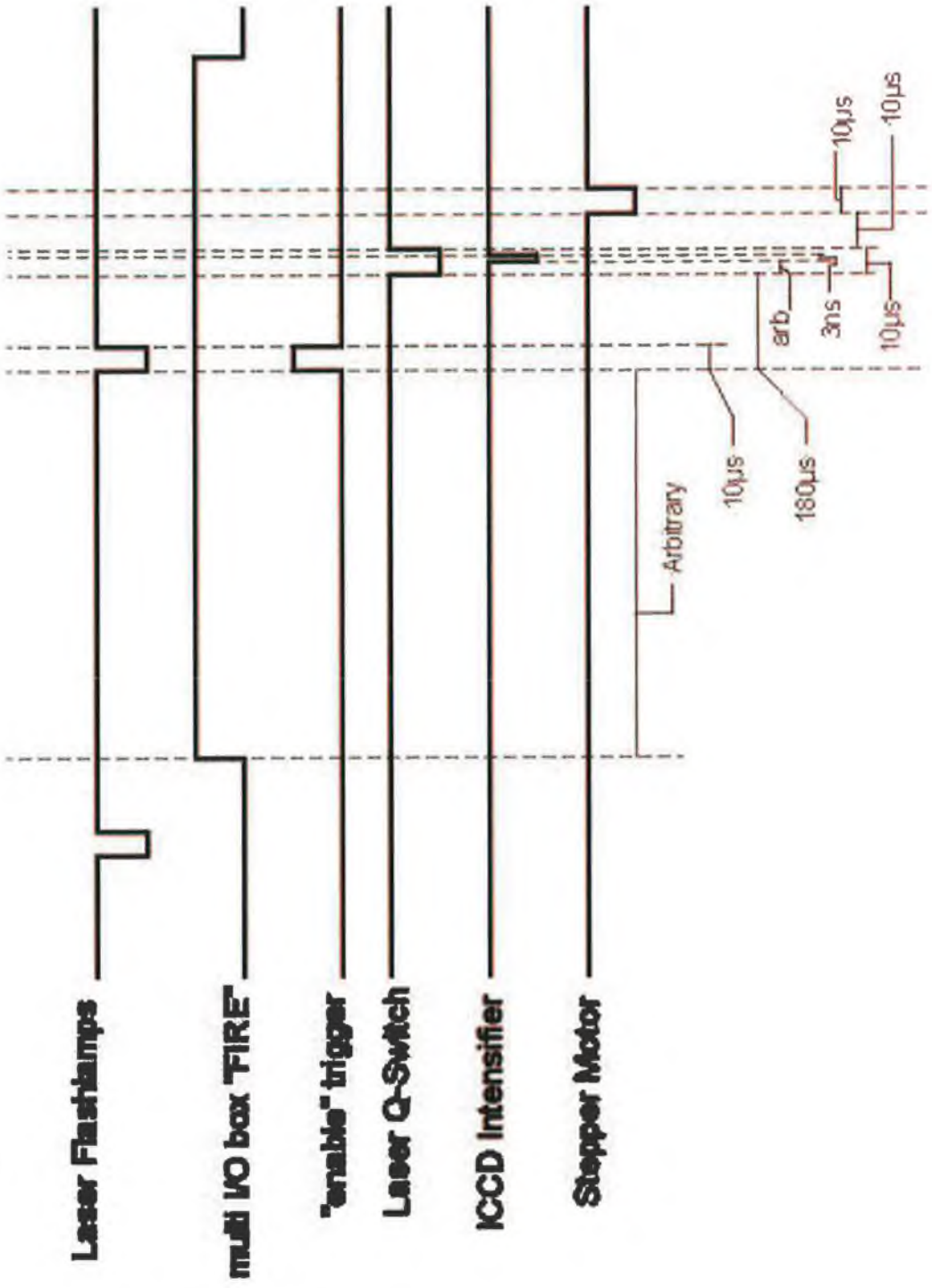

Figure 3.28: Triggering sequence diagram.

Chapter 4

Gallium and Gallium Nitride Results and Analysis

4.1 Spectroscopy

Spectral images of Gallium Nitride plumes expanding into vacuum (10^{-7} mbar N_2) and a background gas (5 mbar N_2) are shown in figure 4.1 using a fluence of 5 Jcm^{-2} and a spotsize of $2 \times 2 \pm 0.005$ mm with different laser wavelengths to ablate the target. These were recorded using photographic film as the detector (see section 3.2.2). The spatial scale is indicated in the images, as is the position of the target surface. One observes from the images that a continuum was present above the target surface which typically extended 1 to 2 mm. Above 2 mm the plume emission consists mainly of discrete atomic or ionic lines. The maximum emission occurs in the continuum region and decreases with distance from target.

It can be seen that a certain number of lines were still emitting up to ~ 30 mm or more away from the target, others tended to emit until ~ 15 mm and still others until just ~ 5 mm. The lines in the vacuum cases were all assigned to gallium lines (see table 4.1 which lists the measured and assigned values of the lines numbered in figure 4.1). In the case of an ambient N_2 gas pressure, the same gallium lines were present and were broadened with respect to the vacuum case, however no N or N^+ lines were observed.

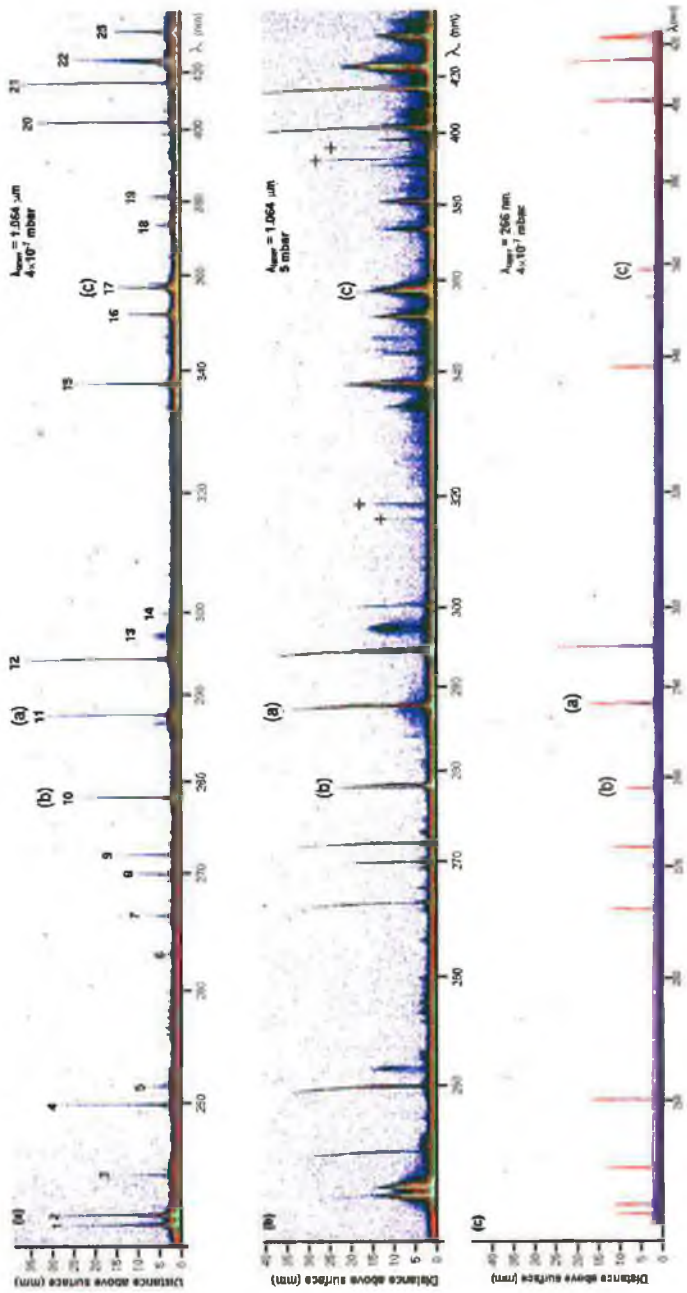

Figure 4.1: Space resolved emission spectrum of an ablation plume of GaN created at a fluence of 5 Jcm^{-2} with different laser wavelengths (λ_{Laser}) and N_2 background pressures (mbar).

Line	Meas. λ (Å)	NIST λ(Å)	Assign.	f_{ki}	g_i-g_k
1	2418	2418.69	Ga I	4.4e-03	4 - 2
2	2424	2423.98	Ga III		
2	2424	2424.36	Ga III		
3	2450	2450.08	Ga I	5.0e-02	2 - 4
4	2500	2500.19	Ga I	4.8e-02	4 - 6
5	2513	2513.55	Ga II		
6	2624	2624.82	Ga I		
7	2659	2659.87	Ga I	1.3e-02	2 - 2
8	2700	2700.47	Ga II		
9	2719	2719.66	Ga I	1.3e-02	4 - 2
10 or (b)	2780	2780.15	Ga II		
11 or (a)	2874	2874.24	Ga I	3.0e-01	2 - 4
12	2943	2943.64	Ga I	2.7e-01	4 - 6
12	2943	2944.17	Ga I	3.5e-02	4 - 4
13	2971	2969.41	Ga II		
13	2971	2971 multiplet	Ga II		
14	2993	2992.84	Ga II		
15	3375	3374.94	Ga II		
15	3375	3375.95	Ga II		
16	3520	3521.77	Ga III		
17 or (c)	3580	3581.19	Ga III		
17	3735	3734.85	Ga II		
19	3808	3806.60	Ga III		
20	4034	4032.99	Ga I	1.2e-01	2 - 2
21	4172	4172.04	Ga I	1.2e-01	4 - 2
22	4253	4251-4 multiplet	Ga II		
23	4381	4380.69	Ga III		
23	4381	4381.76	Ga III		

Table 4.1: Measured values of gallium lines and assignments.

A number of lines appeared which did not originate on the target and these were attributed to excitation in the gas (and not target impurities). These are labelled '+' in fig. 4.1. From figure 4.1 one can see the usefulness of this spatially resolved technique to track the various constituents of PLD plumes, especially if one considers the image in terms of a "steady state" plume.

4.1.1 Emission spectra of Gallium plume

The emission spectra for a Ga plume at 2, 4 and 6 mm above target surface is shown for 1064 nm and 532 nm laser radiation (2.5 Jcm^{-2}) in figures 4.2 and 4.3 . This is the result of scanning across , for example, figure 4.1, at 2, 4 and 6 mm above target, respectively. From figures 4.2 and 4.3 one observes that the intensity of all the plume emission lines diminishes as one looks further away from the target surface, eventually being below the detection limit.

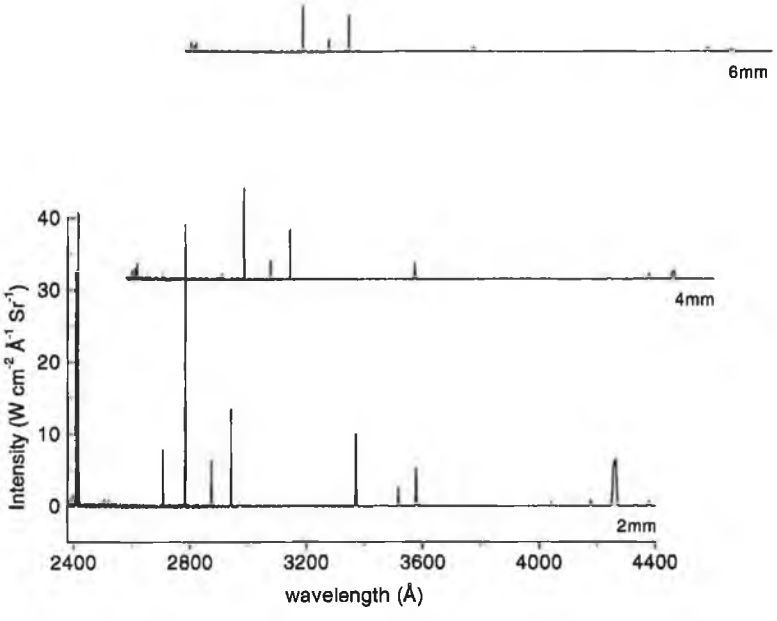

Figure 4.2: Ga in 10^{-7} mbar N_2 at 2, 4 and 6 mm from target surface, $\lambda_{Laser} = 1064$ nm, 2.5 Jcm^{-2}.

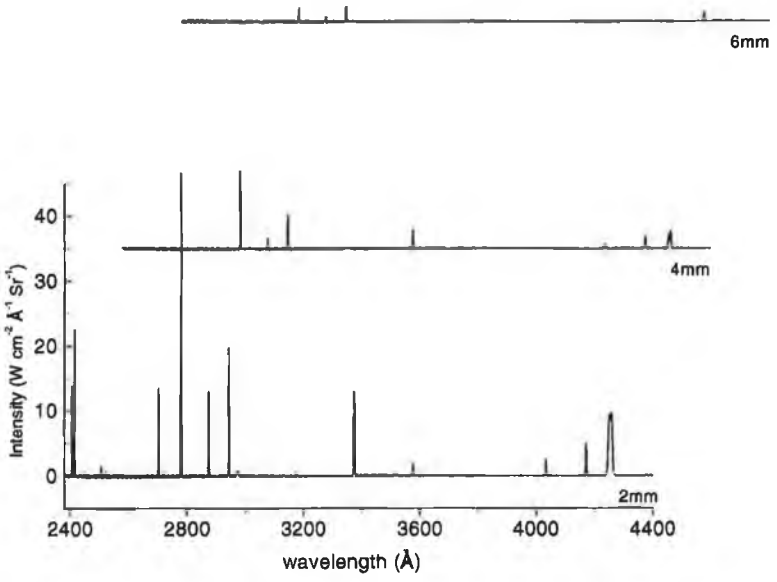

Figure 4.3: Ga in 10^{-7} mbar N_2 at 2, 4 and 6 mm from target surface, $\lambda_{Laser} = 532$ nm 2.5 Jcm^{-2}.

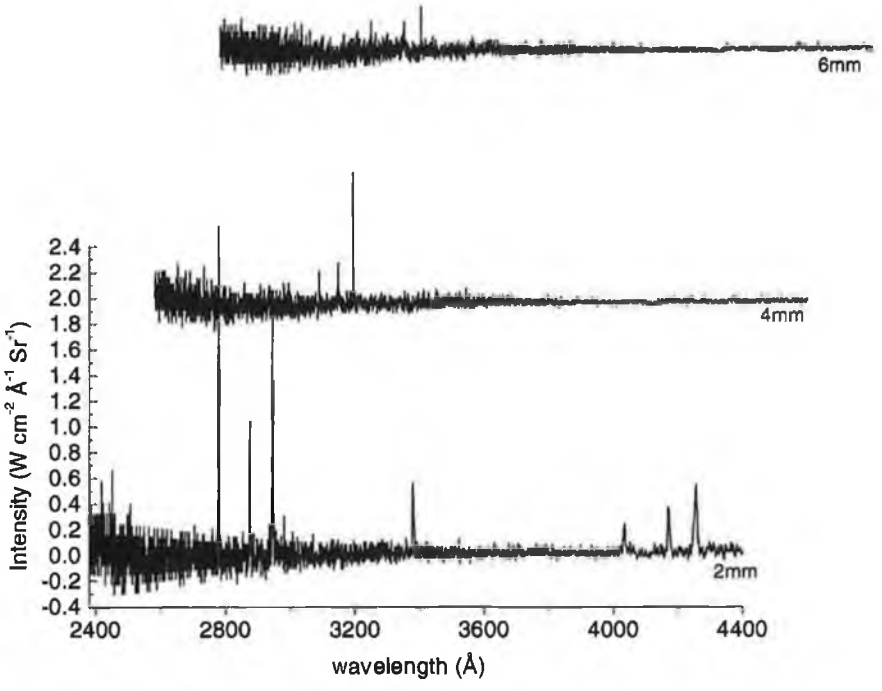

Figure 4.4: Ga in 10^{-7} mbar N_2 at 2, 4 and 6 mm from target surface, $\lambda_{Laser} = 355$ nm 2.5 Jcm^{-2}.

Figures 4.4 and 4.5 shows emission spectra from Ga plumes generated with 355 and 266 nm laser radiation, respectively, and correspond to the same conditions as figures 4.2 and 4.2 (2.5 Jcm^{-2}, 10^{-7} mbar N_2, liquid Ga target).

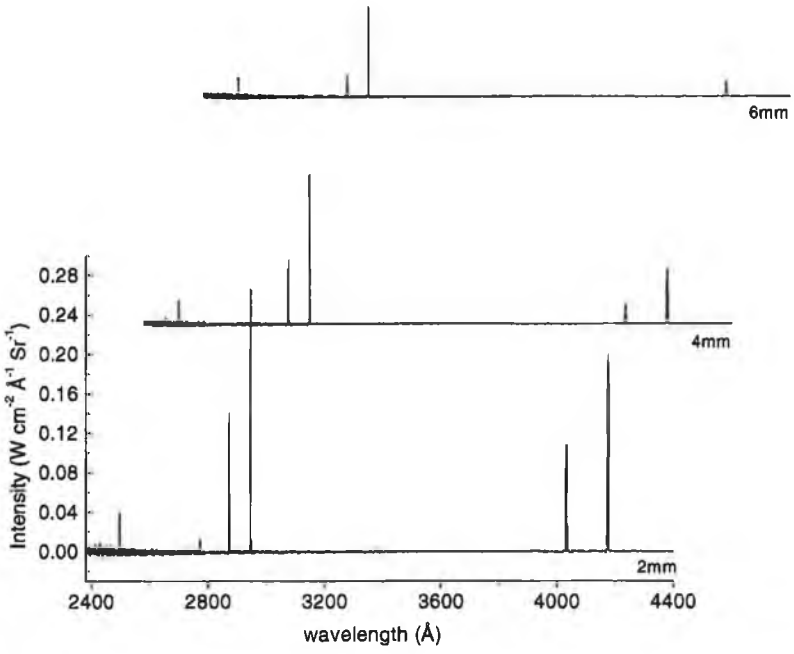

Figure 4.5: Ga in 10^{-7} mbar N_2 at 2, 4 and 6 mm from target surface, $\lambda_{Laser} = 266$ nm 2.5 Jcm^{-2}.

Influence of laser wavelength

One may observe, from the preceding figures, that the emission intensity of the plumes scale downwards with decreasing laser wavelength. This is illustrated in figure 4.6 which plots the integrated intensity of Ga, Ga^{+} and Ga^{2+} marker lines vs laser wavelength at a fluence of 2.5 Jcm^{-2}. These lines are marked as (a), (b) and (c) in figure 4.1 and correspond to the 2874.24 Å , 2780.15 Å and 3581.19 Å lines from table 4.1. This effect does not seem to be strongly dependent on ionisation as a similar pattern is followed by all three lines. However, the effect is less significant for neutral Ga at short laser wavelengths.

Referring to figure 2.1 on page 10 showing the inverse bremsstralung absorption coefficient vs wavelength, we note that the ablation plume absorbs the incident laser radiation to a higher degree at higher laser wavelengths. This absorption excites the particles in the expanding plume, thus the excitation temperature of ablation plumes created with IR radiation will be higher than that of plumes created with UV radiation and they will show a higher emission intensity.

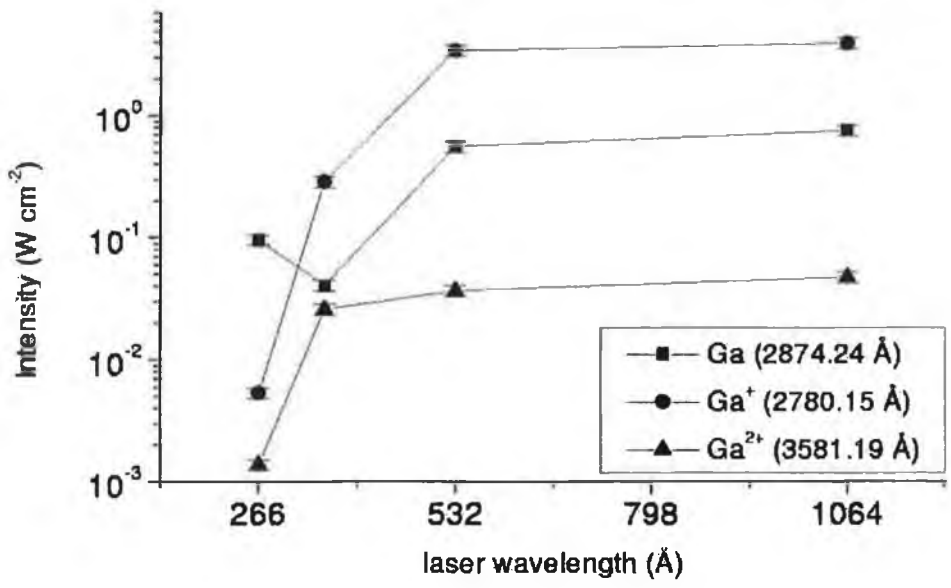

Figure 4.6: Ga emission in 10^{-7} mbar N_2: ion stage vs λ_{Laser}, 2.5 Jcm^{-2}, 5 mm above target.

This increased absorption of higher laser wavelengths also has the effect of lowering the laser intensity reaching the target compared with shorter laser wavelengths [69]. This reduces the amount of material ablated and the energy initially deposited in it, thus driving an expansion which is slower with 1064 nm than 266 nm laser radiation. Thus, with shorter laser wavelengths the laser reaches the target creating a faster, denser but colder (less absorbing) plume and with a higher proportion of neutrals, when compared to longer laser wavelength plumes. This was observed in the case of lithium ablated with 266, 532 and 1064 nm laser raditation at a fluence of 6.5 Jcm^{-2} and is tabulated in table 5.3.

Influence of pressure

The emission spectra from a Ga plume at 10^{-7}, 10^{-2}, 10^{-1} and 5 mbar N_2 background gas pressures is shown at 5 mm above target surface in figures 4.7 and 4.8 for 1064 and 532 nm laser radiation at 2.5 Jcm^{-2} on a liquid gallium target. Figures 4.9 and 4.10 shows emission spectra from Ga plumes generated with 355 and 266 nm laser radiation, respectively, and correspond to the same conditions as figures 4.7 and 4.8 (2.5 Jcm^{-2}, liquid gallium target, 5 mm above target).

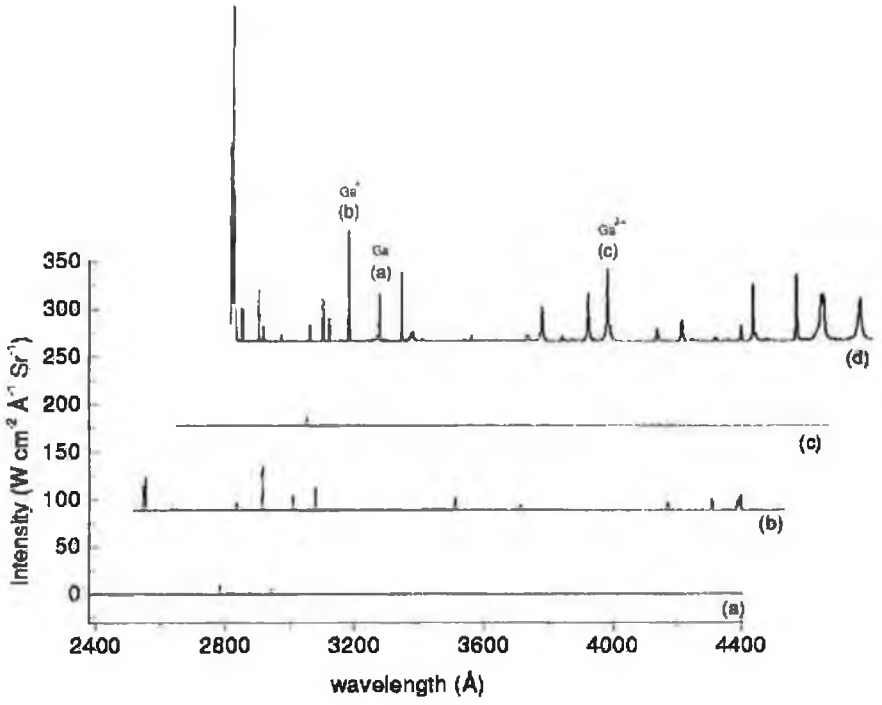

Figure 4.7: Ga in (a) 10^{-7}, (b) 10^{-2}, (c) 10^{-1} and (d) 5 mbar N_2, 5 mm from target surface, $\lambda_{Laser} = 1064$ nm.

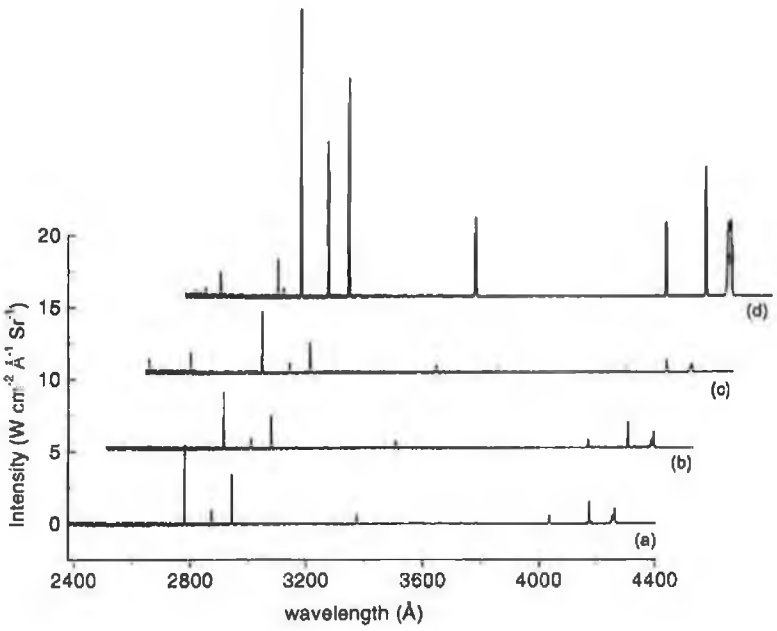

Figure 4.8: Ga in (a) 10^{-7}, (b) 10^{-2}, (c) 10^{-1} and (d) 5 mbar N_2, 5 mm from target surface, $\lambda_{Laser} = 532$ nm.

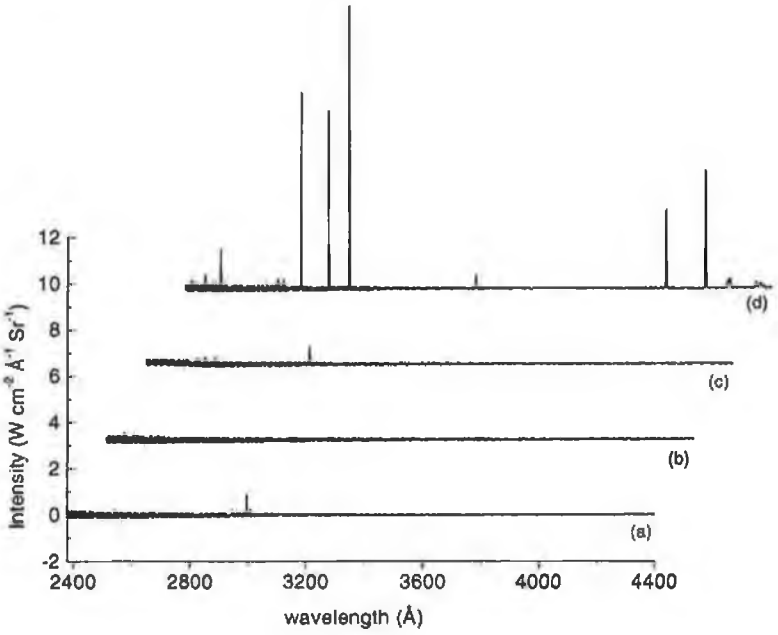

Figure 4.9: Ga in (a) 10^{-7}, (b) 10^{-2}, (c) 10^{-1} and (d) 5 mbar N_2, 5 mm from target surface, $\lambda_{Laser} = 355$ nm.

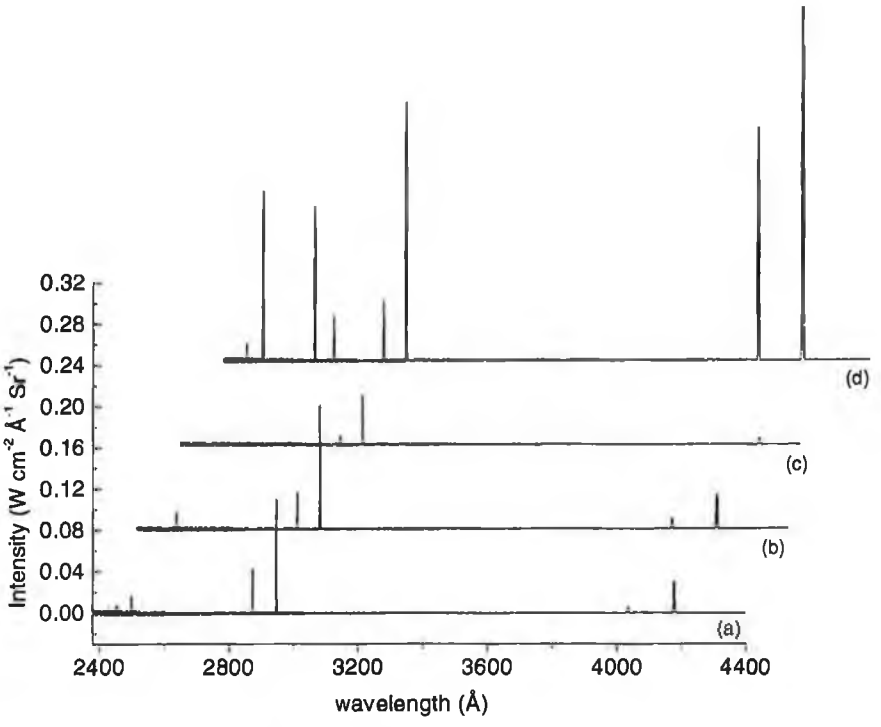

Figure 4.10: Ga in (a) 10^{-7}, (b) 10^{-2}, (c) 10^{-1} and (d) 5 mbar N_2, 5 mm from target surface, $\lambda_{Laser} = 266$ nm.

It may be observed, in all cases, that the emission was substantially enhanced in 5 mbar N_2 whereas in the range of 10^{-7}-10^{-1} mbar gas pressures there were very little differences in the spectra. This pattern was reproduced for all four laser wavelengths. This is illustrated, for 1064 nm laser radiation, in figures 4.11, 4.12 and 4.13 where the integrated intensity (integrated over λ and Ω) is plotted vs distance above target surface for each of the three marker lines, respectively, at each abmient gas pressure. These marker lines have been indicated in figure 4.7.

Figures 4.14, 4.15 and 4.16 shows this for 532 nm laser radiation, 4.17, 4.18 and 4.19 for 355 nm laser radiation and figure 4.20 shows the 266 nm laser radiation case (absence of ionic emission).

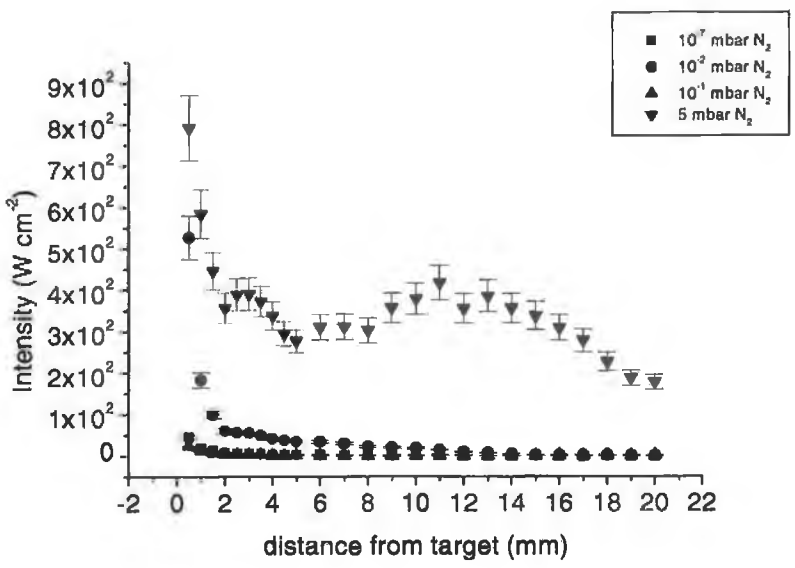

Figure 4.11: Ga: Ga emission intensity vs distance from target surface for a range of pressures of N_2, $\lambda_{Laser} = 1064$ nm.

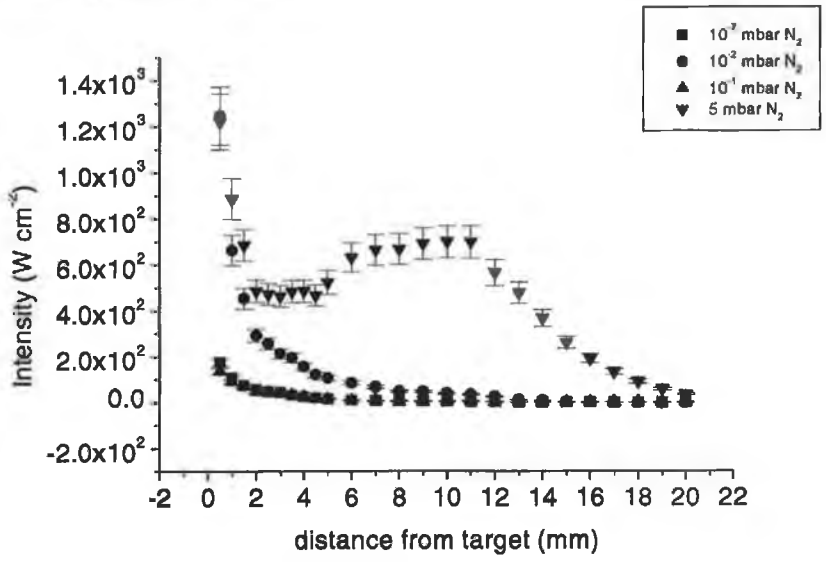

Figure 4.12: Ga: Ga^+ emission intensity vs distance from target surface for a range of pressures of N_2, $\lambda_{Laser} = 1064$ nm.

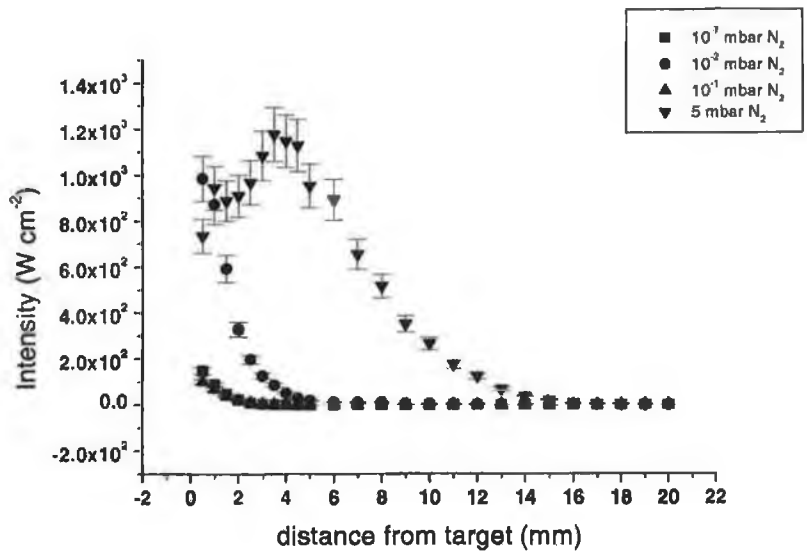

Figure 4.13: Ga: Ga^{2+} emission intensity vs distance from target surface for a range of pressures of N_2, $\lambda_{Laser} = 1064$ nm.

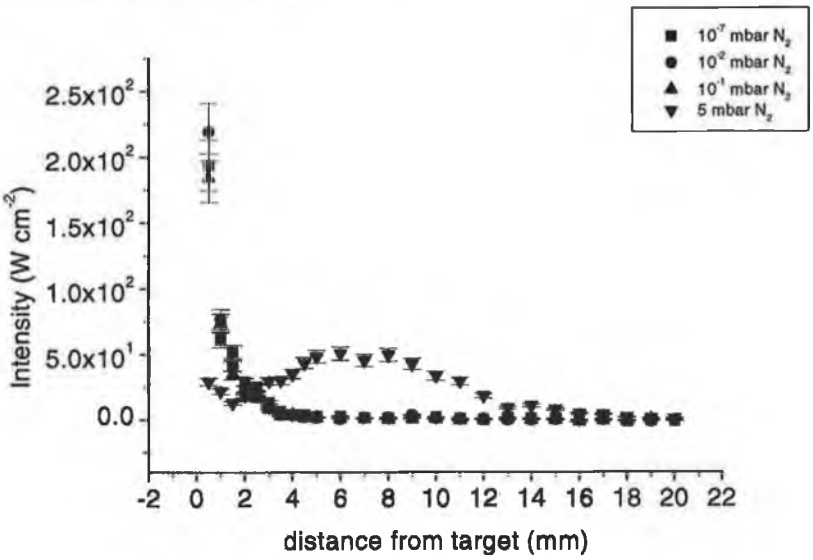

Figure 4.14: Ga: Ga emission intensity vs distance from target surface for a range of pressures of N_2, $\lambda_{Laser} = 532$ nm.

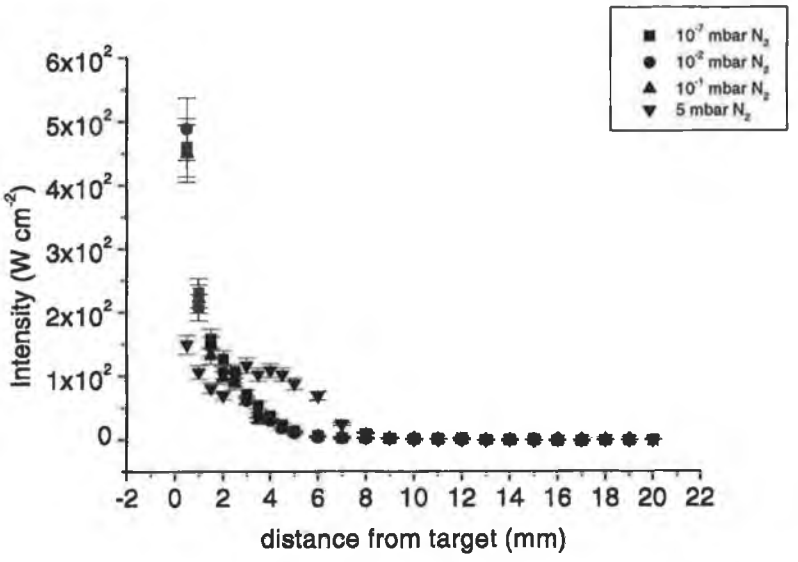

Figure 4.15: Ga: Ga^+ emission intensity vs distance from target surface for a range of pressures of N_2, $\lambda_{Laser} = 532$ nm.

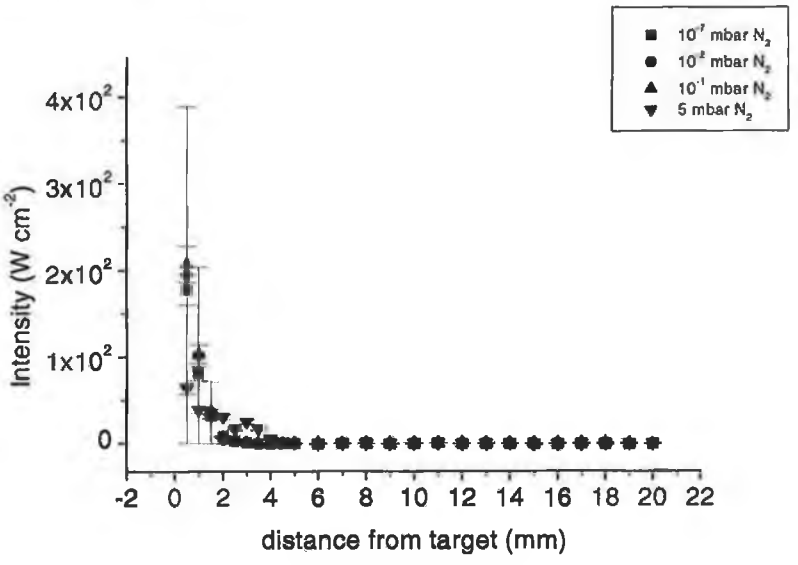

Figure 4.16: Ga: Ga^{2+} emission intensity vs distance from target surface for a range of pressures of N_2, $\lambda_{Laser} = 532$ nm.

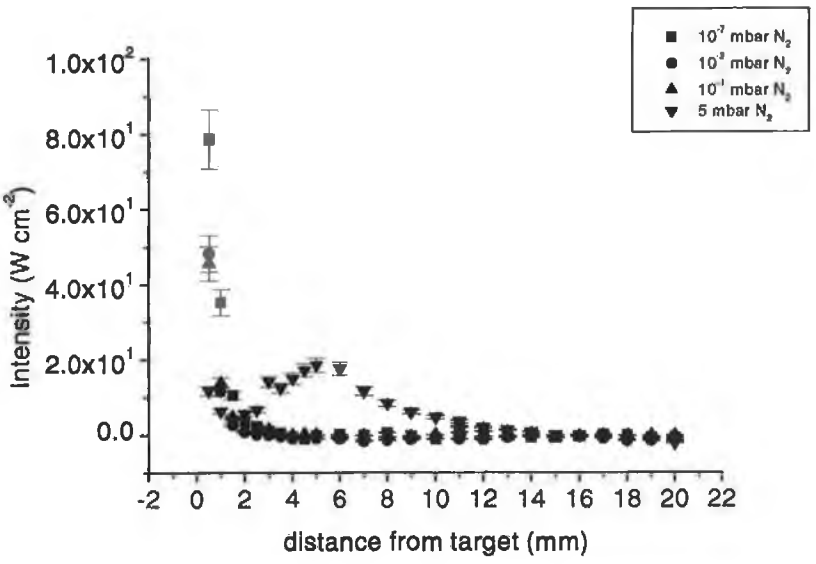

Figure 4.17: Ga: Ga emission intensity vs distance from target surface for a range of pressures of N_2, $\lambda_{Laser} = 355$ nm.

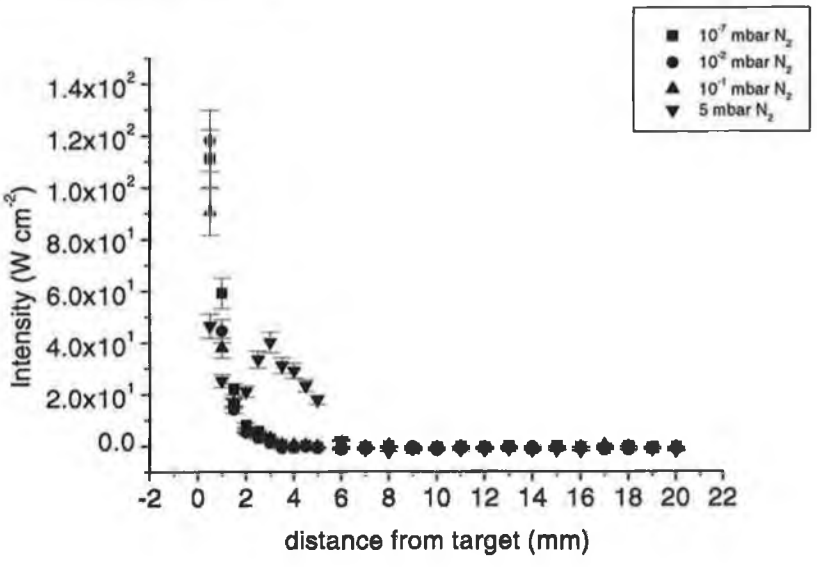

Figure 4.18: Ga: Ga^+ emission intensity vs distance from target surface for a range of pressures of N_2, $\lambda_{Laser} = 355$ nm.

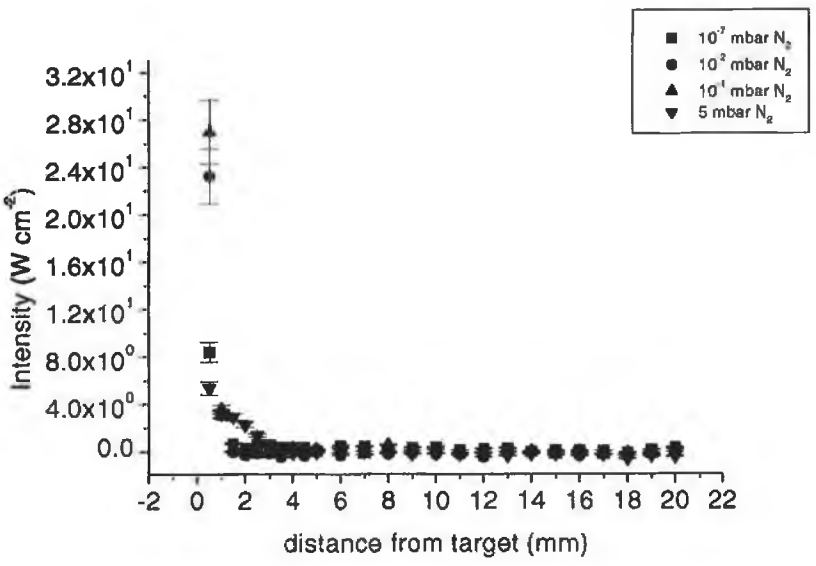

Figure 4.19: Ga: Ga^{2+} emission intensity vs distance from target surface for a range of pressures of N_2, $\lambda_{Laser} = 355$ nm.

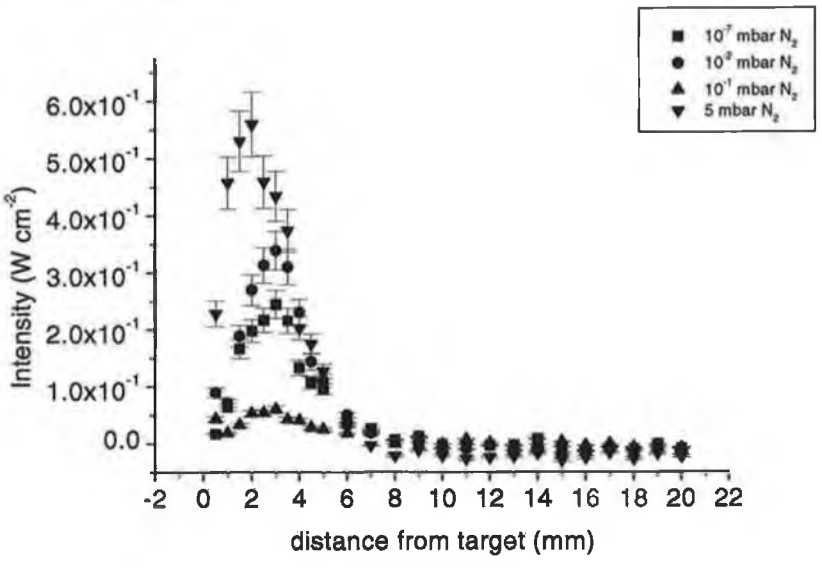

Figure 4.20: Ga: Ga emission intensity vs distance from target surface for a range of pressures of N_2, $\lambda_{Laser} = 266$ nm.

The fast frame imaging technique suggests, in section 4.3, that the plume acts as a piston propogating into the ambient gas at supersonic speeds and forms a compression front which may support a shockwave [30]. This decelerates the plume and heating occurs in the region just behind the compression front [70]. This conversion of the plume particles kinetic energy to thermal energy behind the compression front results in enhanced emission from this region [71].

One can see that for the 5 mbar case at all laser wavelengths that the emission increased sharply from the surface up to a maximum distance and then decreased more slowly. This max distance is listed in table 4.2. The maximum distance for the neutrals and different ion stages vary, being shorter for more highly charged ions. This is because the higher ion stages recombine more quickly in the denser region close to target and has also been observed in ion probe measurements of GaN target ablation in N_2 using KrF 248 nm laser radiation at a fluence of 2.5 Jcm^{-2}, [14], where the ion probe signal is reduced at higher ambient pressures.

λ_{laser} (nm)	Ga	Ga^+	Ga^{2+}
266	3	-	-
355	5	3	1
532	7	4	3
1064	12	9	4

Table 4.2: Position (in mm) of emission peak in 5 mbar N_2 (fluence = 2.5 Jcm^{-2}).

It can be seen from the table that the plume intensity increases with laser wavelength which can be understood in terms of laser absorption in the plume, as discussed in section 4.1.1.

Mah et al, [72], grew GaN films by PLD using a liquid gallium target with KrF 248 nm laser radiation at 8 Jcm^{-2}. The author reports that at pressures of < 3 Torr N_2 (< 2.25 mbar) crystalline GaN could not be grown and, so, N_2 pressures of 5 Torr (3.75 mbar) were used. This suggests that the arrival on target of neutrals and ions, excited in these conditions, plays an important role in film growth.

4.1.2 Ga level populations in Ga plume

From the integrated intensities of the 417.2, 287.4, 272.0 and 250.1 nm lines, and using equation 2.37 and tabulated data [73], one can estimate the populations in the $4s^2 5s$ ($\approx$ 3.1 eV), $4s^2 4d$ ($\approx$ 4.3 eV), $4s^2 6s$ ($\approx$ 4.7 eV) and $4s^2 5d$ ($\approx$ 5.1 eV) excited levels. The estimation of populations hinges on the fact that these are *absolute intensities*. The level populations are shown in figures 4.21, 4.22,

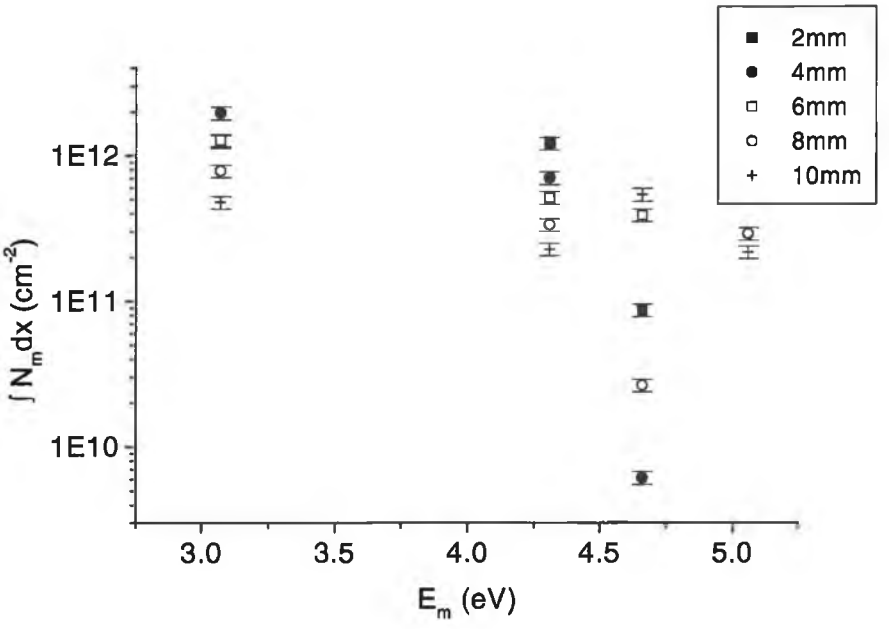

Figure 4.21: Level populations of Ga (Ga plume in 10^{-7} mbar N_2) vs excited state energy at various distances from target surface, $\lambda_{Laser} = 1064$ nm.

4.23 and 4.24 for a Ga plume, generated by 1064, 532, 355 and 266 nm laser radiation, respectively, at various distances above the target surface. Since the spectra are integrated along the line of sight through the plume and over the emission duration, so too are the population estimates. However, as the plume passes any point above the target quite fast, this emission duration is short ($\approx$ 200 - 300 ns, as we shall see in section 4.3.2).

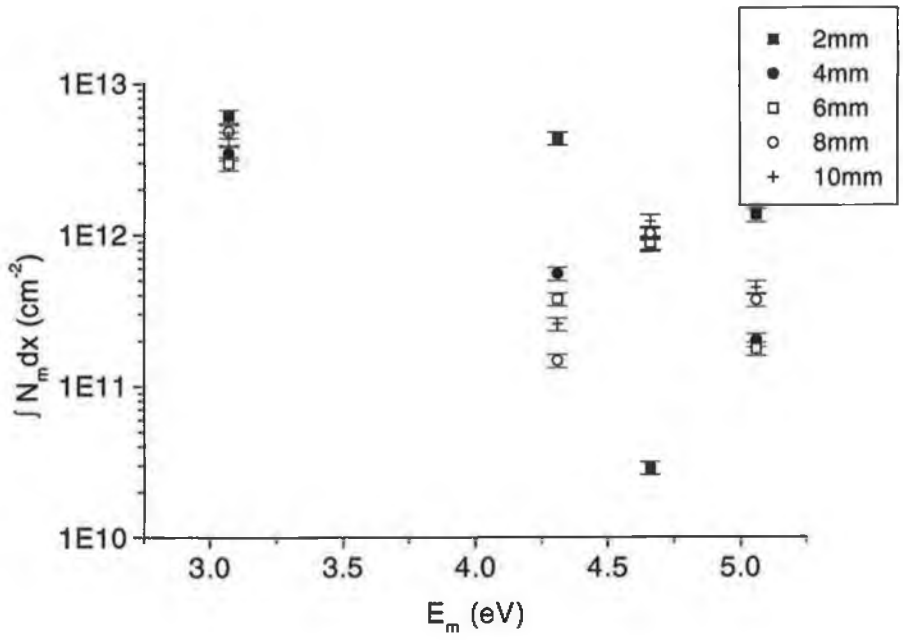

Figure 4.22: Level populations of Ga (Ga plume in 10^{-7} mbar N_2) vs excited state energy at various distances from target surface, $\lambda_{Laser} = 532$ nm.

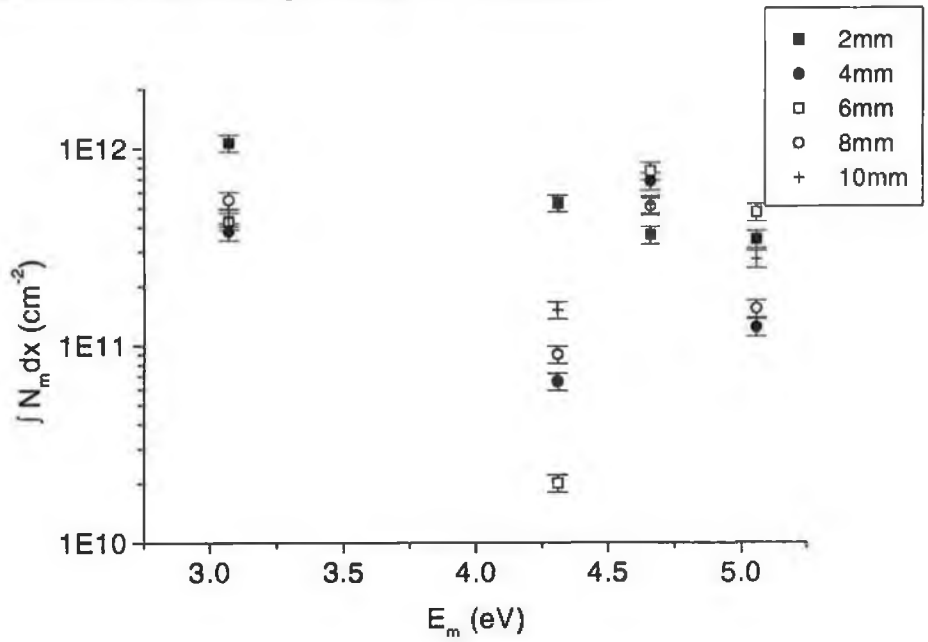

Figure 4.23: Level populations of Ga (Ga plume in 10^{-7} mbar N_2) vs excited state energy at various distances from target surface, $\lambda_{Laser} = 355$ nm.

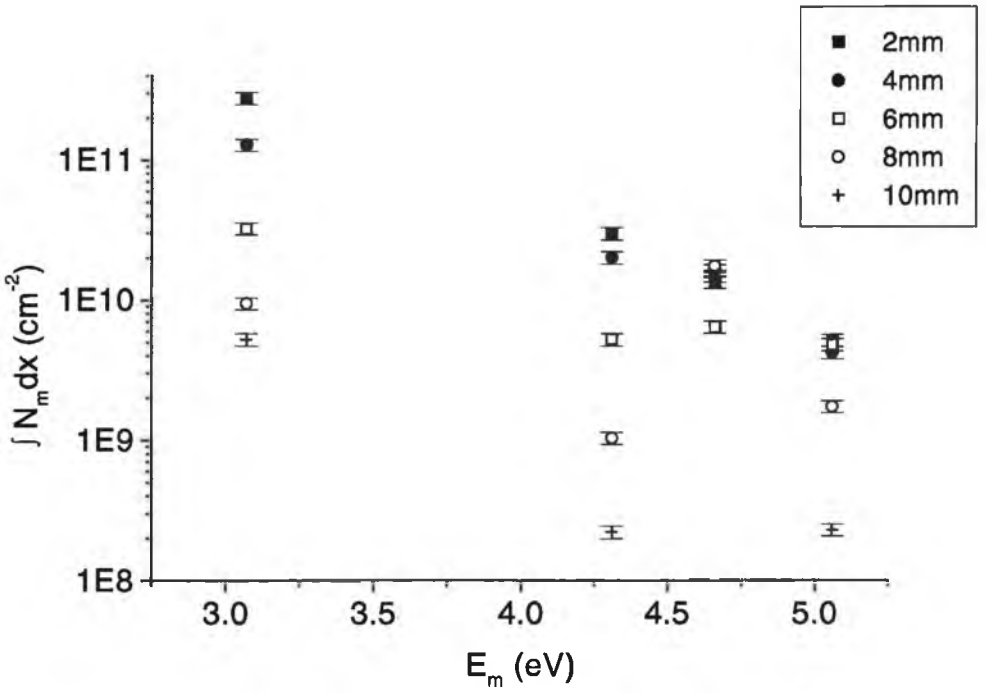

Figure 4.24: Level populations of Ga (Ga plume in 10^{-7} mbar N_2) vs excited state energy at various distances from target surface, $\lambda_{Laser} = 266$ nm.

4.1.3 Excitation temperature in Ga plume

Figures 4.25 and 4.26 display Boltzmann plots for Ga plume in 10^{-7} mbar N_2 ($\lambda_{Laser} = 1064$ nm, fluence = 2.5 Jcm^{-2}) at 2 and 4 mm above target. These were plotted using equation 3.1, section 3.2, and the excitation temperature T_{exc} can be extracted from the slope of such a plot. The error bar is the experimental value combined with a value of 10 % from the oscillator strength (varies from 3 to 50 %). In figures 4.27, 4.28, 4.29 and 4.30 the excitation temperature from these plots are displayed vs distance above target surface in the same conditions ($\lambda_{Laser} = 1064$, 532, 355 and 266 nm, respectively, fluence = 2.5 Jcm^{-2}, 10^{-7} mbar N_2). The errors bars in these figures are from the respective Boltzmann plots for each distance.

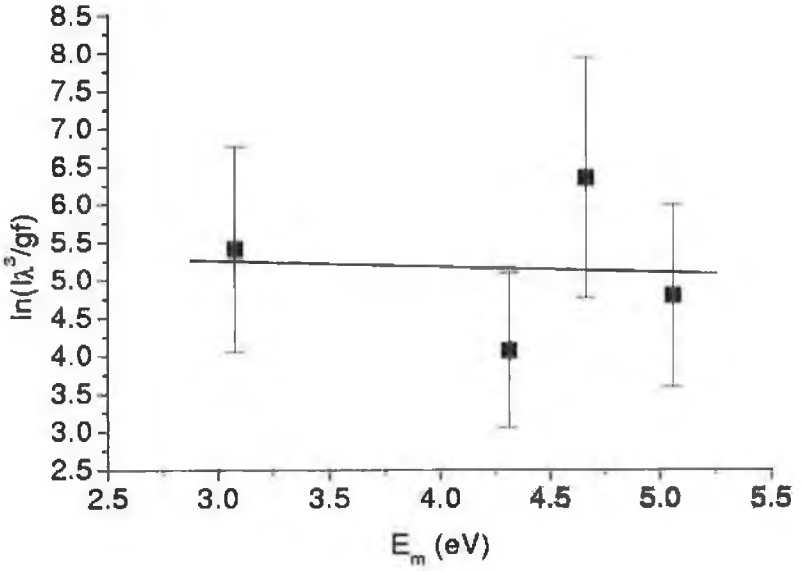

Figure 4.25: Ga Boltzmann Plot (10^{-7} mbar N_2) at 2 mm from target, $\lambda_{Laser} = 1064$ nm.

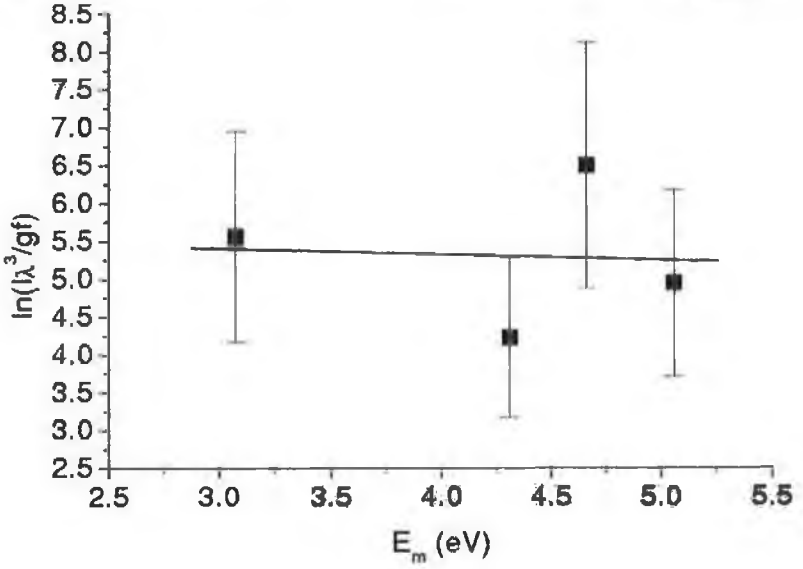

Figure 4.26: Ga Boltzmann Plot (10^{-7} mbar N_2) at 4 mm from target, $\lambda_{Laser} = 1064$ nm.

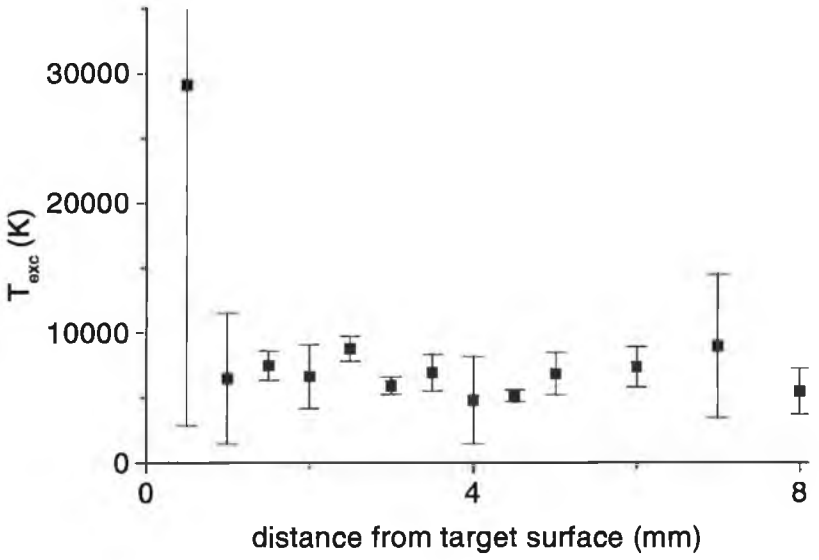

Figure 4.27: Ga: T_{exc} (in 10^{-7} mbar N_2) vs distance from target surface, $\lambda_{Laser} = 1064$ nm.

One observes that the temperature drops off from an initially higher value to a constant value after a few mm. This is more pronounced at 1064 nm where the temperature drops from a maximum value of $\sim$ 30000 K close to target to $\sim$ 7000 K for greater distances. In the 532 nm laser radiation case the temperature is $\sim$ 10000 K close to target, dropping to $\sim$ 5000 K farther away, while at 355 and 266 nm the temperatures are close to $\sim$ 4000 K. This behaviour has been observed by Fuso et al [74] in ablation of Ti with XeCl 308 nm laser radiation at 2 Jcm^{-2} where the time-resolved temperature dropped from a maximum value of $\sim$ 30000 K to $\sim$ 7000 K.

It has also been reported by Hermann et al [75] in ablation of Ti with XeCl 308 nm laser radiation at 12.5 Jcm^{-2}. Here the time-resolved temperature dropped from an maximum value of $\sim$ 3 eV ($\sim$ 35000 K) to less than 1 eV ($\sim$ 11600 K). Toftmann et al [76] report time-resolved temperature estimations using ion probe measurements of Ag ablation plumes created with 355 nm Nd:YAG laser

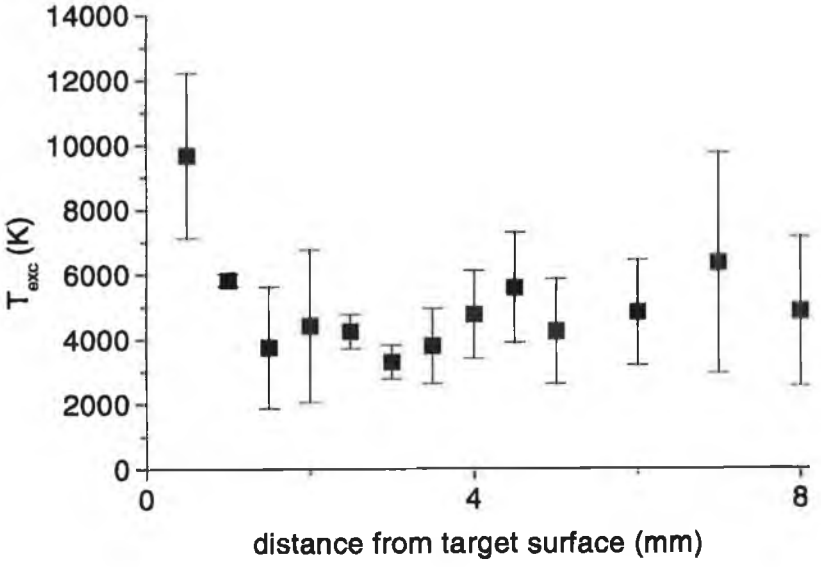

Figure 4.28: Ga: T_{exc} (in 10^{-7} mbar N_2) vs distance from target surface, $\lambda_{Laser} = 532$ nm.

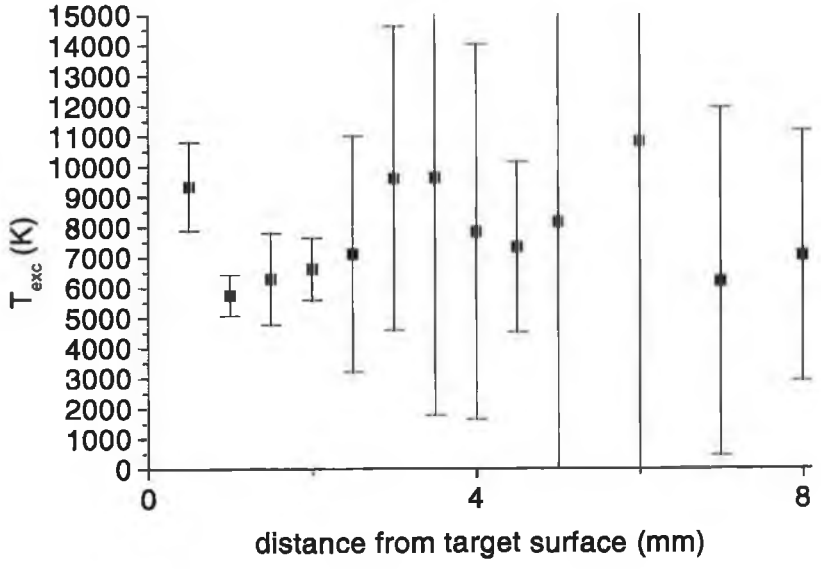

Figure 4.29: Ga: T_{exc} (in 10^{-7} mbar N_2) vs distance from target surface, $\lambda_{Laser} = 355$ nm.

radiation at 0.8 and 1.3 Jcm^{-2}. Temperatures typically dropped from $\sim$ 1 eV to less than 0.5 eV.

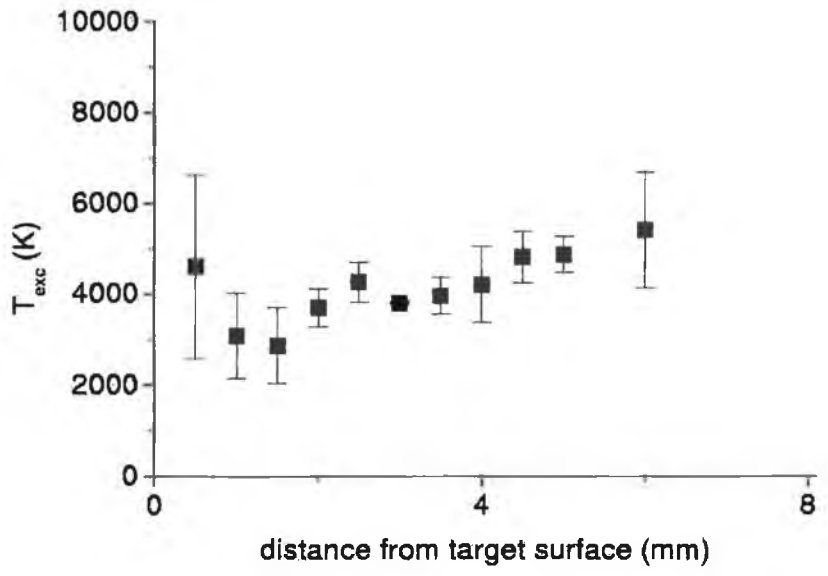

Figure 4.30: Ga: T_{exc} (in 10^{-7} mbar N_2) vs distance from target surface, λ_{Laser} = 266 nm.

The temperatures estimated here support the discussion of section 4.1.1, where we suggested that the ablation plumes created by laser radiation of higher wavelengths would have higher excitation temperatures due to their higher absorption of the laser radiation.

We have also estimated the excitation temperatures in the case of gallium plumes expanding into 5 mbar of N_2. These are shown in figures 4.31, 4.32, 4.33 and 4.34 for plumes ablated with 1064, 532, 355 and 266 nm laser radiation at a fluence of 2.5 Jcm^{-2}.

One observes that the temperatures initially decreased from a high value, as in the vacuum case. However, further from the target surface,the temperature increased to a 2^{nd} maximum value (lower than the initial maximum value) before decreasing more slowly. This supports the discussion of section 4.1.1 where we

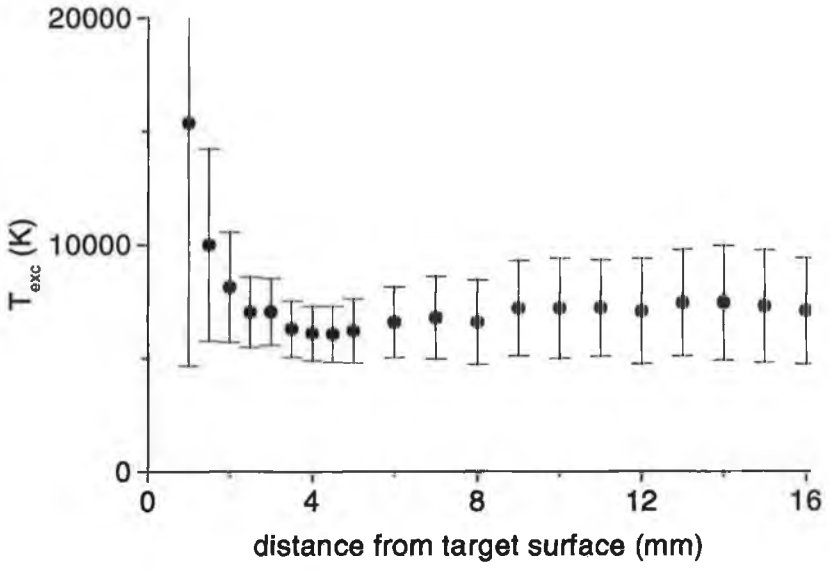

Figure 4.31: Ga: T_{exc} (in 5 mbar N_2) vs distance from target surface, $\lambda_{Laser} = 1064$ nm.

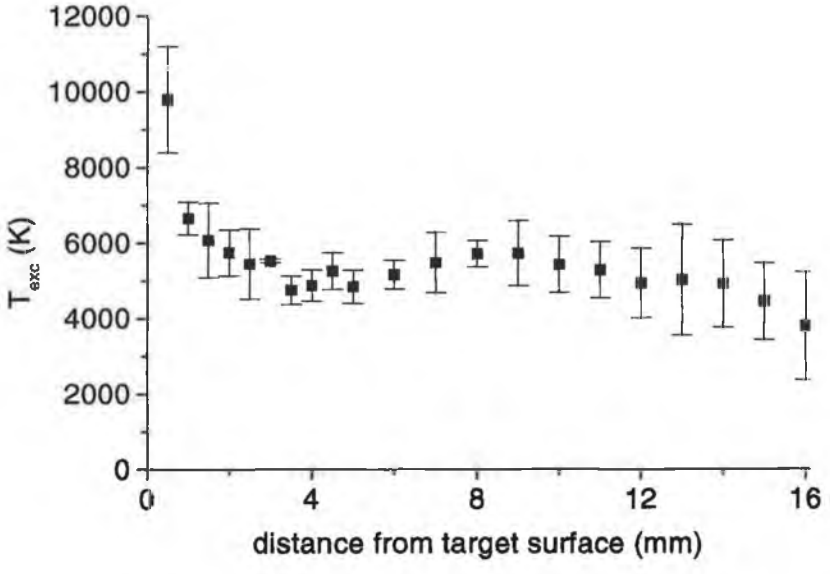

Figure 4.32: Ga: T_{exc} (in 5 mbar N_2) vs distance from target surface, $\lambda_{Laser} = 532$ nm.

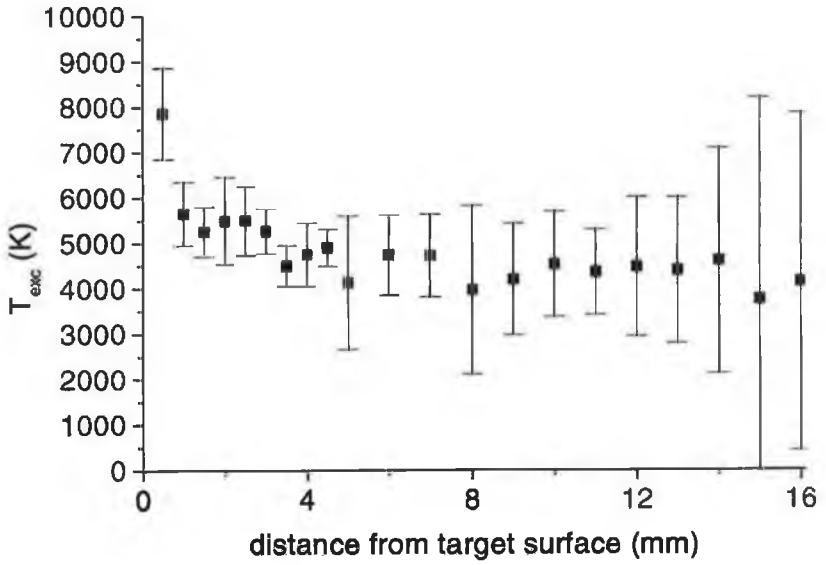

Figure 4.33: Ga: T_{exc} (in 5 mbar N_2) vs distance from target surface, $\lambda_{Laser} = 355$ nm.

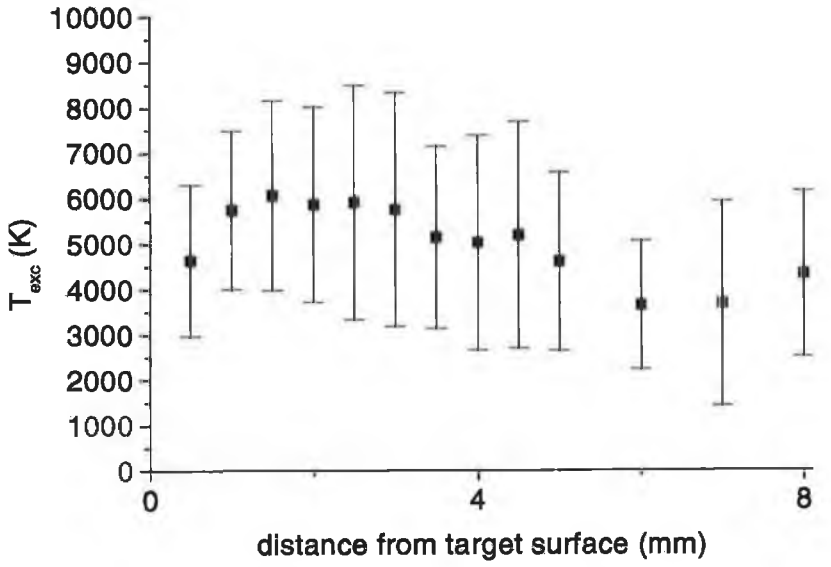

Figure 4.34: Ga: T_{exc} (in 5 mbar N_2) vs distance from target surface, $\lambda_{Laser} = 266$ nm.

suggested that a compression front develops and results in the conversion of the plume particles kinetic energy into thermal energy.

4.1.4 Emission spectra of Gallium Nitride plume

Since many authors have successfully grown GaN films from a GaN target, see section 2.3.1, spectra were also recorded for ablation plumes created on a target of pressed GaN powder. The emission spectra for GaN plumes at 2 mm above target surface are shown for (a) 1064, (b) 532, (c) 355 and (d) 266 nm laser radiation (2.5 Jcm^{-2}, 10^{-7} mbar N_2) in figure 4.35.

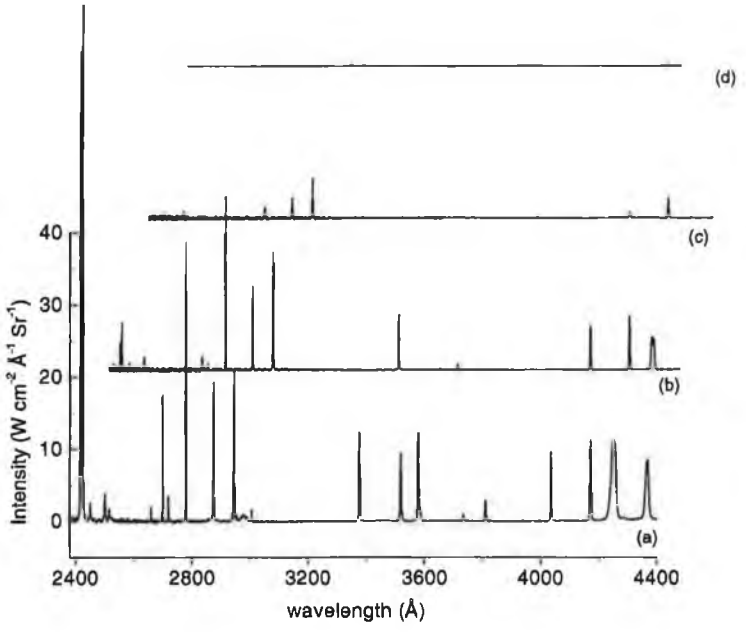

Figure 4.35: GaN ablated with (a) $\lambda_{Laser} = 1064$, (b) $\lambda_{Laser} = 532$, (c) $\lambda_{Laser} = 355$ and (d) $\lambda_{Laser} = 266$ nm at 2.5 Jcm^{-2} in 10^{-7} mbar N_2 at 2 mm from target surface

On comparison with figures 4.2, 4.3, 4.4 and 4.5, which are the corresponding spectra for a liquid gallium target, one sees little difference in the spectra. Again there is an absence of atomic or ionic nitrogen emission, despite the fact that nitrogen is present in the GaN target.

One may, again, observe that the emission intensity of the plumes scale downwards with decreasing laser wavelength, though this is less significant for neutral Ga. This is illustrated in figure 4.36 which plots the integrated intensity of the Ga, Ga^{+} and Ga^{2+} marker lines vs laser wavelength. This figure shows the same behaviour as figure 4.6 and the reader is referred to the discussion in section 4.1.1.

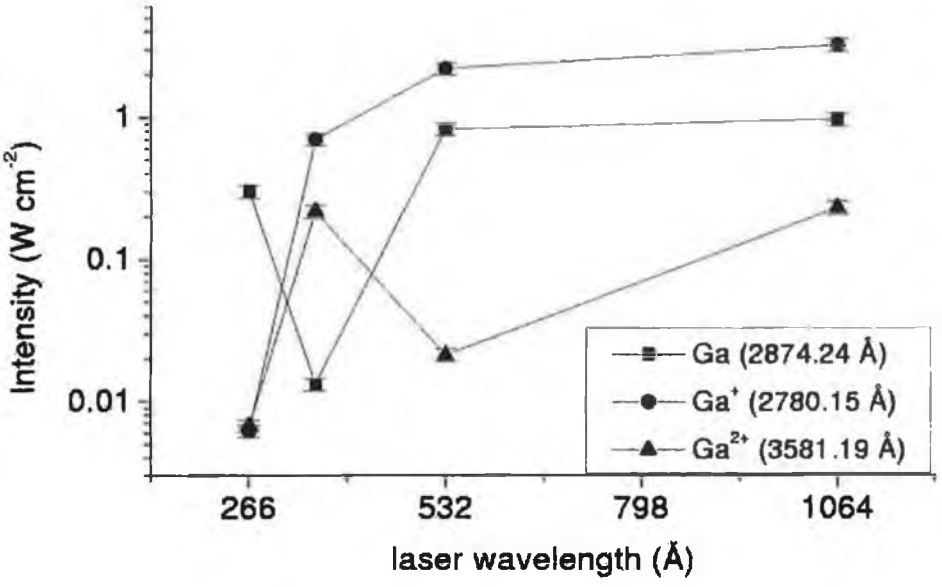

Figure 4.36: GaN emission in 10^{-7} mbar N_2: ion stage vs λ_{Laser}.

The emission spectra from a GaN plume at 5 mbar N_2 background gas pressure is shown at 5 mm above target surface in figure 4.37 for (a) 1064, (b) 532, (c) 355 and (d) 266 nm laser radiation (2.5 Jcm^{-2}).

It may be observed, in all cases, that the emission is substantially enhanced in 5 mbar N_2 when compared with the 10^{-7} mbar case of figure 4.35 due to collisions between the plume particles and those of the gas. This is illustrated, for 1064 nm laser radiation, in figures 4.38, 4.39 and 4.40 where the integrated intensity is plotted vs distance above target surface for each of the three marker lines respectively, at each ambient gas pressure.

Figures 4.41, 4.42 and 4.43 show this for 532 nm laser radiation, 4.44, 4.45

and 4.46 for 355 nm laser radiation and figures 4.47 and 4.48 show the 266 nm laser radiation case.

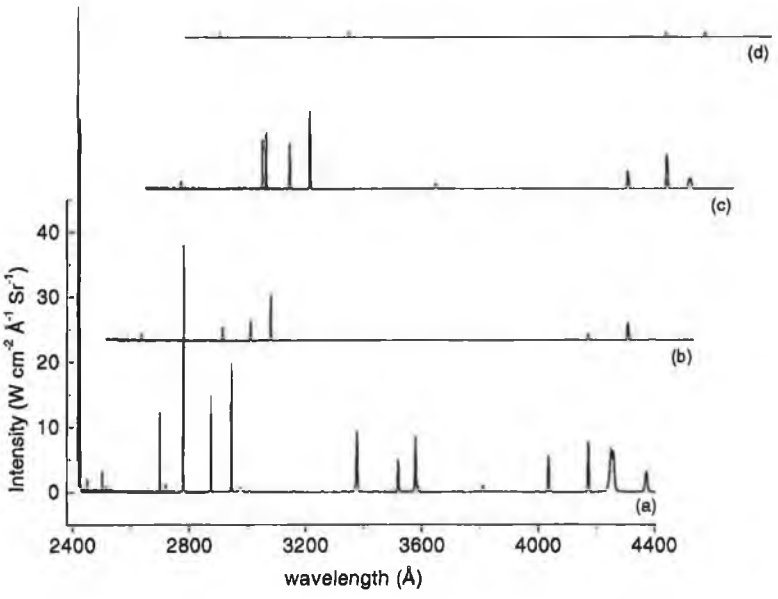

Figure 4.37: GaN ablated with (a) $\lambda_{Laser} = 1064$ nm, (b) $\lambda_{Laser} = 532$ nm, (c) $\lambda_{Laser} = 355$ nm and (d) $\lambda_{Laser} = 266$ nm at 2.5 Jcm^{-2} in 5 mbar N_2 at 5 mm from target surface

One can see that for the 5 mbar case at all laser wavelengths that the emission increased sharply from the surface up to a maximum distance and then decreased more slowly. This pattern of behaviour is identical to that from a liquid gallium metal target and the reader is referred to the discussion of section 4.1.1 where we suggested that collisions between plume and gas leads to enhanced excitation and emission from the plume. This can be related to the fact that various authors successfully grew films in a range of conditions (see section 2.3.1) and points to an underlying common growth mechanism.

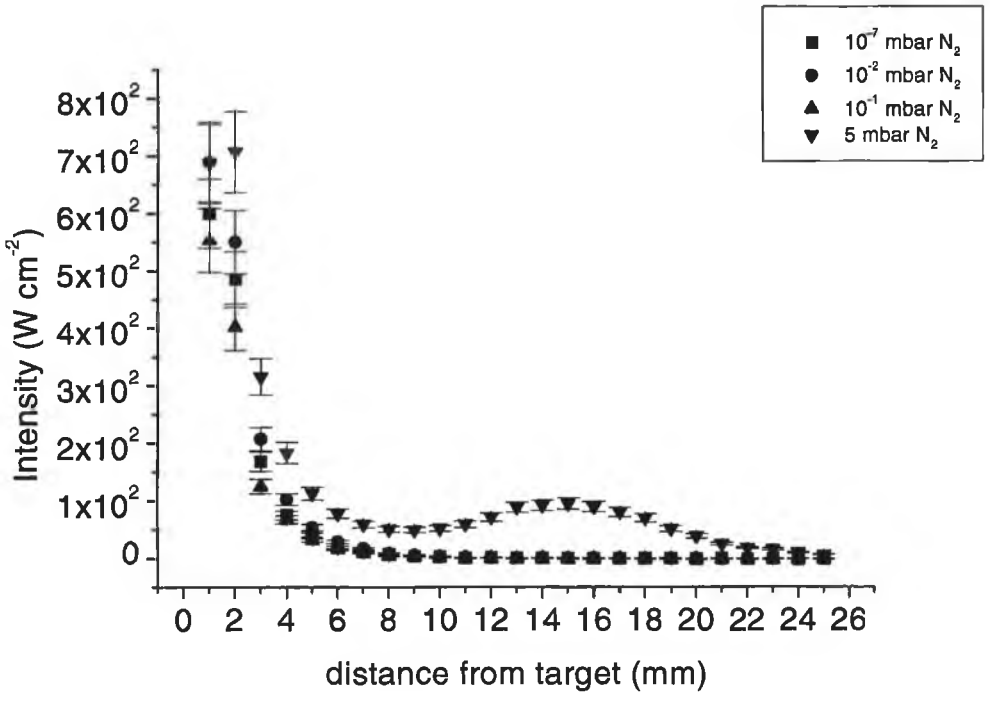

Figure 4.38: GaN: Ga emission intensity vs distance from target surface for a range of pressures of N_2, $\lambda_{Laser} = 1064$ nm.

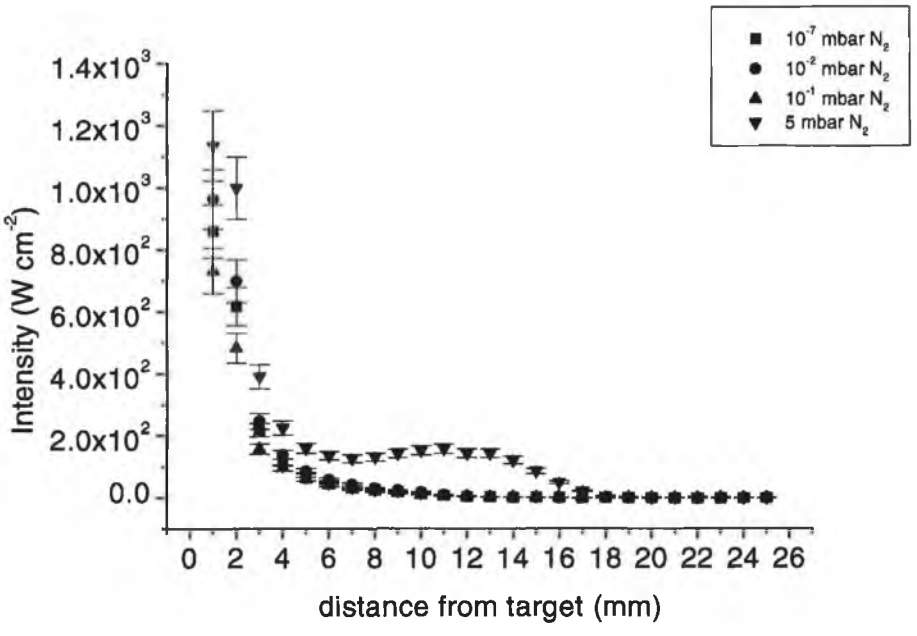

Figure 4.39: GaN: Ga^+ emission intensity vs distance from target surface for a range of pressures of N_2, $\lambda_{Laser} = 1064$ nm.

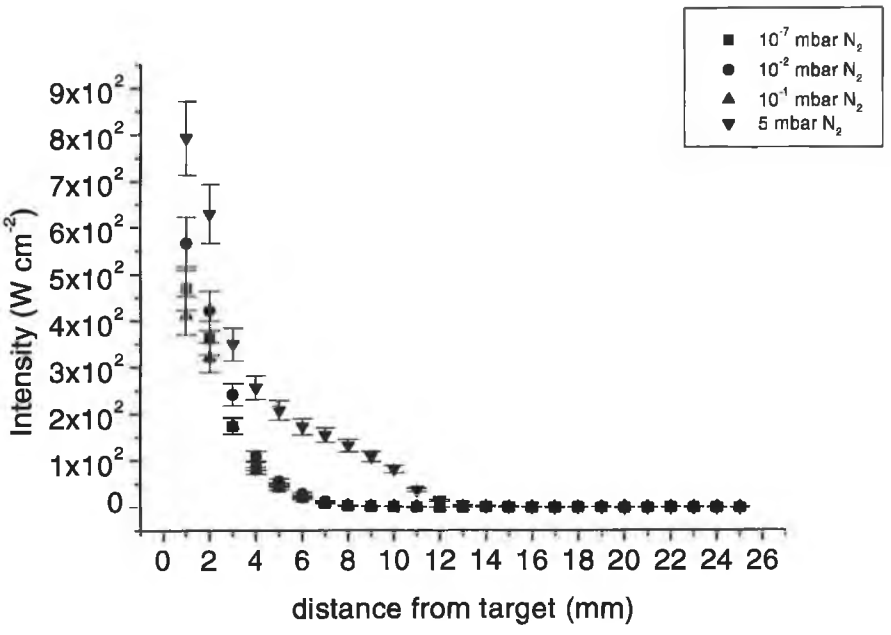

Figure 4.40: GaN: Ga^{2+} emission intensity vs distance from target surface for a range of pressures of N_2, $\lambda_{Laser} = 1064$ nm.

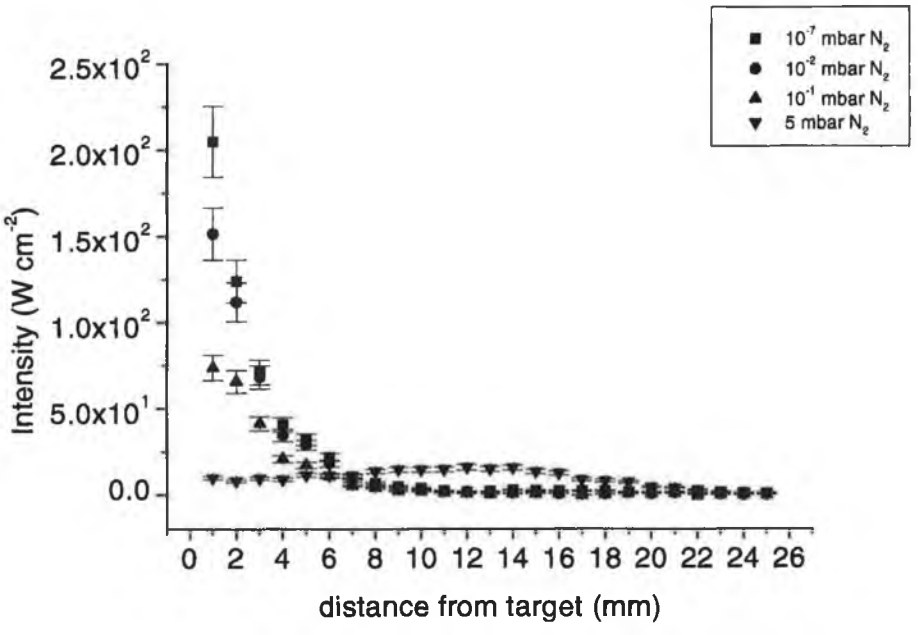

Figure 4.41: GaN: Ga emission intensity vs distance from target surface for a range of pressures of N_2, $\lambda_{Laser} = 532$ nm.

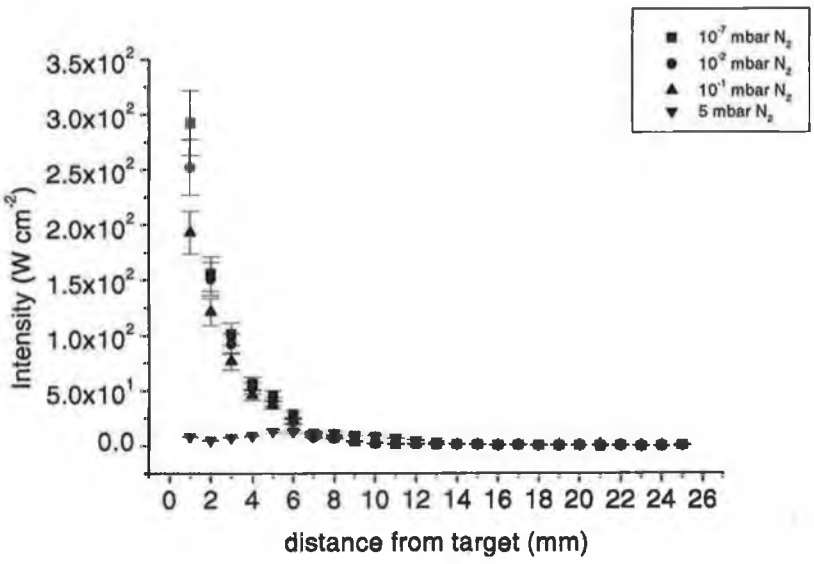

Figure 4.42: GaN: Ga^{+} emission intensity vs distance from target surface for a range of pressures of N_2, $\lambda_{Laser} = 532$ nm.

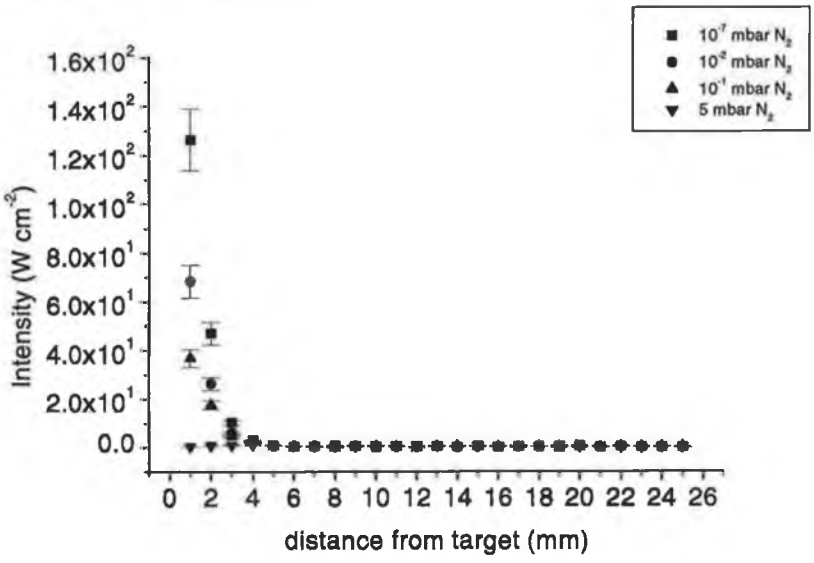

Figure 4.43: GaN: Ga^{2+} emission intensity vs distance from target surface for a range of pressures of N_2, $\lambda_{Laser} = 532$ nm.

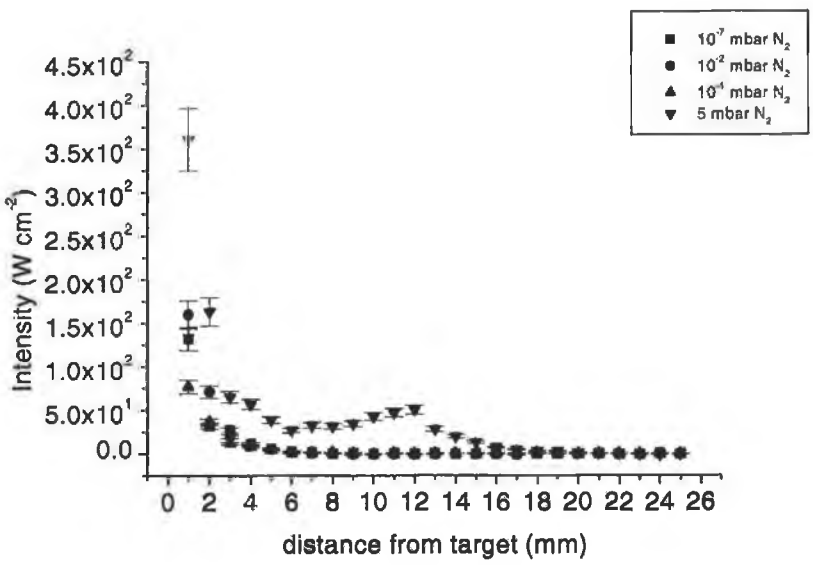

Figure 4.44: GaN: Ga emission intensity vs distance from target surface for a range of pressures of N_2, $\lambda_{Laser} = 355$ nm.

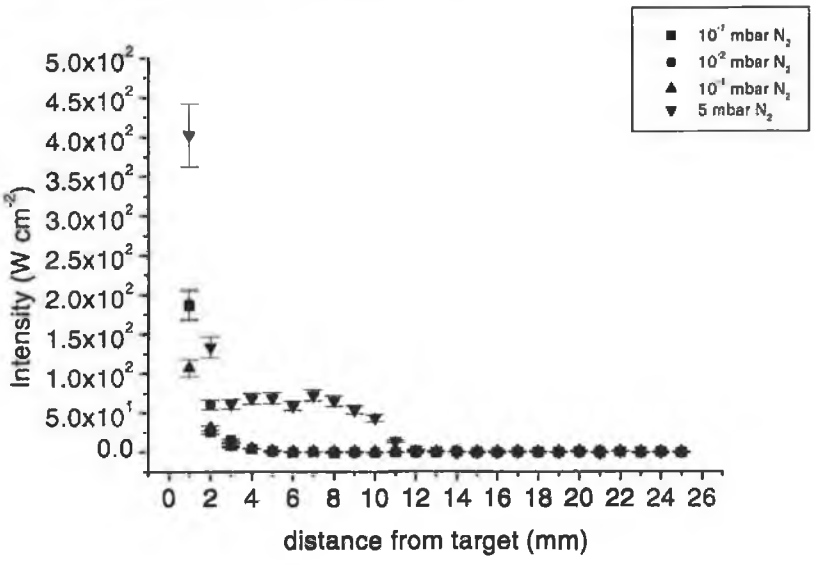

Figure 4.45: GaN: Ga^+ emission intensity vs distance from target surface for a range of pressures of N_2, $\lambda_{Laser} = 355$ nm.

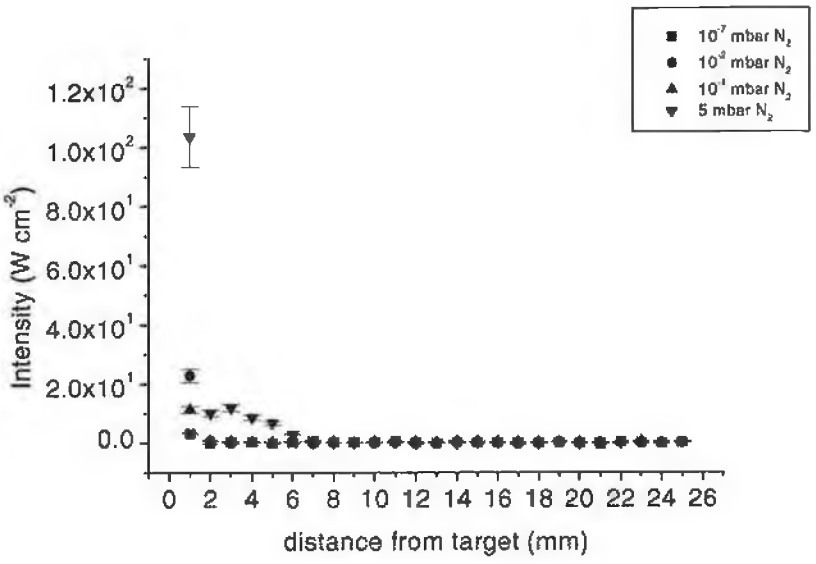

Figure 4.46: GaN: Ga^{2+} emission intensity vs distance from target surface for a range of pressures of N_2, $\lambda_{Laser} = 355$ nm.

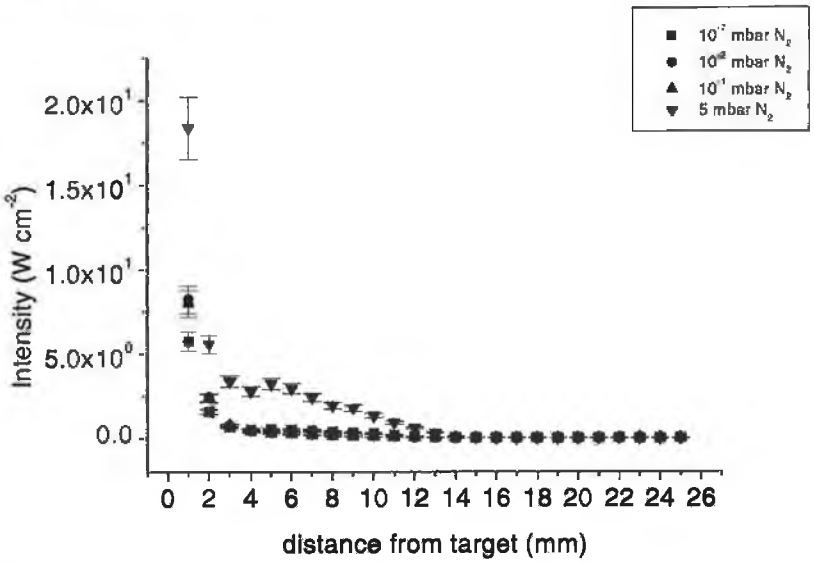

Figure 4.47: GaN: Ga emission intensity vs distance from target surface for a range of pressures of N_2, $\lambda_{Laser} = 266$ nm.

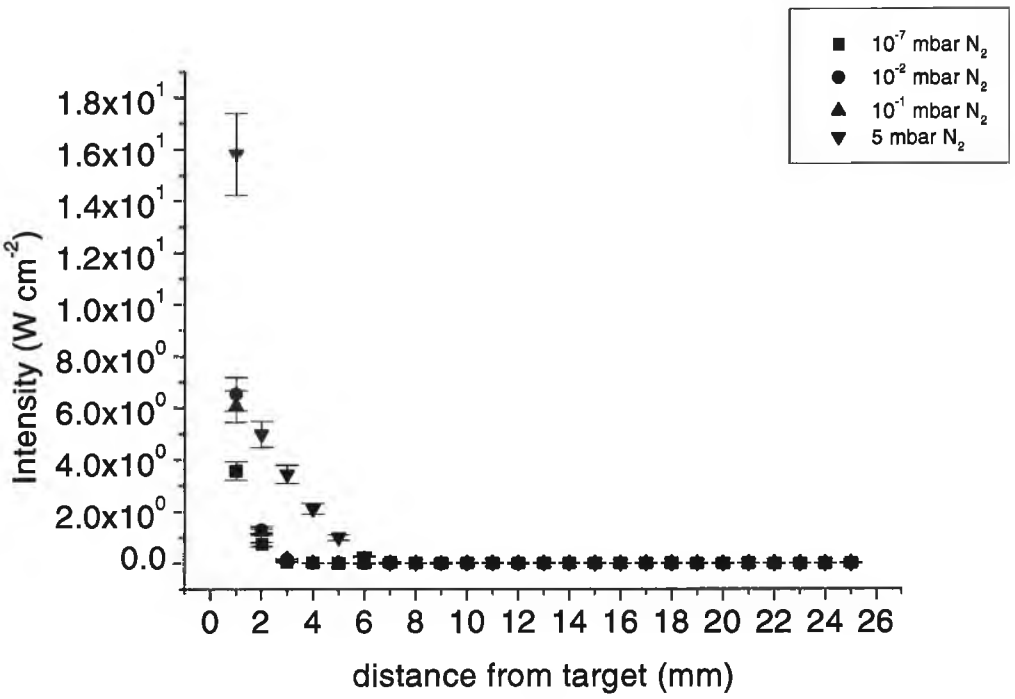

Figure 4.48: GaN: Ga^+ emission intensity vs distance from target surface for a range of pressures of N_2, $\lambda_{Laser} = 266$ nm.

4.1.5 Ga level populations in GaN plume

The populations in the $4s^2 5s$ (≈ 3.1 eV), $4s^2 4d$ (≈ 4.3 eV), $4s^2 6s$ (≈ 4.7 eV) and $4s^2 5d$ (≈ 5.1 eV) excited levels were estimated from the integrated intensities of the 417.2, 287.4, 272.0 and 250.1 nm lines in a manner similar to the previous case of section 4.1.2.

The results are displayed in figures 4.49, 4.50, 4.51 and 4.52 for a GaN plume, generated by 1064, 532, 355 and 266 nm laser radiation, respectively. These show similar behaviour to the gallium metal case. Note: some data points overlap.

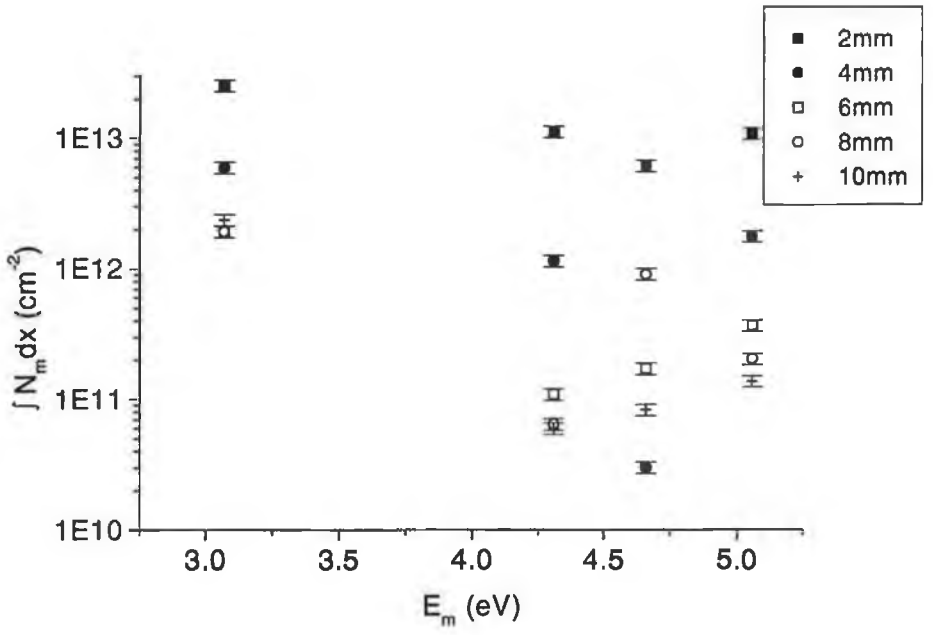

Figure 4.49: Level populations of Ga (GaN plume in 10^{-7} mbar N_2) vs excited state energy at various distances from target surface, $\lambda_{Laser} = 1064$ nm.

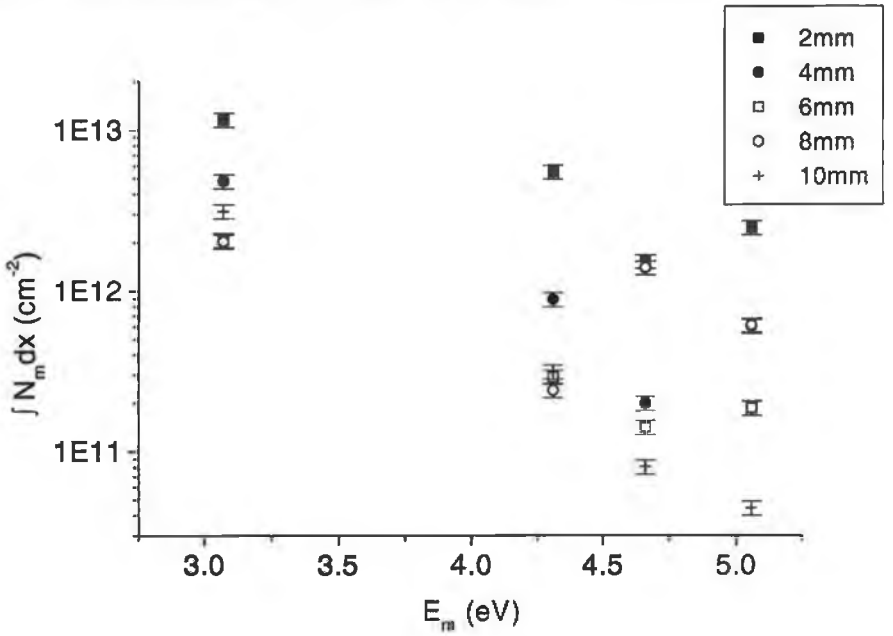

Figure 4.50: Level populations of Ga (GaN plume in 10^{-7} mbar N_2) vs excited state energy at various distances from target surface, $\lambda_{Laser} = 532$ nm.

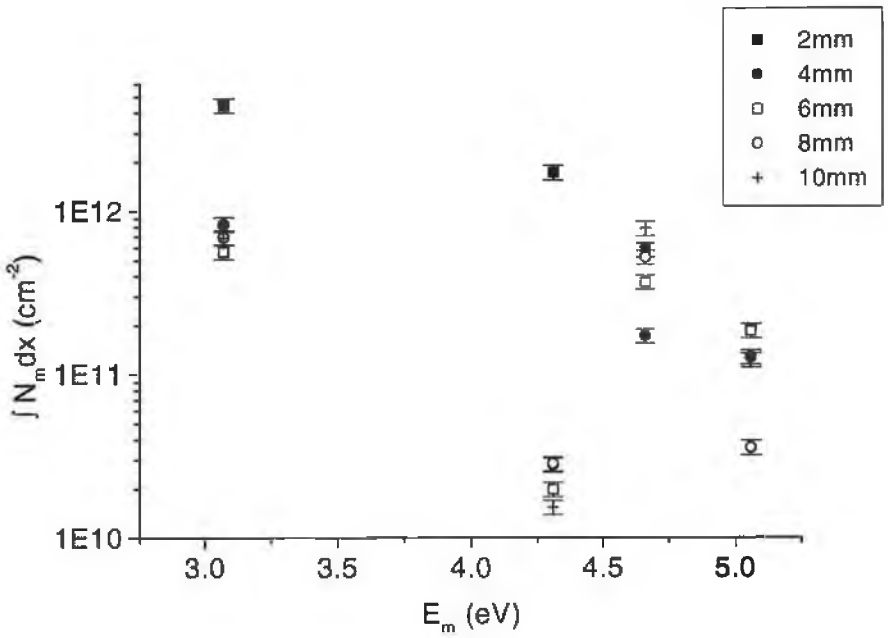

Figure 4.51: Level populations of Ga (GaN plume in 10^{-7} mbar N_2) vs excited state energy at various distances from target surface, $\lambda_{Laser} = 355$ nm.

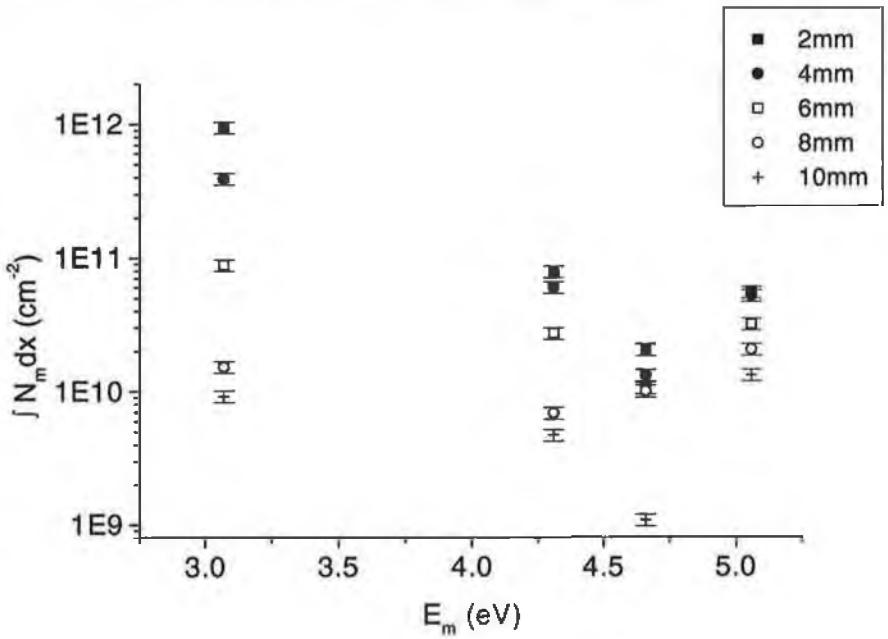

Figure 4.52: Level populations of Ga (GaN plume in 10^{-7} mbar N_2) vs excited state energy at various distances from target surface, $\lambda_{Laser} = 266$ nm.

4.1.6 Excitation temperature in GaN plume

In figures 4.53, 4.54, 4.55 and 4.56 the excitation temperatures, which were estimated from equation 3.1 in a similar manner to section 4.1.3, are displayed vs distance above target surface for a GaN plume created by $\lambda_{Laser} = 1064$, 532, 355 and 266 nm laser radiation, respectively, at a fluence of = 2.5 Jcm^{-2} in 10^{-7} mbar N_2.

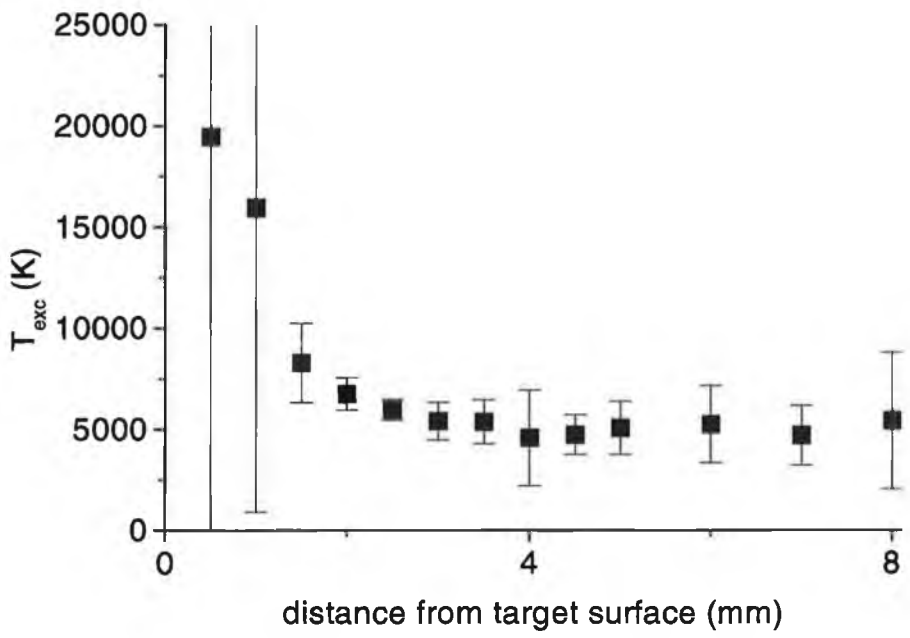

Figure 4.53: GaN: T_{exc} (in 10^{-7} mbar N_2) vs distance from target surface, $\lambda_{Laser} = 1064$ nm.

The excitation temperatures in vacuum, which are similar values to those from gallium metal plumes, drop off with distance from target in a similar fashion to that of gallium metal plumes as discussed in 4.1.3 and also with respect to the laser wavelength and the reader is again referred to section 4.1.1, where we suggested that the higher excitation temperatures at higher laser wavelengths is due to the higher absorption of the laser radiation.

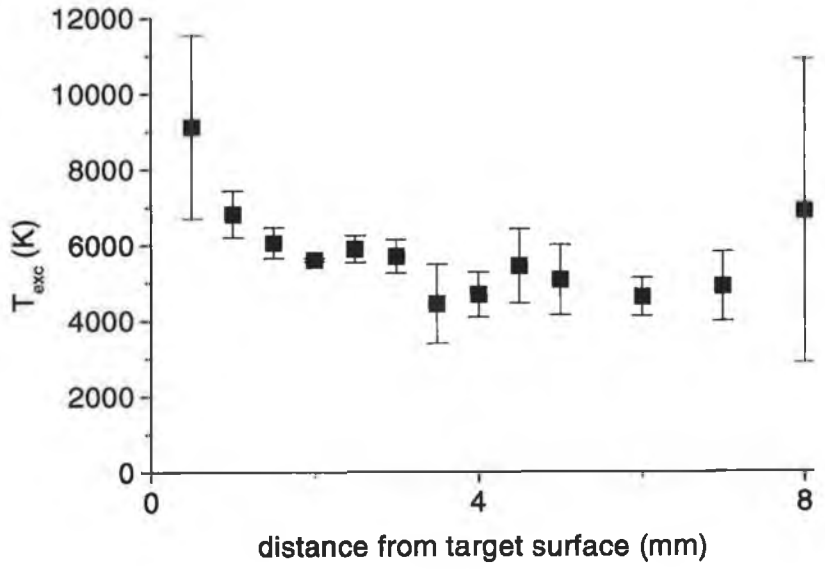

Figure 4.54: GaN: T_{exc} (in 10^{-7} mbar N_2) vs distance from target surface, $\lambda_{Laser} = 532$ nm.

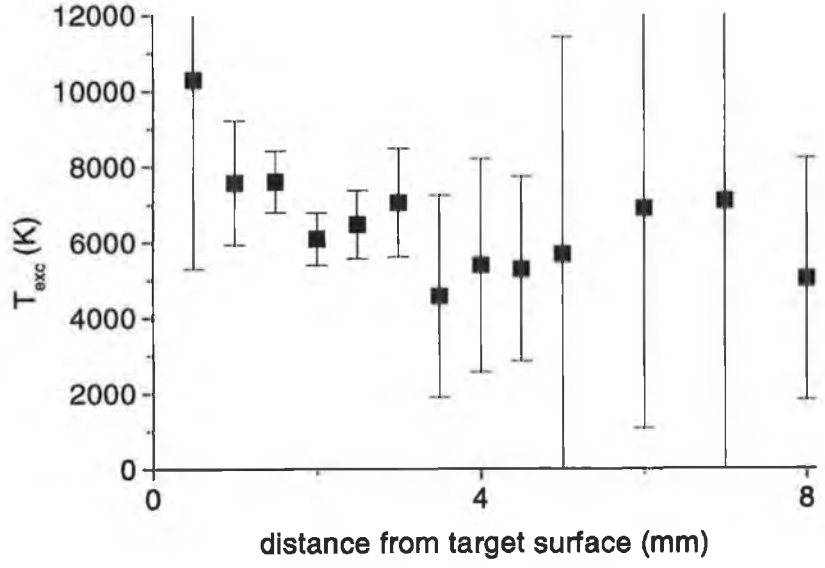

Figure 4.55: GaN: T_{exc} (in 10^{-7} mbar N_2) vs distance from target surface, $\lambda_{Laser} = 355$ nm.

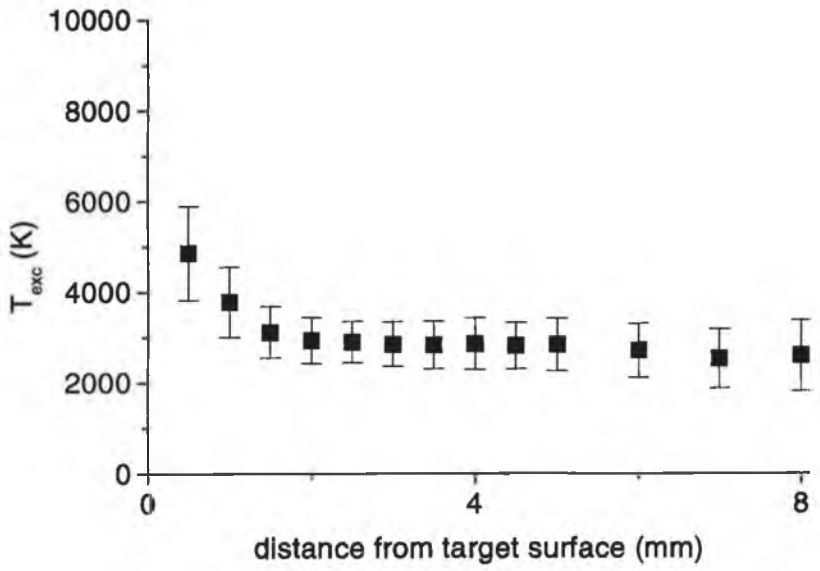

Figure 4.56: GaN: T_{exc} (in 10^{-7} mbar N_2) vs distance from target surface, $\lambda_{Laser} = 266$ nm.

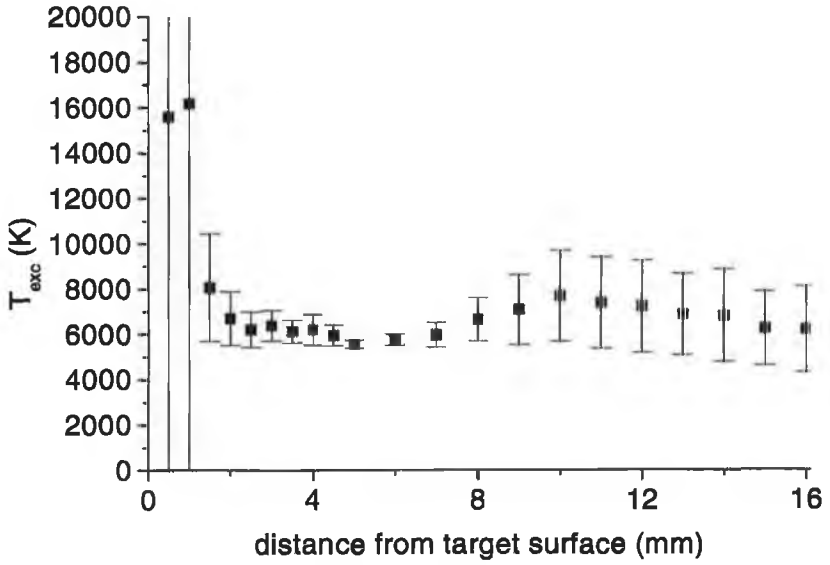

Figure 4.57: GaN: T_{exc} (in 5 mbar N_2) vs distance from target surface, $\lambda_{Laser} = 1064$ nm.

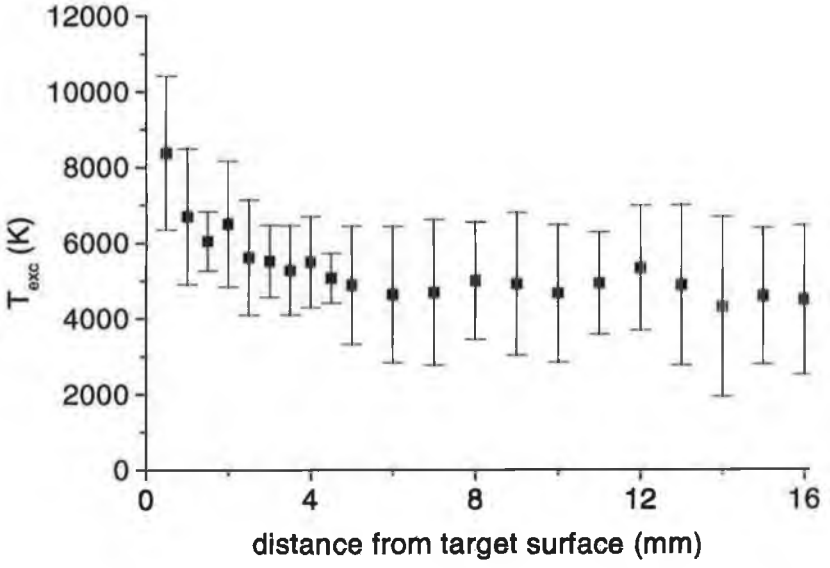

Figure 4.58: GaN: T_{exc} (in 5 mbar N_2) vs distance from target surface, $\lambda_{Laser} = 532$ nm.

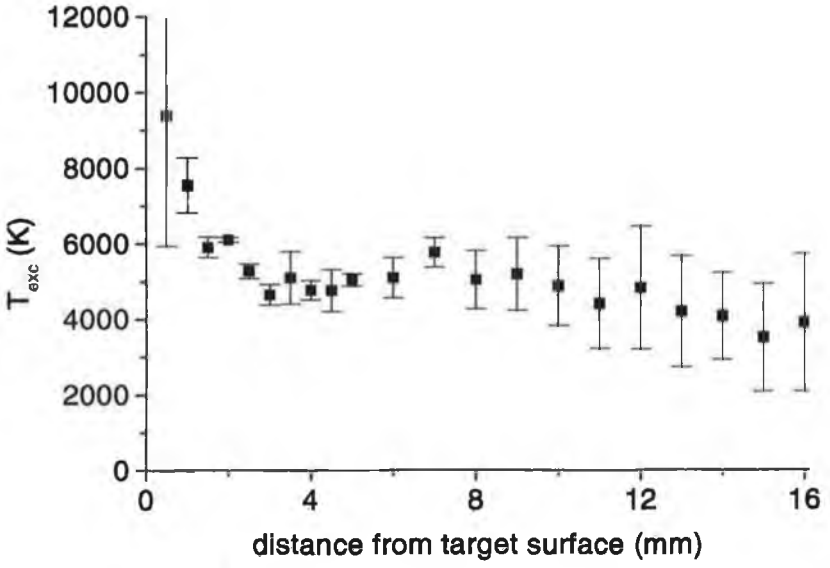

Figure 4.59: GaN: T_{exc} (in 5 mbar N_2) vs distance from target surface, $\lambda_{Laser} = 355$ nm.

For GaN plumes expanding into 5 mbar of N_2, we have also estimated the excitation temperatures. These are shown in figures 4.57, 4.58, 4.59 and 4.60 for plumes ablated with 1064, 532, 355 and 266 nm laser radiation at a fluence of 2.5 Jcm^{-2}.

Similar to the gallium metal target case, the temperatures initially decreased from a high value before increasing to a 2^{nd} maximum value (lower than the initial maximum value) before decreasing more slowly. Again, this supports the discussion of section 4.1.1 where we suggested that the interaction of the plume and ambient gas results in the conversion of the plume particles kinetic energy into thermal energy.

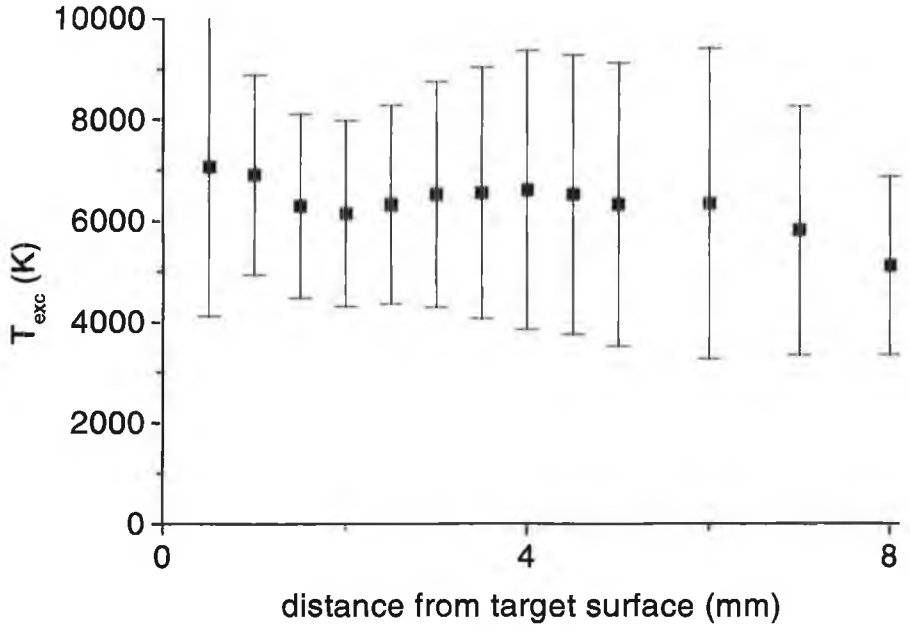

Figure 4.60: GaN: T_{exc} (in 5 mbar N_2) vs distance from target surface, $\lambda_{Laser} = 266$ nm.

4.1.7 Spectral behaviour of nitrogen

Atomic and ionic nitrogen

In the spectra recorded at N_2 pressures up to 10^{-1} mbar, all the lines can be accounted for as transitions in Ga, Ga^+ or Ga^{2+} (see table 4.1) however, atomic databases indicate a wealth of lines in the range 2000-5000 Å for the NI-NVII ionisation stages [73].

However, in the course of the present work, we could not detect any spectral features that could be attributed to known emission lines in atomic nitrogen or its ions. Indeed, as can be seen from, for example, figures 4.2, 4.3, 4.4, 4.5 and 4.35, the Ga and GaN targets always produced similar spectra (free of atomic or ionic nitrogen emission).

We now discuss possible reasons for this absence of nitrogen emission. From [73] it can be seen that the radiation transitions probabilities are very small for low Z elements, and decay is preferentially via Auger emission if energetically possible. Also, Cowan et al [77] have seen that N^- can be produced from $e + e + N^+$, with large cross-sections, suggesting that collisional de-excitation may be very efficient process here.

Another point is that the majority of the excited states involved in transitions that would produce lines in the region of the spectrum recorded have very high excitation potentials. The one exception is a low-lying level with a transition into the ground state, however this is, in fact, a forbidden transition.

Most likely the combination of small transition probabilities with high excitation potentials is the reason we cannot record any atomic or ionic nitrogen emission in our conditions.

Molecular nitrogen

Some extra lines appeared only at a N_2 pressure of 5 of mbar. To aid in the identification of these lines and to determine whether the extra features are source features or ambient gas features, spectra were recorded in 5 mbar Ar. If similar features were observed in high pressure Ar then this would imply that the

features originated in the target.

These lines are attributed [78] to molecular N_2 emission, namely the N_2 2^{nd} positive system and the N_2^+ 1^{st} negative system, and are displayed in figures 4.61, 4.62 and 4.63.

N_2^+ 1^{st} negative system emission has been observed in ablation of graphite in nitrogen using a KrF 248 nm laser at $\sim$ 6 Jcm^{-2} fluence in 0.5 Torr N_2 by Vivien et al [79]. Both systems were observed by Dutouquet et al [80] in 1064 nm ablation of a boron nitride target in N_2. These authors also observe diatomic spectra of CN and BN, respectively, although the absence of lines which could be the GaN molecule does not rule out the presence of GaN molecules.

Comparing figure 4.1 and figure 4.61 we can see that the appearance of these lines spatially above target corresponds to the region where the velocity of the plume edge begins to slow appreciably, that is to say in the compressed region, where there is heating and excitation in the interaction of the plume with the gas.

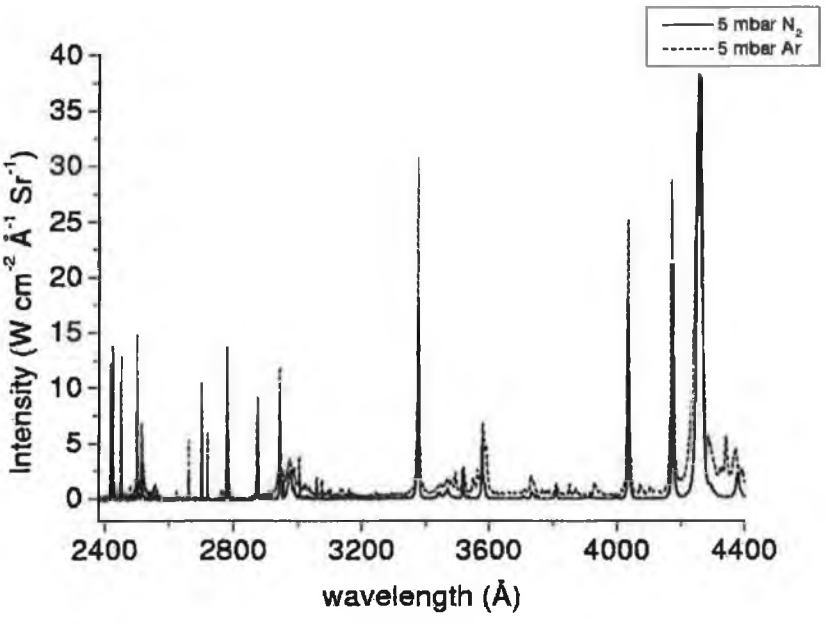

Figure 4.61: Ga spectra in N_2 vs Ar atmospheres, $\lambda_{Laser} = 1064$ nm, 2.5 Jcm^{-2}.

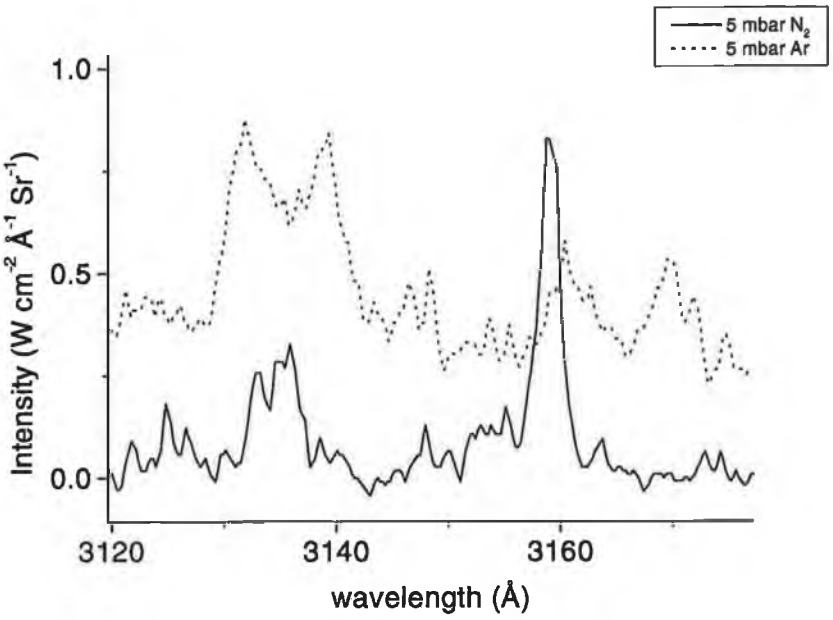

Figure 4.62: 2^{nd} positive system of N_2, $\lambda_{Laser} = 1064$ nm, 2.5 Jcm^{-2}.

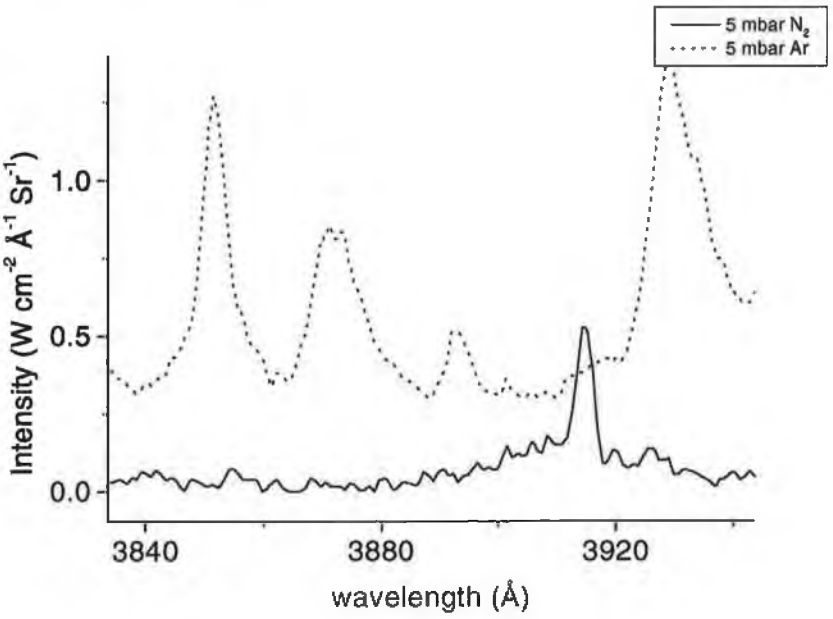

Figure 4.63: 1^{st} negative system of N_2^+, $\lambda_{Laser} = 1064$ nm, 2.5 Jcm^{-2}.

4.2 Ion probe measurements and analysis

Probe measurements were obtained for a GaN target in 10^{-7} mbar N_2 with 1064 nm laser radiation. The cylindrical probe was biased at -30 V. Its dimensions were 10 mm length and 0.5 mm diameter giving an effective area $A = 0.05$ cm^2. The probe was positioned at a distance of 4 cm from the target surface.

Figure 4.64 displays the collected charge as a function of laser fluence and shows a linear yield of ions with fluence. The results of the previous sections were for a fluence of 2.5 Jcm^{-2}. The peak velocity of the ions was measured

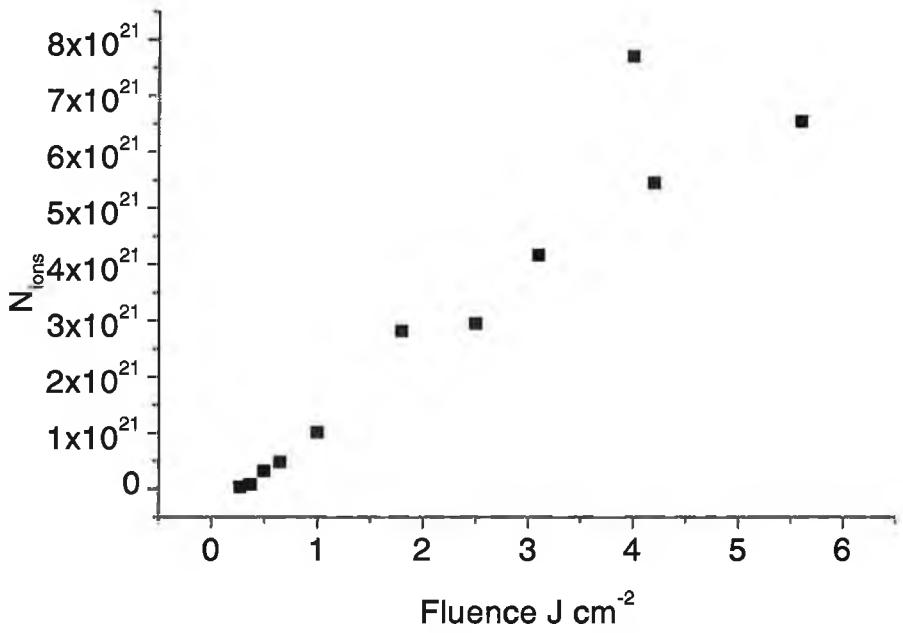

Figure 4.64: GaN (in 10^{-6} mbar N_2); N_{Ga+} collected by probe as a function of fluence, $\lambda_{Laser} = 1064$ nm.

and is shown in figure 4.65. From equation 3.10, the kinetic energy of the peak of the time-of-flight distribution is estimated. This is shown in figure 4.66 as a function of the laser fluence.

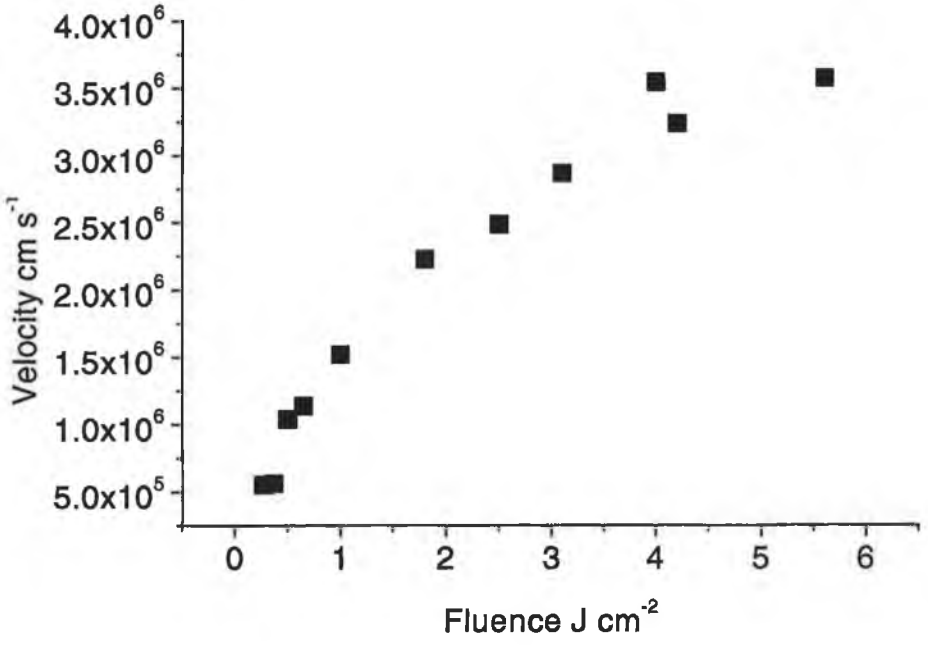

Figure 4.65: GaN (in 10^{-6} mbar N_2); velocity of TOF peak as a function of fluence, $\lambda_{Laser} = 1064$ nm.

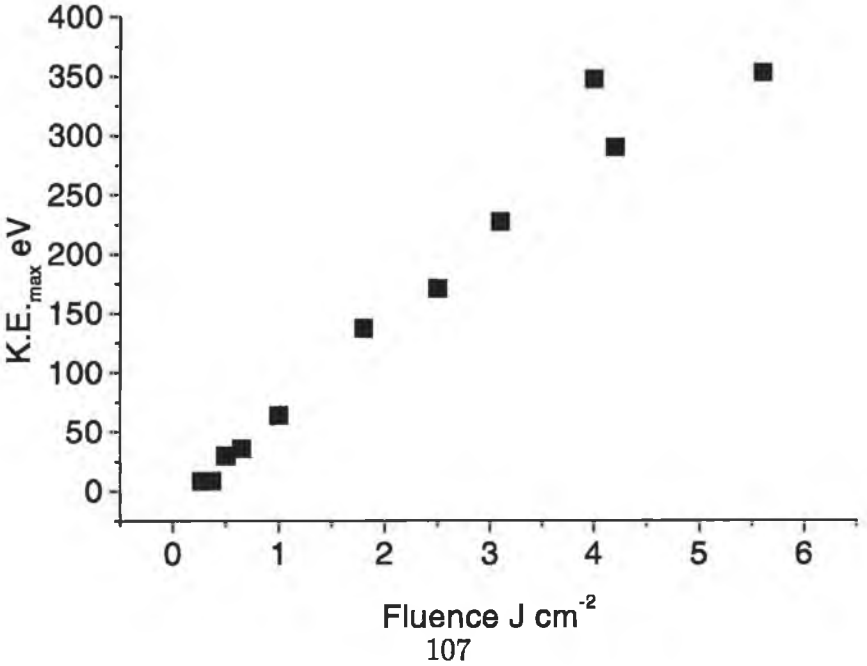

Figure 4.66: GaN (in 10^{-6} mbar N_2); TOF kinetic energies as a function of fluence, $\lambda_{Laser} = 1064$ nm.

The ion probe signal at 4 cm from target for 2.5 Jcm^{-2} ablation of GaN is shown in figure 4.67. Fitting the shifted centre of mass Maxwell Boltzmann distribution of equation 3.9 yields $T_K = 105$ eV and $u_K = -2.9 \times 10^5$ cm^{-1}. This may be compared to the values obtained from optical signals in section 4.3.2. The negative sign may point to the large spotsize would have a gaussian distribution of expansion-driving temperatures, thus the shifted centre of mass Maxwell Boltzmann distribution may not be a good description. In addition we fitted a Maxwell Boltzmann distribution and this yields a temperature of 93 eV.

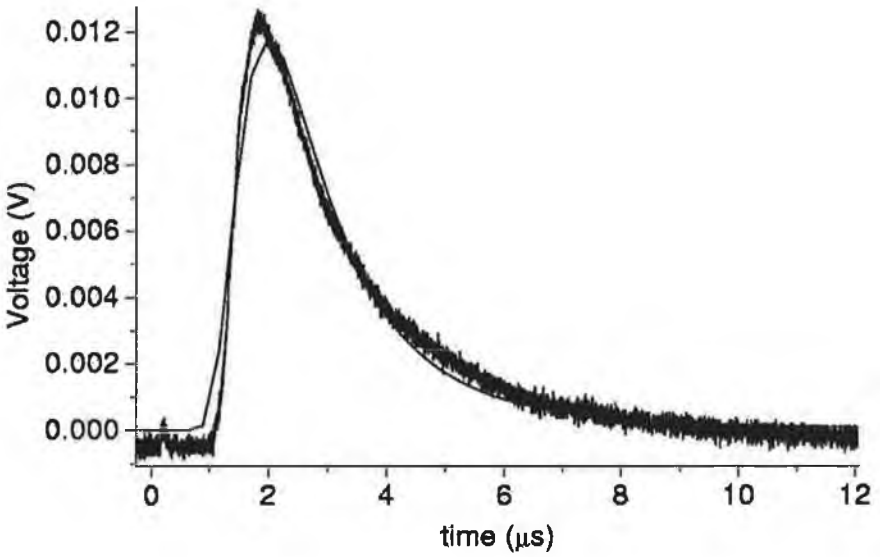

Figure 4.67: Time-of-flight curve of GaN (in 10^{-6} mbar N_2) $\lambda_{Laser} = 1064$ nm.

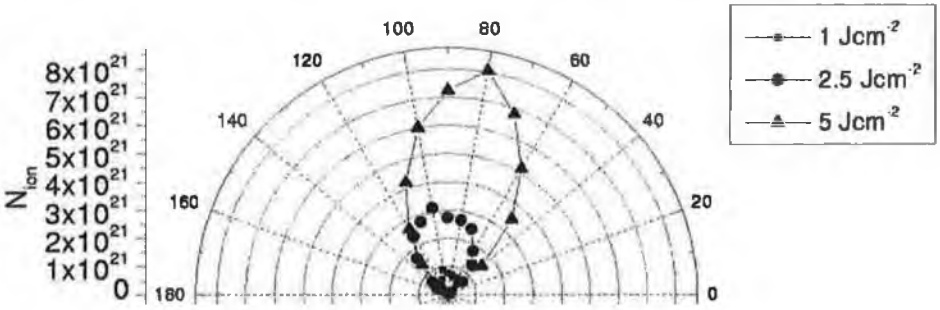

Figure 4.68: GaN (in 10^{-6} mbar N_2): polar plot of distribution of N_{Ga+} collected by the probe, $\lambda_{Laser} = 1064$ nm.

The probe was also positioned at various angles to the target normal (plume expanison axis). This is shown in figure 4.68 as a polar plot and the results of an $Acos^n(\theta)$ fit are listed in table 4.3 for various laser fluences.

Fluence (Jcm^{-2})	n
1.0	2.5
2.5	2.9
5.0	4.9

Table 4.3: $Acos^n(\theta)$ fit to angular distribution of ions.

Kelly [81] gives a similar power dependence for the shifted centre of mass Maxwell Boltzmann velocity distribution where $n \approx (1+M)^{2.1}$ with the degree of forward peaking n related to M, the Mach number. From this we get values of $M = 0.55$, $M = 0.66$ and $M = 1.15$ at 1.0, 2.5 and 5.0 Jcm^{-2}, respectively, suggesting that the plume expansion is subsonic at lower fluences.

4.3 Digital frame photography

A series of images were recorded with the digital framing photography technique described in section 3.3, at various time delays with respect to the laser pulse, for ablation plumes of gallium only. This is justified because in the previous sections of this chapter we have seen that there are little differences between the ablation plumes of Ga and GaN targets.

False colour images of gallium plumes expanding into vacuum (10^{-5} mbar) and various N_2 gas pressures (10^{-2}, 10^{-1}, 1 and 5 mbar N_2) are shown in figures 4.69, 4.70, 4.71, 4.72 and 4.73. The liquid target was ablated with 1064 nm radiation at a fluence of 2.5 Jcm^{-2}. Images are displayed for time delays ranging from 100 to 1000 ns, at intervals of 100 ns, in each case and with an exposure duration of 2.7 ns. (Note: the intensity scales are not scaled with respect to intensifier gain setting in these images but subsequent processed data are.)

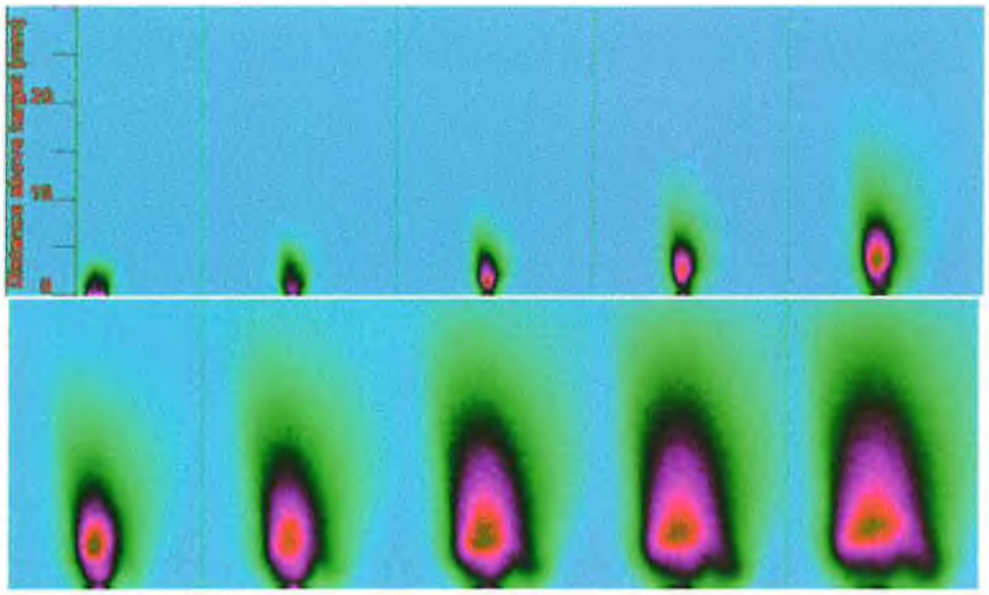

Figure 4.69: ICCD images of Ga plume expansion from 100 ns (top left) to 1000 ns (bottom right) after the laser pulse in 10^{-5} mbar N_2, $\lambda_{Laser} = 1064$ nm.

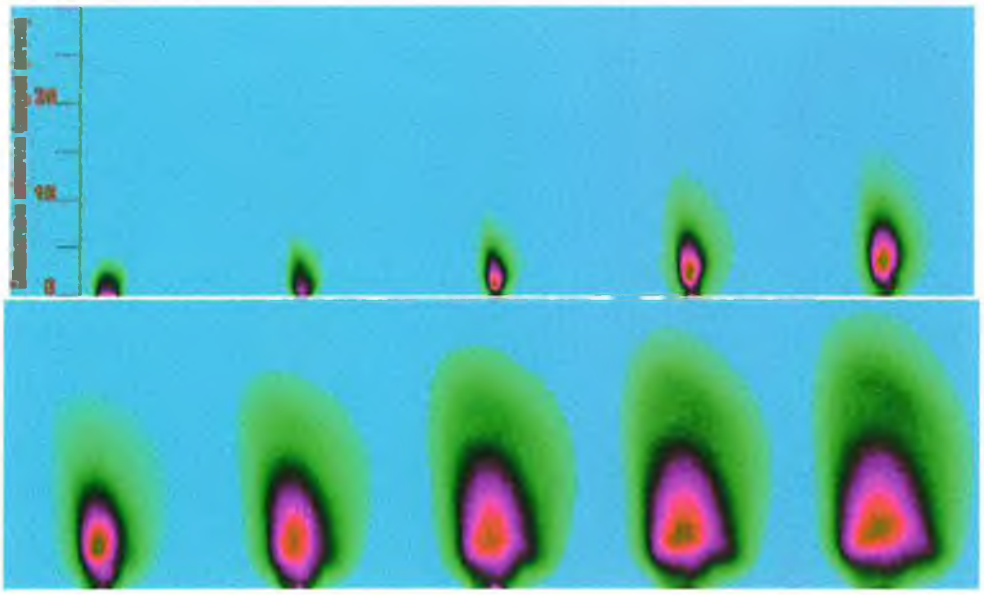

Figure 4.70: ICCD images of Ga plume expansion from 100 ns (top left) to 1000 ns (bottom right) after the laser pulse in 10^{-2} mbar N_2, $\lambda_{Laser} = 1064$ nm.

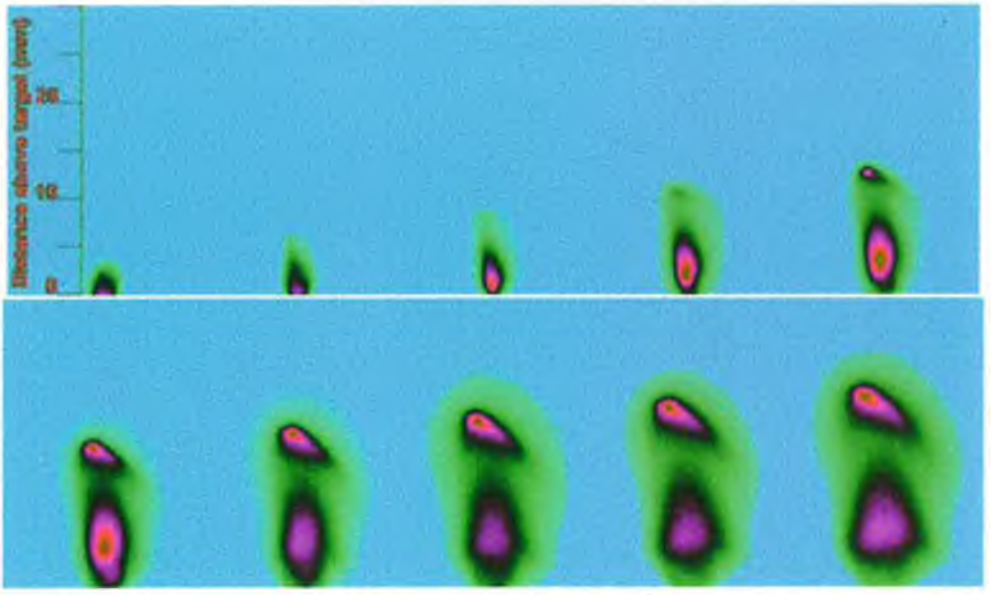

Figure 4.71: ICCD images of Ga plume expansion from 100 ns (top left) to 1000 ns (bottom right) after the laser pulse in 10^{-1} mbar N_2, $\lambda_{Laser} = 1064$ nm.

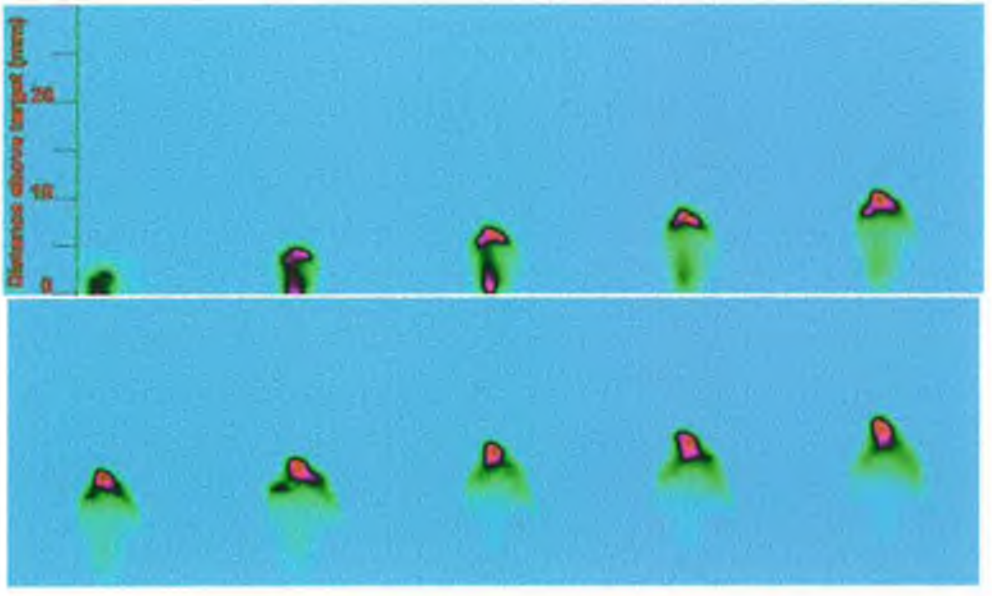

Figure 4.72: ICCD images of Ga plume expansion from 100 ns (top left) to 1000 ns (bottom right) after the laser pulse in 1 mbar N_2, $\lambda_{Laser} = 1064$ nm.

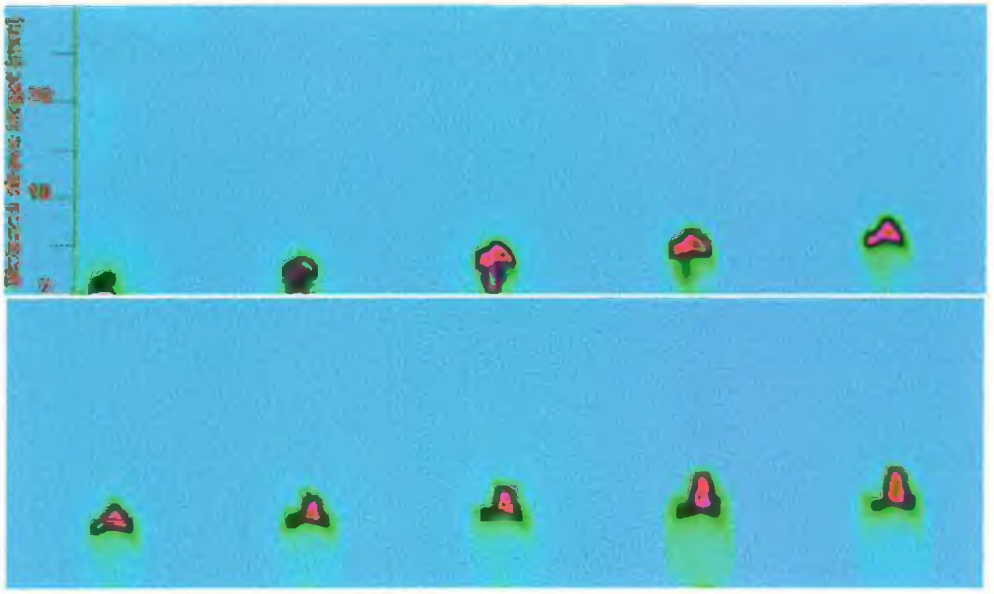

Figure 4.73: ICCD images of Ga plume expansion from 100 ns (top left) to 1000 ns (bottom right) after the laser pulse in 5 mbar N_2, $\lambda_{Laser} = 1064$ nm.

4.3.1 The expansion of the plume

From these images one can extract spatial profiles along the expansion axis of the plume at the various times recorded, as in figure 4.74. In figures 4.75 and 4.76 spatial profiles are plotted for a range of gas pressures at 250 and 500 ns.

It is clear that the expansion behaviour in 10^{-1}, 1 and 5 mbar N_2 is very different to that at 10^{-5} and 10^{-2} mbar N_2. At the higher pressures a bright emission peak is formed at the leading edge of the plume and the so-called plume-splitting behaviour is clearly visible [82]. The intensity of the peak increases with increasing pressure. This increased emission as pressure increases was also evident from the Ga and GaN spectra and has been discussed in section 4.1.1.

The position of the luminous edge of the plume was estimated by taking the second derivative of the spatial profile to find the point of inflection where the emission signal in the image goes to zero. This is shown at the pressures of interest in figures 4.77, 4.78, 4.79, 4.80 and 4.81.

At the two lower pressures (10^{-5} and 10^{-2} mbar N_2), in figures 4.77 and 4.78, the velocity of the leading luminous edge of the plume behaves in a linear fashion typical of the free expansion of a plasma plume. However, one can observe in figures 4.79, 4.80 and 4.81 the quite different expansion behaviour in the presence of higher pressures of N_2.

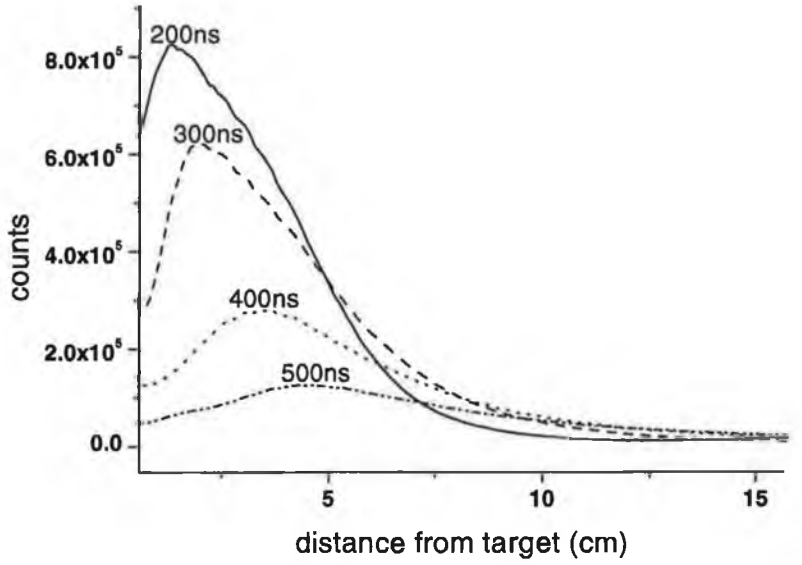

Figure 4.74: Spatial profiles of Ga plume expansion in 10^{-5} mbar N_2, $\lambda_{Laser} = 1064$ nm, 2.5 Jcm^{-2}.

The edge velocities in 10^{-5} and 10^{-2} mbar N_2 were estimated from 4.77 and 4.78 and are given in table 4.4.

P (mbar)	ν_{edge} (cms^{-1})
10^{-5}	$2.8 \pm 0.2 \times 10^6$
10^{-2}	$2.5 \pm 0.2 \times 10^6$

Table 4.4: Plume expansion edge velocities.

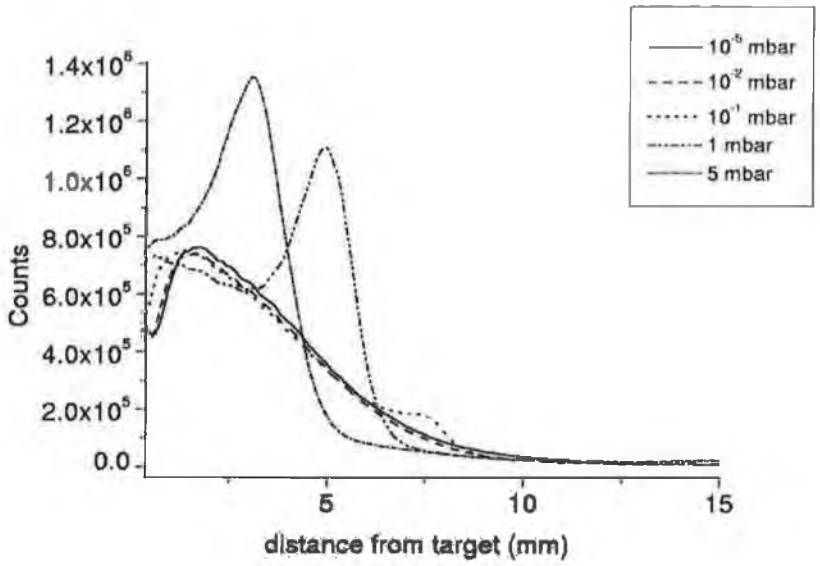

Figure 4.75: Spatial profiles of Ga plume expansion vs pressure at 250 ns, $\lambda_{Laser} = 1064$ nm, 2.5 Jcm^{-2}.

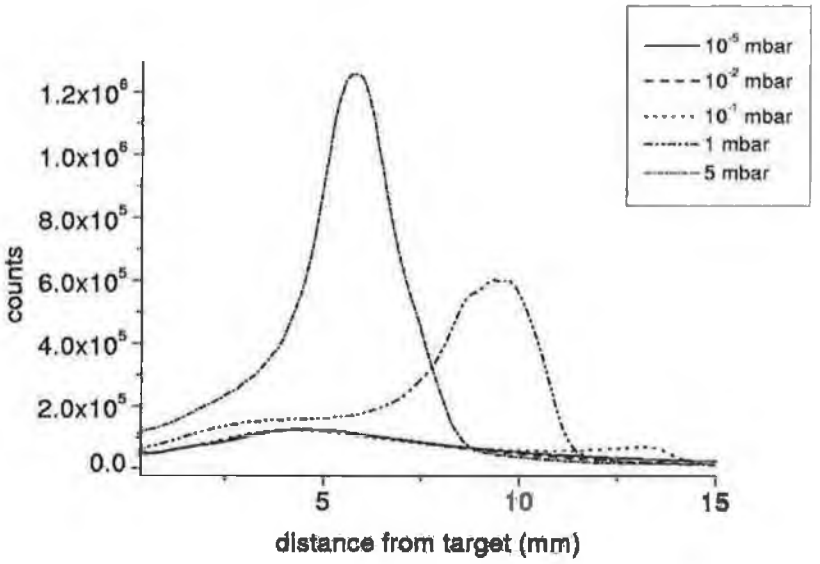

Figure 4.76: Spatial profiles of Ga plume expansion vs pressure at 500 ns, $\lambda_{Laser} = 1064$ nm, 2.5 Jcm^{-2}.

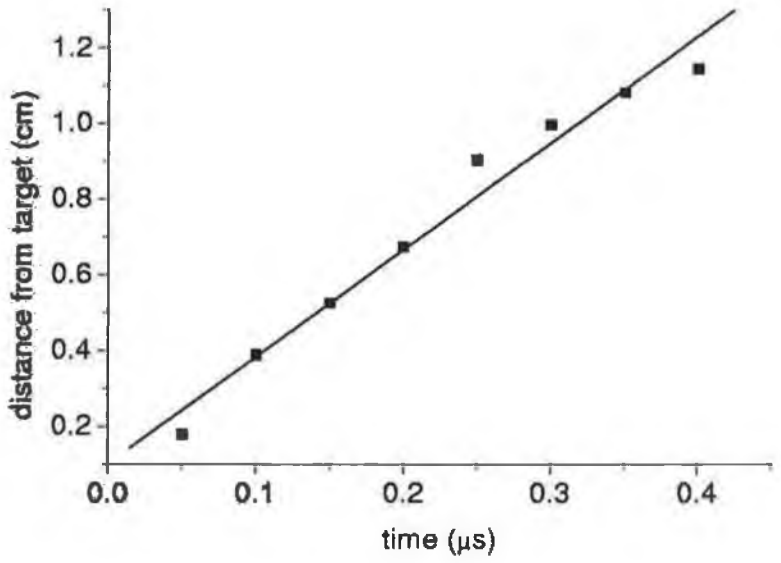

Figure 4.77: Ga plume edge expansion in 10^{-5} mbar N_2, $\lambda_{Laser} = 1064$ nm, 2.5 Jcm^{-2}.

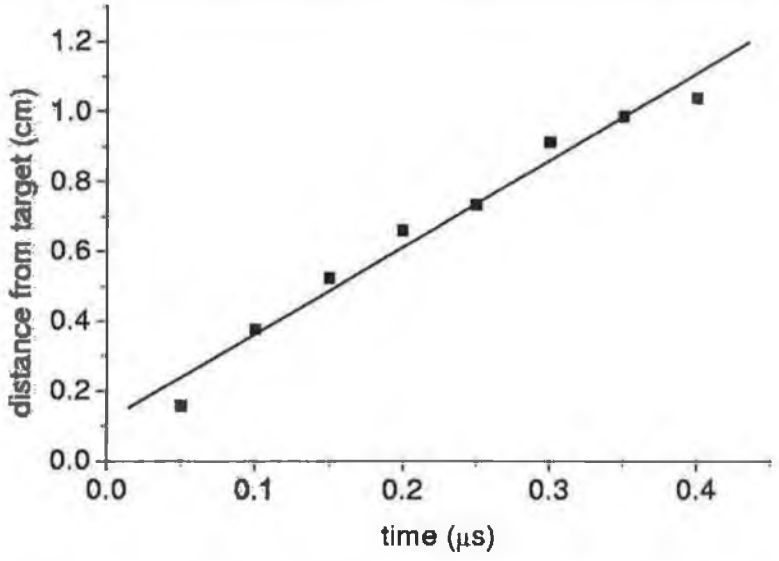

Figure 4.78: Ga plume edge expansion in 10^{-2} mbar N_2, $\lambda_{Laser} = 1064$ nm, 2.5 Jcm^{-2}.

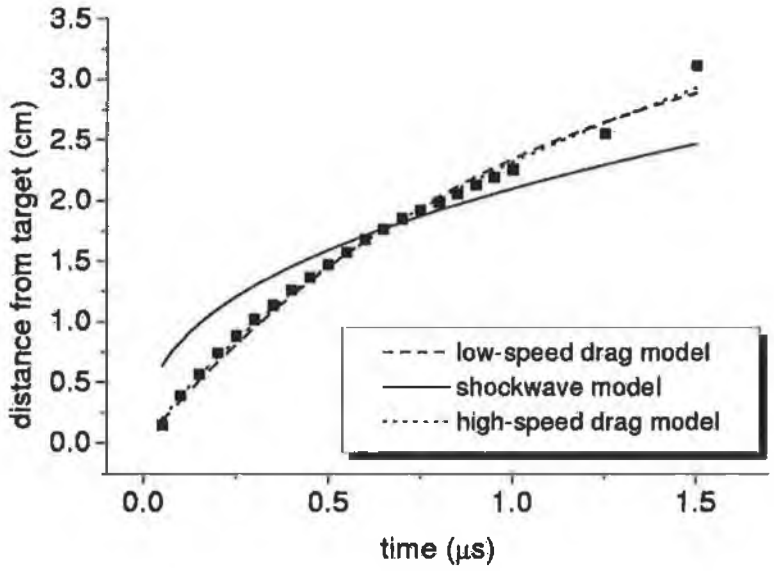

Figure 4.79: Ga plume edge expansion in 10^{-1} mbar N_2, $\lambda_{Laser} = 1064$ nm, 2.5 Jcm^{-2}.

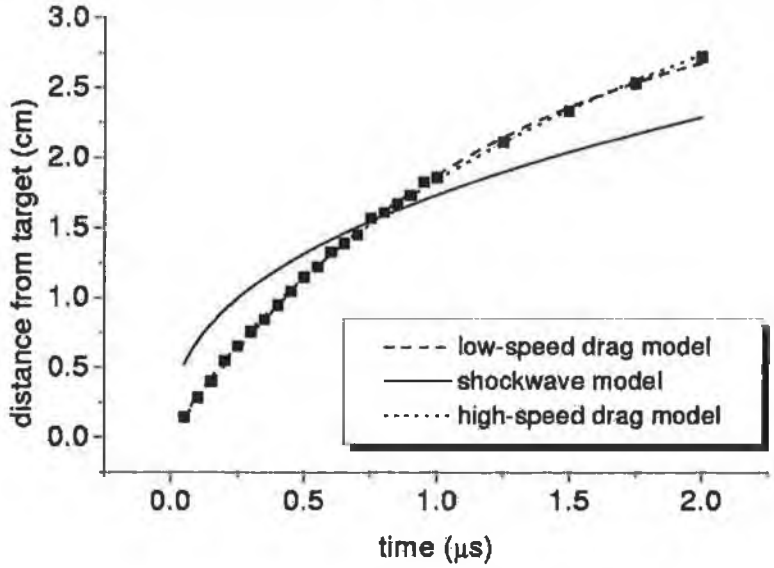

Figure 4.80: Ga plume edge expansion in 1 mbar N_2 mbar, $\lambda_{Laser} = 1064$ nm, 2.5 Jcm^{-2}.

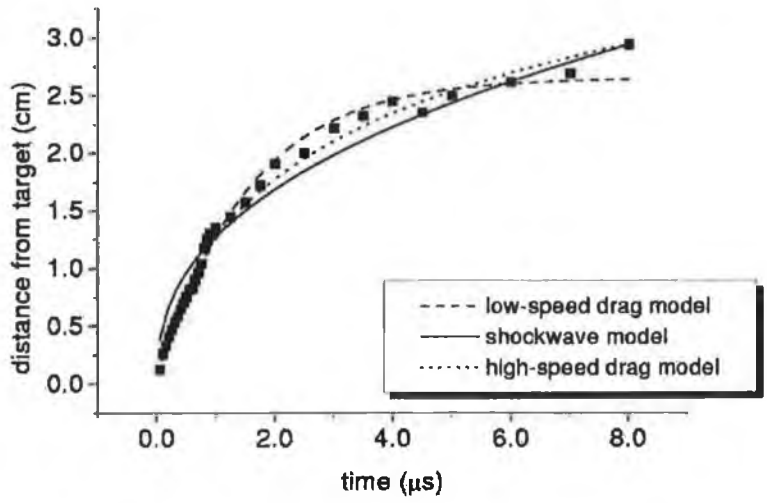

Figure 4.81: Ga plume edge expansion in 5 mbar N_2, $\lambda_{Laser} = 1064$ nm, 2.5 Jcm^{-2}.

The data in figures 4.79, 4.80 and 4.81 (10^{-1}, 1 and 5 mbar N_2) are fitted to the shock model of equation 2.10 in section 2.1.2, however it does not describe the data very well, although the fit improves at higher pressures. The classical drag model of equation 2.12 and the high-speed drag model of equation 2.13 were also fitted. These provided much closer fits to the data at these three higher pressures, with the high-speed drag model being slightly better.

P (mbar)	n (cm^{-3})	λ (cm)
10^{-5}	2.4×10^{11}	6.8×10^{2}
10^{-2}	2.4×10^{14}	6.8×10^{-1}
10^{-1}	2.4×10^{15}	6.8×10^{-2}
1	2.4×10^{16}	6.8×10^{-3}
5	1.2×10^{17}	1.4×10^{-1}
1013	2.5×10^{19}	6.6×10^{-6}

Table 4.5: N_2 Particle densities and Ga mean free paths in N_2 at various pressures.

The pressure "threshold" at which the expansion behaviour of the plume

changes appreciably occurs at $\sim 10^{-1}$ mbar. Below this value the plume passes through the ambient nitrogen gas unhindered. Above this value the plume no longer expands freely but is slowed and heated (see discussion in section 4.1.1).

Table 4.5 lists the mean free paths in N_2 for the various pressures. This is the average distance that a gallium atom travels between collisions with nitrogen molecules and is given by

$$\lambda = \frac{1}{\sqrt{2}\pi d^2 n} \tag{4.1}$$

where $d = 3.7$ Å is the diameter of a nitrogen molecule and n is the molecular number density calculated from $p = nkT$. The "threshold" pressure, above which the plume expansion is modified, coincides with the pressure at which the gas flow state becomes continuous instead of molecular.

4.3.2 The dynamics of the plume

The ICCD images were used to plot the variation of intensity with time at fixed distances above the target surface yielding the plume time-of-flight distribution. In figures 4.82, 4.83, 4.84, 4.85 and 4.86 the time-of-flight curves are plotted for Ga plumes in 10^{-5}, 10^{-2}, 10^{-1}, 1 and 5 mbar N_2. It may be observed that the time-of-flight curves are more intense and have a sharpened profile at the higher pressures and greater distances from target.

Fitting the shifted centre-of-mass Maxwell-Boltzmann distribution, equation 3.9, to the low pressure free-expansion cases yields the values listed in table 4.6. The velocity values for the centre of mass are an order of magnitude higher than the (negative) value estimated from the ion probe measurements (section 4.2).

P (mbar)	T_K (eV)	u_K (cms^{-1})
10^{-5}	-152	6.2×10^6
10^{-2}	-152	6.2×10^6

Table 4.6: Plume expansion in N_2.

The Knudsen layer temperatures are similar in magnitude to the corresponding

ion probe estimate, however they must be considered with caution due to the negative value. This suggests that the velocities do not follow a shifted centre of mass Maxwell-Boltzmann distribution, that is to say that this distribution is not a good description of the plume dynamics and translation temperature. The reason for this probably lies in the fact that since the laser has a gaussian profile, and therefore so has the spot on target (2×2 mm), then so too would the initial plume. This plume would then have a distribution of expansion-driving temperatures as opposed to a single value.

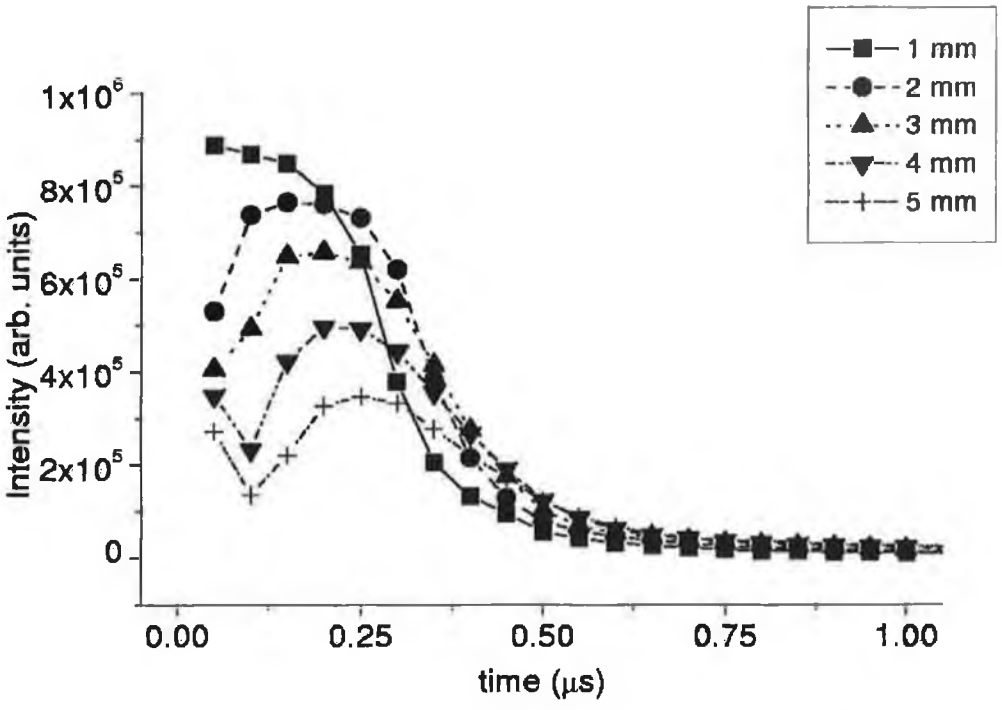

Figure 4.82: Ga plume time-of-flight for various distances above target in 10^{-5} mbar N_2, $\lambda_{Laser} = 1064$ nm, 2.5 Jcm^{-2}.

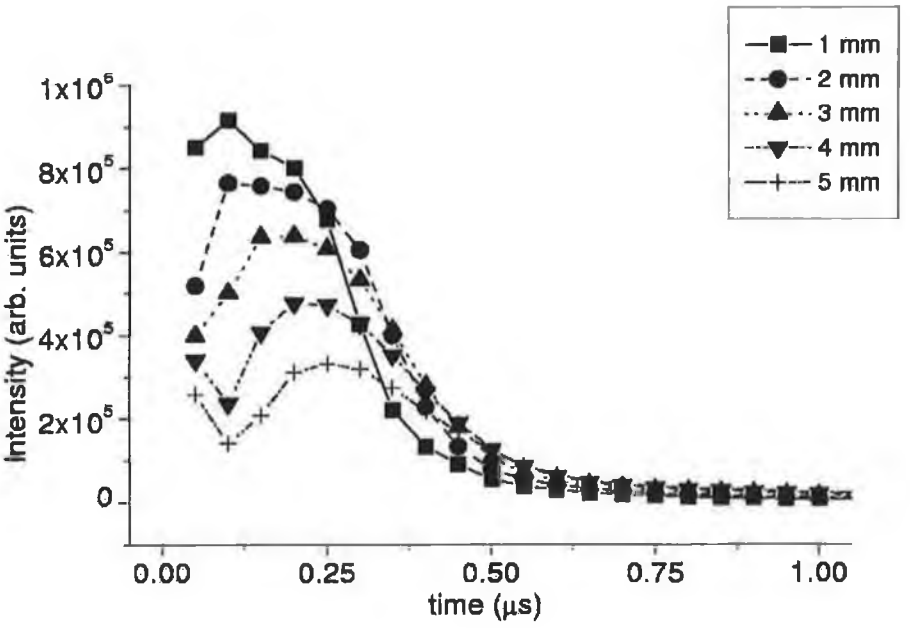

Figure 4.83: Ga plume time-of-flight for various distances above target in 10^{-2} mbar N_2, $\lambda_{Laser} = 1064$ nm, 2.5 Jcm^{-2}.

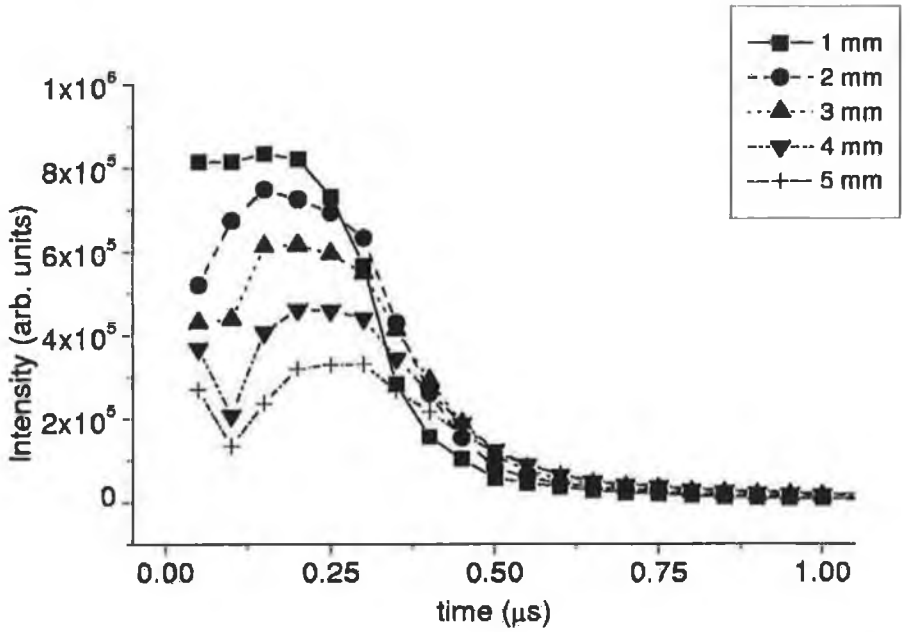

Figure 4.84: Ga plume time-of-flight for various distances above target, in 10^{-1} mbar N_2, $\lambda_{Laser} = 1064$ nm, 2.5 Jcm^{-2}.

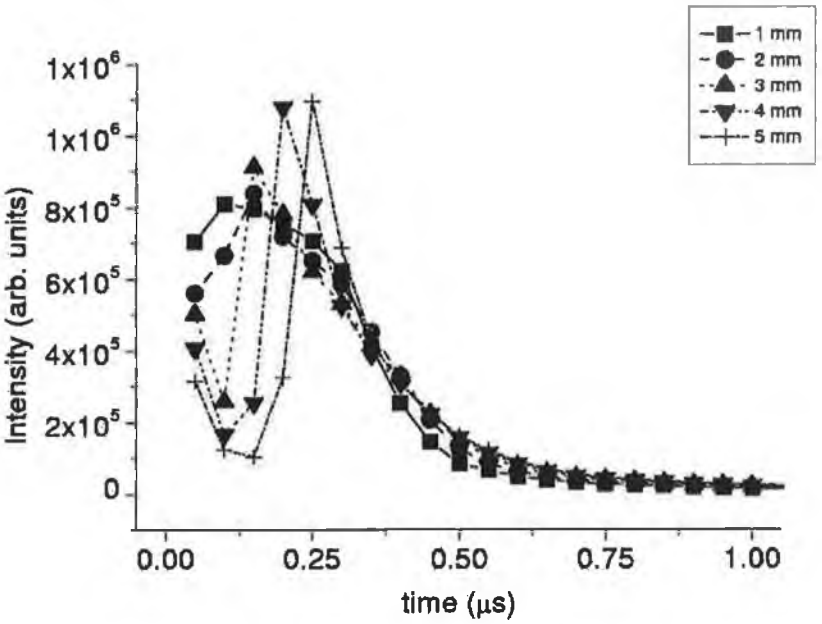

Figure 4.85: Ga plume time-of-flight for various distances above target, in 1 mbar N_2, $\lambda_{Laser} = 1064$ nm, 2.5 Jcm^{-2}.

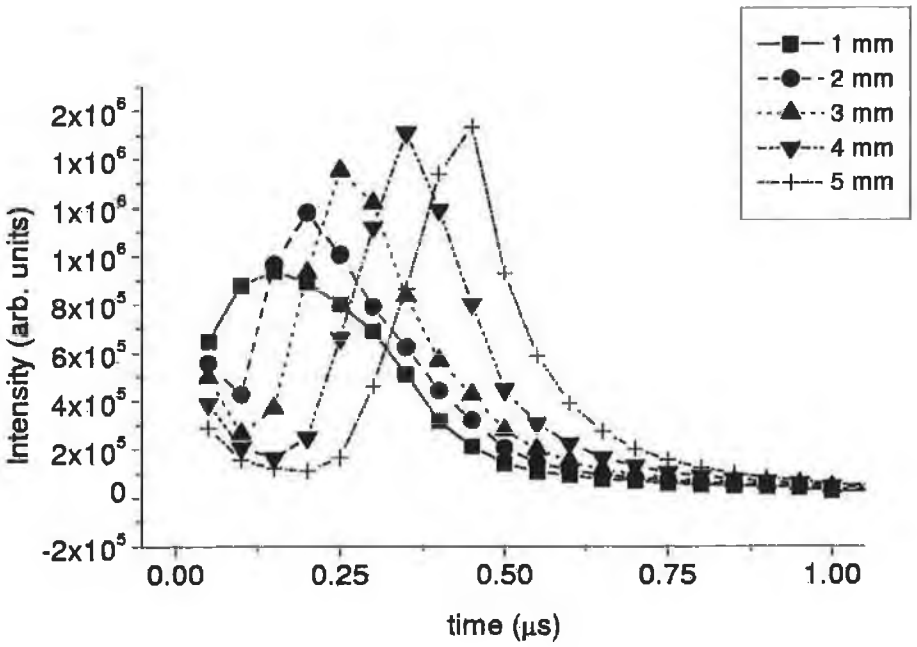

Figure 4.86: Ga plume time-of-flight for various distances above target, in 5 mbar N_2, $\lambda_{Laser} = 1064$ nm, 2.5 Jcm^{-2}.

Chapter 5

Lithium and Lithium Flouride Results and Analysis

5.1 Spectroscopy and Transients

5.1.1 Emission spectra of Lithium

Lithium metal was ablated in vacuum (10^{-5} mbar N_2) using three harmonics of a Nd:YAG laser, 266, 532 and 1064 nm, at fluences of 2.2 Jcm^{-2}, 4.4 Jcm^{-2} and 6.5 Jcm^{-2}, respectively, with a spotsize of 115×80 μm. Spectra were recorded using photographic film as the detector (see section 3.2.2). Figure 5.1 shows the emission spectrum of a lithium plume expanding into vacuum at various distances above the target surface in the 1064 nm case. Figures 5.2 and 5.3 are emission spectra for the 532 and 266 nm cases.

As with Ga and GaN plumes, one observes that the plume emission decreases with decreasing laser wavelength and increasing distance from the target surface, as do the number of emission lines. The lines have all been assigned to transitions in lithium and table 5.1 lists their photographically measured values and assigned values.

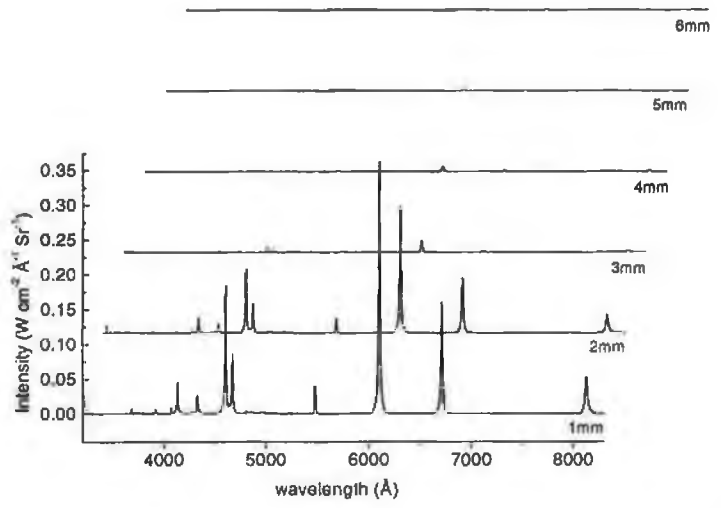

Figure 5.1: Li in 10^{-5} mbar N_2 at various distances from target surface, $\lambda_{Laser} = 1064$ nm, 6.5 Jcm^{-2}, 115×80 μm laser spot.

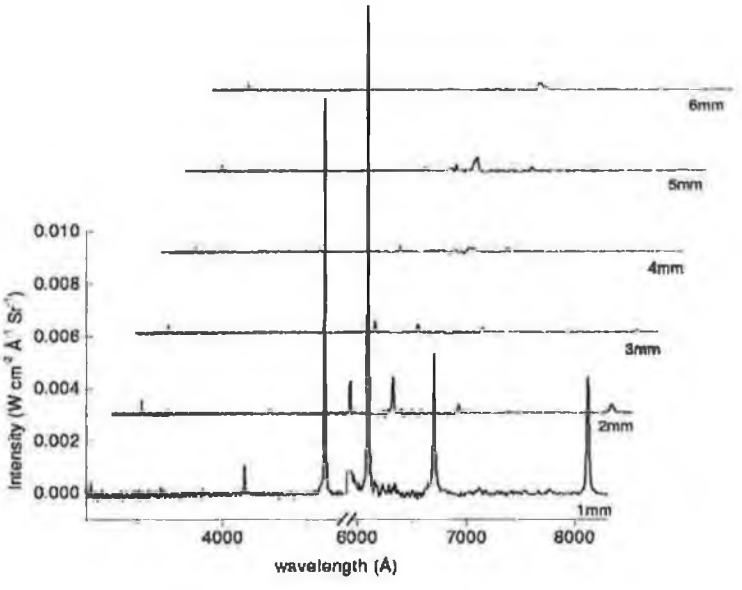

Figure 5.2: Li in 10^{-5} mbar N_2 at various distances from target surface, $\lambda_{Laser} = 532$ nm, 4.4 Jcm^{-2}, 115×80 μm laser spot.

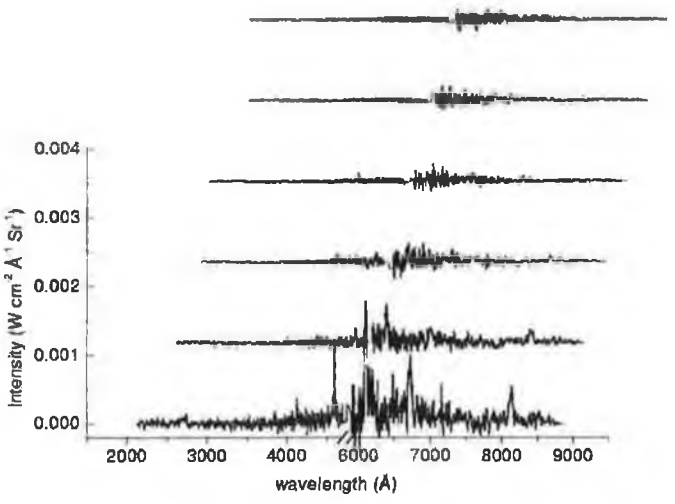

Figure 5.3: Li in 10^{-5} mbar N_2 at various distances from target surface, bottom λ_{Laser} = 266 nm, 2.2 Jcm^{-2}, 115 × 80 μm laser spot.

$\lambda_{meas.}$ (Å)	Assign	λ_{NIST}(Å)	f_{ki}	E_i (eV)	E_k (eV)	Config.	g_i-g_k
3196	Li II	3196.318	1.76e-02	69.58530	73.46315	1s.3d-1s.5f	5 - 5
3196	Li II	3196.318	1.41e-01	69.58530	73.46315	1s.3d-1s.5f	5 - 7
3196	Li II	3196.381	3.56e-04	69.58538	73.46315	1s.3d-1s.5f	7 - 5
3196	Li II	3196.381	1.26e-02	69.58538	73.46315	1s.3d-1s.5f	7 - 7
3196	Li II	3196.381	1.46e-01	69.58538	73.46315	1s.3d-1s.5f	7 - 9
3233	Li I	3232.657	1.83e-03	0.00000	3.834260	$1s^2$.2s-$1s^2$.3p	2 - 2
3233	Li I	3232.657	3.67e-03	0.00000	3.834260	$1s^2$.2s-$1s^2$.3p	2 - 4
3685	Li II	3684.602	1.05e-01	68.78081	72.14478	1s.3s-1s.4p	3 - 5
3685	Li II	3684.700	6.29e-02	68.78081	72.14469	1s.3s-1s.4p	3 - 3
3685	Li II	3684.754	2.10e-02	68.78081	72.14464	1s.3s-1s.4p	3 - 1
3915	Li I	3915.30					

Table 5.1: Measured values of lithium lines and assignments.

$\lambda_{meas.}$ (Å)	Assign	λ_{NIST}(Å)	f_{ki}	E_i (eV)	E_k (eV)	Config.	g_i-g_k
3915	Li I	3915.35					
4133	Li I	4132.557	4.52e-02	1.847819	4.847155	$1s^2.2p$-$1s^2.5d$	2 - 4
4133	Li I	4132.613	4.07e-02	1.847861	4.847157	$1s^2.2p$-$1s^2.5d$	4 - 6
4133	Li I	4132.615	4.53e-03	1.847861	4.847155	$1s^2.2p$-$1s^2.5d$	4 - 4
4273	Li I	4273.062	4.19e-03	1.847819	4.748535	$1s^2.2p$-$1s^2.5s$	2 - 2
4273	Li I	4273.124	4.20e-03	1.847861	4.748535	$1s^2.2p$-$1s^2.5s$	4 - 2
4325	Li II	4325.342	3.83e-01	69.36922	72.23488	1s.3p-1s.4d	3 - 5
4325	Li II	4325.415	1.27e-01	69.36922	72.23483	1s.3p-1s.4d	3 - 3
4325	Li II	4325.419	4.28e-01	69.36936	72.23496	1s.3p-1s.4d	5 - 7
4325	Li II	4325.542	7.66e-02	69.36936	72.23488	1s.3p-1s.4d	5 - 5
4325	Li II	4325.615	5.10e-03	69.36936	72.23483	1s.3p-1s.4d	5 - 3
4325	Li II	4325.784	5.10e-01	69.36947	72.23483	1s.3p-1s.4d	1 - 3
4603	Li I	4602.821	1.22e-01	1.847819	4.540722	$1s^2.2p$-$1s^2.4d$	2 - 4
4603	Li I	4602.889	1.10e-01	1.847861	4.540725	$1s^2.2p$-$1s^2.4d$	4 - 6
4603	Li I	4602.893	1.22e-02	1.847861	4.540722	$1s^2.2p$-$1s^2.4d$	4 - 4
4672	Li II	4671.629	8.98e-01	69.58530	72.23854	1s.3d-1s.4f	5 - 7
4672	Li II	4671.764	2.27e-03	69.58538	72.23854	1s.3d-1s.4f	7 - 5
4672	Li II	4671.764	8.05e-02	69.58538	72.23854	1s.3d-1s.4f	7 - 7
4672	Li II	4671.764	9.30e-01	69.58538	72.23854	1s.3d-1s.4f	7 - 9
4672	Li II	4671.880	1.01e+00	69.58545	72.23854	1s.3d-1s.4f	3 - 5
5485	Li II	5483.462	3.43e-02	59.02083	61.28126	1s.2s-1s.2p	3 - 1
5485	Li II	5484.403	1.71e-01	59.02083	61.28087	1s.2s-1s.2p	3 - 5
5485	Li II	5485.086	1.03e-01	59.02083	61.28059	1s.2s-1s.2p	3 - 3
5485	Li II	5485.65					
6104	Li I	6103.53	6.67e-01	1.847819	3.878609	$1s^2.2p$-$1s^2.3d$	2 - 4
6104	Li I	6103.64	6.00e-01	1.847861	3.878614	$1s^2.2p$-$1s^2.3d$	4 - 6
6104	Li I	6103.66	6.65e-02	1.847861	3.878609	$1s^2.2p$-$1s^2.3d$	4 - 4
6708	Li I	6707.76	5.02e-01	0.00000	1.847861	$1s^2.2s$-$1s^2.2p$	2 - 4

Table 5.1: Measured values of lithium lines and assignments.

$\lambda_{meas.}$ (Å)	Assign	λ_{NIST}(Å)	f_{ki}	E_i (eV)	E_k (eV)	Config.	g_i-g_k
6708	Li I	6707.91	2.51e-01	0.00000	1.847819	$1s^2.2s$-$1s^2.2p$	2 - 2
8126	Li I	8126.22	1.15e-01	1.847819	3.373130	$1s^2.2p$-$1s^2.3s$	2 - 2
8126	Li I	8126.45	1.15e-01	1.847861	3.373130	$1s^2.2p$-$1s^2.3s$	4 - 2

Table 5.1: (continued)

Figures 5.4 and 5.5 show emission spectra from 1064 nm laser radiation ablation of lithium with a spotsize of 2000×2000 μm at 10 Jcm^{-2} and 1 Jcm^{-2} fluences. One observes Li^+ (548.4 nm) emission from the 6.5 Jcm^{-2}(figure 5.1) and 10 Jcm^{-2} cases, but not at 1 Jcm^{-2}.The emission spectra when 532 nm laser radiation was used to ablate lithium are displayed in figures 5.6 and 5.7. The spotsize was 2000×2000 μm and the fluences were 10 and 1 Jcm^{-2}, respectively. The Li^+ (548.4 nm) emission is overshadowed by scattered laser light, and this, in fact, dominates all spectra. For this reason the wavelength axis is broken in this region so as to ease the display of the rest of the spectrum.

The observation of ionic lithium lines can be understood in simple terms of inverse bremmstrahlung absorption, see figure 2.1 showing the inverse bremmstralung absorption coefficient and section 4.1.1 where similar behaviour was discussed in the case of the gallium plumes. This increases the excitation temperature and, thus, the ionisation fraction. The integrated intensity of the 610.3 and 670.8 nm lines (see table 5.1) is plotted in figure 5.8 for each laser wavelength in the case of a 115×80 μm spot size and in figure 5.9 for each laser wavelength in the case of a 2000×2000 μm spot size.

For the lithium plumes created with laser higher fluences there is a larger intensity of this radiation available for absorption in the plasma, and the larger spotsize produces more particles, so a higher emission intensity is recorded from these plumes (figure 5.9).

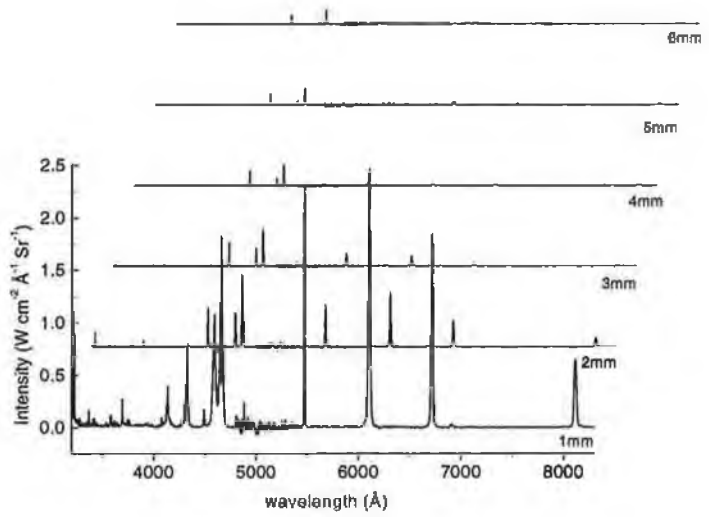

Figure 5.4: Li in 10^{-5} mbar N_2 at various distances from target surface, $\lambda_{Laser} = 1064$ nm, 10 Jcm^{-2}, 2000 × 2000 μm.

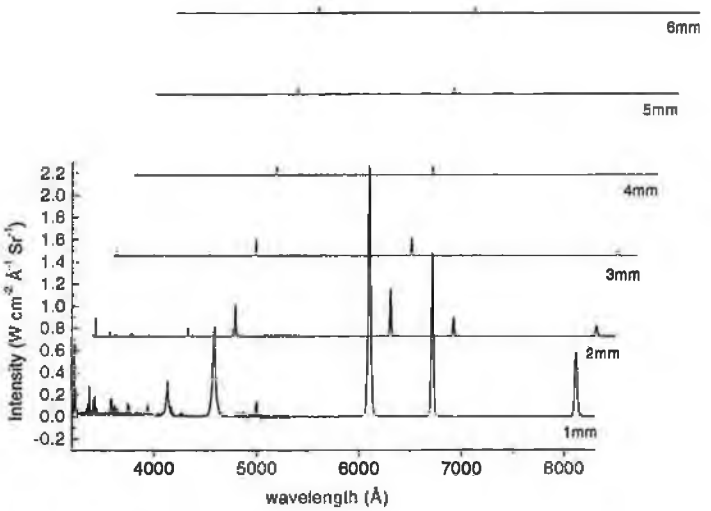

Figure 5.5: Li in 10^{-5} mbar N_2 at various distances from target surface, $\lambda_{Laser} = 1064$ nm, 1 Jcm^{-2}, 2000 × 2000 μm.

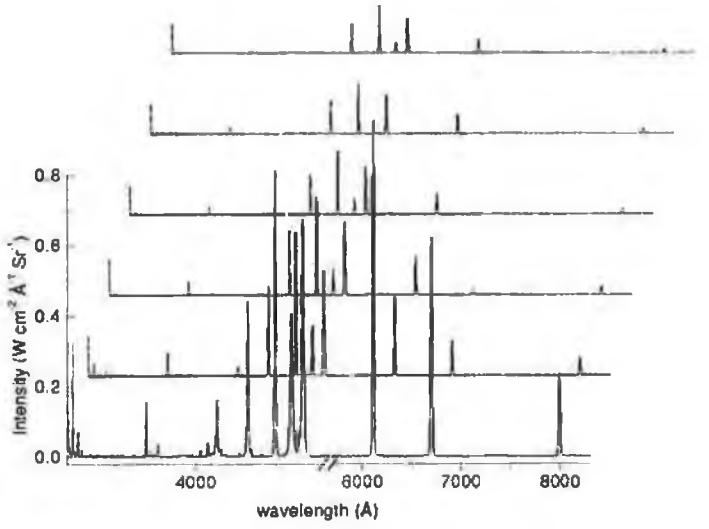

Figure 5.6: Li in 10^{-5} mbar N_2 at various distances from target surface, $\lambda_{Laser} = 532$ nm, 10 Jcm^{-2}, 2000 × 2000 μm.

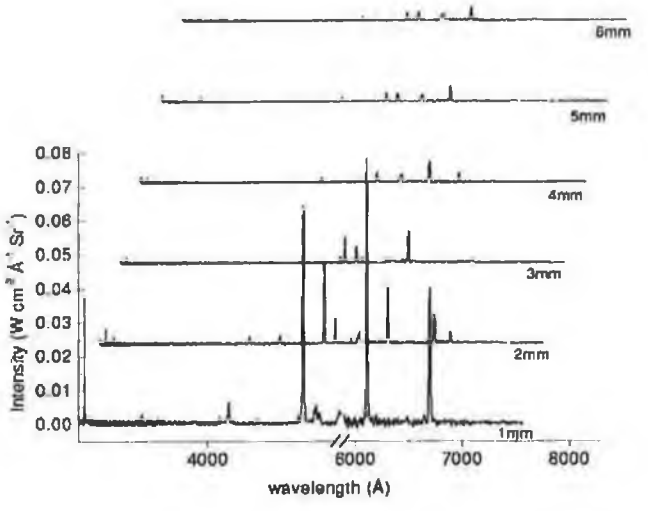

Figure 5.7: Li in 10^{-5} mbar N_2 at various distances from target surface, $\lambda_{Laser} = 532$ nm, 1 Jcm^{-2}, 2000 × 2000 μm.

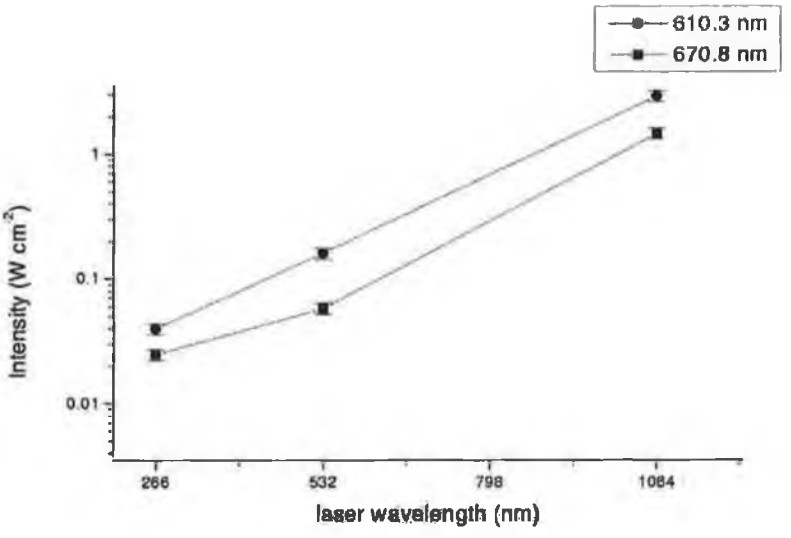

Figure 5.8: Li plume emission vs laser wavelength, 115 x 80 μm spot.

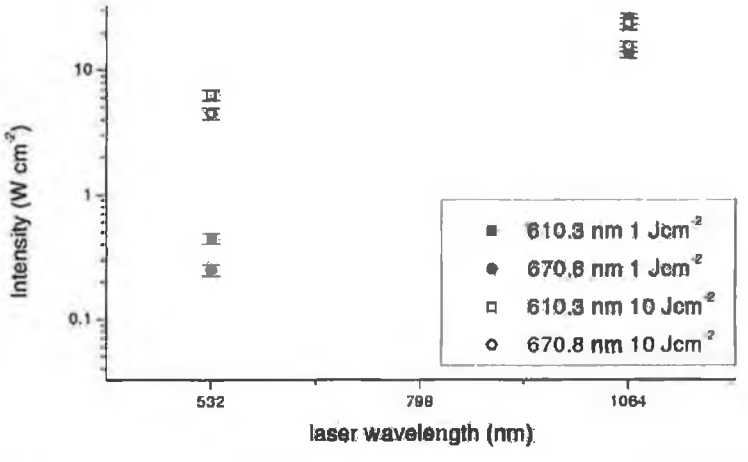

Figure 5.9: Li plume emission vs laser wavelength, 2000 x 2000 μm spot.

5.1.2 Li level populations in plume

The populations in the $1s^2 2p$ ($\approx$ 1.85 eV), $1s^2 3s$ ($\approx$ 3.37 eV), $1s^2 3d$ ($\approx$ 3.88 eV), $1s^2 4d$ ($\approx$ 4.54 eV) and $1s^2 5d$ ($\approx$ 4.85 eV) excited levels can be estimated using equation 2.37 and the integrated *absolute* intensities of the 670.8, 812.6, 610.3, 460.2 and 413.2 nm spectral lines.

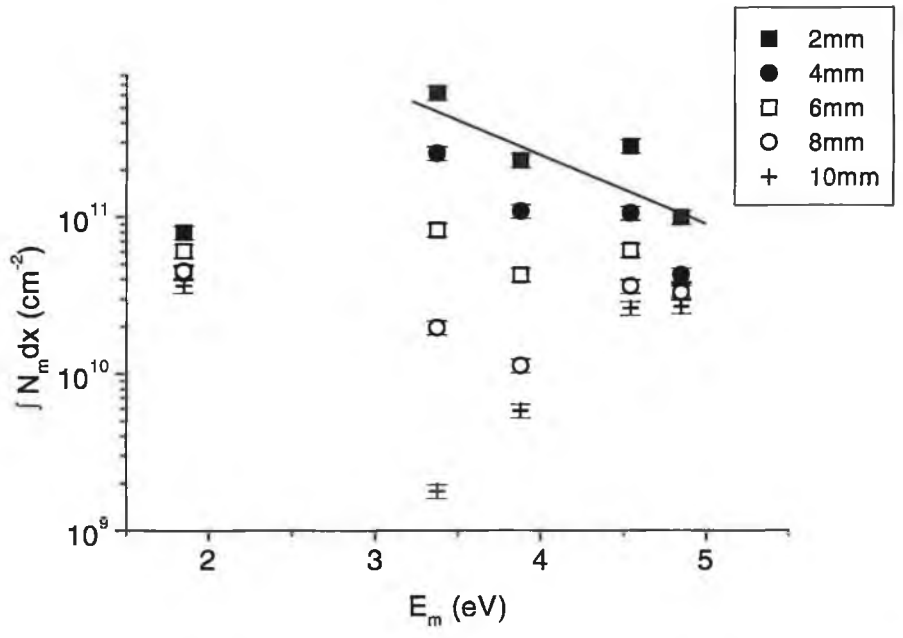

Figure 5.10: Level populations of Li at various distances from target surface, λ_{Laser} = 1064, 6.5 Jcm^{-2}, 115 x 80 μm laser spot.

These populations are plotted for each laser wavelength in figures 5.10, 5.11 and 5.12 for various distances above the target surface. One observes, with all three laser wavelengths, that one can fit a straight line to the integrated populations of the $1s^2 3s$, $1s^2 3d$, $1s^2 4d$ and $1s^2 5d$ excited levels but that the population of the $1s^2 2p$ excited level would not lie along this line. This suggests that the plume is in partial LTE and this will be further discussed in section 5.1.3. Populations are also plotted for the larger spotsize at 1 Jcm^{-2} and 10 Jcm^{-2} in figures 5.13 and 5.14 for 1064 nm laser radiation and 5.15 and 5.16 for 532 nm.

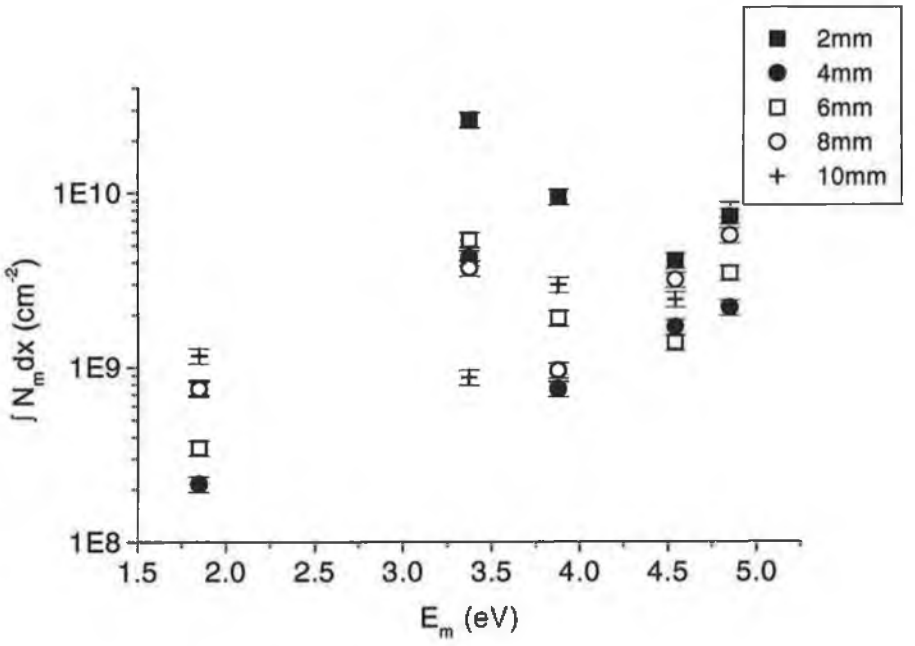

Figure 5.11: Level populations of Li at various distances from target surface, $\lambda_{Laser} = 532$, 4.4 Jcm^{-2}, 115 × 80 μm laser spot.

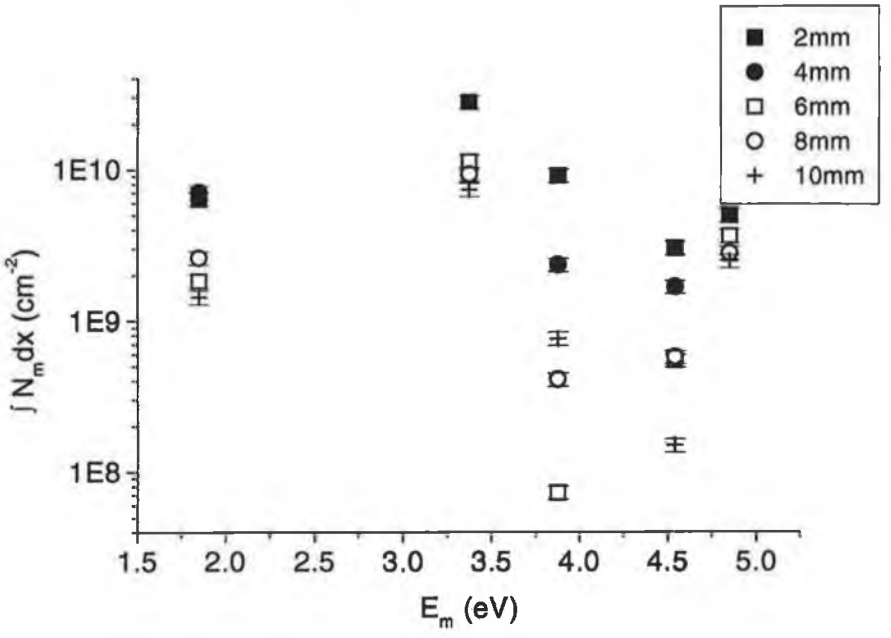

Figure 5.12: Level populations of Li at various distances from target surface, $\lambda_{Laser} = 266$ nm, 2.2 Jcm^{-2}, 115 × 80 μm laser spot.

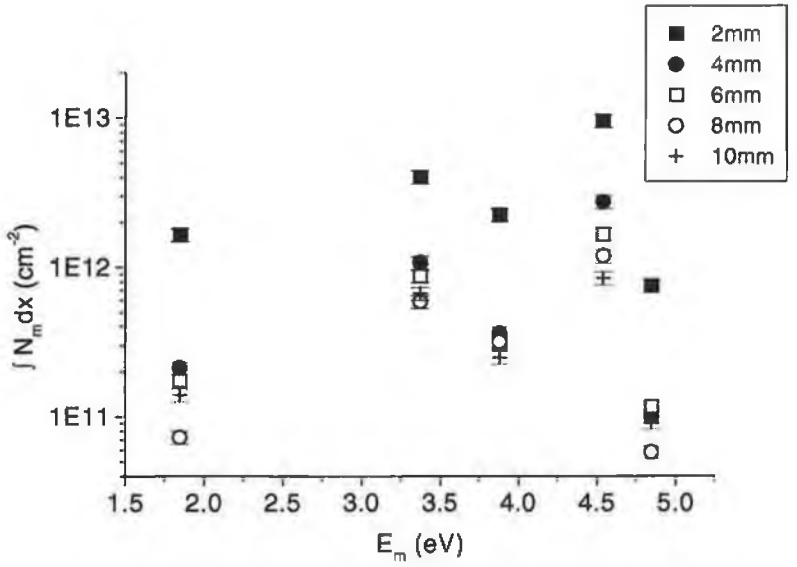

Figure 5.13: Level populations of Li at various distances from target surface, $\lambda_{Laser} = 1064$ nm, 10 Jcm^{-2}, 2000 × 2000 μm spot.

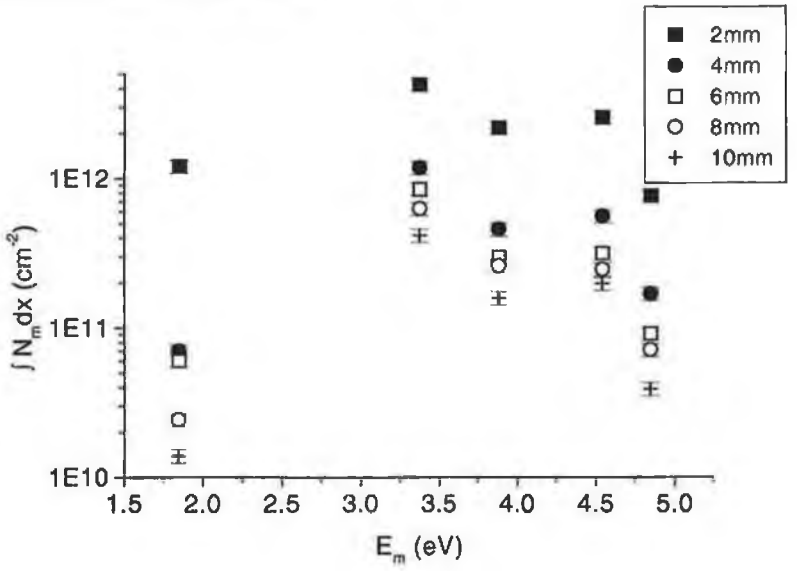

Figure 5.14: Level populations of Li at various distances from target surface, $\lambda_{Laser} = 1064$ nm, 1 Jcm^{-2}, 2000 × 2000 μm spot.

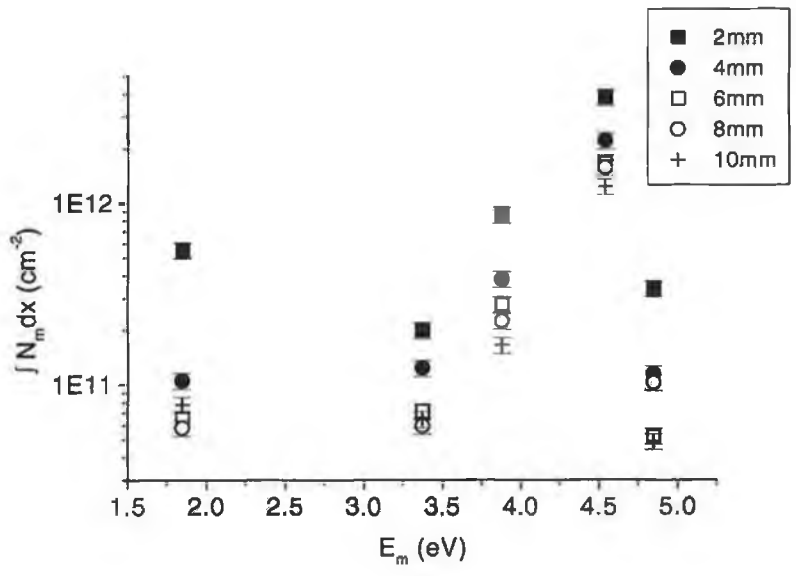

Figure 5.15: Level populations of Li at various distances from target surface, $\lambda_{Laser} = 532$ nm, 10 Jcm^{-2}, 2000 × 2000 μm spot.

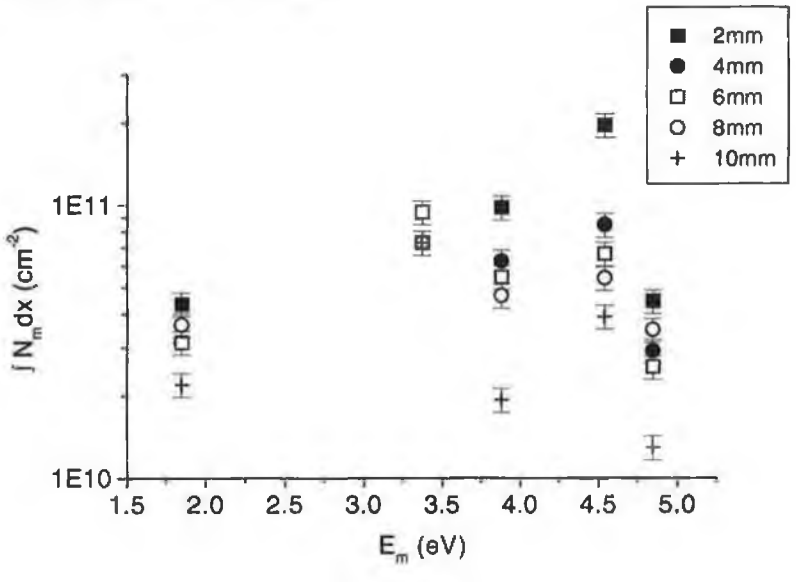

Figure 5.16: Level populations of Li at various distances from target surface, $\lambda_{Laser} = 532$ nm, 1 Jcm^{-2}, 2000 × 2000 μm spot.

5.1.3 Excitation temperature in Li plume

Figures 5.17, 5.18 and 5.19 display the excitation temperatures for lithium ablated with 1064, 355 and 266 nm, at fluences of 6.5 Jcm^{-2}, 4.4 Jcm^{-2} and 2.2 Jcm^{-2}, respectively, with a spotsize of $115 \times 80 \pm 5$ μm. These were estimated from equation 3.1 in a similar manner to that employed in section 4.1.3.

The populations estimates of section 5.1.2 suggest that the $1s^2 2p$ excited level is not in thermal equilibrium with the $1s^2 3s$, $1s^2 3d$, $1s^2 4d$ and $1s^2 5d$ excited levels. Fujimoto et al [83] define levels as being in partial LTE from level p if equation 2.17 applies to it and all higher-lying levels, so we have estimated the excitation temperature using the $1s^2 3s$, $1s^2 3d$, $1s^2 4d$ and $1s^2 5d$ excited levels.

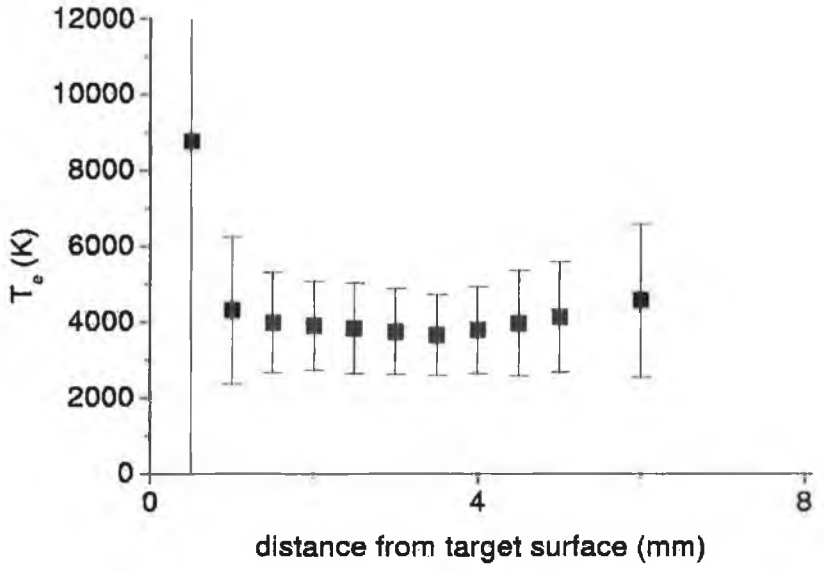

Figure 5.17: Li T_{exc} at various distances from target surface, λ_{Laser} = 1064 nm, 6.5 Jcm^{-2}, 115×80 μm laser spot.

The excitation temperature is also plotted for the larger $2000 \times 2000 \pm 5$ μm spotsize at fluences of 1 Jcm^{-2} and 10 Jcm^{-2} in figures 5.13, 5.14, 5.15 and 5.16 for 1064 and 532 nm laser radiation , respectively.

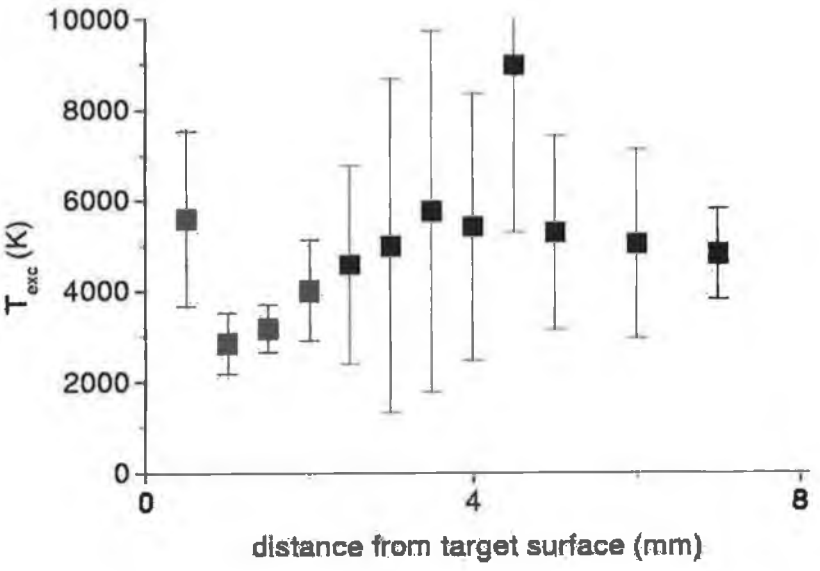

Figure 5.18: Li T_{exc} at various distances from target surface, λ_{Laser} = 532 nm, 4.4 Jcm^{-2}, 115 × 80 μm laser spot.

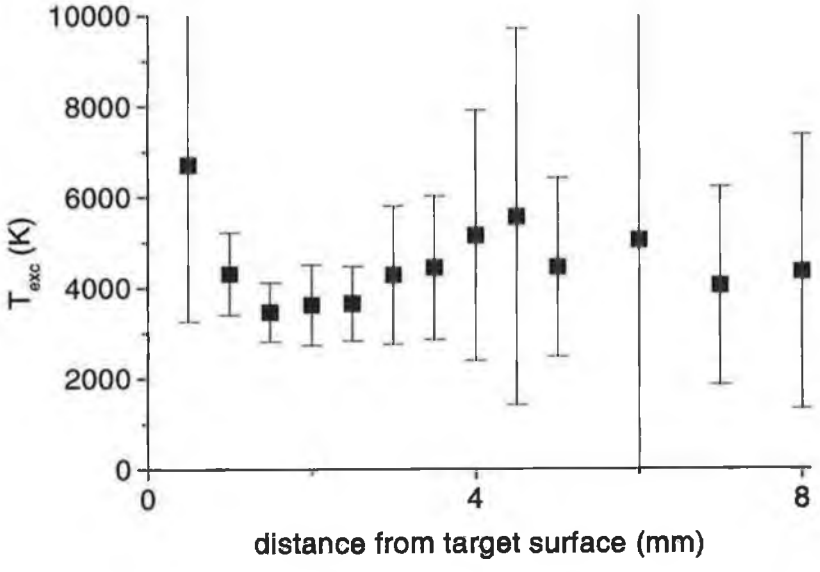

Figure 5.19: Li T_{exc} at various distances from target surface, λ_{Laser} = 266 nm, 2.2 Jcm^{-2}, 115 × 80 μm laser spot.

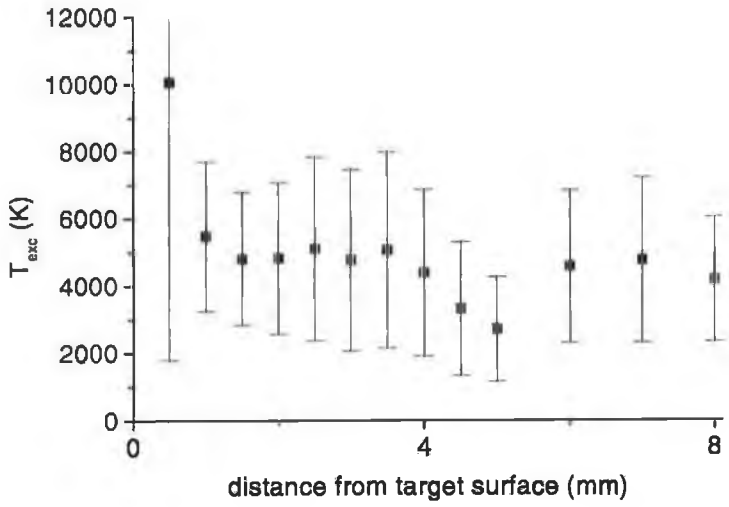

Figure 5.20: Li T_{exc} at various distances from target surface, λ_{Laser} = 1064, 10 Jcm^{-2}, 2000 × 2000 μm spot.

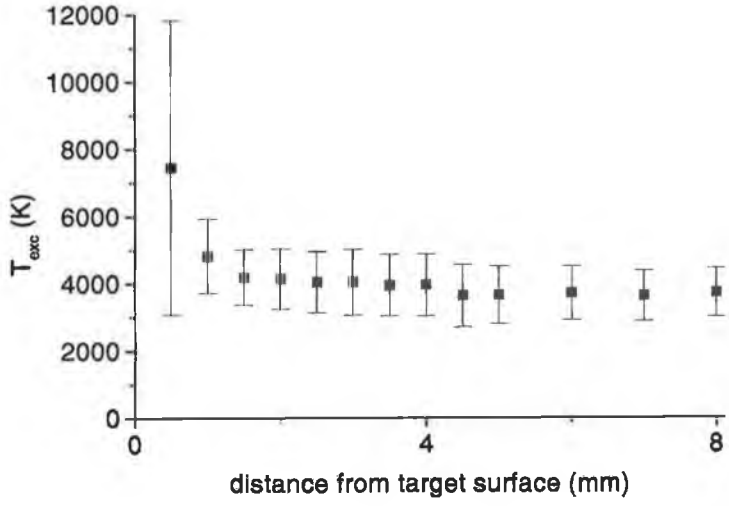

Figure 5.21: Li T_{exc} at various distances from target surface, λ_{Laser} = 1064, 1 Jcm^{-2}, 2000 × 2000 μm spot.

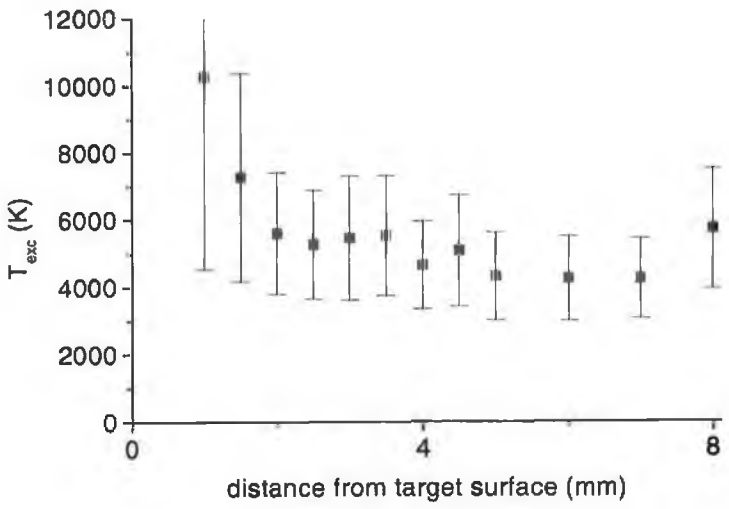

Figure 5.22: Li T_{exc} at various distances from target surface, λ_{Laser} = 532, 10 Jcm^{-2}, 2000 × 2000 μm spot.

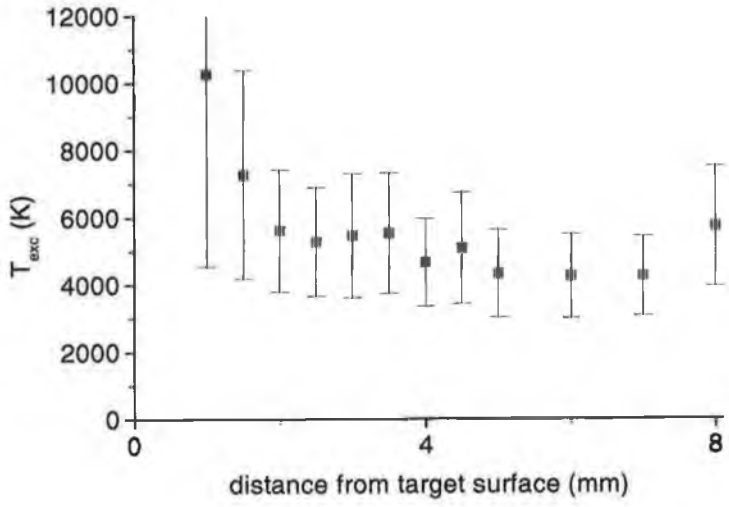

Figure 5.23: Li T_{exc} at various distances from target surface, λ_{Laser} = 532, 1 Jcm^{-2}, 2000 × 2000 μm spot.

Similar to the Ga and GaN cases, one observes that the lithium excitation temperature drops off from an initially higher value to a constant value of about $\sim$ 4000 K after a few mm. Gordillo-Vazquez [84] reported the excitation temperature using Nb emission lines in plumes of $LiNbO_3$, ablated with 193 nm ArF laser radiation at 1.2 Jcm^{-2}, giving values of $\sim$ 0.7 eV ($\sim$ 8100 K) for both time-resolved and time-integrated measurements. Sherrill et al [60] reported an excitation of 1 eV ($\sim$ 11000 K) in LiAg plumes ablated with 1064 nm laser at 1 Jcm^{-2}.

5.1.4 Lithium Flouride

Spectra of LiF ablation plumes were recorded using the setup described in section 3.2.3 at various distances above the target surface.

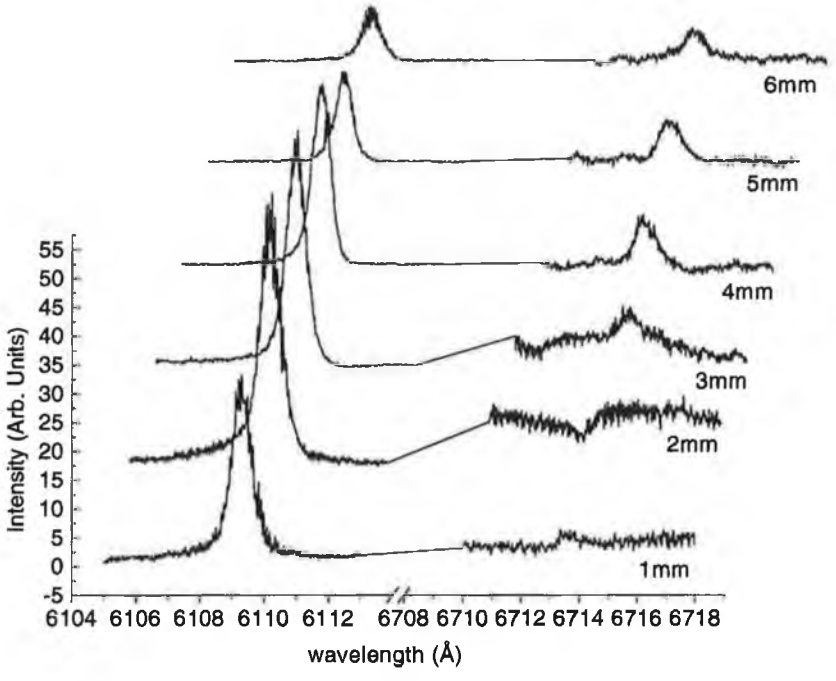

Figure 5.24: Spatially resolved spectra of LiF, 10^{-5} mbar N_2, 1.5 Jcm^{-2}, λ_{Laser} = 193 nm.

These are shown in figure 5.24 for the 610.3 and 670.8 nm lines, where ablation was carried out with 193 nm radiation, from an ArF excimer laser, at a fluence of 1.5 Jcm^{-2} and the plume expanded into vacuum (6×10^{-6} mbar Ar). The spectra are integrated over the plume duration.

Excitation temperatures were estimated using equation 3.1 and the peak heights of the 610.3, 460.2 and 413.2 nm lines (latter two lines not shown) in collaboration with F.J. Gordillo-Vazquez at Madrid. This is plotted as a function of distance in figure 5.25, where the error bars are estimated at $\pm 10\%$. Again, similar to the Ga, GaN and pure lithium cases, the levels corresponding to these lines are probably in partial LTE.

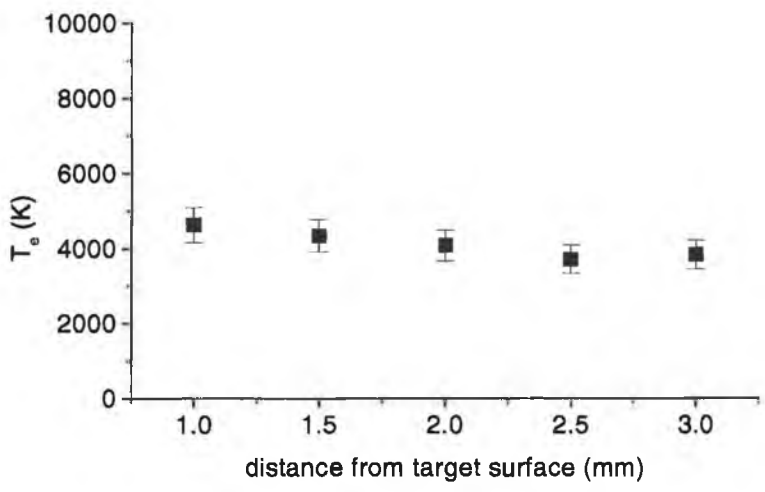

Figure 5.25: T_{exc} from lithium emission spectrum obtained from ablation of LiF, 10^{-5} mbar N_2, 1.5 Jcm^{-2}, $\lambda_{Laser} = 193$ nm.

Using equation 2.46 in the case of the 610.3 nm line, together with the instrument function width, the electron density, N_e, was calculated, in collaboration with F.J. Gordillo-Vazquez, and is plotted in figure 5.26 as a function of distance above target. Bekefi [85] suggests that the errors in these type of measurements are in the 20-30% range, and so we have given an error bar of 30%, accordingly.

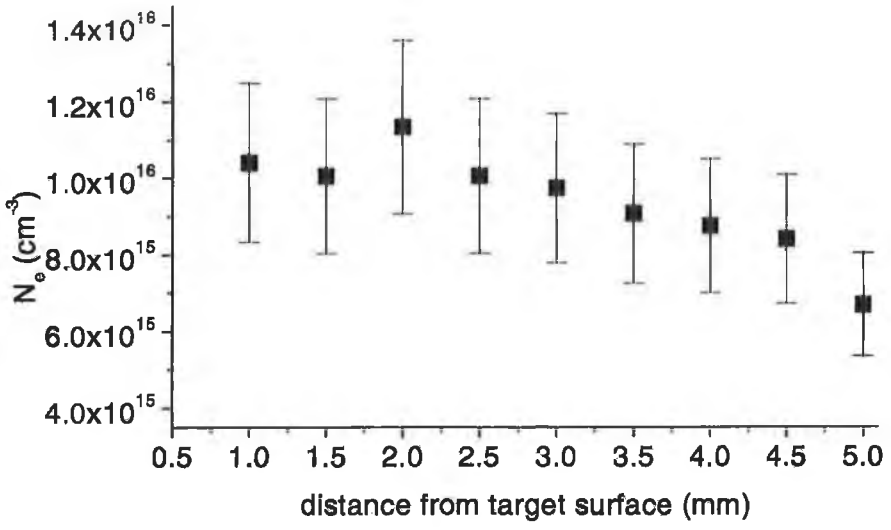

Figure 5.26: N_e from lithium emission spectrum obtained from ablation of LiF, 10^{-5} mbar N_2, 1.5 Jcm^{-2}, $\lambda_{Laser} = 193$ nm.

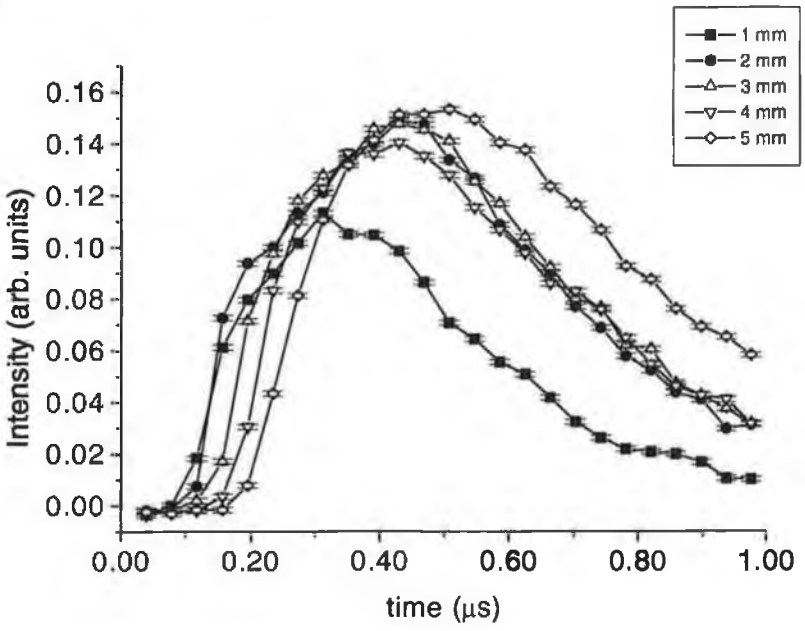

Figure 5.27: LiF plume time-of-flight for various distances above target, 10^{-5} mbar N_2, 1.5 Jcm^{-2}, $\lambda_{Laser} = 193$ nm.

Monochromator traces were recorded by setting the wavelength at the centre of the 610.3 nm line and recording the emission intensity as a function of time at various heights above the target (see section 3.2.3).

These time-of-flight curves are plotted in figure 5.27. From these transients one obtains velocities of 5×10^6 cms^{-1} and 3×10^6 cms^{-1} for the leading edge and transient peak, respectively (figures 5.29 and 5.29).

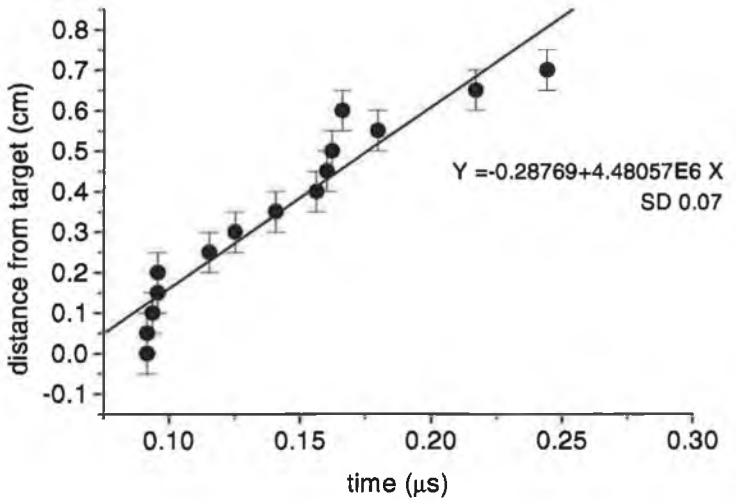

Figure 5.28: Expansion of LiF plume luminous edge, 10^{-5} mbar N_2, 1.5 Jcm^{-2}, λ_{Laser} = 193 nm.

Fitting shifted centre of mass Maxwell-Boltzmann velocity distribution, equation 2.19, to these curves yields average values of 7 eV for T_K and -2×10^6 cms^{-1} for u_k.

All the spectra recorded contained just four lithium lines (670.8, 610.3, 460.2 and 413.2 nm) and no emission lines from flourine despite quite a number of lines in the range 4000Å to 8500Å listed in atomic databases [73]. This is a similar situation to that of the absence of atomic nitrogen from the GaN ablation plumes of chapter 4.

From [73] it can be seen that all of the flourine excited states that would pro-

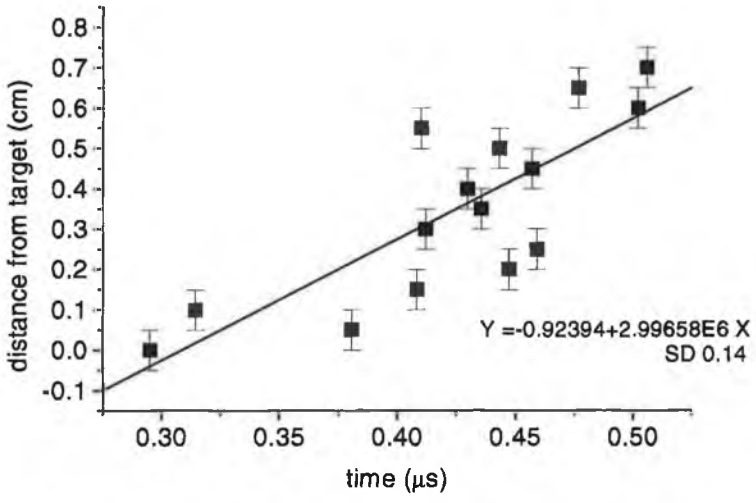

Figure 5.29: Expansion of LiF plume luminous peak, 10^{-5} mbar N_2, 1.5 Jcm^{-2}, λ_{Laser} = 193 nm.

duce lines in the region of interest have very high excitation potentials. Therefore, at this low fluence, it is possible that the LiF plume was not at a high enough excitation temperature (less than $\frac{1}{2}$ eV from figure 5.25) to excite the flourine out of its ground state excited level, and, so, flourine emission would not be observed. Also, as in the case of nitrogen, the radiation transitions probabilities are very small [73] in F, suggesting weak emission line intensities.

From previous discussions on the influence of the laser wavelength (sections 2.1.1, 4.1.1 and 5.1.1), we note that the inverse bremsstrahlung absorption coefficient is low for 193 nm laser radiation (figure 2.1) and thus little excitation of the plume via Inverse Bremsstrahlung would take place. This is supported by the value of the excitation temperature of less than $\frac{1}{2}$ eV from figure 5.25, whereas $T_K = 7$ eV represents the average kinetic energy of expansion. However, this value of T_K should be considered with caution as u_k comes out of the numerical fit with a negative sign suggesting that the shifted centre of mass Maxwell-Boltzmann velocity distribution may not be a good description.

5.2 Digital frame photography

The temporal and spatial evolution of lithium plumes expanding into vacuum (5×10^{-6} mbar N_2) were recorded for three harmonics of the Nd:YAG laser (266, 355 and 1064 nm) and various ablation spot sizes and fluences, see table 5.2.

The images were recorded either unfiltered or through interference filters for the 610.4 and 670.8 nm lines using the setup described in section 3.3.

λ (nm)	spot dimension	Fluence (Jcm^{-2})
266	$115 \times 80 \pm 15$ μm	2.2
532	$115 \times 80 \pm 15$ μm	4.4
1064	$115 \times 80 \pm 15$ μm	6.5
1064	$340 \times 250 \pm 15$ μm	6.5
1064	$590 \times 525 \pm 15$ μm	6.5
1064	$1 \times 1 \pm 0.015$ mm	6.5
1064	$2 \times 2 \pm 0.015$ mm	6.5

Table 5.2: ICCD imaging conditions.

5.2.1 The expansion of the lithium plume

Spatial profiles were extracted from unfiltered images the along the expansion axis of the plumes. Typical profiles are displayed in figure 5.30. From these profiles the luminous edge position was obtained. This is plotted as a function of time, together with the luminous peak position (centre of luminosity, COL) in figures 5.31, 5.32 and 5.33 for the 115×80 μm spotsize at 1064 nm, 532 nm and 266 nm.

Figures 5.34, 5.35, 5.36 and 5.37 plot the larger spotsize, 340×250 μm, 590×525 μm, 1×1 mm and 2×2 mm) cases at constant fluence (6.5 Jcm^{-2}). The resulting velocities are given in table 5.3 for these cases.

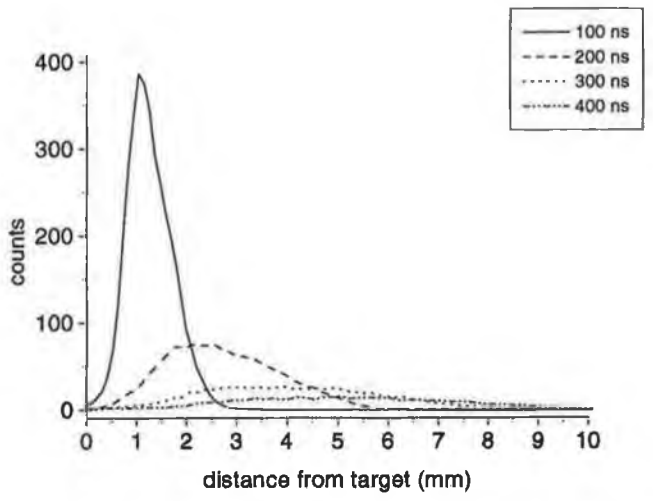

Figure 5.30: Spatial profiles of Li plume expansion (unfiltered), 115×80 μm spot, λ_{Laser} = 1064 nm, fluence = 6.5 Jcm^{-2}.

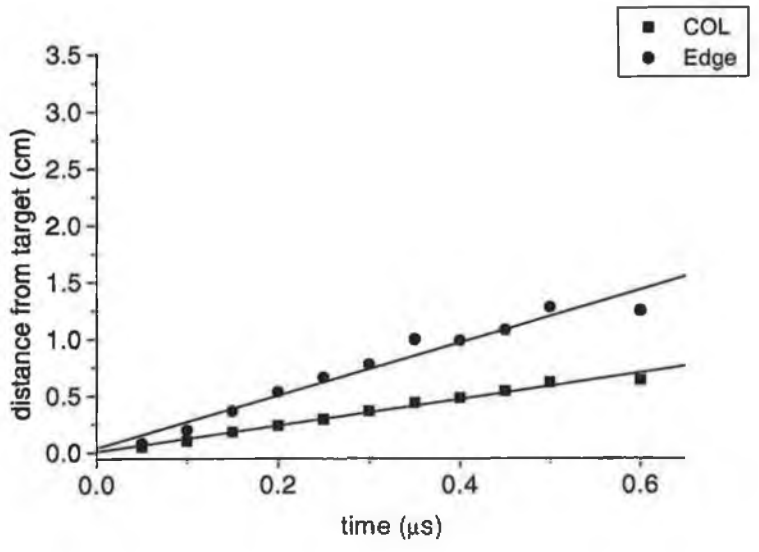

Figure 5.31: Li plume expansion (unfiltered), λ_{Laser} = 1064 nm, 115×80 μm spot, 6.5 Jcm^{-2}.

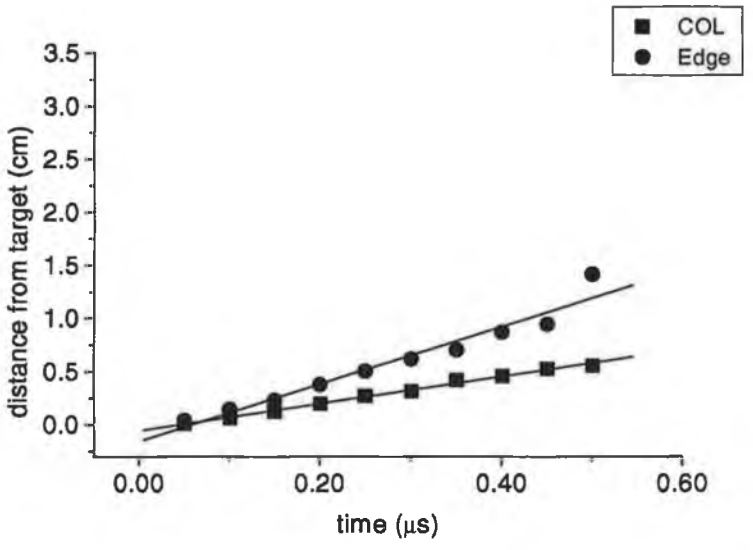

Figure 5.32: Li plume expansion (unfiltered), λ_{Laser} = 532 nm, 115 × 80 μm spot, 4.4 Jcm^{-2}.

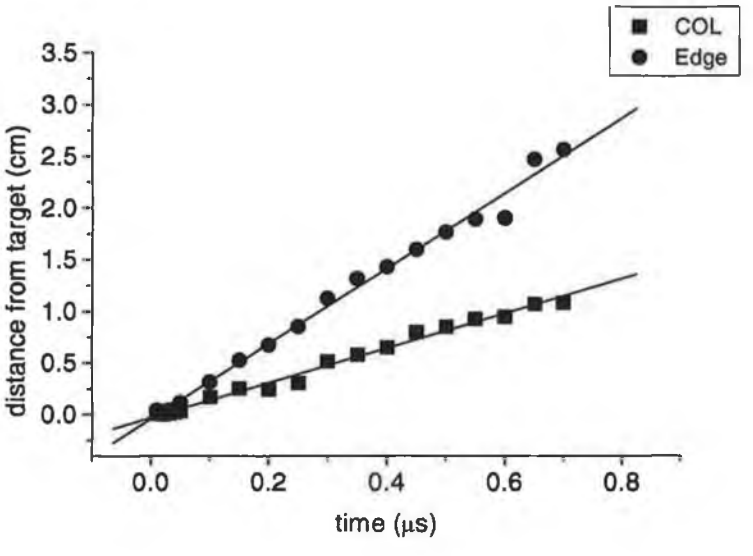

Figure 5.33: Li plume expansion (unfiltered), λ_{Laser} = 266 nm, 115 × 80 μm spot, 2.2 Jcm^{-2}.

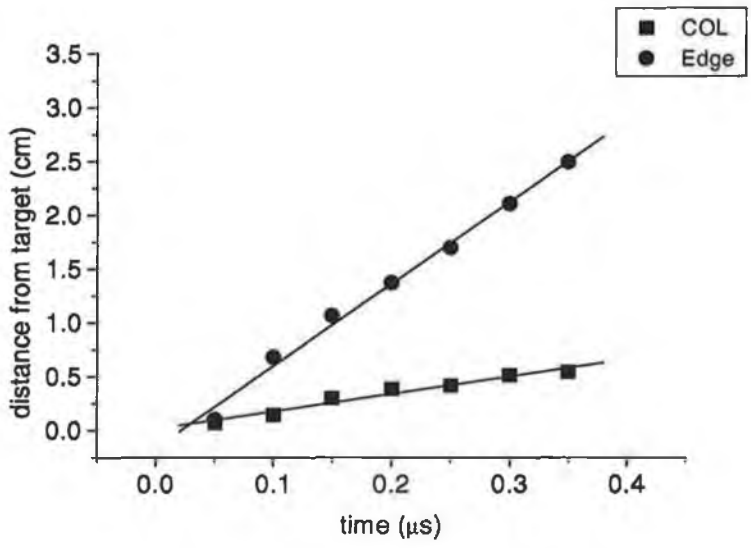

Figure 5.34: Li plume expansion (unfiltered), $\lambda_{Laser} = 1064$ nm, 340 × 250 μm spot, 6.5 Jcm^{-2}.

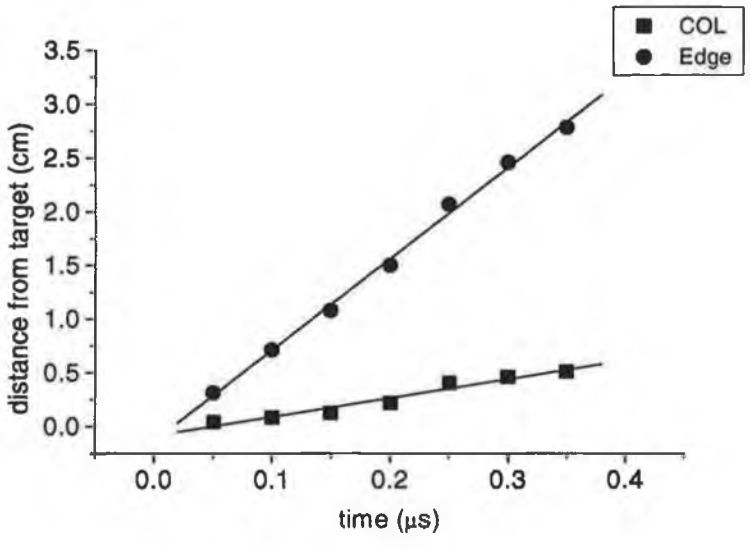

Figure 5.35: Li plume expansion (unfiltered), $\lambda_{Laser} = 1064$ nm, 590 × 525 μm spot, 6.5 Jcm^{-2}.

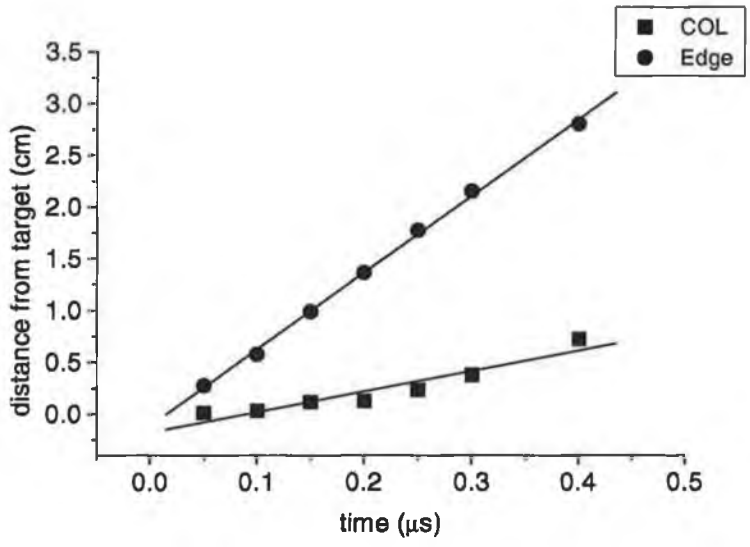

Figure 5.36: Li plume expansion (unfiltered), λ_{Laser} = 1064 nm, 1 × 1 mm spot, 6.5 Jcm^{-2}.

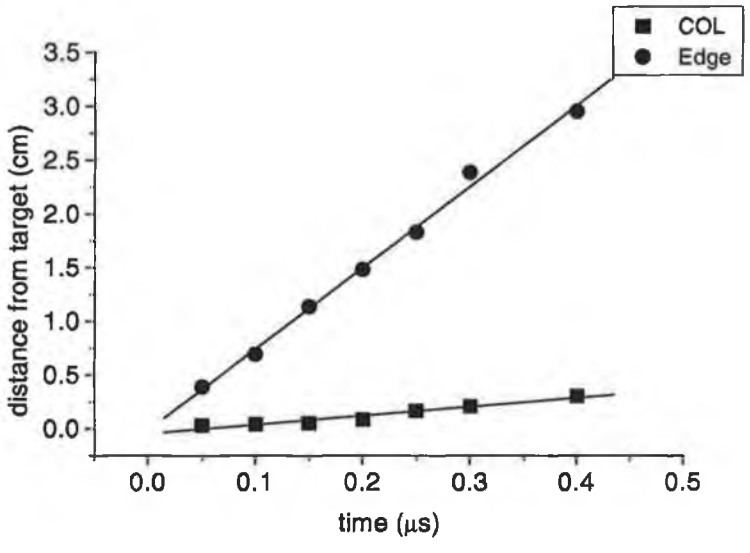

Figure 5.37: Li plume expansion (unfiltered), λ_{Laser} = 1064 nm, 2 × 2 mm spot, 6.5 Jcm^{-2}.

λ (nm)	spot dimension	ν_{edge} (cms^{-1})	ν_{COL} (cms^{-1})
266	$115 \times 80 \pm 15$ μm	3.6×10^6	1.7×10^6
532	$115 \times 80 \pm 15$ μm	2.7×10^6	1.3×10^6
1064	$115 \times 80 \pm 15$ μm	2.3×10^6	1.2×10^6
1064	$340 \times 250 \pm 15$ μm	7.6×10^6	1.6×10^6
1064	$590 \times 525 \pm 15$ μm	8.5×10^6	1.8×10^6
1064	$1 \times 1 \pm 0.015$ mm	7.4×10^6	2.0×10^6
1064	$2 \times 2 \pm 0.015$ mm	7.6×10^6	0.8×10^6

Table 5.3: Lithium plume velocities (white light).

Spatial profiles were also extracted for the images images recorded with the interference filters. The resulting luminous edge and peak positions (centre of luminosity, COL) are plotted as a function of time, in figures 5.38, 5.40 and 5.42 for the 115×80 μm spotsize at 1064 nm, 532 nm and 266 nm using the 610.3 nm filter. The luminous edge and peak positions (centre of luminosity, COL) are plotted for the 670.8 nm filter in figures 5.39, 5.41 and 5.43 for the 115×80 μm spotsize at 1064 nm, 532 nm and 266 nm using the 610.3 nm filter. The resulting velocities are given in tables 5.4 for the 610.3 nm line and 5.5 for the 670.8 nm line.

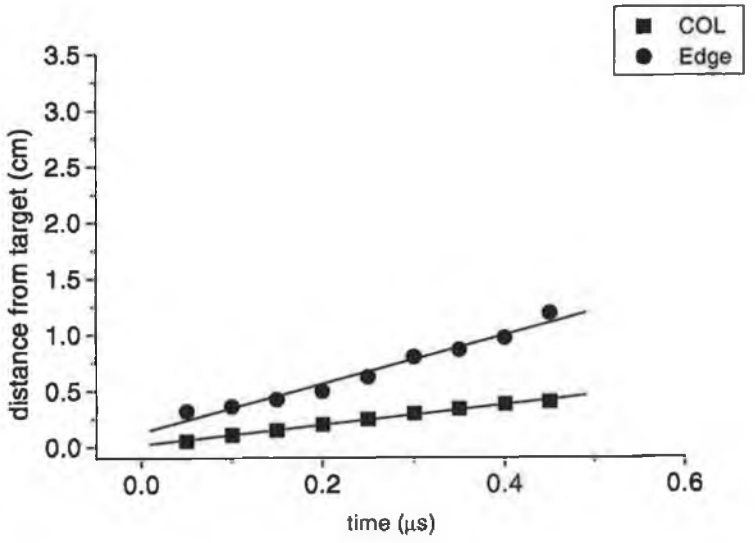

Figure 5.38: Li plume expansion, 610.3 nm line, $\lambda_{Laser} = 1064$ nm, 115×80 μm spot, 6.5 Jcm^{-2}.

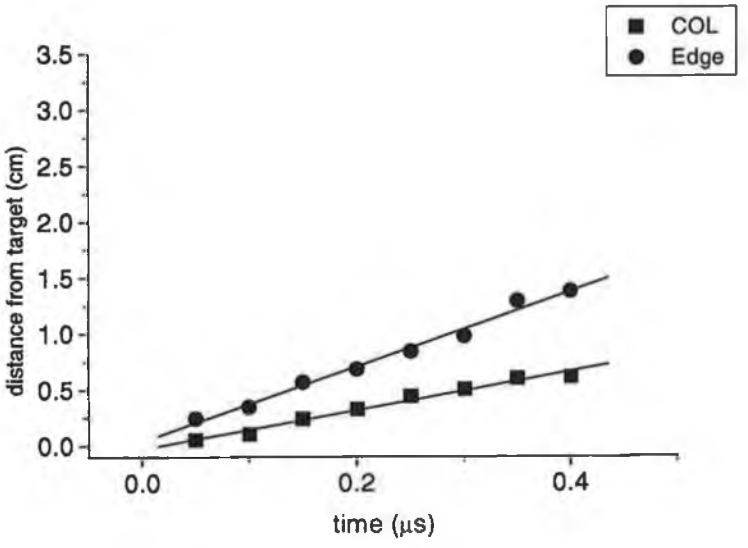

Figure 5.39: Li plume expansion, 670 nm line, $\lambda_{Laser} = 1064$ nm, 115×80 μm spot, 6.5 Jcm^{-2}.

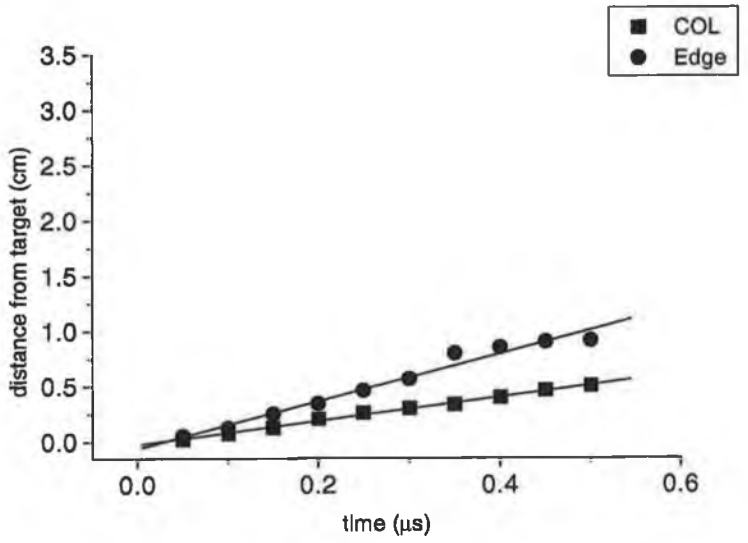

Figure 5.40: Li plume expansion, 610.3 nm line, $\lambda_{Laser} = 532$ nm, 115×80 μm spot, 4.4 Jcm^{-2}.

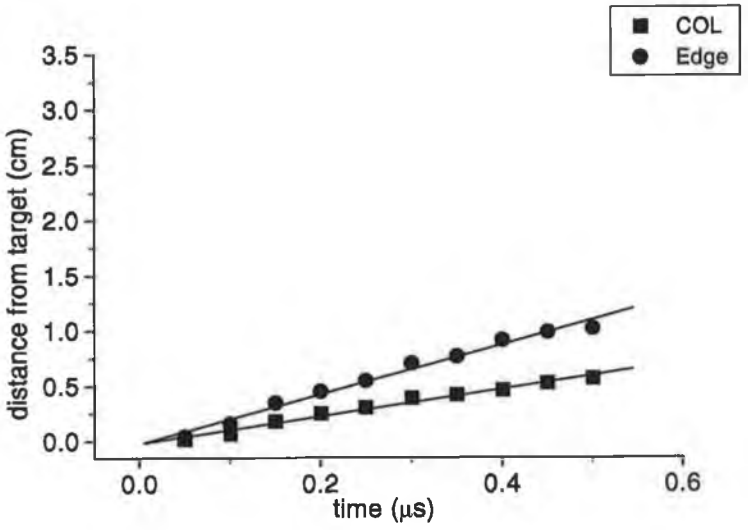

Figure 5.41: Li plume expansion, 670 nm line, $\lambda_{Laser} = 532$ nm, 115×80 μm spot, 4.4 Jcm^{-2}.

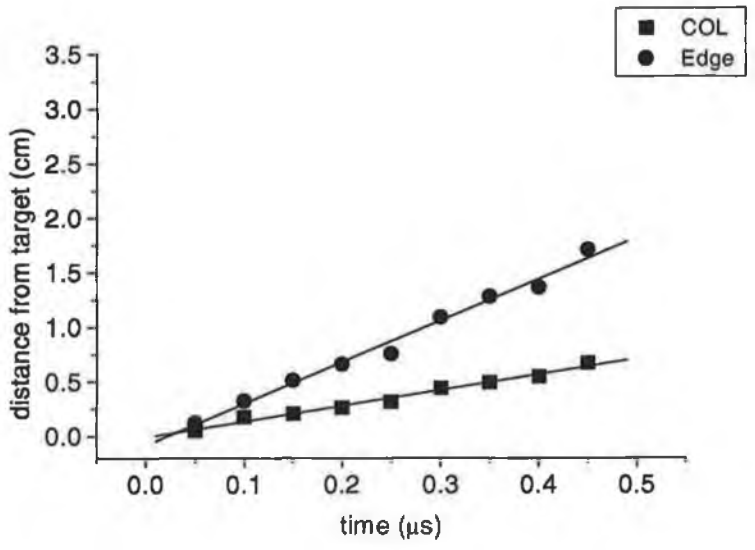

Figure 5.42: Li plume expansion, 610.3 nm line, $\lambda_{Laser} = 266$ nm, 115 × 80 μm spot, 2.2 Jcm^{-2}.

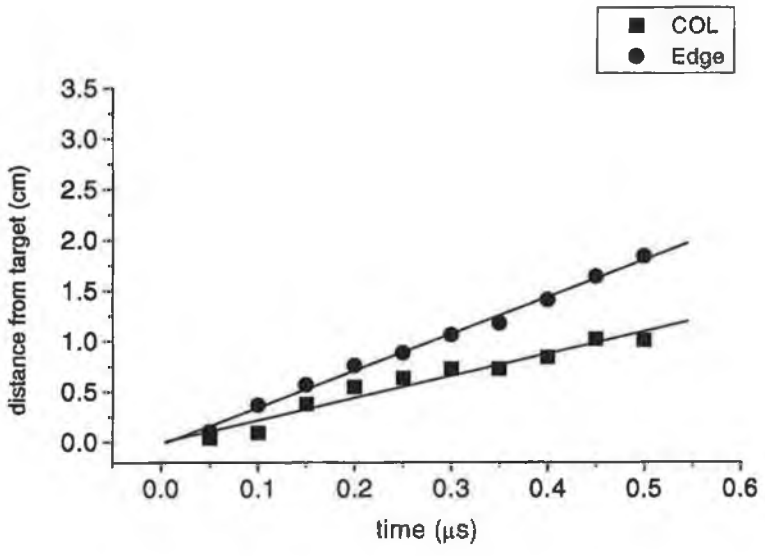

Figure 5.43: Li plume expansion, 670 nm line, $\lambda_{Laser} = 266$ nm, 115 × 80 μm spot, 2.2 Jcm^{-2}.

λ (nm)	ν_{edge} (cms^{-1})	ν_{COL} (cms^{-1})
266	3.7×10^6	1.4×10^6
532	2.1×10^6	1.1×10^6
1064	2.2×10^6	0.9×10^6

Table 5.4: Lithium plume velocities at 610.3 nm.

λ (nm)	ν_{edge} (cms^{-1})	ν_{COL} (cms^{-1})
266	3.7×10^6	2.2×10^6
532	2.3×10^6	1.2×10^6
1064	3.3×10^6	1.7×10^6

Table 5.5: Lithium plume velocities at 670.8 nm.

The general pattern is that the plume created with 266 nm laser radiation travels faster than that created with 532 nm radiation, which is, in turn, faster than the 1064 nm case at a constant spot size. This suggests that more laser energy is absorbed initially with 266 nm laser radiation (shorter skin depth implies higher absorption) and this drives a faster expansion than at longer wavelengths.

The inverse bremsstrahlung absorption coefficient may also, simultaneously, play a role. The laser radiation at 1064 nm is absorbed more strongly by the plume, and thus contributes less to driving the expansion than in the shorter wavelength cases. Instead it goes into plume excitation, which manifests itself in the plume emission as discussed previously. At shorter laser wavelengths the radiation propogates through to the target and ablates a plume that has more mass and momentum, but less excitation.

The velocities listed in tables 5.4, for the 610.3 nm line, and 5.5, for the 670.8 nm line, suggest that the plume velocity is largely independent of the wavelength of emission from the plume. This suggests that the same atomic kinetics applies throughout the plume and it justifies an approach in which the hydrodynamics can be evaluated first (for example to provide densities), with the atomic kinetics

calculated from the resulting parameters.

5.2.2 The dynamics of the Lithium plume

The variation of intensity as a function of time at fixed distances above the target surface was extracted from unfiltered lithium ICCD images. In figures 5.44, 5.45, 5.46, 5.47, 5.48, 5.49 and 5.50 the TOF curves are plotted for all cases (table 5.2). One observes that the intensity and width of the time-of-flight curves increases with spot size (from a width of $\sim$ 150 ns to $\sim$ 300 ns), as previously seen in the spectra.

The shifted centre of mass Maxwell-Boltzmann distribution of equation 3.9 was fitted to the data and gave the average temperatures and average velocities listed in table 5.6.

λ (nm)	spot dimension	T_K (eV)	u_K (cms^{-1})
266	$115 \times 80 \pm 15$ μm	3.5	4.4×10^5
532	$115 \times 80 \pm 15$ μm	3.2	5.5×10^5
1064	$115 \times 80 \pm 15$ μm	3.3	5.5×10^5
1064	$340 \times 250 \pm 15$ μm	98	-1.0×10^7
1064	$590 \times 525 \pm 15$ μm	340	-2.3×10^7
1064	$1 \times 1 \pm 0.015$ mm	71	-8.9×10^6
1064	$2 \times 2 \pm 0.015$ mm	-48	1.0×10^7

Table 5.6: Lithium plume shifted centre of mass Maxwell-Boltzmann temperatures and velocities.

Comparing table 5.6 with tables 5.3, 5.4 and 5.5, the fit appears to be much better for the 115×80 μm spotsize than the larger spotsize cases, with the plume centre-of-mass travelling at speed comparable to the centre-of-luminosity and with temperatures a few times greater than the corresponding excitation temperature values.

Since the laser intensity has a gaussian profile so too has the spot on target. The initial plume would then have a distribution of expansion-driving tempera-

tures with this profile. However, as the spotsize is reduced considerably this initial plume becomes smaller and more point-like and the profile more "top-hat". The adiabatic expansion of an isothermal plume [28] would then describe the plume behaviour. Conversely, at larger spotsizes, this laser profile leads to distribution of expansion-driving temperatures, as opposed to a single value, and the plume behaviour would be better described by the isentropic model of [29]. This is confirmed by Stapleton [86] in computer simulations of lithium plumes.

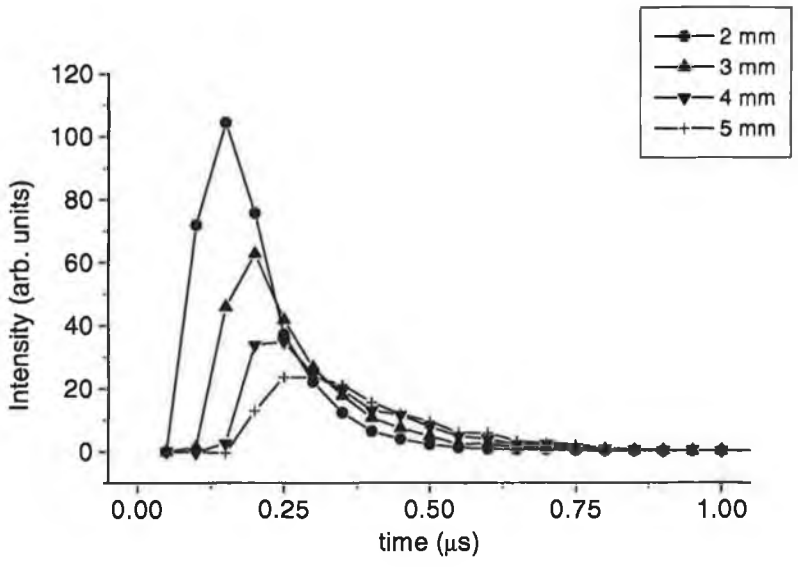

Figure 5.44: Li plume time-of-flight for various distances above target, 115 x 80 μm spot, λ_{Laser} = 1064 nm, 6.5 Jcm^{-2}.

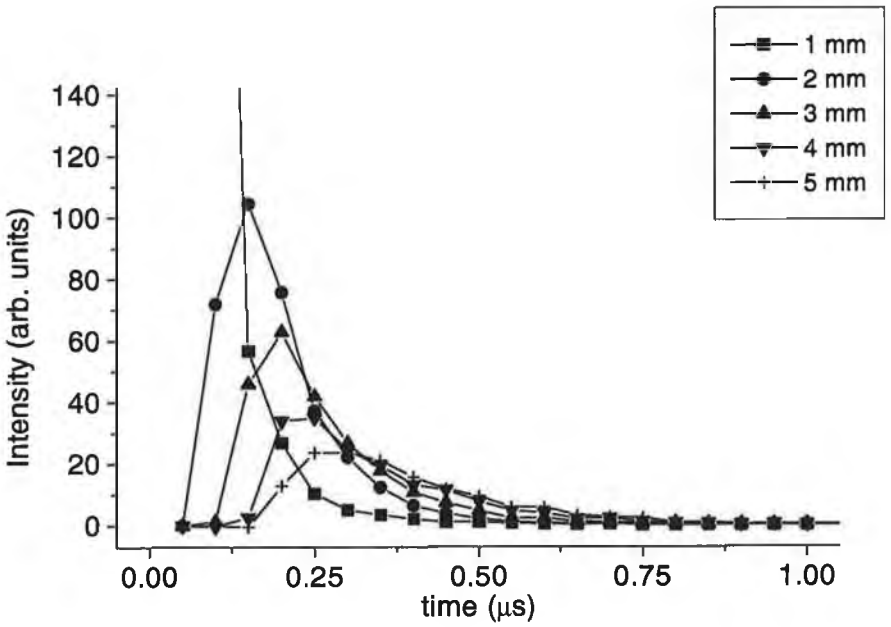

Figure 5.45: Li plume time-of-flight for various distances above target, 115 × 80 μm spot, λ_{Laser} = 532 nm, 4.4 Jcm^{-2}.

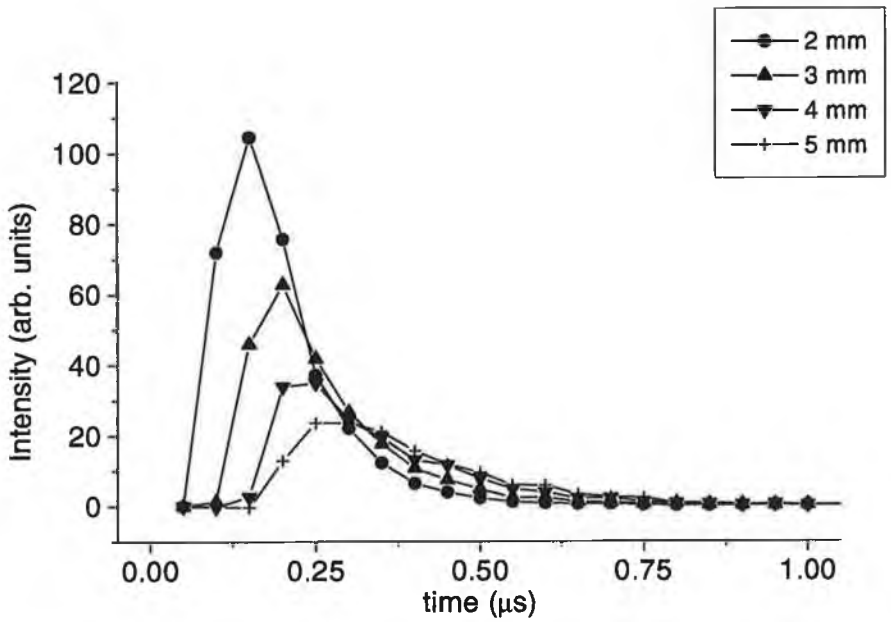

Figure 5.46: Li plume time-of-flight for various distances above target, 115 × 80 μm spot, λ_{Laser} = 266 nm, 2.2 Jcm^{-2}.

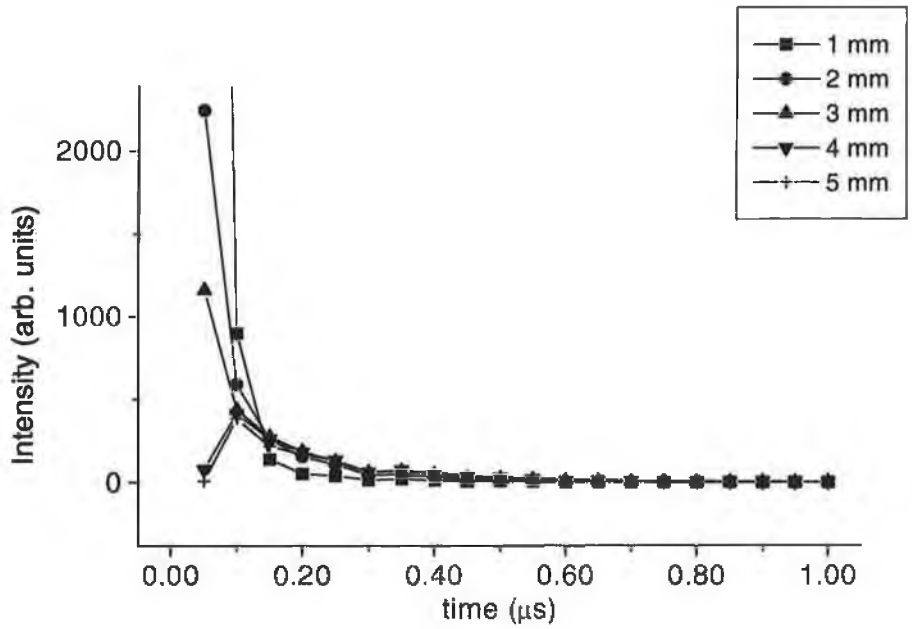

Figure 5.47: Li plume time-of-flight for various distances above target, 340×250 μm spot, $\lambda_{Laser} = 1064$ nm, 6.5 Jcm^{-2}.

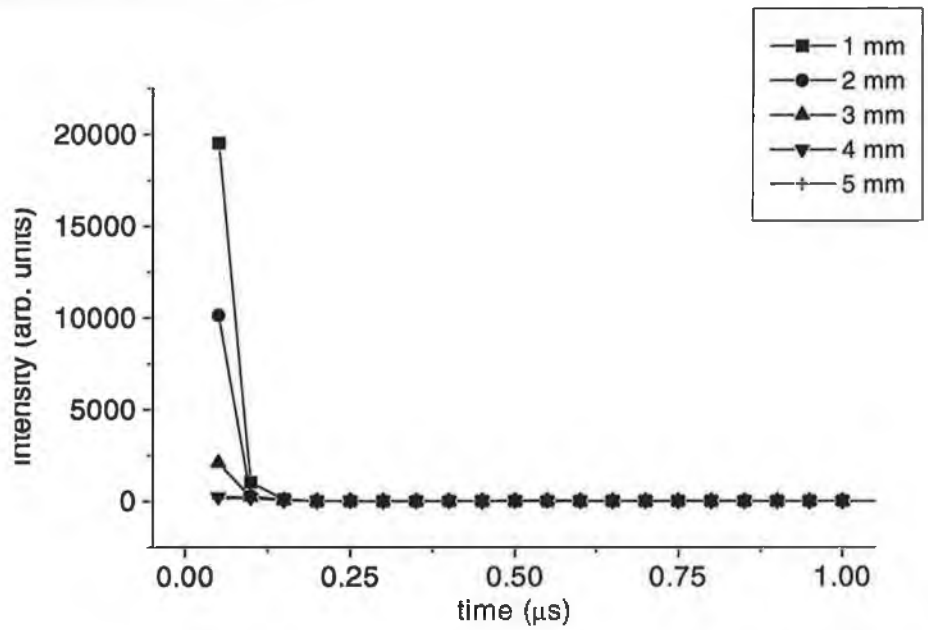

Figure 5.48: Li plume time-of-flight for various distances above target, 590×525 μm spot, $\lambda_{Laser} = 1064$ nm, 6.5 Jcm^{-2}.

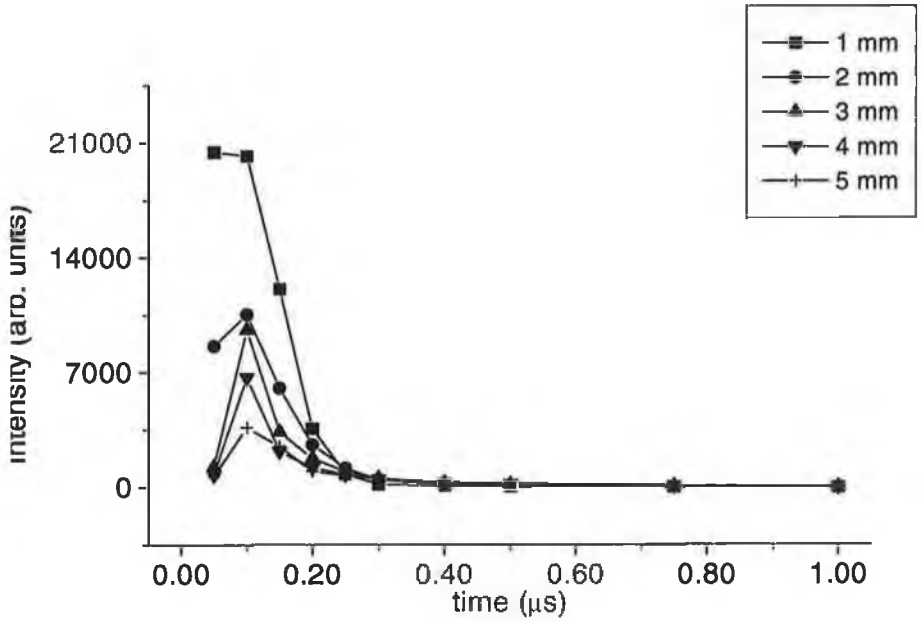

Figure 5.49: Li plume time-of-flight for various distances above target, 1 × 1 mm spot, λ_{Laser} = 1064 nm, 6.5 Jcm^{-2}.

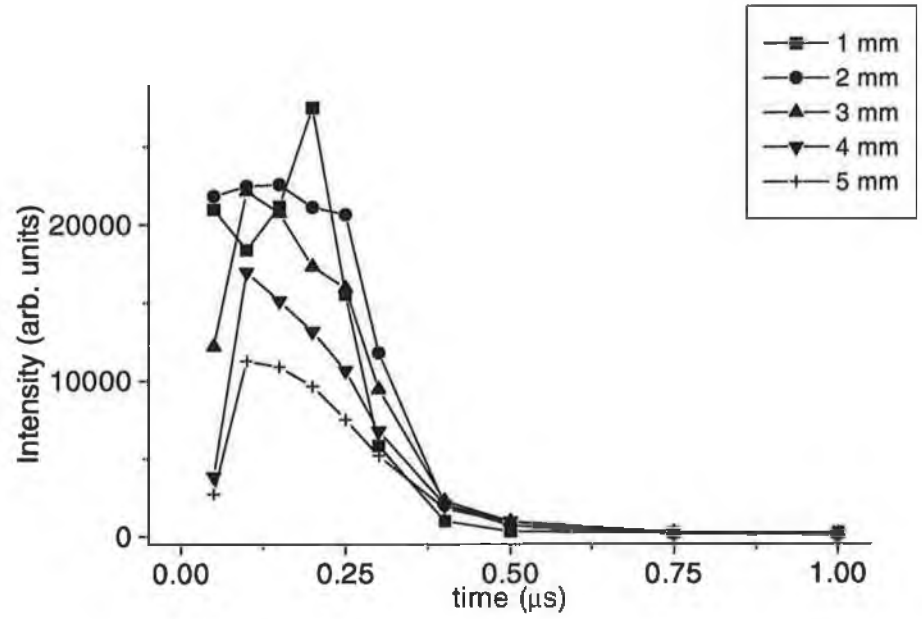

Figure 5.50: Li plume time-of-flight for various distances above target, 2 × 2 mm spot, λ_{Laser} = 1064 nm, 6.5 Jcm^{-2}.

5.3 Anomalous line intensity ratio in Li spectra

From the table of lithium lines and energy levels (5.1) one expects, in Maxwell-Boltzmann equilibrium, that the 670.8 nm line ($1s^2 2p$-$1s^2 2s$), which is the resonance line, would be the more intense emission line in comparison to the 610.3 nm line ($1s^2 3d$-$1s^2 2p$). However, it is clear from figures 5.1, 5.2 , 5.3, 5.4, 5.5 and 5.6 , in various experimental conditions, that this is only the case at large distances above the target surface.

We also observed this effect in 193 nm ablation of LiF (see figure 5.24). Figures 5.51, 5.52, 5.53, 5.54, 5.55 and 5.56 show the integrated intensities of the two lines as a function of distance above target surface.

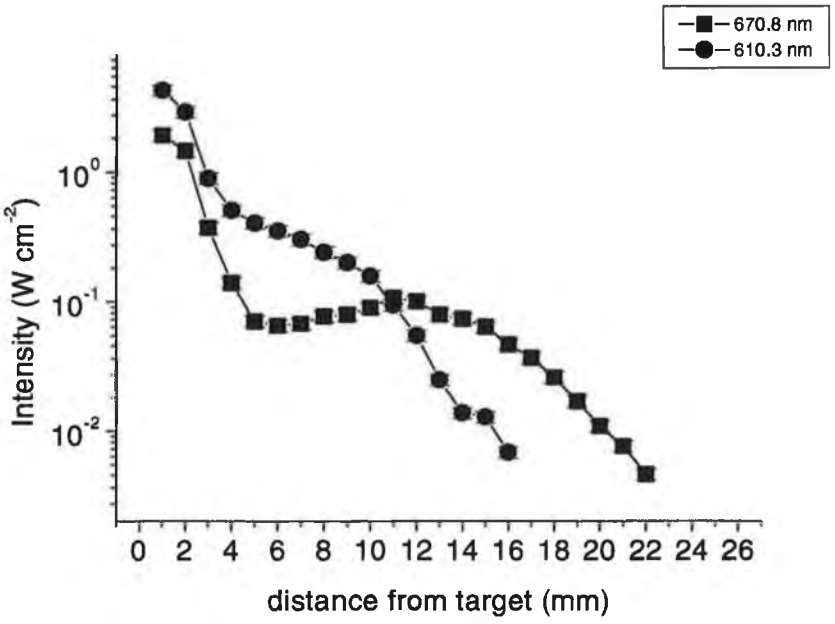

Figure 5.51: Integrated intensities of 610.3 nm and 670.8 nm lines, 115 × 80 μm spot, λ_{Laser} = 1064 nm, 6.5 Jcm^{-2} .

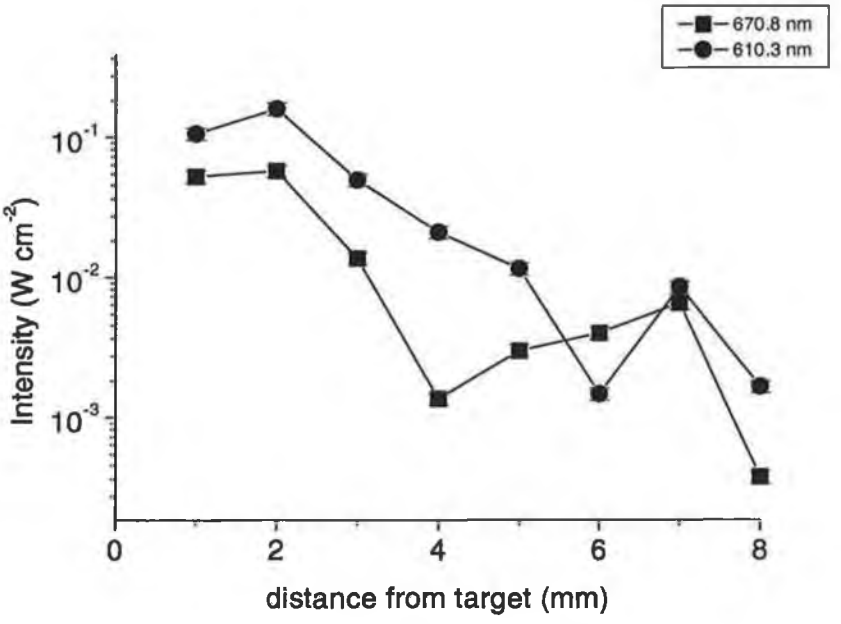

Figure 5.52: Integrated intensities of 610.3 nm and 670.8 nm lines, 115 × 80 μm spot, λ_{Laser} = 532 nm, 4.4 Jcm^{-2} .

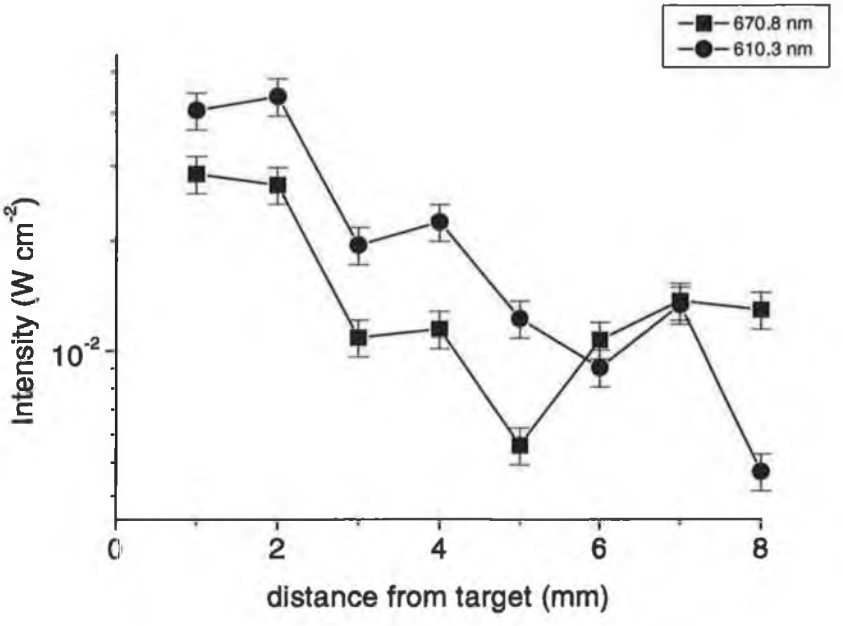

Figure 5.53: Integrated intensities of 610.3 nm and 670.8 nm lines, 115 × 80 μm spot, λ_{Laser} = 266 nm, 2.2 Jcm^{-2}.

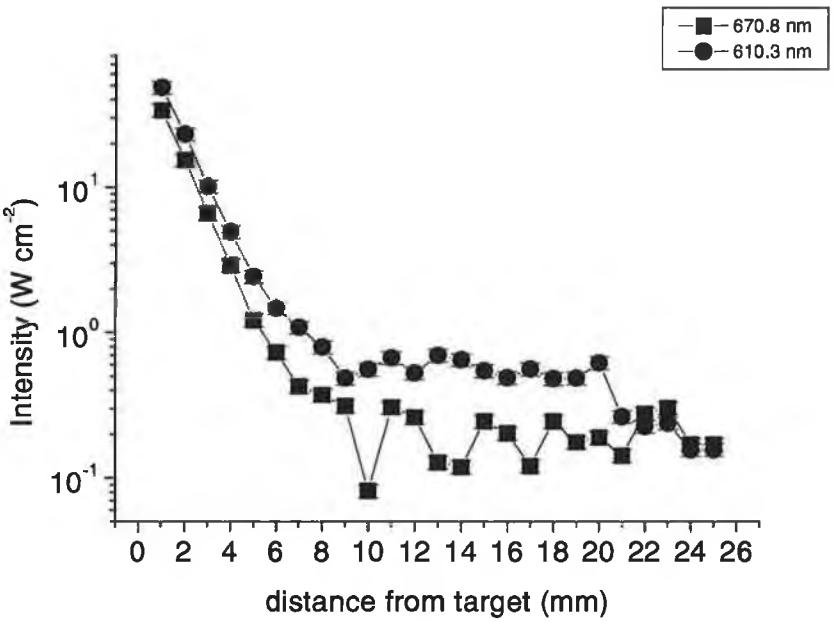

Figure 5.54: Integrated intensities of 610.3 nm and 670.8 nm lines, 10 Jcm^{-2}, λ_{Laser} = 1064 nm, 2000 × 2000 μm spot.

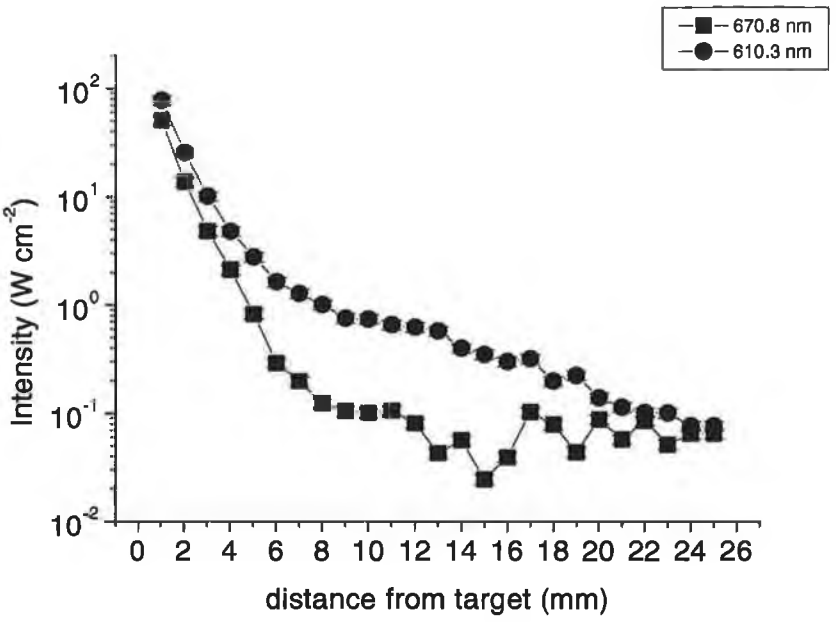

Figure 5.55: Integrated intensities of 610.3 nm and 670.8 nm lines, 1 Jcm^{-2}, λ_{Laser} = 1064 nm, 2000 × 2000 μm spot.

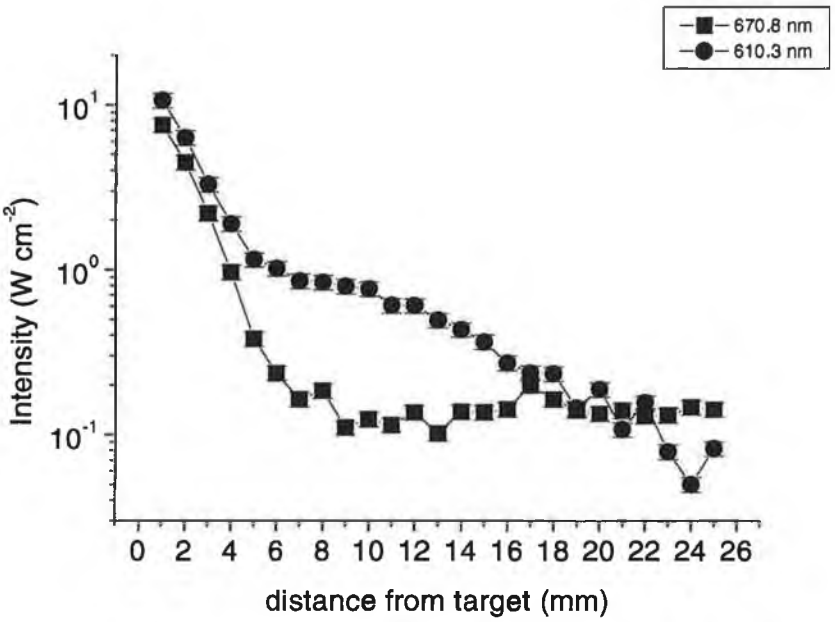

Figure 5.56: Integrated intensities of 610.3 nm and 670.8 nm lines, 10 Jcm^{-2}, $\lambda_{Laser} = 532$ nm, 2000 × 2000 μm spot.

One observes, in figures 5.51, 5.52, 5.53, 5.54, 5.55 and 5.56 that the 610.3 nm line intensity is greater than that of the 670.8 nm line for a certain distance above target (depending on laser wavelength, fluence and spotsize) before reverting to the situation where the 670.8 nm is most intense.

Henley et al [58] observed this intensity reversal in LiF plumes using 193 nm ArF laser radiation at 6 Jcm^{-2}, while Sherrill et al [60, 61] have observed the effect in plumes of LiAg ablated with 1064 nm laser at 1 Jcm^{-2}.

Sherrill [60, 61] observes that the 670.8 nm line is more intense than the 610.3 at 50 ns after the laser pulse, but the 610.3 nm line is more intense at 75 ns. This is observable in the time domain, for our conditions, in figures 5.57, 5.58 and 5.59 where the ratio of the intensities of images (corrected for transmission) recorded with the tuned interference filters are plotted. It is observed that the inversion ratio is large and lasts for most of the plume duration close to the target while at greater distances the ratio is reduced but still long lasting. This suggests

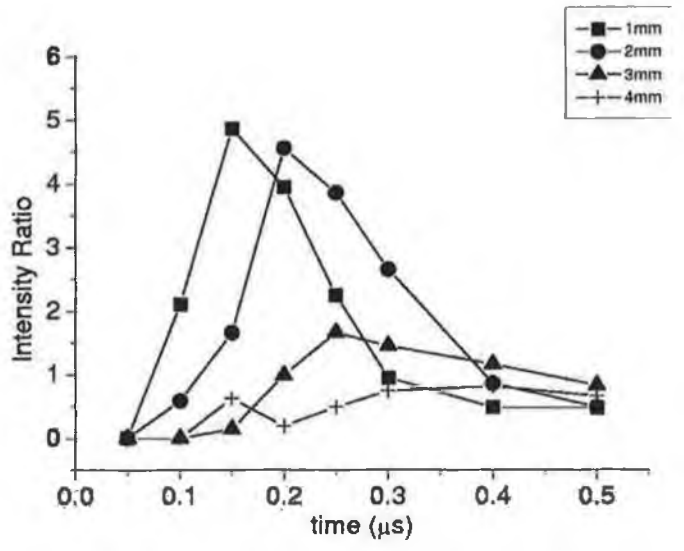

Figure 5.57: Ratio of 610.3 nm line to 670.8 nm line vs time at various disatances above target, $\lambda_{Laser} = 1064$ nm, 115×80 μm spot, 6.5 Jcm^{-2}.

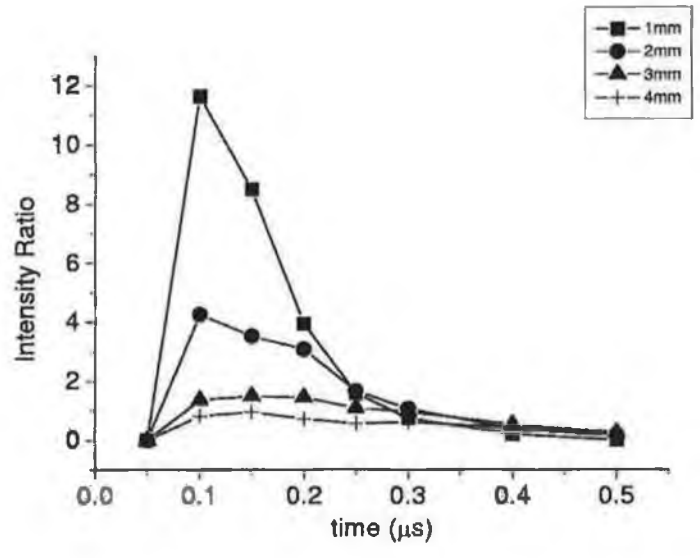

Figure 5.58: Ratio of 610.3 nm line to 670.8 nm line vs time at various disatances above target, $\lambda_{Laser} = 532$ nm, 115×80 μm spot, 4.4 Jcm^{-2}.

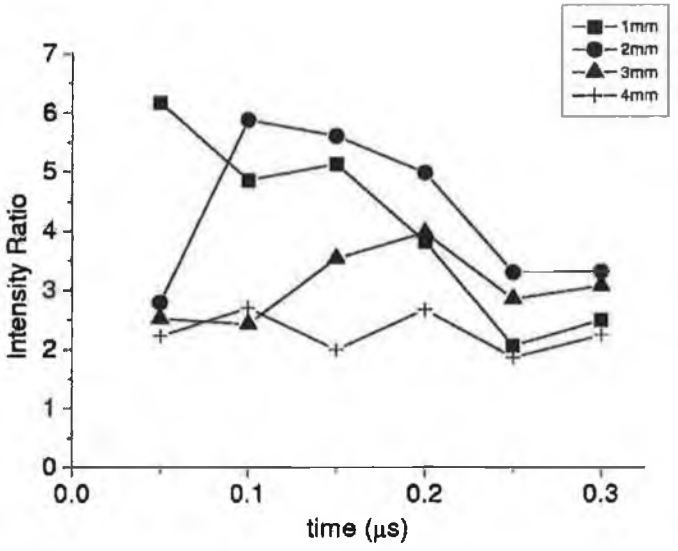

Figure 5.59: Ratio of 610.3 nm line to 670.8 nm line vs time at various disatances above target, $\lambda_{Laser} = 266$ nm, 115×80 μm spot, 2.2 Jcm^{-2}.

that the level populations are not in a Boltzmann equilibrium (see sections 5.1.2 and 5.1.3) and that eventually all levels decay to the $1s^2 2s$ ground level via the 670.8 nm line.

Sherrill et al [60, 61] suggest that time-dependent effects on the atomic kinetics of the plasma plume are important. In this case electron-ion recombination takes place much slower than if the atomic kinetics were in steady-state (in steady-state conditions equilibria are quickly restored).

Henley et al [58] suggest that the effect is due to self-absorption in the 670.8 nm line, since this line has a very high f value and terminates on the ground state. The significant concentration of ground state lithium atoms will absorb some of the 670.8 nm radiation before it escapes from the plume.

Modelling by [86], in the same conditions as our experiments, suggests that the effect is neither opacity nor time-dependent atomic kinetics, but in the rate coefficients for the levels involved, in steady-state conditions.

Chapter 6

Conclusions

GaN nitride is a key material for semiconductor technology due to its wide bandgap and it has been successfully grown by many authors using the technique of Pulsed Laser Deposition (PLD). This has been achieved under a wide range of experimental conditions such as laser wavelength (from 193 nm to 1064nm), background gas pressures (from $\sim 1\times^{-10}$ mbar to ~ 4 mbar of N_2) and target material (Ga metal or pressed GaN powder). Lithium-based compounds, such as $LiNbO_3$ and LiF, are also of interest in optoelectronics. A literature review was carried out and revealed a dearth of spectroscopic studies relating to laser ablation of Ga, GaN, Li and LiF in the Pulsed Laser Deposition regime. Thus, the design and implementation of a Pulsed Laser Deposition diagnostic system was carried out.

Emission spectra of Ga and GaN ablation plumes, in typical PLD conditions, were obtained with this system and presented as a function of N_2 ambient gas pressure from 1×10^{-7} to 5 mbar and ablation laser wavelengths of 266, 355, 532 and 1064 nm . Atomic level populations and excitation temperatures were estimated from these spectra. A series of temporally resolved images of the luminous plume expanding into N_2 pressures of 1×10^{-5}, 1×10^{-2}, 1×10^{-1}, 1 and 5 mbar were recorded and plume velocities were estimated from these data. Such data are important as they provide a quantitative picture of the plume at the deposition substrate.

The behaviour of plumes of Ga and GaN was found to be not strongly dependent on whether the target was gallium metal or pressed gallium nitride powder. On the other hand, it was found to be strongly dependent on the ablation laser wavelength and the ambient gas pressure. It was observed that shorter laser wavelengths drive faster expansions (higher kinetic energy temperature) whereas the 1064 nm laser always produced spectra 2 or 3 orders of magnitude brighter than those of shorter laser wavelengths (higher excitation of the plume). This can be understood in terms of the greater absorption of the radiation in the target at shorter wavelengths creating higher kinetic energy plumes. In addition, the higher Inverse Bremsstrahlung absorption coefficient at longer wavelengths increases the absorption of the laser in the plume (and the excitation temperature) and also shields the target from the incoming laser radiation. These two processes result in relatively highly excited low velocity plumes with long laser wavelengths and lowly excited fast velocity plumes with shorter laser wavelengths.

The behaviour in a background gas was observed to have two distinct regimes. At low pressures free expansion of the plume took place, while the known phenomenon of plume splitting was observed at pressures higher than 10^{-1} mbar N_2, together with increased emission. The expansion at higher pressures was best described as high-speed drag in which the plume travelled through a gas which was in the continuous flow state. It was postulated that a compression front formed. The increased collisions in this region led to the increased plume emission and provide excited species at the substrate. These results are supported by recent experiments on growth, for example Takahashi et al [87] have grown GaN films on $LiGaO_2$ substrates for the first time, using 248 nm laser radiation at 3 Jcm^{-2} and a N_2 gas pressure of 10^{-1} Torr.

Emission spectra were also presented for Li and LiF plumes expanding into vacuum and the corresponding atomic level populations and excitation temperatures were estimated. Ultrafast images were recorded as a function of laser wavelength (266, 532 and 1064nm) and spotsize (115×80, 340×250, 90×525, 1000×000 and 2000×2000 μm) yielding plume velocities. Again the absorption of the material and plume as a function of wavelength was found to be important

in determining the evolution of the plume. It was found that the plume behaviour could be described using the Knudsen layer shifted Maxwell-Boltzmann velocity distribution and it was suggested that with smaller spotsizes the plume behaviour is more isothermal. An anomalous emission line ratio feature of these spectra was observed and discussed.

This diagnostic system is capable of monitoring the evolution of ablation plumes temporally, spatially and spectrally, and can provide valuable information on the PLD technique. Some improvement, however, could be of benefit. Absorption measurements, particularly using Laser Induced Flourescence, would allow one to probe the non-emitting atomic and molecular species, thus enhancing the knowledge of the growth process. This could be combined with electronic detection on the focal plane of the spectrograph, for example an apparatus consisting of a photodiode array or a ccd array could enhance the excellent spectral and spatial imaging characteristics of this instrument by providing a fast, stable and user-friendly detection setup.

Bibliography

[1] S. Nakamura. Light emission moves into the blue. *Physics World*, 11(2):31, 1998.

[2] S. Nakamura et al. *Jpn. J. Appl. Phys.*, 34(10B):L1332–L1335, 1995.

[3] L.F. Eastman and U.K. Mishra. *IEEE Spectrum Online*, 2002. http://www.spectrum.ieee.org/WEBONLY/publicfeature/may02/gani.htm.

[4] S.J. Pearton et al. *Materials Today*, June ed.:24–31, 2002.

[5] D.B Chrisey and G.K. Hubler, editors. *Pulsed Laser Deposition of Thin Films*. Wiley, 1994.

[6] M. Allegrini et al. *Appl. Surf. Sci*, 106:438–446, 1996.

[7] R. Zheng et al. *Spectrochimica Acta*, Part B(52):339–352, 1997.

[8] Y. Yamagata et al. *J. Appl. Phys.*, 86:4154, 1999.

[9] A.A. Voevodin et al. *Surface Coatings Tech*, 76-77:670–674, 1995.

[10] Wolfgang Koutek et al. *Appl. Surf. Sci.*, pages 158–165, 1996.

[11] D. Bauerle et al. *Appl. Phys. A*, COLA'99:S45, 1999.

[12] K.W. Mah et al. *J. Crystal Growth*, 222:497–502, 2001.

[13] K.W. Mah et al. *Mat. Sci. and Eng.*, (B82):128–130.

[14] D. O'Mahony et al. *Solid State Elec.*, 47:533–547, 2003.

[15] D. Cole et al. *Mat. Sci. Eng.*, B50:20, 1997.

[16] P.G. Middleton et al. *Mat. Sci. Eng.*, B59:133, 1999.

[17] M. Cazzanelli et al. *Mat. Sci. Eng.*, B59:98–103, 1999.

[18] F.J. Gordillo-Vazquez. *J. Appl. Phys.*, 90(2):599, 2001.

[19] W. Lochte-Holtgreven. *Plasma Diagnostics*. New York: AIP Press, 1995.

[20] Eugene Hecht. *Optics*. Addison-Wesley, 2 edition, 1989.

[21] P.R. Willmott and J.R. Huber. *Rev. Mod. Phys.*, 72(1):315, 2000.

[22] J.F. Ready. *Industrial Applications of Lasers*. Academic Press, 2nd edition, 1997.

[23] N. Bloembergen. Laser ablation: Mechanisms and applications-ii. In J.C Miller and D.B. Goehegan, editors, *AIP Conference Proceedings 288*. New York: AIP Press, 1993.

[24] J.F Ready. *Effects of High-Power Laser Radiation*. Academic Press, 1971.

[25] Francis F. Chen. *Introduction to Plasma Physics and Controlled Fusion*, volume 1. Plenum Press, 2 edition, 1984.

[26] C.R. Phipps and R.W. Dreyfus. *Laser Ionisation Mass Analysis*. Wiley, 1993.

[27] Tudor Wyatt Johnston and John M. Dawson. *The Physics of Fluids*, 16(5):722, 1973.

[28] R.K Singh and J. Narayan. *Physical Review B*, 41(13):8843–8859, 1990.

[29] S.I. Anisimov et al. *Phys. Rev. B*, 48(16):12076, 1993.

[30] David B. Goehegan. *Appl. Phys. Lett.*, 60(22):2732, 1992.

[31] P.E. Dyer and J. Sidhu. *J. Appl. Phys.*, 64(9):4657, 1988.

[32] William Whitty. PhD thesis, Physical Sciences, Dublin City University, 1998.

[33] Roger Kelly and R.W. Dreyfus. *Surf. Sci.*, pages 263–276, 1988.

[34] T.P. Hughes. *Plasmas and laser light*. Hilger, Bristol, 1975.

[35] D. Colombant and G.F. Tonon. *J. Appl. Phys.*, 44(8):3524–3537, 1973.

[36] H.R. Griem. *Plasma Spectroscopy*. McGraw-Hill, New York, 1964.

[37] Peter A. Jansson, editor. *Deconvolution with Applications in Spectroscopy*. Academic Press, 1984.

[38] Wolfgang Demtroder. *Laser Spectroscopy*. Springer, 2 edition, 1996.

[39] R.F. Xiao et al. *Appl. Surf. Sci.*, 127-129:471–476, 1998.

[40] P.R. Willmott et al. *J. Appl. Phys.*, 88:188, 2000.

[41] M. Niehus et al. *Solid State Elec.*, 47:569–573, 2003.

[42] Hiroyuki Takahashi et al. *Thin Solid Films*, 407:114–117, 2002.

[43] X.L. Tong et al. *Appl. Surf. Sci.*, 217:28–33, 2003.

[44] P. Sanguino et al. *Solid State Elec.*, 47:559–563, 2003.

[45] C. Vinegoni et al. *Surf. and Coat. Tech.*, 124:272–277, 2000.

[46] D. Cole et al. *Mat. Sci. Eng.*, B48:239–243, 1997.

[47] Rong-Ping Wang et al. *Opt. Mats.*, 23:15–20, 2003.

[48] J. Ohta et al. *J. Crys. Growth*, 237-239:1153–1157, 2002.

[49] J. Ohta et al. *Appl. Surf. Sci.*, 190:352–355, 2002.

[50] G.S. Sudhir et al. *Appl. Surf. Sci.*, 127-129:471–476, 1998.

[51] S. Ito et al. *Appl. Surf. Sci.*, 197-198:384–386, 2002.

[52] Armelle Basillais et al. *Appl. Surf. Sci.*, 186:416–422, 2002.

[53] T. M. Di Palma et al. *Appl. Surf. Sci.*, 127-129:350–354, 1998.

[54] K.W. Mah et al. *Appl. Surf. Sci.*, 168:158–153, 2000.

[55] K. Mizuno et al. *Appl. Surf. Sci.*, 197-198:490–493, 2002.

[56] R.I. Tomov et al. *Vacuum*, 58:396–403, 2000.

[57] D. Ghica et al. *Appl. Surf. Sci.*, 138-139:617–621, 1999.

[58] S.J. Henley et al. *Appl. Surf. Sci.*, 217:68–77, 2003.

[59] A. Perea et al. *Appl. Surf. Sci.*, 138-139:533–537, 1999.

[60] Manolo E. Sherrill et al. *Rev. Sci. Inst.*, 72(1):957–960, 2001.

[61] Sherrill et al. 3935, pages 14–22. SPIE, 2000.

[62] N. Konjevic. *Physics Reports*, 316:339–401, 1999.

[63] *CRC Handbook of Chemistry and Physics.* Chemical Rubber Company.

[64] C.S. Williams and O.A. Becklund. *Introduction to the Optical Transfer Function.* John Wiley and Sons, 1989.

[65] J.C. Danity and R. Shaw. *Image Science.* Academic Press, 1974.

[66] J. Gonzalo et al. *J. Appl. Phys.*, 77(12):6588–6593, 1995.

[67] *A user's guide to Andor ICCDs.*

[68] Andor Technology. www.andor-tech.com.

[69] M. Aden and E.W. Kreutz. *Appl. Surf. Sci.*, 96-98:39–44, 1996.

[70] A.M. Marapaung et al. *J. Phys. D: Appl. Phys.*, 34:758–771, 2001.

[71] D.C. Emmony and J. Irving. *Brit. J. Appl.Phys. (J. Phys. D)*, page 1186, 1969.

[72] K.W. Mah et al. *Applied Physics Letters*, 80(18):3301–3303, 2002.

[73] http://www.physics.nist.gov/.

[74] F. Fuso et al. *Appl. Surf. Sci.*, 96-98:181–185, 1996.

[75] J. Hermann et al. *Appl. Surf. Sci.*, 127-129:645–649, 1998.

[76] B. Toftmann et al. *Appl. Surf. Sci.*, 186:293–297, 2002.

[77] R.D. Cowan et al. *J. Phys. B: At. Mol. Opt.*, 30:1457–1466, 1997.

[78] A.G. Gaydon R.W.B. Pearse. *The Identification of Molecular Spectra*. Chapman and Hall, London, 1965.

[79] C. Vivien et al. *J. Phys. D: Appl. Phys.*, 31:1263–1272, 1998.

[80] C. Dutouquet et al. *Spectrochim. Acta. Part B*, 56:629–635, 2001.

[81] Roger Kelly. *J. Chem. Phys.*, 92(8):5047, 1990.

[82] R.F. Wood et al. *Phys. Rev. Lett.*, 79(8):1571, 1997.

[83] Takashi Fujimoto and R.W.P. McWhirter. *Phys. Rev. A*, 42(11):6588, 1990.

[84] F.J. Gordillo-Vazquez et al. *Appl. Phys. Lett.*, 78(1):7, 2001.

[85] George Bekefi, editor. *Principles Of Laser Plasmas*. John Wiley and Sons, 1976.

[86] M.W. Stapleton. PhD thesis, Physical Sciences, Dublin City University, 2003.

[87] H. Takahashi et al. *J. Crys. Growth*, 259:36–39, 2003.

List of Figures

List of Tables

Appendix A

Publications and Conferences

Publications

A.P. McKiernan and J.-P. Mosnier, Appl. Surf. Sci., 197-198:325-330, 2002

Conferences

"6th International Conference on Laser Ablation", 2001, Tsukuba, Japan

"Quantum, Atomic, Molecular and Plasma Physics Conference", 2003, Milton Keynes, UK

"7th International Conference on Laser Ablation", 2003, Crete, Greece

Appendix B

Photographs of System

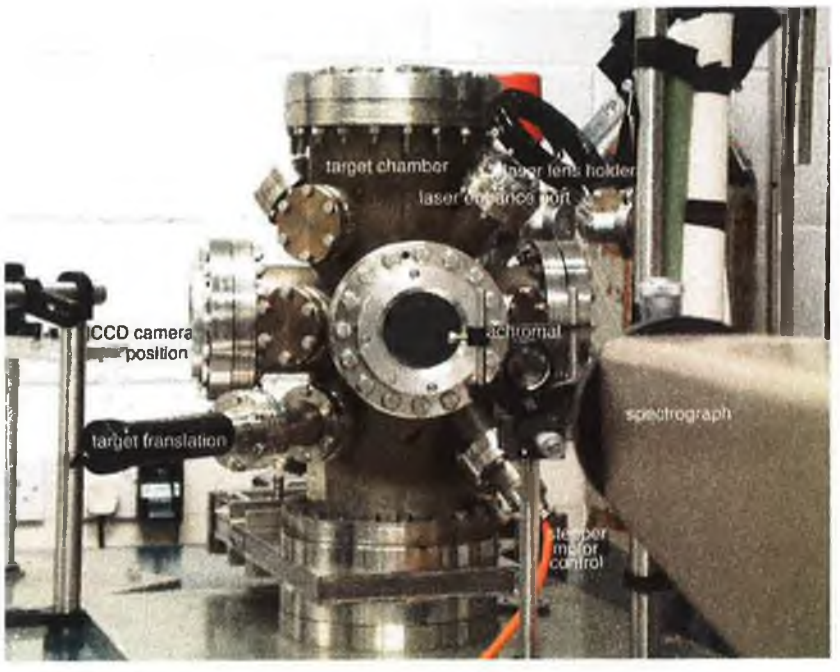

Figure B.1: Picture of target chamber showing achromat lens and spectroscope.

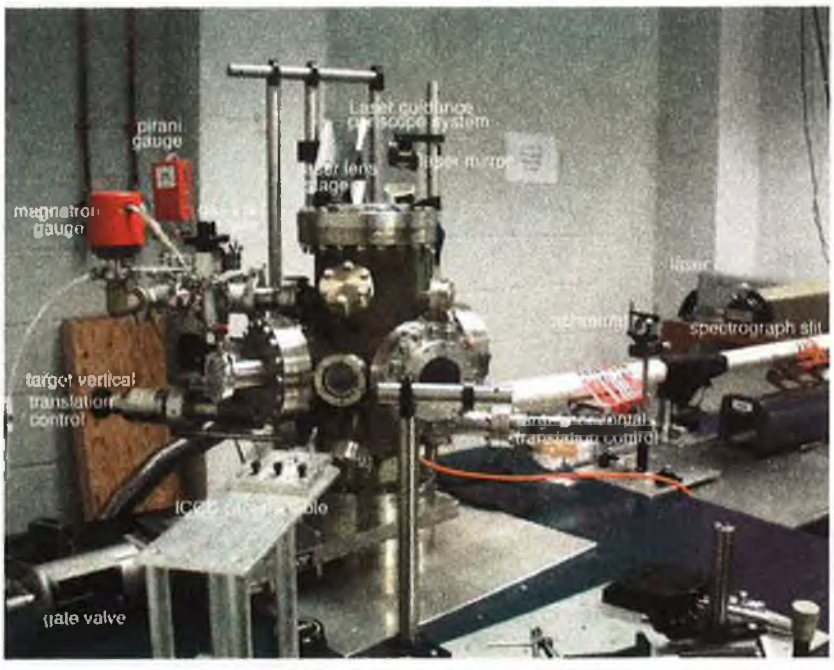

Figure B.2: Another view of target chamber.

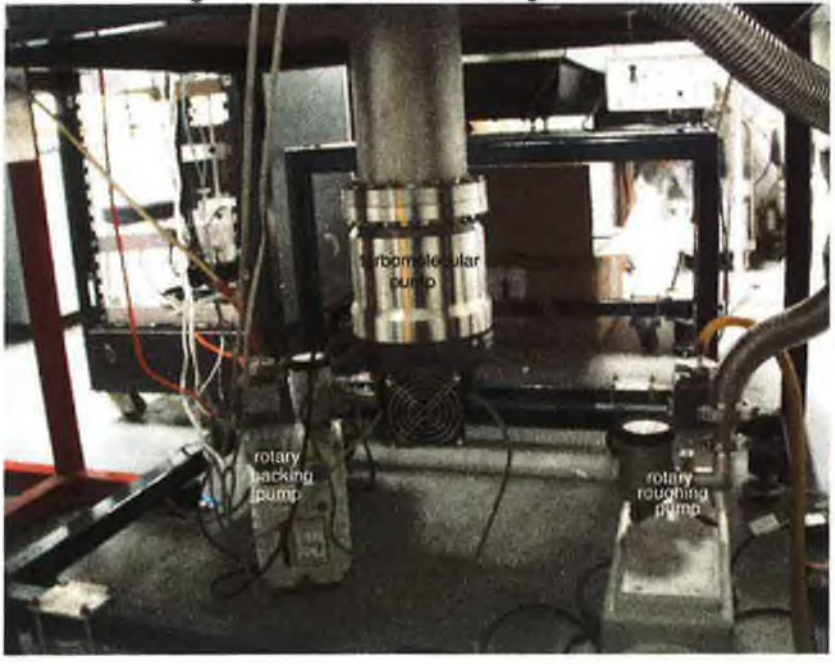

Figure B.3: Chamber pumping system

Figure B.4: The Hilger medium quartz spectrograph.

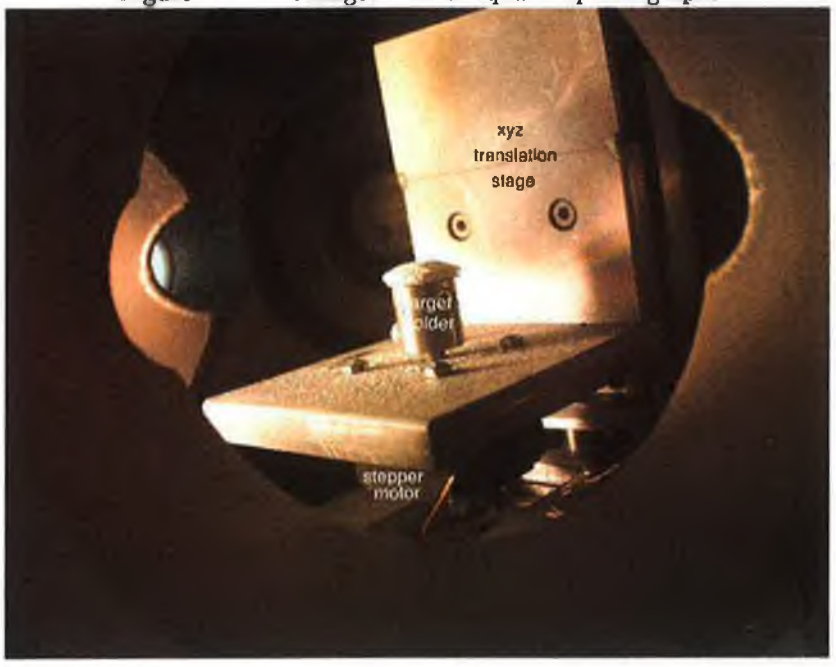

Figure B.5: A view of the target holder, translation and rotation setup.

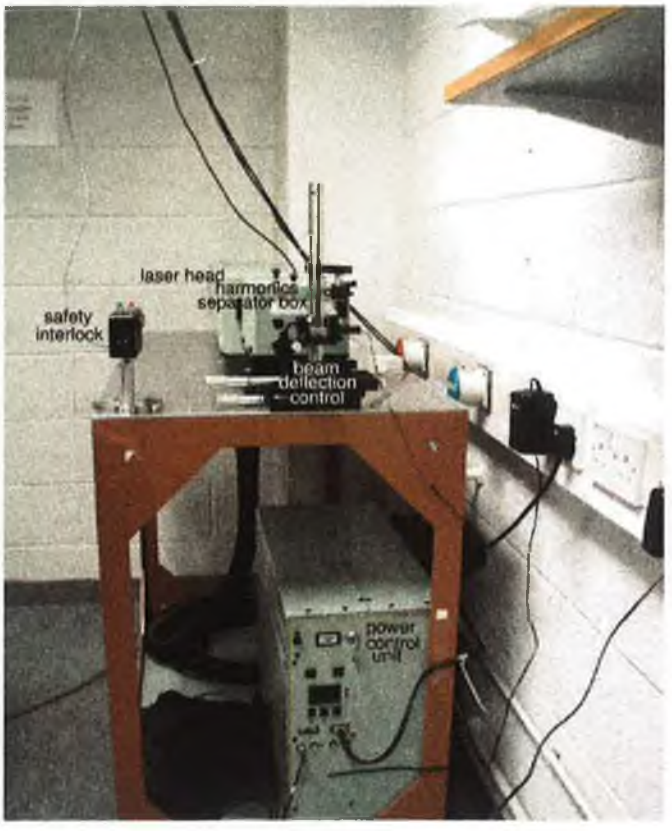

Figure B.6: The self-contained laser, harmonics separator and power unit setup.

Appendix C

Photographic Film Specifications

KODAK PROFESSIONAL High-Speed Infrared Film

—NOTICE—

Discontinuance of Sheet Format
KODAK High-Speed Infrared Film / HSI / 4143

Due to declining demand, sheet sizes of KODAK High-Speed Infrared Film / HSI have been discontinued.

Note: KODAK High-Speed Infrared Film will continue to be available in 35 mm format.

KODAK PROFESSIONAL High-Speed Infrared Film is a high-speed film with moderately high contrast, sensitive to light and radiant energy to 900 nanometres (nm) in wavelength. It is useful for haze penetration and for special effects in commercial, architectural, fine art, and landscape photography. With development variations, you can use this film for scientific, medical, aerial photography, and document copying. You can also use it for photomicrography, photomechanical, and remote-sensing applications.

Infrared films are sensitive to infrared radiation, some ultraviolet radiation, and to all wavelengths of visible radiation (light). They are not as sensitive to green light.

Whatever the ultimate purpose of your photographs, infrared photography provides unusual effects obtainable by few other means.

Note:

- Normal ISO speed values do not apply to this film.
- A filter is necessary for most applications.
- This film may not be suitable for a high degree of enlargement.

FEATURES	BENEFITS
• Moderately fine grain	• Good for producing high-quality infrared images
• Medium resolving power	• Good rendition of detail
• High-speed infrared sensitivity	• Expanded sensitivity versus other manufacturers' film infrared films—sensitivity ranges through the visible spectrum to about 900 nm in the infrared region
• Special sensitivity applications	• For aerial, astronomical, biological, documentary, industrial, laser, landscape, medical, and scientific photography • Suitable for distant haze penetration and abstract pictorial effects

SIZES AVAILABLE

Rolls

Roll	Base	Letter Code	CAT No.
135-36	4-mil ESTAR	HIE	169 2065

STORAGE AND HANDLING

Handle this film only in *total darkness*. Test your camera, film holders, processing equipment, and darkroom to ensure that they are opaque to infrared radiation. Load and unload your camera in *total darkness*. Store loaded film holders and cameras in subdued light, or total darkness if possible. Do not use a safelight during handling or processing.

Infrared films are susceptible to static markings at low relative humidity. If static problems persist, grounding the camera may be necessary to avoid a buildup of static electricity.

High temperatures or high humidity may produce unwanted quality changes. Store *unexposed* film at 55°F (13°C) or lower in the original package. Always store film (exposed or unexposed) in a cool, dry place. For best results, process film as soon as possible after exposure.

Protect *processed* film from strong light, and store it in a cool, dry place. For more information on storing negatives, *see* KODAK Publication No. E-30, *Storage and Care of Photographic Materials—Before and After Processing*.

EXPOSURE

Trial Exposures

We cannot give exact speed numbers for this film because the ratio of infrared to visible energy varies, and most exposure meters measure only visible radiation. Make test exposures to determine the proper exposure for your application. For trial exposures under average conditions, use the meter settings in the table on page 3. Use these settings with exposure meters marked for ISO, ASA, or DIN speeds or exposure indexes; they are based on development in KODAK Developer D-76.

Filters

To enhance the infrared effect on the film, you must use a filter over the lens (or light source) to absorb the ultraviolet radiation and blue light to which the film is also sensitive. A KODAK WRATTEN Gelatin Filter No. 25 (red) works well for most daylight applications. This filter blocks UV radiation and blue light; however, it passes red light that allows visual focusing. If you want to record *only* infrared radiation, use a filter that blocks all UV and visible radiation, such as KODAK WRATTEN Gelatin Filter No. 87, 87C, or 89B. Your choice of filter depends on the photographic effect you want to create.

Filters for Photography in the Infrared Region of the Spectrum

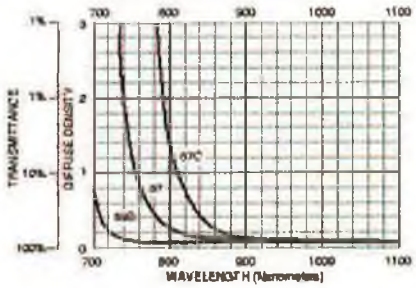

Wavelength	Percent Transmittance of Infrared Filters		
	No. 87	No. 87C	No. 89B
700	—	—	11.2
10	—	—	32.4
20	—	—	57.5
30	—	—	69.1
40	0.8	—	77.5
50	3.5	—	83.1
60	12.3	—	85.0
70	22.1	—	86.1
80	33.2	—	87.0
90	44.9	0.55	87.7
800	56.9	3.0	88.1
10	63.2	6.8	88.4
20	68.0	18.2	88.6
30	73.3	25.7	88.8
40	76.3	38.0	89.0
50	78.5	48.4	89.2
60	79.5	57.5	89.4
70	80.4	65.3	89.6
80	80.7	72.5	89.8
90	81.4	78.5	89.9
900	81.9	80.6	90.0
10	82.1	82.2	90.1
20	82.7	83.3	90.2
30	83.1	84.7	90.3
40	83.4	85.5	90.4
50	83.8	86.4	90.5
60	84.0	87.2	90.5
70	84.3	87.7	90.5
80	84.6	88.3	90.5
90	84.9	88.8	90.5
1000	85.3	89.2	90.5
10	85.6	89.7	90.5
20	85.9	90.1	90.5
30	86.2	90.5	90.5
40	86.6	90.8	90.5
50	87.0	91.3	90.5
60	87.5	91.7	90.5
70	87.8	92.2	90.5
80	88.1	92.5	90.5
90	88.3	92.7	90.5
1100	88.5	93.0	90.5

Film Speed

You cannot make exact meter readings to determine exposure for infrared films. Exposure meters are not calibrated for infrared radiation, and the ratio of infrared to visible radiation varies with the light source.

Make trial or bracketing exposures over a five-stop range to determine the proper exposure for your application. Under average conditions, use the following speed ratings to make starting-point exposures with ***handheld meters or through-the-lens light meters***. For through-the-lens camera

meters, make your readings before mounting the filter over the lens. Then ignore the meter reading/readout after attaching the filter.

Suggested Film Speeds Using a Handheld Light Meter		
KODAK WRATTEN Gelatin Filter	Daylight or Electronic Flash	Tungsten
No. 25, 89, or 89B	50/18*	125/22†
No. 87	25/15*	64/18*
No. 87C	10/11*	25/15*
No filter	80/20*	200/24*

* If you are using a camera with a through-the-lens meter and a filter over the lens, use EI 200.
† If you are using a camera with a through-the-lens meter and a filter over the lens, use EI 500.

Focusing

Lenses do not focus infrared radiation in the same plane as visible radiation. Because infrared radiation is longer in wavelength than visible radiation, the focus point is farther from the camera lens. Therefore, the lens must be moved slightly farther from the film to focus an infrared image. This focus difference is most critical when using filters to block all visible radiation from the film.

Most camera lenses have an auxiliary infrared focusing mark. Consult your camera manual for the appropriate one.

For best definition, make all exposures at the smallest lens opening that conditions permit. If you must use large apertures and the lens has no auxiliary infrared focusing mark, establish a focus setting by trial and error. Try extending the lens by 0.25 percent of its focal length beyond the correct focus for visible light.

For example, a 200 mm lens would require a 0.50 mm extension as 200 mm x 0.0025 = 0.50 mm.

Daylight

For subjects in bright or hazy sunlight (distinct shadows):

Exposed through a KODAK WRATTEN Gelatin Filter No. 25		No Filter
Distant Scenes	Nearby Scenes	Distant Scenes
1/125 sec at f/11	1/60 sec at f/8	1/125 sec at f/16

Electronic Flash

Use the appropriate guide number in the following table as a starting point for your equipment. Select the unit output closest to the number given by your flash manufacturer. Then find the guide number for feet or meters. To determine the lens opening, divide the guide number by the flash-to-subject distance. If the negatives are consistently too dense (overexposed), use a higher guide number; if they are too thin (underexposed), use a lower number.

Unit Output (BCPS)*	Guide Number Distances in Feet/Meters
350	20/6
500	24/7
700	30/9
1000	35/11
1400	40/12
2000	50/15
2800	60/18
4000	70/21
5600	85/26
8000	100/30

* BCPS = beam candlepower seconds

DARKROOM RECOMMENDATIONS

Do not use a safelight. Handle unprocessed film in total darkness.

Darkrooms must block all infrared radiation as well as light. Painted windows, plastic sheeting, etc., though opaque, may freely transmit infrared radiation and fog this film.

Note: Infrared films are susceptible to static markings at low relative humidity. Handle with care in the darkroom. If static electricity problems persist, grounding the camera may be necessary during loading and unloading to avoid a building of static electricity.

EXPOSURE ADJUSTMENTS FOR LONG AND SHORT EXPOSURES

Multiply the normal (unfiltered) exposure time by the filter factor.

Indicated Exposure Time (sec)	Multiply Exposure Time by This Filter Factor
1/1 000	1.25
1/100	1.0
1/10	1.0
1	1
10	1.0
100	1.5

MANUAL PROCESSING

Starting-Point Recommendations

The various pictorial, scientific, and technical applications of this film may require negatives of different contrast indexes. The following starting-point recommendations are intended to produce a contrast index close to that listed in the table. Make tests to determine the best development time for your application.

Note: Development times shorter than 5 minutes may produce unsatisfactory uniformity.

Small-Tank Processing (8- or 16-ounce tank)—Rolls

With small single- or double-reel tanks, drop the loaded film reel into the developer and attach the top to the tank. Firmly tap the tank on the top of the work surface to dislodge any air bubbles. Provide initial agitation of 5 to 7 inversion cycles in 5 seconds, i.e., extend your arm and vigorously twist your wrist 180 degrees.

Then repeat this agitation procedure at 30-second intervals for the rest of the development time.

KODAK High Speed Infrared Film / Hie						
KODAK Developer	CI	Small Tank* Development Time (Minutes)				
		65°F (18°C)	68°F (20°C)	70°F (21°C)	72°F (22°C)	75°F (24°C)
XTOL	0.52	6 1/2	5 1/2	5	—	4
XTOL	0.58	7 1/4	6	5 1/2	—	4 1/2
XTOL	0.65	8	6 3/4	6	—	5
XTOL	0.75	9 1/4	7 3/4	7	—	5 3/4
XTOL	0.85	10 1/2	9	8	—	6 1/2
XTOL (1:1)	0.52	—	6	7 1/2	—	6 1/4
XTOL (1:1)	0.58	—	6 3/4	6 1/4	—	7
XTOL (1:1)	0.65	—	9 3/4	9	—	7 1/2
XTOL (1:1)	0.75	—	10 3/4	10	—	8 1/2
XTOL (1:1)	0.85	—	12 1/2	11 1/2	9 1/4	7 1/2
D-76	0.70	9 1/2	8 1/2	7 1/2	7	6
HC-110 (Dil B)†	0.60	6	5	5	4 1/2	4
D-19‡	1.65	7	6	5 1/2	5	4
T-MAX (1.50 D-max)	0.55	—	—	—	—	4
T-MAX (1.75 D-max)	0.60	—	—	—	—	5
T-MAX (2.00 D-max)	0.91	—	—	—	—	8
T-MAX (2.35 D-max)	1.03	—	—	—	—	7
T-MAX (2.41 D-max)	1.15	—	—	—	—	8

* With agitation at 30-second intervals. Development times shorter than 6 minutes may produce unsatisfactory uniformity.
† For scientific use.
‡ For maximum contrast.

Tray Processing

Provide continuous agitation; rotate the sheets 90 degrees as you interleave them.

KODAK High Speed Infrared Film / HSI						
KODAK Developer	CI	Development Time (Minutes)				
		65°F (18°C)	68°F (20°C)	70°F (21°C)	72°F (22°C)	75°F (24°C)
D-76	0.70	11	9½	8½	7½	6½
HC-110 (Dil B)*	0.80	5	4½	4½	4¼	4
D-19†	1.65	5½	5	5	4½	4

* For scientific use
† For maximum contrast

Large-Tank Processing (1½- to 3½-gallon tank)—Rolls and Sheets

Agitate continuously for the first 15 to 30 seconds by raising and lowering the basket, rack, or spindle ½ inch. Do not agitate the basket, rack, or spindle for the remainder of the first minute. Then agitate once per minute by lifting the basket, rack, or spindle out of the developer, tilting it approximately 30 degrees, draining it for 5 to 10 seconds, and immersing it. Alternate the direction of tilting the basket, rack, or spindle.

KODAK High Speed Infrared Film / HIE and HSI						
KODAK Developer	CI	Large Tank*—Rolls or Sheets Development Time (Minutes)				
		65°F (18°C)	68°F (20°C)	70°F (21°C)	72°F (22°C)	75°F (24°C)
XTOL	0.52	8½	6¾	6	—	4¾
XTOL	0.58	10	8	7	—	5½
XTOL	0.65	11½	9	8	—	6¼
XTOL	0.75	13	10½	9	—	7
XTOL	0.85	14½	11½	10	—	7¾
D-76	0.70	10	9	8	7½	6½
HC-110 (Dil B)†	0.80	6½	5½	5½	5	4½
D-19‡	1.65	8½	7½	6½	6	5

* With manual agitation at 1-minute intervals. Development times shorter than 6 minutes may produce unsatisfactory uniformity
† For scientific use
‡ For maximum contrast

KODAK High Speed Infrared Film / HIE						
KODAK Developer	CI	Large Tank*—Rolls Development Time (Minutes)				
		65°F (18°C)	68°F (20°C)	70°F (21°C)	72°F (22°C)	75°F (24°C)
T-MAX (1.50 D-max)	0.65	—	—	—	—	8
T-MAX (1.76 D-max)	0.80	—	—	—	—	6
T-MAX (2.00 D-max)	0.91	—	—	—	—	5
T-MAX (2.36 D-max)	1.08	—	—	—	—	6
T-MAX (2.44 D-max)	1.15	—	—	—	—	7

* With manual agitation at 1-minute intervals. Development times shorter than 6 minutes may produce unsatisfactory uniformity

FINAL STEPS IN TANK, TRAY AND ROTARY-TUBE PROCESSING—

65 to 75°F (18 to 24°C)

Step/Solution	Time (min:sec)
Rinse—with agitation:	
KODAK Indicator Stop Bath	0:30
KODAK EKTAFLO Stop Bath	0:30
Fix—with frequent agitation:	
KODAK Fixer	5:00 to 10:00
KODAK Rapid Fixer	2:00 to 4:00
KODAFIX Solution—Fixer	5:00 to 10:00
KODAK POLYMAX—Fixer	5:00 to 10:00
Wash:	
Running water —OR— Rinse with water KODAK Hypo Clearing Agent Running water	20:00 to 30:00 0:30 1:00 to 2:00 5:00
Final rinse:	
KODAK PHOTO-FLO Solution	0:30
Dry—in a dust-free place	

IMAGE-STRUCTURE CHARACTERISTICS

The following information is based on development in KODAK D-76 Developer, 68°F (20°C), for 10 minutes.

KODAK High Speed Infrared Film / HIE and HIR	
Diffuse rms Granularity*	18 Fine

* Read at a net diffuse density of 1.0, using a 48 micron aperture, 12X magnification.

Characteristic Curves for KODAK PROFESSIONAL High-Speed Infrared Film / HIE

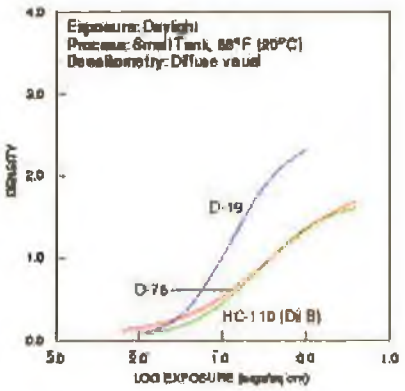

Characteristic Curves for KODAK PROFESSIONAL High-Speed Infrared Film / HIR

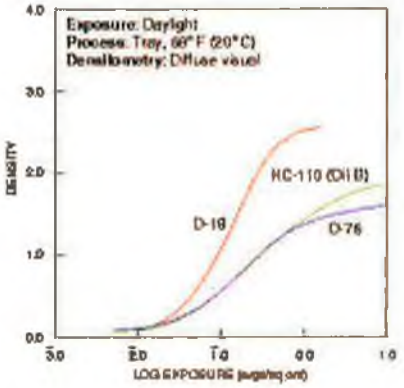

Contrast-Index Curves for KODAK PROFESSIONAL High-Speed Infrared Film / HIR

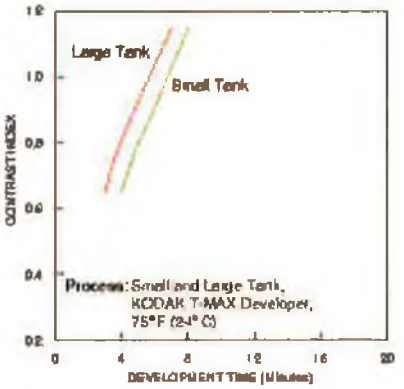

Spectral-Sensitivity Curves for KODAK PROFESSIONAL High-Speed Infrared Film / HIE and HSI

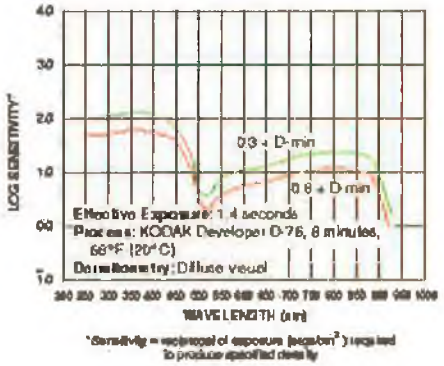

*Sensitivity = reciprocal of exposure (lux-sec) required to produce specified density

Modulation-Transfer Curves for KODAK PROFESSIONAL High-Speed Infrared Film / HIE and HSI

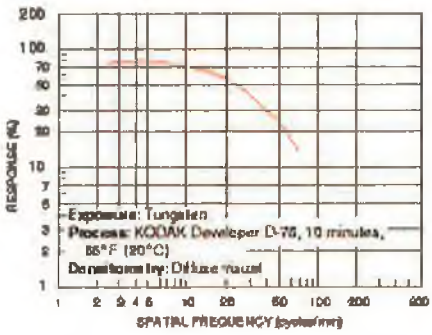

NOTICE: The sensitometric curves and data in this publication represent product tested under the conditions of exposure and processing specified. They are representative of production coatings, and therefore do not apply directly to a particular box or roll of photographic material. They do not represent standards or specifications that must be met by Eastman Kodak Company. The company reserves the right to change and improve product characteristics at any time.

MORE INFORMATION

Kodak has many publications to assist you with information on Kodak products, equipment, and materials.

The following publications are available from Kodak Customer Service, from dealers who sell Kodak products, or you can contact Kodak in your country for more information.

E-30	*Storage and Care of KODAK Photographic Materials—Before and After Processing*
E100BF	*KODAK PROFESSIONAL Black-and-White Films*
E100CF	*Chemicals for KODAK PROFESSIONAL Black-and-White Films*
J-24	*KODAK HC-110 Developer*
J-78	*KODAK Developers D-76*
J-86	*KODAK T-MAX Developers*
J-100	*KODAK XTOL Developer*
K-4	*How Safe Is Your Safelight?*

For the latest version of technical support publications for KODAK PROFESSIONAL Products, visit Kodak on-line at
http://www.kodak.com/go/professional

In the U.S.A.
1-800-242-2424, Ext. 19 Monday–Friday
9 a.m.–7 p.m. (Eastern time)

In Canada
1-800-465-6325, Monday–Friday
8 a.m.–5 p.m. (Eastern time)

Note: The Kodak materials described in this publication for use with KODAK PROFESSIONAL High-Speed Infrared Film are available from dealers who supply KODAK PROFESSIONAL Products. You can use other materials, but you may not obtain similar results.

Kodak Professional

KODAK PROFESSIONAL
High-Speed Infrared Film
KODAK Publication No. F-13
CAT 135 1221

Minor Revision 12-02
Printed in U.S.A.